Resonant Inelastic X-ray Scattering Study of Kitaev Spin Liquid Candidates

Von der Fakultät Mathematik und Physik der Universität Stuttgart zur Erlangung der Würde eines Doktors der Naturwissenschaften (Dr. rer. nat.) genehmigte Abhandlung

Vorgelegt von:
Zichen Yang
aus Shaanxi, China

Hauptberichter:	Prof. Dr. Bernhard Keimer
Mitberichter:	Prof. Dr. Martin Dressel
Prüfungsvorsitzender:	Prof. Dr. Maria Daghofer

Tag der mündlichen Prüfung: 02.07.2024

Max-Planck-Institut für Festkörperforschung
Universität Stuttgart

Stuttgart, 2024

Written confirmation of the independently provided performance in accordance with § 6 section (3) of the doctoral degree regulations of the University of Stuttgart

The submitted thesis on the topic

Resonant Inelastic X-ray Scattering Study of Kitaev Spin Liquid Candidates

represents my independently provided performance.
I have exclusively used the sources and means indicated. I have marked as such information taken over literally or in content from other works.
I confirm the correctness of the information given here and assure that I have explained the truth to the best of my knowledge.

Stuttgart, 22.05.2024

_____

(signature of doctoral student)

Contents

Acronyms

RIXS Resonant inelastic X-ray scattering

XAS X-ray absorption spectroscopy

TEY Total electron yield

FY Fluorescence yield

INS Inelastic neutron scattering

EELS Electron energy loss spectroscopy

IXS inelastic X-ray scattering

PES photoemission spectroscopy

IRIXS Intermediate resonant inelastic X-ray scattering

$RuCl_3$ α-$RuCl_3$

DESY Deutshes Elektronen-Synchrotron

ESRF European Synchrotron Radiation Facility

DCM Double crystal monochromator

4B inline HRM Four-bounce inline high resolution monochromator

KB mirror Kirkpatrick-Baez mirror

SDD Silicon drift detector

CCD Charge coupled device

AFM Antiferromagnetic

FM Ferromagnetic

QSL Quantum spin liquid

FWHM Full-width half-maixmum

2D Two-dimensional

VdW Van der Waals

PDMS Polydimethylsiloxane

PPC Poly-propylene carbonate

IETS Inelastic electron tunneling spectroscopy

hBN Hexagonal boron nitride

UHV Ultrahigh vacuum

SOC Spin-orbit coupling

QEP Quasielastic peak

XLD X-ray linear dichroism

XMCD X-ray magnetic circular dichroism

Zusammenfassung

Resonante inelastische Röntgenstreuung (RIXS im Folgenden) ist eine leistungsfähige spektroskopische Technik zur Untersuchung von Quantenmaterialien, deren Konzept mit der Einführung von Synchrotronanlagen der dritten Generation möglich wurde und in den letzten Jahrzehnten aufgrund kontinuierlich verbesserter Synchrotron-Technologien und leistungsfähiger Röntgenquellen weltweit eine Renaissance erlebte. Diese experimentelle Technik wurde auf eine Vielzahl von Materialsystemen angewendet, wie Übergangsmetalloxide, und hat eine Vielzahl fruchtbarer Ergebnisse geliefert, die die elektronischen und Spin-Strukturen sowie Ladungs-, Orbital- und magnetische Ordnungen und Fluktuationen in diesen Materialien aufzeigen, und damit wertvolle experimentelle Anhaltspunkte für das Verständnis ihrer Physik und für die Entwicklung der Grundlagenwissenschaften bereitstellen. Diese Arbeit präsentiert eine umfassende RIXS-Studie, einschließlich experimenteller, instrumenteller und theoretischer Aspekte, die sich auf Quantenmaterialien mit starken Korrelationseffekten konzentriert, insbesondere auf Festkörpersysteme, die möglicherweise Spin-Korrelationen in einer speziellen Form, bekannt als Kitaev-Spin-Flüssigkeit, aufweisen.

Bisher wurden RIXS-Messungen fast ausschließlich in den Energiebereichen von weichen Röntgenstrahlen (<2 keV) und harten Röntgenstrahlen (>5 keV) durchgeführt, während der Energiebereich dazwischen (bekannt als Tender- oder Intermediate-Röntgenstrahlen) aufgrund technischer und technologischer Herausforderungen im Zusammenhang mit der Verwendung optischer Elemente, die für dieses Regime geeignet sind, weitgehend unerschlossen ist. Um diese Lücke zu überbrücken, hat unsere Gruppe das Intermediate-RIXS (IRIXS)-Spektrometer an der P01-Beamline des Deutschen Elektronen-Synchrotrons (DESY) in Hamburg entworfen und gebaut, mit dem wir eine Vielzahl interessanter Beobachtungen an verschiedenen auf Ruthenium basierenden oder Ruthenium enthaltenden Verbindungen gemacht haben. Allerdings ist das Potenzial dieses Spektrometers bisher noch nicht voll ausgeschöpft worden. Einerseits ist die Energieauflösung dieses Spektrometers als zentrale Metrik der RIXS-Spektrometrie nicht hoch genug, um feinere Details in den

Spektren zu unterscheiden, wie zum Beispiel niederenergetische magnetische Anregungen oder kleine Energieverschiebungen und spektrale Veränderungen aufgrund struktureller Verzerrungen, obwohl die Energieauflösung seit der Inbetriebnahme von über 140 meV auf etwa 70 meV erhöht wurde. Tatsächlich stellte die ursprüngliche Konfiguration des Spektrometers Grenzen für weitere Verbesserungen dar, und als Konsequenz haben wir ein neues Spektrometer gebaut, das eine deutlich bessere Energieauflösung erreicht, die auf bis zu 30 meV verbessert werden kann. Andererseits waren spektroskopische Studien in diesem unerforschten Bereich der intermediären Röntgenstrahlen lange Zeit auf die Ru-L_3-Absorptionskante beschränkt, teilweise aufgrund der technischen Herausforderungen im Zusammenhang mit dem optischen Design in diesem intermediären Energiebereich. Kürzlich haben wir erfolgreich mehrere neue Analysatoren für das IRIXS-Spektrometer mit Rowland-Layout hergestellt und den verfügbaren Energiebereich auf bis zu ca. 3500 eV erweitert.

Mit dieser weltweit einzigartigen Instrumentierung konnten wir RIXS-Spektren an verschiedenen Quantenmaterialien sammeln. Insbesondere konzentriert sich diese Arbeit auf zwei Kitaev-Spin-Flüssigkeitskandidaten: α-$RuCl_3$ ($RuCl_3$ im Folgenden) und $Na_3Co_2SbO_6$. In den letzten Jahren haben magnetische Systeme mit frustrierten Wechselwirkungen viel Forschungsaufmerksamkeit auf sich gezogen, da sie die Fähigkeit haben, ungewöhnliche Phasen in Festkörpern zu beherbergen. Dieser Wechselwirkungsbereich umfasst die bekannte Kitaev-Spin-Flüssigkeit, eine aufgrund ihrer exakten Lösbarkeit und potenziellen Anwendung in fehlertoleranten Quantenberechnungen ausführlich diskutierte Phase. Der Vorteil von RIXS, sowohl elektronische als auch magnetische Anregungen zu messen, macht es zu einer leistungsfähigen Sonde, um die zugrunde liegenden Wechselwirkungsmechanismen aufzudecken. Mit dieser Technik haben wir das theoretische Bild eines Spin-Bahn-verschränkten Pseudospin-1/2-Grundzustands bestätigt und Einblicke in die Impuls- und Temperaturabhängigkeit magnetischer Korrelationen in diesen beiden Materialien gewonnen.

Interessanterweise ist $RuCl_3$ nicht nur ein Kandidat für ein Spin-Flüssigkeitssystem, sondern gehört auch zur Familie der zweidimensionalen Van-der-Waals-Materialien (konventionell als 2D-Materialien bezeichnet). Die Entwicklung der mechanischen Exfoliationstechnik zur Herstellung atomar dünner Monolagen von 2D-Materialien ist eine der prominestesten Entdeckungen der letzten 20 Jahrein in der Festkörperforschung. Die Exfoliationstechnik hat tatsächlich einen eine breite Plattform für Anwendungen und Grundlagenforschung in der Physik niedriger Dimensionen geschaffen. Die geringe Streuvolumen der Monolagen

hat jedoch deren Charakterisierung durch Röntgenspektroskopie eingeschränkt, und RIXS-Studien an dünnen Schichten oder Heterostrukturen sind technisch anspruchsvoll und besonders selten. Diese Herausforderung haben wir durch die Entwicklung einer integrierten Methode zur Probenpräparation gelöst, und wir haben RIXS-Spektren an $RuCl_3$-Nanolagen mit verschiedenen Dicken gemessen, um die Entwicklung ihrer elektronischen Struktur bei Annäherung an die 2D-Grenze zu untersuchen.

Diese Arbeit ist in folgende Kapitel unterteilt:

Kapitel 1 gibt einen Überblick über RIXS, das primäre spektroskopische Werkzeug, das in dieser Studie verwendet wird. Es erläutert die zugrunde liegenden physikalischen Mechanismen von RIXS und hebt seine Vorteile gegenüber alternativen spektroskopischen Methoden hervor. Darüber hinaus untersucht dieses Kapitel die Ableitung des Streuquerschnitts und führt den Modell-Hamiltonian ein, der die elektronische Struktur des Materialsystems beschreibt, aus der wir die Energie und die relativen Intensitäten der RIXS-Merkmale berechnen können.

Kapitel 2 stellt die wichtigste Infrastruktur für unsere RIXS-Messungen vor: die P01-Beamline am DESY und das Intermediate RIXS Spectrometer, der bisher weltweit einzige RIXS-Spektrometer, das im Tender-Röntgenenergiebereich mit einer Energieauflösung von unter 100 meV arbeitet. Bis heute kann es an den Absorptionskanten von Ru-L_3, Rh-$L_{2,3}$ und U-M_5 arbeiten und eine Energieauflösung von 30 meV an der Ru-L_3-Kante erreichen. Ich werde die Struktur, die technischen Parameter und die Leistung der Instrumente im Detail vorstellen und einige der vorläufigen Ergebnisse präsentieren, die mit diesem Spektrometer gesammelt wurden, um seine Fähigkeiten zur Durchführung verschiedener RIXS-Messungen an verschiedenen Absorptionskanten zu zeigen.

Kapitel 3 wird die wichtigsten Ergebnisse der Ru-L_3-RIXS-Messungen an $RuCl_3$-Bulkeinkristallen präsentieren. Wir haben mehrere spektrale Merkmale beobachtet, darunter Spin-Bahn-Exzitonen, sowie dd- und Landungstransfer-Anregungen, aus denen wir die wichtigsten Wechselwirkungsparameter von Spin-Bahn-Kopplung, Kristallfeldaufspaltung und Hund-Kopplung bestimmt haben. Wenn die Temperatur leicht über dem magnetischen Phasenübergangspunkt liegt, zeigt die Intensität des quasielastischen Peaks ein lokales Maximum im Brillouin-Zentrum, während kein Peak am Wellenvektor der antiferromagnetischen Ordnung, was auf das Vorhandensein konkurrierender magnetischer Ordnungen hinweist und die Bedeutung der ferromagnetischen Korrelation zur Verständnis des ungewöhnlichen magnetischen Grundzustands von $RuCl_3$ erneut bestätigt.

Anschließend wird in Kapitel 4 die Ru-L_3-RIXS-Studie an abgeschälten $RuCl_3$-Nanolagen vorgestellt. Durch Anwendung mehrerer Herstellungstechniken konnten wir die besten Nanolagen mit kleiner lateraler Größe auswählen und RIXS-Spektren mit akzeptablem Signal-Rausch-Verhältnis auf $RuCl_3$-Lagen mit einer Dicke von bis zu 3,5 nm erhalten. Wir haben festgestellt, dass die Anregungsenergie des Spin-Bahn-Exzitons eine nahezu vernachlässigbare Dickenabhängigkeit aufweist, während die d-d-Anregung deutlich rotverschiebt, wenn die 2D-Grenze erreicht wird. Diese Energieverschiebung zeigt eine enge Beziehung zur verringerten Kristallfeldaufspaltung, die vermutlich von der Gitterverzerrung an der Oberfläche der $RuCl_3$-Nanolage herrührt, in Übereinstimmung mit anderen Forschungsergebnissen.

Kapitel 5 stellt die spektroskopische Studie an dem $Na_3Co_2SbO_6$-Einkristall vor. Das Co^{2+}-Ion in dieser Verbindung hat eine $3d^7$-Konfiguration und ist ein weiteres Kandidatsystem der Kitaev-Spin-Flüssigkeitsphase, wie von mehreren theoretischen Arbeiten vorgeschlagen. Wir haben einen kombinierten Ansatz auf der Grundlage der optischen Raman- und Co-L_3-RIXS-Spektroskopie verwendet und Spin-Bahn-Exziton-, Spin-Übergangs- und d-d-Anregungen beobachtet und eine integrierte Beschreibung der elektronischen Struktur dieses Materials bereitgestellt. Mit Hilfe von Modellberechnungen haben wir festgestellt, dass der Pseudospin-1/2-Grundzustand anisotroper ist als die in früheren Arbeiten berichteten Ergebnisse. Darüber hinaus zeigen die Impuls- und Temperaturabhängigkeit von $Na_3Co_2SbO_6$ klare Analogien zu denen von $RuCl_3$ und deuten möglicherweise auf ähnliche magnetische Korrelationen hin.

Kapitel 6 ist eine kurze Zusammenfassung der wissenschaftlichen Ergebnisse, die wir in dieser Arbeit erzielt haben.

Abstract

Resonant inelastic X-ray scattering (RIXS hereafter) is a powerful spectroscopic technique to study quantum materials which became possible with the advent of third generation synchrotrons and has seen a revival in the recent decades due to the continuously improving synchrotron technologies and high quality X-ray sources around the world. This experimental technique has been applied to a variety of material systems such as transition metal oxides and yielded a plethora of fruitful results revealing the electronic and spin structures as well as charge-, orbital- and magnetic- orders and fluctuations in these materials, thereby providing valuable experimental evidence for the understanding of their physics and for the development of fundamental science. This thesis presents a comprehensive RIXS study including experimental, instrumental and theoretical aspects, focused on quantum materials with strong correlation effects, and especially, solid state systems which possibly exhibit spin correlations in a particular form known as Kitaev spin liquid.

To date, RIXS measurements were extensively carried out in the energy ranges of soft X-rays (<2 keV) and hard X-rays (>5 keV), whereas the energy range in between (known as tender or intermediate X-rays) is largely untapped due to technical and technological challenges related to the use of of optical elements appropriate for this regime. To bridge this gap, our group has designed and built the intermediate RIXS (IRIXS) spectrometer at the P01 beamline of Deutsches Elektronen-Synchrotron (DESY) in Hamburg, by which we have obtained a number of interesting observations on various Ru-based or ruthenate compounds. However, the potential of this spectrometer is not fully exploited so far. On one hand, as a central metric of RIXS spectrometry, the energy resolution of this spectrometer is not high enough to distinguish the finer details in the spectra, such as low energy magnetic excitations or small energy shifts and spectral evolutions due to structural distortions, although the energy resolution has dramatically improved from over 140 meV at commissioning down to around 70 meV by now. In fact, the original configuration of the spectrometer was imposing limits to further improvements, and as a consequence, we built a new spectrometer that achieves a much better energy resolution that can be pushed down

to 30 meV. On the other hand, for a long period of time the spectroscopic studies in this unexplored intermediate X-rays range were limited to the Ru-L_3 absorption edge, partly due to the technical challenges connected with the optics design in this intermediate energy range. Recently, we have successfully fabricated several new analyzers for the IRIXS spectrometer with Rowland layout and extended the available incoming energy range up to around 3500 eV.

With this state-of-the-art instrumentation which is unique worldwide in its capabilities, we were able to collect RIXS spectra on various quantum materials with exotic physics. In particular, this Thesis is focused on two Kitaev spin liquid candidates: α-$RuCl_3$ ($RuCl_3$ hereafter) and $Na_3Co_2SbO_6$. In recent years, magnetic systems with frustrated interactions have drawn much research attention for their capability to host unusual phases in solids. This interaction regime includes the well-known Kitaev spin liquid, an extensively discussed phase due to its exact solvability and potential application in fault-tolerant quantum computations. The advantage of RIXS to measure both electronic and magnetic excitations makes it an ideal probe to reveal the underlying interaction mechanisms. By using this technique, we confirmed the theoretical picture of a spin-orbit entangled pseudospin-1/2 ground state and provided insight into the momentum- and temperature-dependence of magnetic correlations in these two materials.

Interestingly, $RuCl_3$ is not only a candidate spin-liquid system, but also belongs to the two-dimensional (2D) van der Waals (VdW) material family (conventionally referred as 2D materials). The development of the mechanical exfoliation technique to obtain atomically thin monolayers of 2D materials is one of the most important discoveries over the last 20 years for material science, physics and technology at large. The exfoliation technique has in fact provided a wide playground for both applications and basic research of low dimensional physics. Nevertheless, the small scattering volume of the monolayers has restricted their characterization by X-ray spectroscopy, and RIXS studies on thin layers or heterostructures are technically nontrivial and particularly scarce. We have solved this challenge by developing an integrated method of sample preparation, and we have measured RIXS spectra on $RuCl_3$ nanolayers with various thicknesses to study the evolution of its electronic structure when approaching the 2D limit.

This thesis is organized into the following chapters:

Chapter 1 provides an overview of RIXS, the primary spectroscopic tool employed in this study. It elucidates the underlying physical mechanisms of RIXS, highlighting its advantages over alternative spectroscopic methods. Furthermore, this chapter explores the derivation of the scattering cross-section and introduces the model Hamiltonian governing the electronic structure of the material system, from which we can calculate the energies and relative intensities of the RIXS features.

Chapter 2 introduces the key infrastructure for our RIXS measurements: the P01 beamline at DESY and intermediate RIXS spectrometer, which is so far the only RIXS spectrometer in the world that works in the tender X-ray energy range with sub-100 meV energy resolution. To date, it can work at the absorption edges of Ru-L_3, Rh-$L_{2,3}$ and U-M_5, and reach an energy resolution of 30 meV at the Ru-L_3 edge. I will present the structure, technical parameters and performance of the instrument in detail, and present some of the preliminary results collected by this spectrometer to show its capabilities to carry out various RIXS measurements at different absorption edges.

Chapter 3 will present the key results of Ru-L_3 RIXS measurements on $RuCl_3$ bulk single crystals. We observed several spectral features including spin-orbit excitons, d-d and charge transfer excitations, from which we determined the key interaction parameters of spin-orbit coupling, crystal field splitting and Hund's coupling. When the temperature is slightly above the magnetic phase transition point, the intensity of the quasielastic peak shows a local maximum at the Brillouin zone center whereas no peak appears at the characteristic Bragg wavevector of zigzag magnetic order, which suggests the existence of competing magnetic orders and reconfirms the importance of ferromagnetic correlations to understand the intriguing magnetic ground state of $RuCl_3$.

Following this work, Chapter 4 will present the Ru-L_3 RIXS study on exfoliated $RuCl_3$ nanolayers. By applying several fabrication techniques, we were able to select the best nanolayers with small lateral size and obtain RIXS spectra with reasonable signal-to-noise ratio on $RuCl_3$ flakes as thin as 3.5 nm. We observed that the excitation energy of the spin-orbit exciton shows a nearly negligible thickness dependence, whereas the d-d excitation clearly red-shifts when approaching the 2D limit. This energy shift shows a close relationship to the decreased crystal field splitting, which is conjectured to originate from lattice distortions at the $RuCl_3$ nanolayer surface, in line with the result from the recent literature.

Chapter 5 presents a spectroscopic study on a $Na_3Co_2SbO_6$ single crystal. The Co^{2+} ion in this compound has a $3d^7$ configuration and is another candidate system of the Kitaev spin liquid phase, as suggested by several theoretical works. We used a combined approach based on optical Raman and Co-L_3 RIXS spectroscopy and observed the spin-orbit exciton, spin transition and d-d excitations and provided an integrated description of the electronic structure of this material. With the assistance of model calculations, we found that the pseudospin-1/2 ground state is more anisotropic than the results reported in the previous literature. Moreover, the momentum- and temperature- dependence of RIXS data of $Na_3Co_2SbO_6$ show clear analogies to that of $RuCl_3$ and possibly indicate a similar underlying physics.

Chapter 6 is a brief conclusion of the scientific results we obtained in this Thesis.

1 Resonant Inelastic X-ray Scattering

Resonant inelastic X-ray scattering (RIXS hereafter) is a powerful experimental probe in studying quantum materials with strong correlation effects physics. This spectroscopic method has several useful properties, such as charge-neutrality, resonance enhancement, element selectivity and momentum resolution.[1, 2] These features cannot be achieved at the same time by any other spectroscopic method, making RIXS uniquely suitable to study the electronic and magnetic properties of solid state systems. Whereas the energy resolution of RIXS for collective magnetic and vibrational excitations remains lower than the one of inelastic neutron scattering (INS), the latest generation of RIXS instruments has enabled detection of such excitations in many materials, and RIXS additionally probes charge and orbital excitations over a wide spectral range (meV to eV). Crucially, the large resonant enhancement of the scattering cross section at X-ray absorption edges, combined with the high photon flux at modern synchrotron sources, endow RIXS with a sensitivity that greatly exceeds the one of INS and has allowed the detection of excitations from microcrystals and thin films [3, 4, 5, 6].

In the following sections of this Chapter, I will start with a general introduction of this technique from the experimental point of view, including the interaction schemes during the scattering process and the elementary excitations that can be detected by RIXS. The scattering process naturally leads to the unique features stated above, and I will also discuss situations where RIXS significantly overperforms other spectroscopic methods. Based on these reasons, I have chosen RIXS as the primary experimental method for the study of condensed matter systems presented in this Thesis.

Following the review of the experimental aspects, I will present a more theoretical description of the physical process by deriving the scattering cross section. This cross section is however hard to evaluate without the knowledge of the eigenstates of the material. To tackle this problem, I will introduce the single ion model and Hamiltonian which is widely used in the study of insulating compounds. This Hamiltonian seems to be

oversimplified at the first glance, but it is able to provide a concise interaction scheme of the transition metal ions and capture the major spectral features of RIXS. With this model we can calculate the relative RIXS intensity, which has been a crucial complementary ingredient of the experiment data to understand the physics of the investigated materials, as we will see in the following chapters. At last, I will briefly discuss the self absorption effect and derive its correction factor.

1.1 Introduction

Resonant inelastic X-ray scattering is a photon in-photon out synchrotron-based spectroscopic technique.[1, 2] The idea of this spectroscopy was first proposed and experimentally carried out in 1970s,[7] but the wide application of this method on material studies was largely restricted by the synchrotron flux intensity and energy resolution. In the past two decades, the rapidly developed synchrotron sources have significantly improved the performance of existing beamlines, including flux intensity, monochrometry and energy resolution. These factors helped to overcome the obstacles and lead to a "Renaissance"(in word of A. Katoni and S. Shin, Ref[1]) of this experimental probe. Soon RIXS exhibits its great power in studying the elementary excitations in solid state systems, including electronic, magnetic and orbital structures and ordering phenomena.[8, 9, 10, 11] In particular, the capabilities of RIXS manifested themselves in the research of strong correlated systems exhibiting a great potential in providing information and shining light onto complex interactions schemes, such as the pairing mechanism in high temperature superconductor cuprates.[12, 13] One can in fact take full advantage of the large energy and momentum of X-ray photons, as well as the symmetry information indicated by polarization.

A remarkable feature of RIXS spectroscopy is that the incoming X-ray photon is resonantly absorbed by the target material. To be more specific, the energy of the incident X-ray photon is chosen such that it coincides with (and is hence resonant with) one of the atomic X-ray transitions of the system, and the incoming X-ray photon excites a core electron to a shallower state. The resonance can greatly enhance the scattering cross section, even by many orders of magnitude, and therefore help to obtain enough scattered photons to collect spectra with decent signal-to-noise ratio in a reasonable time.

The absorption energy can be roughly estimated from the binding energy of the excited core electron. In a hydrogen-like model, the binding energy is given by $E_n = -Z^2 Ry/n^2$, where Z is the atomic number, $Ry = 13.6$ eV is the Rydberg energy ($i.e.$ the binding energy of the hydrogen atom), and n is the principal quantum number. As the element becomes heavier, the absorption energy grows approximately by $\sim Z^2$, which leads to a energy that typically ranges from the order of ~ 100 eV to ~ 10 keV for transition metals. This energy scale is several orders of magnitude higher than the inter- and intra-band excitations of the valence electrons near the Fermi surface, and the production of X-ray photon beams with such high energy usually requires synchrotron radiation as light source. Nonetheless, we need to point out that the Rydberg model does not take into account any electron-electron interaction, while in a delicate treatment the Z^2 term needs to be renormalized as the result of screening effects. In practice, the absorption energy is experimentally determined by X-ray absorption spectroscopy (XAS) to select the best incident energy for RIXS measurements. The XAS can be either measured in total electron yield(TEY) mode by the drain current, or in total fluorescence yield (TFY) mode by measuring the fluorescence intensity from the sample. The absorption edges are named after the core electron shell by K, L, M, N... for n=1, 2, 3, 4 etc. To distinguish the fine structures within the shell, the absorption edges are further labeled by subscripts 1, 2, 3... ranked by the binding energy in descending order. For example, the L_1, L_2, L_3 edges corresponds to excitation from $2s$, $2p_{1/2}$ and $2p_{3/2}$ states, respectively.

1.2 RIXS process

Fig 1.1 shows a sketch of the RIXS process. Firstly the energy of the incoming photon $\hbar\omega_{k_i}$ is tuned to the selected absorption edge. This photon will be resonantly absorbed and excites a core electron to the empty valence band. This intermediate state is unstable, and another electron will soon fill the core hole, leave behind an excitation with energy $\hbar\omega$ and momentum $\hbar\vec{q}$, and emit another X-ray photon $\hbar\omega_{k_o}$. The whole process follows the energy and momentum conservation rule:

$$\hbar\omega = \hbar\omega_{k_i} - \hbar\omega_{k_o} \tag{1.1}$$

$$\hbar\vec{q} = \hbar\vec{k}_i - \hbar\vec{k}_o \tag{1.2}$$

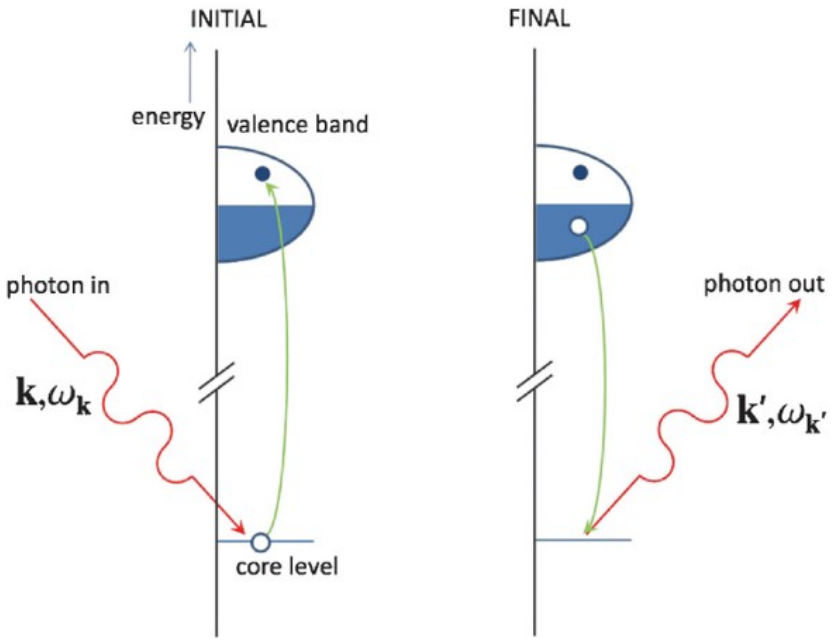

Figure 1.1: A direct RIXS scattering is described by a two-step process: resonant absorption (left panel) and emission (right panel). The incoming X-ray photon excites an electron from the core level into an unoccupied valence state. The unstable core hold is then filled by an valence electron and omits a X-ray photon with different energy and momentum. Figure reproduced from Ref [2].

where $\hbar\vec{k}_i$ and $\hbar\vec{k}_o$ are the momentum of the incoming and scattered photon, respectively. By the energy and momentum loss one can get the dispersion relation of the observed excitation. Notably, during the intermediate state another scattering between the valence electron and the core hole might occur due to the Coulomb interaction between these two quasiparticles. This is referred to indirect RIXS process, in contrast to the direct RIXS process discussed above. The indirect scattering process usually contributes a higher order term to the cross section of direct scattering and can be safely neglected. However, in the case when the direct process is forbidden, the RIXS cross section mainly relies on the indirect scattering channels.

Fig 1.2 shows a schematic of the variety of excitations RIXS can detect, ranging from phonons, magnons, d-d excitations and charge transfer excitations. Here we particularly focus on d-d excitations and magnetic excitations measured at the L_3 edge, which has provided unique insight to the material systems in comparison to other spectroscopic methods. From these excitations, we can obtain knowledge of magnetic correlation and local coordinates, as discussed in Chapter 3,4 and 5.

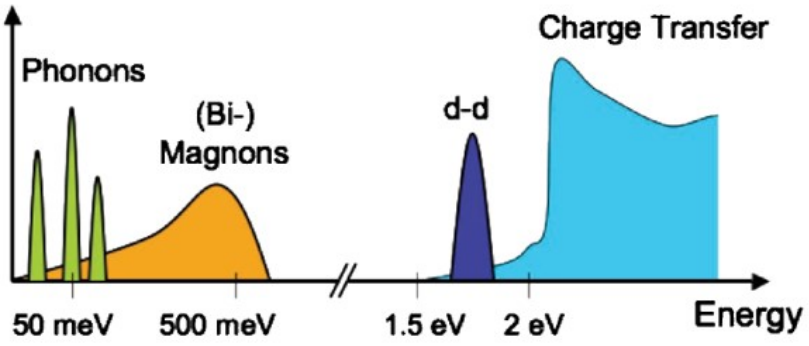

Figure 1.2: A sketch of the fundamental excitations that can be probed by RIXS, including phonons, magnons, d-d excitations and charge transfers. Figure reproduced from Ref [2].

In transition-metal compounds, the metal ion is usually surrounded by several ligand ions. These ligands generate a electrostatic field whose symmetry is lower than spherical and therefore splits the degenerate orbitals in the metal ion, a phenomenon known as crystal field splitting. In RIXS measurements, the transition between different crystal field states is commonly observed around 1~3 eV, which is also named as d-d excitation. Notably, d-d excitations ($\Delta l = 0$) are forbidden in dipole approximation whose selection rule requires $\Delta l = \pm 1$, but is possible in RIXS due to the two-step nature of the scattering process: the absorption and emission process in Fig. 1.1 are both dipole allowed. This feature makes RIXS a unique tool to directly probe d-d excitations in materials and investigate lattice deformations, as will be discussed in Chapter 4.

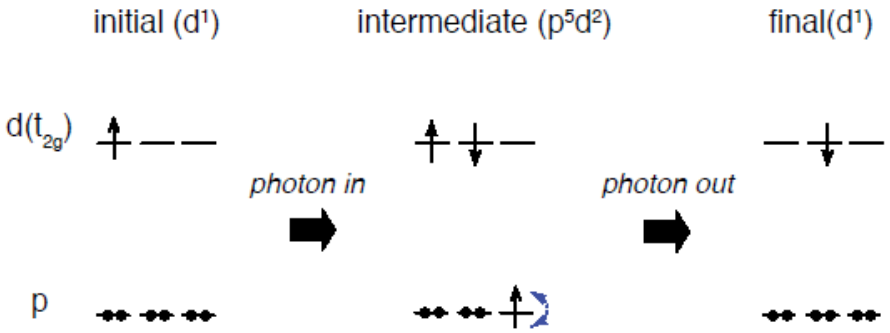

Figure 1.3: A schematic of L_3-RIXS process that creates a spin-flip in the d orbital. For simplicity the case of d^1 configuration is shown here. Figure reproduced from Ref[14]

Another remarkable feature of RIXS is the capability to detect magnetic excitations. Traditionally, INS has been an ideal tool to probe the magnetic excitations in solids. However, this spectroscopic technique is limited by the weak neutron-matter interaction and one has to prepare single crystals with large volume so as to elicit measurable scattering signals. This drawback is severe for ruthenates and other $4d$ transition-metal compounds due to the difficulty related to the growth of large crystals. In this case, RIXS provides an alternative choice. Since a photon carries angular momentum of $L = 1$, the RIXS process can transfer $\Delta L_z = 0, 1, 2$ to the electrons. This includes the cases of single magnon ($\Delta L = 1$) and bi-magnon ($\Delta L = 2$), as well as quasi-elastic spin fluctuations. Figure 1.3 shows a typical RIXS process that creates excitations with spin-flip. In the absorption step, an electron with down spin is excited from a $2p_{3/2}$ state and leaves a core hole. Due to the strong spin-orbit coupling of the $2p_{3/2}$ state, the spin may not be conserved and the spin of the core electron flips. In the emission step, the spin-up d electron decays to fill the core hole, leaving an electron with opposite spin in the d orbitals. Notably, in a system with fully-quenched orbital moment, the RIXS cross section reduces to the spin-spin correlation function.

In summary, RIXS spectroscopy uses X-ray photons as probe to reveal the excitations in material systems, whose information is given by the difference between the incoming and scattering photon states, including energy, momentum, and polarization. In light of this, RIXS can be classified into the family of energy-loss spectroscopy, including INS, electron energy loss spectroscopy (EELS), Raman spectroscopy and inelastic X-ray scattering (IXS) etc. Nonetheless, the light-matter interaction mechanism and resonant nature still make RIXS a unique experimental method in the study of condensed matter physics. Hereafter I clarify the major advantages of RIXS.

First, as a photon in-photon out technique, no charge is injected or emitted from the material during the scattering process, so that the system is kept charge neutral. On the contrary, in some other spectroscopic techniques such as photoemission spectroscopy (PES), electrons are ejected as the consequence of the light-matter interaction and a local hole is formed. If the target material is an insulator, the hole cannot be promptly filled from the external circuit and the final state will have less electrons compared to initial state. This fact usually brings unwanted charging problems and shifts the resulting spectra in energy. For RIXS, however, charging effects are not an issue.

Second, RIXS is element selective, due to the resonant absorption at a certain absorption edge. On one hand, the target material is easily distinguishable from any other element inside and around the sample, such as capping layer, substrate, holding device and sample holder and any tape, paint or paste used around and/or on top of the sample. This feature is of crucial importance in studying nanolayer samples with small lateral size (see Chapter 4). The target material exhibits strong absorption and fluorescence compared to non-resonant parts, which allows us to easily locate the tiny sample without a camera in the sample chamber. In addition, the intensity loss due to absorption from capping layers is largely suppressed compared to non-resonant spectroscopic methods such as Raman spectroscopy. Moreover, RIXS spectra exclusively capture the inelastic response from the target material that contains the element with resonant absorption effect, and other unwanted signals are blocked out except for minor contributions to the elastic signal of the collected spectra. This feature is powerful to study heterostructures, in the sense that the properties of different materials in different active layers can be studied separately. On the other hand, it is also possible to differentiate between the same element with inequivalent chemical environments or valence in the target material as long as the absorption edges are distinguishable.

Third, RIXS contains rich information about the properties of the excitations in the target material. This information includes three dimensions: energy, momentum and polarization. In RIXS measurements, the energy of incoming photons ranges from several hundreds eV (soft X-ray) to the order of 10 keV (hard X-ray), much greater than that of neutron scattering ($\sim$ 100 meV) or optical spectroscopy (Raman/infrared, $\sim$ 1 eV). As a consequence, RIXS is able to detect excitations with high energy, such as interband transitions, d-d excitations and charge transfer excitations *etc*. The large momentum of X-ray photons also enables one to cover a large momentum range in the reciprocal space to study the dispersive nature of the elementary excitations. In comparison, the momentum of optical photons is negligible compared to the size of the Brillouin zone, so that only excitations near the Γ point can be detected. The polarization degree of freedom also gives insights about the excitation symmetry and the shape of the involved electronic orbitals. By carefully selecting the polarization configuration of incoming and scattered light, one can get access to scattering channels with distinct symmetry. Remarkably, a polarization change necessarily indicates a change of orbital angular momentum of the electrons in the material, and indeed RIXS is capable to detect magnetic processes involving spin-flips, as discussed above. However, a full control of X-ray polarization is technically nontrivial. In practice, the incoming beam from a synchrotron source is always polarized but the polarization of scattered light is usually not analyzed.

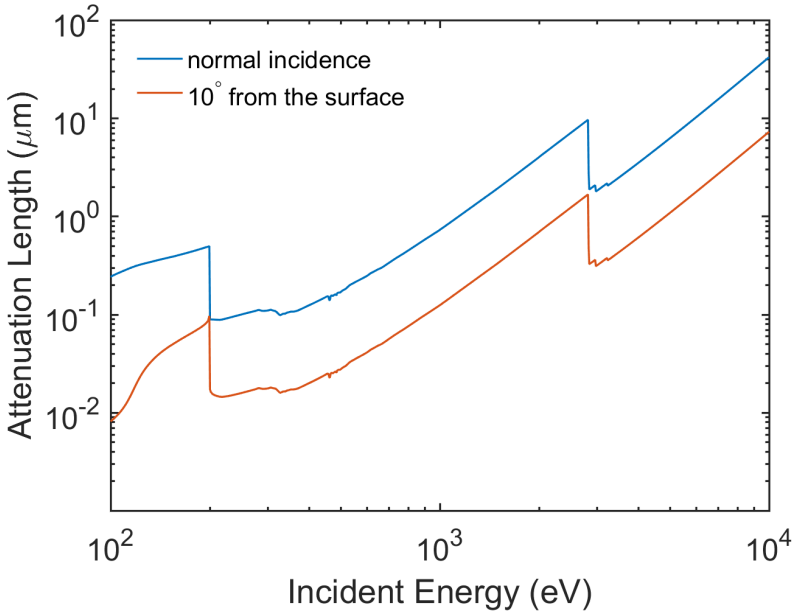

Figure 1.4: Attenuation length of $RuCl_3$ as a function of incoming photon energy. The blue and yellow curves shows the case of normal incidence and incident angle fixed at 10°, respectively. The data is simulated from Ref [15].

Another important capability of RIXS is the possibility to study both bulk and small samples. The electromagnetic interaction between the incoming X-ray and the studied material is much stronger, compared to the neutron-matter interaction cross section. In addition, a synchrotron source also delivers many order of magnitude more particles per second than a neutron source. This fact makes RIXS measurements possible on very tiny samples, such as thin films, surfaces layers and nano-objects. Meanwhile, RIXS is also bulk-sensitive in the sense that the typical penetration length ranges from tens of nanometers for soft X-rays to hundreds of micrometers for hard X-rays, as shown in Fig. 1.4. This fact can help to suppress the scattering from imperfect surfaces and interfaces and focus more on the bulk excitations. In contrast, EELS for example is only sensitive to the surface due to the strong scattering between the incoming electron and the electric field in the sample.

Nevertheless, RIXS still has also some limitations. To date, the best energy resolution one can reach with soft- and intermediate X-ray spectrometer is around 25 $\sim$ 30 meV, which is still much larger than that INS and Raman spectroscopy which can easily achieve an energy resolution of 1 meV. This leads to difficulty in distinguishing fine structures in the RIXS spectra, such as measuring the magnetic structure whose energy is below 10 meV,

or observing the small splitting due to slightly distorted crystal field. Another drawback is the "photon-hungry" nature of RIXS. Being a second-order scattering process, RIXS has a small scattering cross section even with the resonance enhancement, therefore a synchrotron light source with high brilliance is essential to carry out RIXS measurements. Thanks to the development of third generation synchrotrons, in recent years most RIXS spectra can be collected within a reasonable amount of time. Nevertheless, in some special cases the flux intensity remains an obstacle to RIXS studies. For example, in Chapter 2, we will see the trade-off between intensity and energy resolution in the intermediate RIXS (IRIXS) spectrometer. In Chapter 4, measurements on samples with extremely small volume will be discussed and require a considerable accumulation time to obtain a workable signal-to-noise ratio. It is expected that synchrotrons of the next generation and new designs of X-ray optics will provide solutions to many of these challenges in the future.

1.3 RIXS cross section

This section reviews the fundamental theories of RIXS and derives the expression of its scattering cross section, following the lines of Ref [2] and the references therein. The whole scattering process is discussed in the theoretical frame of light-matter interaction. In this frame, the incident X-ray beam is treated as an electromagnetic field and described by the vector potential $\mathbf{A}(\mathbf{r}, t)$. Meanwhile the interaction Hamiltonian terms are small, controlled by the fine structure constant $\alpha = e^2/4\pi\epsilon_0\hbar c \approx 1/137$ (SI unit), where e is the magnitude of elementary charge, ϵ_0 the permittivity of free space. As a consequence, the interaction can be safely treated as perturbation in this interacting system.

In order to introduce the Hamiltonian, one needs to take two limits. The first limit is the non-relativistic limit, i.e. the travel speed v of electrons in consideration is small compared to the speed of light c. This is a good approximation for electrons in materials. The second limit is that the potential describing the interaction between electrons and photons in the system are small compared to twice the mass of the electron ($e\phi/2mc^2, e\,|\mathbf{A}|\,/2mc \ll 1$).

For the currently available X-ray sources this limit is also satisfied. In these two limits, one obtains the Hamiltonian of a system with N electrons in SI units:

$$
\begin{aligned}
H &= \sum_i^N \Big(\frac{[\mathbf{p}_i + e\mathbf{A}(\mathbf{r}_i)]^2}{2m} - e\phi(\mathbf{r}_i) + \frac{e\hbar}{2m}\sigma_i \cdot \mathbf{B}(\mathbf{r}_i) \\
&+ \frac{e\hbar}{2(2mc)^2}\sigma_i \cdot \{\mathbf{E}(\mathbf{r}_i) \times [\mathbf{p}_i + e\mathbf{A}(\mathbf{r}_i)] - [\mathbf{p}_i + e\mathbf{A}(\mathbf{r}_i)] \times \mathbf{E}(\mathbf{r}_i)\} \\
&+ \frac{e\hbar^2\rho(\mathbf{r}_i)}{8(mc)^2\epsilon_0}\Big) + \int d\mathbf{k} \sum_\epsilon \hbar\omega_{\mathbf{k}}(a^\dagger_{\epsilon,\mathbf{k}} a_{\epsilon,\mathbf{k}} + \frac{1}{2})
\end{aligned} \tag{1.3}
$$

where $\mathbf{p}_i, \mathbf{r}_i$ and σ_i are the momentum and the position operators and the Pauli matrices acting on electron i, respectively. $\mathbf{E}(\mathbf{r}) = -\nabla\phi(\mathbf{r}) - \partial_t\mathbf{A}(\mathbf{r})$ and $\mathbf{B}(\mathbf{r}) = \nabla \times \mathbf{A}(\mathbf{r})$ are the electric and magnetic field corresponding to the potential $(\mathbf{A}(\mathbf{r}), \phi(\mathbf{r}))$. $a^\dagger_{\epsilon,\mathbf{k}}$ ($a_{\epsilon,\mathbf{k}}$) creates (annihilates) a photon with wave-vector $\mathbf{k}$ and polarization ϵ

The first two terms in the above Hamiltonian describe the electron kinetic and potential energy in the electromagnetic field $(\mathbf{A}(\mathbf{r}), \phi(\mathbf{r}))$. The third term is the Zeeman term which yields the Zeeman splitting. The fourth term denotes the spin-orbit coupling. The term proportional to $\rho(\mathbf{r})$ is the Darwin term emerging from relativistic correction. This term changes the effective potential at the nucleus and smears out the electrostatic interaction between the electron and the nucleus due to the rapid quantum oscillations of the electron. Unlike spin-orbit coupling, this term only affects the s orbitals, *i.e.* the only ones with a non-vanishing wave function at the core location. Finally the last term is the Hamiltonian of the radiation field in the second quantization form, expressed by summing up the Hamiltonian of each photon mode. The electron-electron interaction and electron-nuclei interaction are omitted.

In the framework of perturbation theory, the Hamiltonian H is split into the perturbation part (H') which describes the electron-photon interaction, and the main part H_0, which describes the electron (H_{el}) and photon (H_p) dynamics without interaction. Given that in H_0 the Hamiltonian of electron and photon are decoupled, the eigenstates can be expressed by the direct product of eigenstates of H_{el} and the eigenstates of H_p. For the photon part, with Fock base the eigenstates can be expressed by using creation operators on the vacuum state $|0\rangle$, where

$$
c_{\epsilon,\mathbf{k}}|0\rangle = 0, \quad \forall\epsilon, \mathbf{k} \tag{1.4}
$$

We assume that in the initial state there is a single incoming photon with momentum $\hbar\mathbf{k}_i$, energy $\hbar\omega_{\mathbf{k}_i}$ and polarization ϵ_i, and is scattered to $(\hbar\mathbf{k}_o, \hbar\omega_{\mathbf{k}_o}, \epsilon_o)$ in the final state. The scattering process induces a change in the material from ground state $|g\rangle$ to final state $|f\rangle$ with energies E_g and E_f, respectively. Therefore the ground state and final state of the whole system can be expressed by $|\mathrm{g}\rangle = |g\rangle|1_{\epsilon_i,\mathbf{k}_i}\rangle$ and $|\mathrm{f}\rangle = |f\rangle|1_{\epsilon_o,\mathbf{k}_o}\rangle$, where $|1_{\epsilon_i,\mathbf{k}_i}\rangle = a^\dagger_{\epsilon_i,\mathbf{k}_i}|0\rangle$ and $|1_{\epsilon_o,\mathbf{k}_o}\rangle = a^\dagger_{\epsilon_o,\mathbf{k}_o}|0\rangle$. The transition rate w given by the Fermi golden rule to the second order is thus:

$$w = \frac{2\pi}{\hbar}\sum_{\mathrm{f}}\left|\langle \mathrm{f}|H'|\mathrm{g}\rangle + \sum_n \frac{\langle \mathrm{f}|H'|n\rangle\langle n|H'|\mathrm{g}\rangle}{E_g + \hbar\omega_{\mathbf{k}_i} - E_n}\right|^2 \delta((E_f + \hbar\omega_{\mathbf{k}_o}) - (E_g + \hbar\omega_{\mathbf{k}_i})) \tag{1.5}$$

Here $|n\rangle$ is the eigenstate of H_0 with eigenenergy E_n.

In the case of RIXS where the absorption shows a strong resonant behavior, the second term will dominate over the first term due to the intermediate states $|n\rangle$ whose $E_n \approx E_g + \hbar\omega_{\mathbf{k}_i}$. On the contrary, the first term yields only non-resonant scattering and will be neglected. Next, by classifying the terms in Eqn.1.3 by the power of $\mathbf{A}(\mathbf{r})$ and omit the second order resonant scattering, Eqn.1.5 can be simplified as:

$$\begin{aligned} w &= \frac{e^2\hbar}{2m^2V\epsilon_0\sqrt{\omega_i\omega_o}}\sum_n\sum_{j,l}^{N}\frac{\langle f|e^{-i\mathbf{k_o}\cdot\mathbf{r}_l}[\epsilon_o^*\cdot\mathbf{p}_l - (i\hbar/2)\sigma_l\cdot\mathbf{k}_o\times\epsilon_o^*]|n\rangle}{E_g + \hbar\omega_{\mathbf{k}_i} - E_n + i\Gamma_n} \\ &\times \langle n|e^{i\mathbf{k}_i\cdot\mathbf{r}_j}(\epsilon_i\cdot\mathbf{p}_j + \frac{i\hbar}{2}\sigma_j\cdot\mathbf{k}_i\times\epsilon_i)|g\rangle \end{aligned} \tag{1.6}$$

where a lifetime broadening Γ_n is introduced for the intermediate states, as the result of many nonradiative interaction terms which are not included in H' such as Auger decay. This results shows that resonant scattering can occur via a magnetic and a nonmagnetic term. An estimate shows that the non-magnetic term dominates so that for simplicity we can neglect the magnetic term.

If we consider the dipole approximation, *i.e.* $e^{i\mathbf{k}\cdot\mathbf{r}}$ varies slowly at the length scale of the atomic wavefunction and can be treated as $e^{i\mathbf{k}\cdot\mathbf{r}} = 1 + i\mathbf{k}\cdot\mathbf{r} + \ldots \approx 1$, then the scattering cross section can be further reduced to:

$$\begin{aligned} w &= \frac{e^2\hbar}{2m^2V\epsilon_0\sqrt{\omega_i\omega_o}}\sum_n\sum_{j,l}^{N}\frac{\langle f|\epsilon_o^*\cdot\mathbf{p}_l|n\rangle\langle n|\epsilon_i\cdot\mathbf{p}_j|g\rangle}{E_g + \hbar\omega_{\mathbf{k}_i} - E_n + i\Gamma_n} \\ &\approx \frac{e^2\hbar}{2m^2V\epsilon_0}\sqrt{\omega_i\omega_o}\sum_n\sum_{j,l}^{N}\frac{\langle f|\epsilon_o^*\cdot\mathbf{r}_l|n\rangle\langle n|\epsilon_i\cdot\mathbf{r}_j|g\rangle}{E_g + \hbar\omega_{\mathbf{k}_i} - E_n + i\Gamma_n} \end{aligned}$$

The last step is obtained by noticing that $\mathbf{p} = im[H_0, \mathbf{r}]/\hbar$ and that $\langle n|\epsilon_i \cdot [H_0, \mathbf{r}]|g\rangle = (E_n - E_g)\langle n|\epsilon_i \cdot \mathbf{r}|g\rangle \approx \hbar\omega_{\mathbf{k}_i}\langle n|\epsilon_i \cdot \mathbf{r}|g\rangle$. With the above transition rate one can finally obtain the double differential cross section by:

$$d^2\sigma(\omega, \mathbf{k}_i, \mathbf{k}_o, \epsilon_i, \epsilon_o) = w\frac{V^2\mathbf{k}_o^2 d|\mathbf{k}_o| d\Omega}{c(2\pi)^3} = w\frac{V^2\omega_{\mathbf{k}_o}^2 d(\hbar\omega) d\Omega}{\hbar c^4(2\pi)^3}$$

and proceeds to the final expression (in dipole approximation):

$$\frac{d^2\sigma}{d(\hbar\omega)d\Omega} = r_e^2 m^2 \omega_{\mathbf{k}_i}\omega_{\mathbf{k}_o}^3 \sum_f \left| \sum_n \sum_{j,l}^{N} \frac{\langle f|\epsilon_o^* \cdot \mathbf{r}_l|n\rangle\langle n|\epsilon_i \cdot \mathbf{r}_j|g\rangle}{E_g + \hbar\omega_{\mathbf{k}_i} - E_n + i\Gamma_n} \right|^2$$

This expression is the well-known Kramers-Heisenberg equation for light scattering. In a RIXS process, two radiative transitions are present, as embodied by the product of two dipole operators. The denominator describes the broadening of the excitation peak due to finite quasiparticle lifetime and becomes very small in the resonant absorption case, therefore increases the RIXS process' cross section. Notably the presence of lifetime term $i\Gamma_n$ gives a finite linewidth to each excitation and also avoids the singularity. The δ function guarantees the overall energy conservation, $i.e.$ the excitation energy equals the energy loss or gained by the photons. As a result, in the RIXS spectra a well-defined excitation is always found at constant transferred energy at $E_f - E_g$. However, despite the cross section being enhanced by the resonant absorption, the matrix element of this second order process is still very small, so that a light source with high brilliance is still necessary.

1.4 Single-ion model of transition metal compounds

To explicitly evaluate the scattering cross section presented in the previous section, we still need the knowledge of the eigenstates of the material system. Hereafter I introduce the simple but powerful single ionic model which is widely used in material science, physics, and chemistry studies. In Chapter 3,4 and 5, we will see that this model helps us understand the electronic structures of α-$RuCl_3$ ($RuCl_3$ hereafter) and $Na_3Co_2SbO_6$ in a simplified but insightful way.

The concept of the single-ion model is grounded in the fact that the electronic and magnetic structures of valence d electrons in transition metals play a pivotal role in determining the properties of compounds. In light of this, it becomes a valid approximation to concentrate solely on these d orbitals and conduct multiplet calculations using their wavefunctions as the basis. The wavefunctions are given by:

$$|\psi_\tau(\vec{r})\rangle = R_{nl}(r)Y_l^m(\theta,\phi) \tag{1.7}$$

Here τ contains a complete set of quantum numbers of the electron, including principal quantum number n, orbital angular momentum l, magnetic quantum number m and spin σ, and $Y_l^m(\theta,\phi)$ is the spherical harmonic function. In zero-order approximation, the states in a same shell are degenerate in energy. With this formalism, the calculation of excitation energy and states can be carried out in a Hilbert space with finite dimension. Here we take $RuCl_3$ as an example. In this compound, the Ru^{3+} ion has d^5 configuration. The dimension of the Hilbert space is then given by the total number of filling states with ten d orbitals and five electrons, *i.e.* $C_{10}^5 = 252$. Here $C_m^n = m!/n!(m-n)!$ denotes the combinatorial number. In a RIXS and XAS process where p electrons are also involved, the dimension of Hilbert space expands to $C_{16}^{11} = 4368$, although most of which are not accessible by dipole transition. Under this basis, the matrix elements of the Hamiltonian described below can be explicitly evaluated as long as the interaction parameters are given, and by calculating the eigenvalues one can obtain the excitation energies of this multiplet system.

Under this approximation, the transition metal ion and its ligands are treated as "molecule-like", which can be described by a set of well-defined quantum states with discrete energies. In crystal systems with translational symmetries, however, the ions are organized in a periodic pattern and these states entangle into energy bands via inter-atomic hopping. The state mixture between adjacent ions then raises the question if the use of the single ion model can be justified. In fact, for metallic samples where the state mixtures is strong and the wavefunctions are delocalized, such single ion model usually fails. On the contrary, for insulating materials where d electrons are largely localized, the mixing and bandwidth are usually small and approximating these bands by discrete energy levels is still a valid approach to a large extent, as we see in Chapter 3 and 4 for $RuCl_3$ and Chapter 5 for $Na_3Co_2SbO_6$.

A comparison between theory and core-level spectra such as those measured via XAS or RIXS usually includes dynamics of core p electrons in addition to the interaction between d electrons. The Hamiltonian of p and d electrons conventionally consists of the following terms:

$$H = H_C + H_{CF} + H_{SOC} \tag{1.8}$$

These three terms correspond to intra-ionic Coulomb interaction, crystal field splitting, and spin-orbit coupling, respectively. We will derive the operator form of these terms and discuss their effect on forming the electronic structure of transition metal ions. In the following sections the $c_i, c_i^\dagger$ and n_i denote the annihilation, creation and number operator of state i. The numerical calculations performed in this Thesis are carried out using the Quanty package.[16, 17, 18]

1.4.1 Coulomb interaction

In the Hatree-Fock approximation, the Coulomb interaction between electrons is substituted by an effective mean potential field.[19] In strongly correlated materials, however, the Coulomb interaction between each pair of electrons has to be considered individually. In second quantization formalism, the Hamiltonian of the Coulomb term H_C is given by:

$$H_C = \frac{1}{2} \sum_{\tau_1\tau_2\tau_3\tau_4} U_{\tau_1\tau_2\tau_3\tau_4} c^\dagger_{\tau_1} c^\dagger_{\tau_2} c_{\tau_3} c_{\tau_4} \delta_{\sigma_1\sigma_3} \delta_{\sigma_2\sigma_4} \tag{1.9}$$

$$U_{\tau_1\tau_2\tau_3\tau_4} = \langle \psi_{\tau_1}(\vec{r}_1)| \langle \psi_{\tau_2}(\vec{r}_2)| \frac{e^2}{|\vec{r}_1 - \vec{r}_2|} |\psi_{\tau_3}(\vec{r}_1)\rangle |\psi_{\tau_4}(\vec{r}_2)\rangle \tag{1.10}$$

We have assumed that the wave function of d electrons can be separated into the radial part and an angular part described by spherical-harmonic functions. We use the identity:

$$\frac{1}{|\vec{r}_1 - \vec{r}_2|} = \sum_{k=0}^{\infty} \sum_{m=-k}^{m=k} \frac{4\pi}{2k+1} \frac{min[r_1, r_2]^k}{max[r_1, r_2]^{k+1}} Y_k^m(\theta_1, \phi_1) Y_k^m(\theta_2, \phi_2) \tag{1.11}$$

Then $U_{\tau_1\tau_2\tau_3\tau_4}$ can be rewritten as:

$$\begin{aligned} U_{\tau_1\tau_2\tau_3\tau_4} &= -\delta_{\sigma_1,\sigma_3}\delta_{\sigma_2,\sigma_4} \sum_{k=0}^{\infty} c^{(k)}[l_1, \tau_1; l_3, \tau_3] c^{(k)}[l_4, \tau_4; l_2, \tau_2] \\ &\times R^{(k)}[\tau_1\tau_2\tau_3\tau_4] \end{aligned} \tag{1.12}$$

The Coulomb interaction described in this form is sometimes referred as Slater Hamiltonian. The coefficient here is given by:

$$c^{(k)}[l_1, m_1; l_2, m_2] = \sqrt{\frac{4\pi}{2k+1}} \langle Y_{l_1}^{m_1} | Y_k^{m_1 - m_2} | Y_{l_2}^{m_2} \rangle \tag{1.13}$$

$$\begin{aligned} R^{(k)}[\tau_1\tau_2\tau_3\tau_4] &= e^2 \int_0^\infty \int_0^\infty \frac{min[r_i, r_j]^k}{max[r_i, r_j]^{k+1}} \\ &\times R_{n_1 l_1}(r_i) R_{n_2 l_2}(r_j) R_{n_3 l_3}(r_i) R_{n_4 l_4}(r_j) dr_i dr_j \end{aligned} \tag{1.14}$$

The angular integration $c^{(k)}[l_1, \tau_1; l_2, \tau_2]$ can be evaluated explicitly. To calculate the radial integration $R^{(k)}[\tau_1\tau_2\tau_3\tau_4]$, one can either use first principle numerical method, or fit this unknown parameter from experiment data, as we do in Chapter 3,4 and 5.

We first consider the Coulomb interaction between d electrons in the same shell. This term affects excitation energy detected by RIXS measurements. In this case, we have $n_1 = n_2 = n_3 = n_4$ (=3 for Co and =4 for Ru), and $l_1 = l_2 = l_3 = l_4 = 2$. Then the selection rule of $c^{(k)}[l_1, \tau_1; l_2, \tau_2]$ requires $k = 0, 2, 4$ in order to make the integration nonzero. As a result, the radial part reduce to three parameters:

$$F_{dd}^k = e^2 \int_0^\infty \int_0^\infty \frac{min[r_i, r_j]^k}{max[r_i, r_j]^{k+1}} R_{n2}^2(r_i) R_{n2}^2(r_j) dr_i dr_j \tag{1.15}$$

When considering the $L_{2,3}$-edge RIXS process where transition take place between $2p$ orbitals and d orbitals, we should further take into account the Coulomb interaction in between. In this case, we have $l_1 = 1$ and $l_2 = 2$, and the radial integration is divided into two types: the direct term with $l_3 = l_1, l_4 = l_2$, and exchange term $l_3 = l_2, l_4 = l_1$. The direct term gives:

$$F_{pd}^k = \int_0^\infty \int_0^\infty \frac{min[r_i, r_j]^k}{max[r_i, r_j]^{k+1}} R_{n1}^2(r_i) R_{n2}^2(r_j) dr_i dr_j \tag{1.16}$$

selection rule gives k = 0,2. The exchange term gives:

$$\begin{aligned} G_{pd}^k &= e^2 \int_0^\infty \int_0^\infty \frac{min[r_i, r_j]^k}{max[r_i, r_j]^{k+1}} \\ &\times R_{nl_1}(r_i) R_{nl_1}(r_j) R_{nl_2}(r_i) R_{nl_2}(r_j) dr_i dr_j \end{aligned} \tag{1.17}$$

where k = 1,3. These parameters will function as the coefficients of the Coulomb Hamiltonian in Quanty package.

For interactions between d electrons, another conventionally used parameter set is the Racah parameters A, B, and C. The Racah parameters and radial integration introduced above can equivalently describe the strength of correlation between electrons and satisfy the following linear transformation:[20]

$$\begin{aligned} A &= F^0 - \frac{1}{9}F^4 \\ B &= \frac{1}{49}F^2 - \frac{5}{441}F^4 \\ C &= \frac{5}{63}F^4 \end{aligned} \tag{1.18}$$

For realistic material systems, it was found that the ratio $\gamma = C/B$ falls between 4 and 5.[21] This ratio is sometimes referred as Tanabe-Sugano ratio. We will adhere to this restriction when adjusting the interaction parameters in the following Chapters.

We need to point out that F^0 and A include the Hubbard interaction U, whose contribution to the energy is given by $E_H = N(N-1)U/2$, where N is the total number of electrons in this orbital. When the considered excitation process does not contain charge transfer between the transition metal ion and the ligand ions or neighboring transition metals ions, then this term simply contributes a constant energy for all states. As a consequence, the value of U does not influence the excitation energy or shape of calculated spectra, *i.e.* U (and therefore F^0 and A as well) can be set to an arbitrary value in the calculation. In the following chapters, we will always take $F^0 = 0$.

1.4.2 Crystal field splitting

The crystal field describes the splitting due to the surrounding ligand ions which lowers the spherical symmetry of the transition metal ion at the center.[22, 23] In our work, the most common crystal field is cubic with symmetry given by the O_h point group. This crystal field can be generated from the octahedron formed by ligand ions, such as the $RuCl_6$ octahedron in Chapter 3 and 4, or the CoO_6 octahedron in Chapter 5. Figure 1.5 shows a sketch of this structure and the local coordinate we use. The position of the six ligand ions $R_i (i = 1, 2, ...6)$ is given by $(\pm a, 0, 0)$, $(0, \pm a, 0)$, $(0, 0, \pm a)$ with charge q_c. If we further

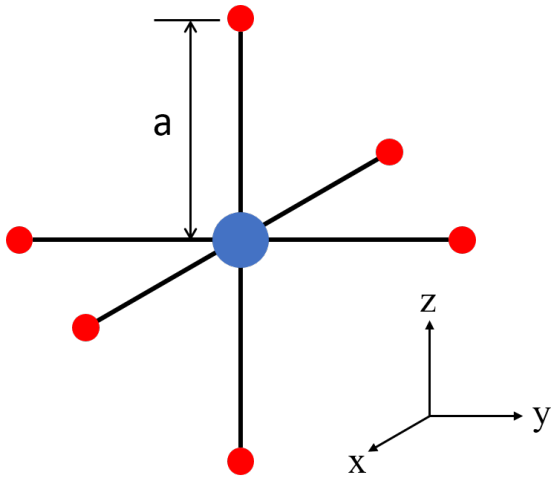

Figure 1.5: Sketch of octahedral crystal field and the local coordinate. The transition metal ion (blue) is located at the origin point and is surrounded by six ligand ions (red). The bond length between center ion and ligand is given by a.

approximate the ligand ion by a point charge, then the electrostatic potential energy created by the ligand field is given by:

$$V_{oct}(\vec{r}) = \sum_{i=1}^{6} \frac{1}{4\pi\epsilon_0} \frac{qq_c}{|\vec{r} - \vec{R}_i|} \approx \frac{qq_c}{4\pi\epsilon_0} \frac{35}{4a^5}(x^4 + y^4 + z^4 - \frac{3}{5}r^4) + V_0 \tag{1.19}$$

where $V_0 = -6eq_c/a$ is a constant and will be neglected hereafter. Here we assume that the electrons are tightly bound to the transition metal ion and their average distance is small compared to bond length a, so higher order terms of r/a are omitted. With spherical harmonic function, the first term of the potential can be rewritten as:

$$V_{oct} = \frac{1}{4\pi\epsilon_0} \frac{7\sqrt{\pi}eq_c}{3} \frac{r^4}{a^5}(Y_4^0(\theta,\phi) + \sqrt{\frac{5}{14}}(Y_4^{-4}(\theta,\phi) + Y_4^4(\theta,\phi))) \tag{1.20}$$

Let $q = 2e\langle r^4\rangle/105$ and $D = (1/4\pi\epsilon_0)(35q_c/4a^5)$ then the matrix elements of this potential operator can be evaluated explicitly under the basis of d electron state. There are four nonzero terms:

$$\begin{aligned}
\langle\psi_{nd0}|V_{oct}|\psi_{nd0}\rangle &= +6Dq \\
\langle\psi_{nd\pm1}|V_{oct}|\psi_{nd\pm1}\rangle &= -4Dq \\
\langle\psi_{nd\pm2}|V_{oct}|\psi_{nd\pm2}\rangle &= +Dq \\
\langle\psi_{nd\pm2}|V_{oct}|\psi_{nd\mp2}\rangle &= +5Dq
\end{aligned}$$

The spin state is irrelevant to the crystal field splitting and left out. By diagonalizing the potential operator, it is found that the degenerate five-fold d states splits into two-fold e_g states with energy $E_1 = 6Dq$ and three-fold t_{2g} states with energy $E_2 = -4Dq$ eigenstates under O_h crystal field. The eigenstates are given by:

(1.21)
$$\begin{aligned}
e_g: \quad |3z^2 - r^2\rangle &= |\psi_{nd0}\rangle \\
|x^2 - y^2\rangle &= \frac{1}{\sqrt{2}}(|\psi_{nd2}\rangle + |\psi_{nd-2}\rangle) \\
t_{2g}: \quad |xy\rangle &= \frac{i}{\sqrt{2}}(|\psi_{nd2}\rangle - |\psi_{nd-2}\rangle) \\
|xz\rangle &= \frac{1}{\sqrt{2}}(|\psi_{nd1}\rangle - |\psi_{nd-1}\rangle) \\
|yz\rangle &= \frac{i}{\sqrt{2}}(|\psi_{nd1}\rangle + |\psi_{nd-1}\rangle)
\end{aligned}$$

the splitting is $\Delta_{oct} = 10Dq$. In practice, this splitting is treated as a whole and determined by experiment. The Hamiltonian of octahedral crystal field splitting is then given by:

(1.22)
$$H_{oct} = 10Dq(\frac{3}{5}n_{e_g} - \frac{2}{5}n_{t_{2g}})$$

where $n_{e_g} = n_{3z^2-r^2} + n_{x^2-y^2}$ and $n_{t_{2g}} = n_{xy} + n_{yz} + n_{xz}$ are the number operator of e_g states and t_{2g} states, respectively.

In realistic material systems, the surrounding octahedron is usually imperfect, *i.e.* the O_h symmetry is further lowered by a small distortion. Hereafter we consider two types that are commonly observed: tetragonal splitting and trigonal splitting.

A tetragonal distortion can be considered as a stretch/compression along the z direction (0,0,1). As a consequence, the four-fold rotational symmetry is maintained, while the three-fold rotational symmteries are broken. The degeneracy of both t_{2g} states and e_g states will be lifted. The Hamiltonian is given by:

$$H_{tetra} = \frac{1}{3}\Delta(n_{xz} + n_{yz} - 2n_{xy}) + \frac{1}{2}\Delta_e(n_{3z^2-r^2} - n_{x^2-y^2}) \tag{1.23}$$

where Δ and Δ_e are the energy splitting of t_{2g} and e_g states, respectively.

A trigonal distortion keeps the three-fold rotational symmetry along the (1,1,1) direction and breaks the four-fold rotational symmetries. As a consequence, the double-degenerated e_g states are not affected, but the three-fold t_{2g} states splits. The Hamiltonian is given by:

$$H_{tri} = \frac{\Delta_{tri}}{3}(2n_{a_{1g}} - n_{e'^{+}_g} - n_{e'^{-}_g}) \tag{1.24}$$

$$|a_{1g}\rangle = \frac{1}{\sqrt{3}}(|yz\rangle + |zx\rangle + |xy\rangle) \tag{1.25}$$

$$|e'^{\pm}_g\rangle = \pm\frac{1}{\sqrt{3}}(e^{\pm i\frac{2\pi}{3}}|yz\rangle + e^{\mp i\frac{2\pi}{3}}|zx\rangle + |xy\rangle)$$

where Δ_{tri} is the energy splitting of a_{1g} and e'_g states.

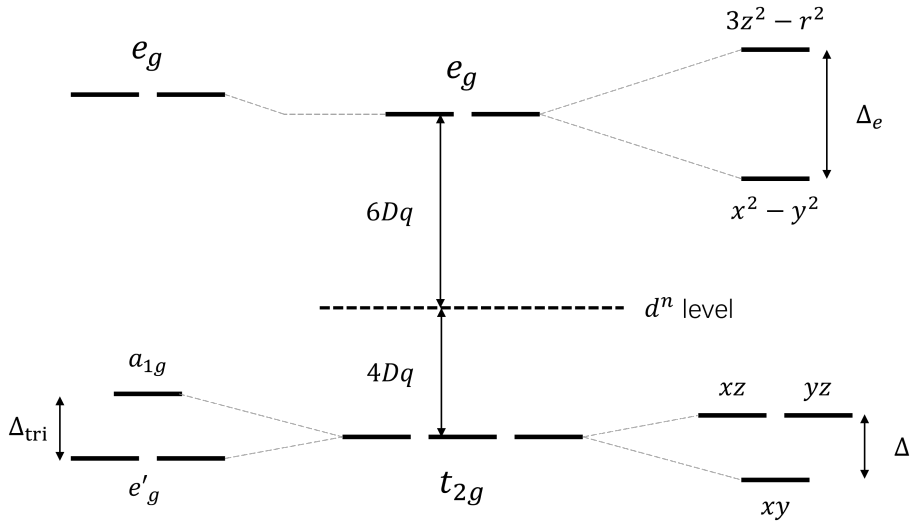

Figure 1.6: Sketch of energy level diagrams in the presence of crystal field interactions, for octahedral (center), trigonal (left) and tetragonal (right) splitting. Note that the sign of Δ and Δ_{tri} may be negative.

We need to point out that the point charge model is an oversimplified method to derive crystal field splitting, and a strict treatment relies on group theory and the fact that degenerate perturbation does not change the "center of mass" of the states. For example, in the case of the octahedral field, the representation of d electrons Γ^d of the O_h group can be written as the direct sum of two irreducible representations: $\Gamma^d = e_g \bigoplus t_{2g}$, which have dimensions of 2 and 3, respectively. As a consequence the five-fold d state (neglecting the spin degree of freedom) splits into two-fold and three-fold degenerate states, and the relative energy shift is given by 3:2. Nevertheless, the point charge model offers a direct estimate of the sign and strength of the crystal field, as well as a rationale to understand the interdependence between energy splitting and geometric parameters such as bond length and angle. By using this formula, one can roughly estimate the extent of atom displacement when the crystal structure is slightly distorted, as we will see in Chapter 4.

1.4.3 Spin-orbit Coupling

The spin-orbit coupling is given by:

$$
\begin{aligned}
H_{SOC} &= \sum_i \zeta \, \vec{s}_i \cdot \vec{l}_i \\
&= \sum_{m=-1}^{m=l} \sum_{\sigma} m\sigma c^{\dagger}_{m\sigma} c_{m\sigma} \\
&+ \sum_{m=-l}^{m=l-1} \frac{1}{2}\sqrt{l+m+1}\sqrt{l-1}(c^{\dagger}_{m+1,\downarrow} c_{m,\uparrow} + c^{\dagger}_{m,\uparrow} c_{m+1,\downarrow})
\end{aligned} \tag{1.26}
$$

$$
\zeta = \langle R(r)| \frac{1}{2m_e^2 c^2} \frac{1}{r} \frac{dV(r)}{dr} |R(r)\rangle \tag{1.27}
$$

where the sum runs over all electrons in this orbital. Here m_e is the mass of electron, c is the speed of light in vacuum, and $V(r)$ is the electric potential energy at r. In a Hydrogen-like atom, the spin-orbit coupling strength ζ grows in the order of $\sim Z^4$, where Z is the atomic number. As a consequence, spin-orbit coupling is especially important for heavy elements.

1.4.4 Low energy electronic structures and approximations

In transition metal compounds with $3d$ or $4d$ electrons and O_h crystal field splitting, the energy scale of spin-orbit coupling is usually small compared to $10Dq$. For example, for $RuCl_3$, $\zeta = 0.15$ eV, $10Dq = 2.44eV$; (Chapter 3) for $Na_3Co_2SbO_6$, $\zeta = 71meV$, $10Dq = 1.05$ eV.(Chapter 5) The substantial energy difference between t_{2g} and e_g states allows the approximation that the Hilbert space of d electrons can be effectively treated as the direct sum of t_{2g} and e_g subspaces. Relying on this decoupling assumption, low-energy electronic structures and magnetic correlations can be evaluated conveniently within one of these subspaces, where theoretical approaches often employ an equivalent model to substitute the interaction Hamiltonian previously mentioned. In this Section, we will establish connections between the theoretical effective parameters and formalism with experimentally measurable quantities, and discuss of the validity of these decoupling assumptions.

The first term being reformalized is the spin-orbit coupling. In Eqn.1.27, $\vec{s_i}$ and $\vec{l_i}$ are the spin and angular momentum of each electron. In an effective model, these two terms are replaced by total spin and angular momentum:

$$\begin{aligned} \vec{S} &= \sum_i \vec{s_i} \\ \vec{L} &= \sum_i \vec{l_i} \\ H_{SOC} &= \lambda \vec{S} \cdot \vec{L}_{eff} \end{aligned} \tag{1.28}$$

Here we have $\vec{S} = 2S\vec{s_i}$ and $\vec{L} = \alpha \vec{L}_{eff}$, where $2S$ is the total number of unpaired spin and α is the conversion coefficient between effective and actual orbital angular momentum which depends on the electronic configuration. Therefore the relationship between ζ and λ is given by $\lambda = (\alpha/2S)\,\zeta$. As an example, for Co^{2+} we have $2S = 3$ and $\alpha = -3/2$,[23] and thus $\lambda = -1/2$. Here the minus sign accounts for the opposite direction of $\vec{L}_{eff}$ and $\vec{L}$.

In the t_{2g} subspace, this Coulomb Hamiltonian H_C can also be reformalized and reduces to the well-known Kanamori Hamiltonian: [24]

$$
\begin{aligned}
H_C^{t_{2g}} &= U \sum_m n_{m\uparrow} n_{m\downarrow} + U' \sum_{m \neq m'} n_{m\uparrow} n_{m'\downarrow} \\
&+ (U' - J_H) \sum_{m<m',\sigma} n_{m\sigma} - J_H \sum_{m \neq m'} c^\dagger_{m\uparrow} c_{m\downarrow} c^\dagger_{m'\downarrow} c_{m'\uparrow} \\
&+ J_H \sum_{m \neq m'} c^\dagger_{m\uparrow} c^\dagger_{m\downarrow} c_{m'\downarrow} c_{m'\uparrow}
\end{aligned} \tag{1.29}
$$

with effective Hund's-rule coupling $J_H = 3B + C$, B and C being the Racah parameters. In the spherical approximation, we further assume $U' = U - 2J_H$, and the Kanamori Hamiltonian reduces to the rotational-invariant form:

$$
H_{t_{2g}} = (U - 3J_H) \frac{N(N-1)}{2} - 2J_H \vec{S}^2 - \frac{J_H}{2} \vec{L}^2_{eff} + \frac{5}{2} J_H N \tag{1.30}
$$

J_H is especially useful when considering the low energy Hamiltonian, since it directly gives the intra-atomic electron repulsion. For this reason, we will use J_H and Tanabe-Sugano ratio γ as the tuning parameter in modeling the RIXS spectra of $RuCl_3$ and $Na_3Co_2SbO_6$. The F^2 and F^4 parameters are then given by:

$$
\begin{aligned}
F^2 &= \frac{49 + 7\gamma}{3 + \gamma} J_H \\
F^4 &= \frac{63\gamma}{5(3 + \gamma)} J_H
\end{aligned} \tag{1.31}
$$

For 3d and 4d transition metal elements, J_H and $10Dq$ typically have similar order of magnitude, and their relative strength is crucial in determining the filling state of electrons in the transition metal ions. To be more specific, crystal field splitting $10Dq$ tends to align the electrons within the t_{2g} subspace and forms a low-spin ground state. In contrast, J_H is in favor of a high-spin state where electrons align in parallel and occupy different orbitals, which naturally leads to a population in both e_g and t_{2g} states (The second case is also known as Hund's rule in free atoms). In the case of Ru^{3+} and Co^{2+} ions, when an electron is lifted from t_{2g} to e_g state, the energy penalty is roughly given by $\Delta E = 10Dq - 3J_H$. This gives us a direct criterion to determine the ground state of the electron system. As an example, in $RuCl_3$ where $10Dq = 2.44$ eV and $J_H = 0.34$ eV, we have $\Delta E > 0$ and the

ground state of Ru^{3+} is given by t_{2g}^5 instead of $t_{2g}^3 e_g^2$. Meanwhile, for $Na_3Co_2SbO_6$ where $10Dq = 1.05$ eV and $J_H = 0.745$ eV, we have $\Delta E < 0$ and the ground state of Co^{2+} is given by $t_{2g}^5 e_g^2$ instead of $t_{2g}^6 e_g^1$.

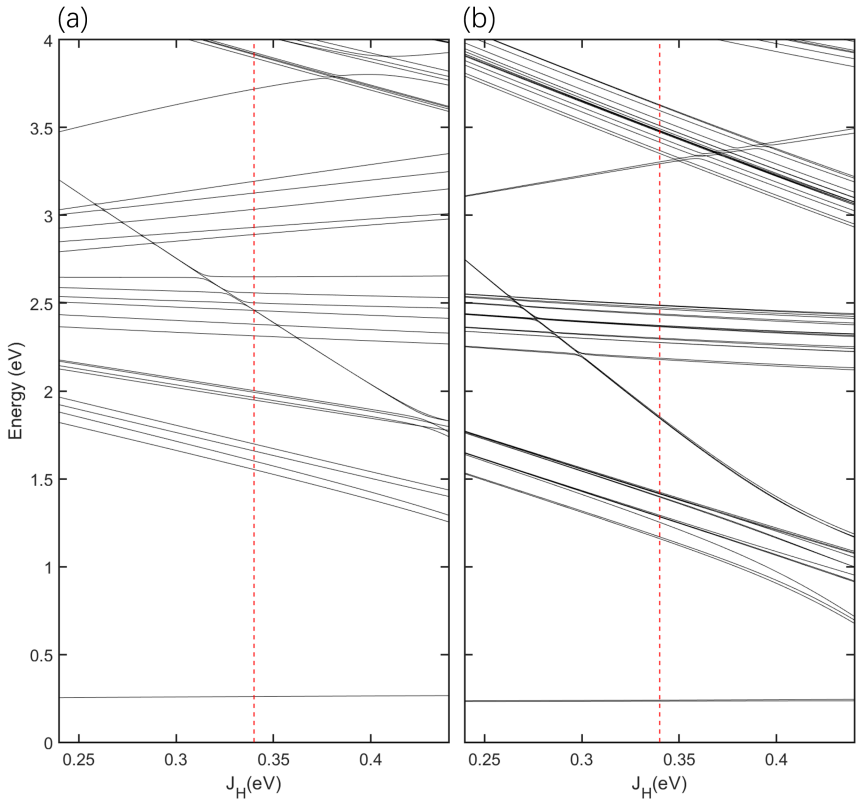

Figure 1.7: Energy level diagram of $RuCl_3$ as a function of J_H, using two Coulomb interactions: (a) realistic (Slater) Hamiltonian and (b) Kanamori Hamiltonian. The other parameters are fixed at the realistic value, *i.e.* $(10Dq, \lambda) = (2.44, 0.15)$ eV. For Slater Hamiltonian, we have $\gamma = 5$.

Here we need to point out the distinct difference between the Slater Hamiltonian described by Eqn.1.9 and the Kanamori Hamiltonian Eqn.1.30. The difference is obvious: to describe Coulomb interaction, the former requires two independent parameters, *i.e.* (F^2, F^4), (B, C), or (J_H, γ), whose relationship is given by Eqn.1.18 and 1.31. Meanwhile the Kanamori Hamiltonian only requires one (namely J_H). However, we still noticed that in some literature these two Hamiltonians are treated as equivalant to each other. This is only mathematically correct when $10Dq$ is large compared to other energy scales and the approximation that t_{2g} states are decoupled from e_g states holds, and the excitations in consideration are within the t_{2g} subspace. This condition is usually not fulfilled when describing a RIXS measurement.

For example, in order to model the d-d excitations one inevitably takes into account an excitation from t_{2g} to e_g states, and the Kanamori Hamiltonian will give an incorrect Coulomb repulsion. For example, the Coulomb repulsion between e_g electrons is given by $4B + C$, which deviate from the t_{2g} subspace ($J_H = 3B + C$).[20] To reconcile the different form between two subspaces, one has to fix Racah B at 0, or equivalently the Tanabe-Sugano ratio $\gamma = \infty$, which deviates largely from the realistic value $\gamma = 4 \sim 5$. As an example, we compare the excitation states generated with realistic parameters from $RuCl_3$ by two Hamiltonians. Fig. 1.7 shows the Tanabe-Sugano diagram of the energy levels as a function of Hund's coupling J_H. In panel (a), the Slater Hamiltonian with $\gamma = 5$ is used. Panel (b) shows the calculation result with a generalized Kanamori Hamiltonian (*i.e.* the sum in Eqn.1.30 also takes into account e_g states besides t_{2g} states). The energy of the spin-orbit excitation at around 240 meV is essentially unchanged because the transition takes place within the t_{2g} subspace. On contrary, the d-d excitations shows clear difference because e_g states are involved. In consideration of this deviation, the Kanamori Hamiltonian usually fails to capture the electronic structure at high energies and should not be used in the interpretation of RIXS data.

1.5 XAS, FY and RIXS operators and formalism

In RIXS experiments, the intensity of the spectra cannot be accurately calculated due to the complicated light-matter interaction dynamics and sample geometry. Instead, the relative intensity is usually calculated in substitution. For this purpose, we can discard the constant factors in Eqn.1.7 and reduce this formula to a form in compliance with the above stated single ion model.

Here we consider an incident beam with polarization $\vec{\epsilon} = (\epsilon_x, \epsilon_y, \epsilon_z)$. The dipole transition operator is given by:

$$
\begin{aligned}
T &= \vec{\epsilon} \cdot \hat{r} \\
&= \epsilon_x \sin\theta\cos\phi + \epsilon_y \sin\theta\sin\phi + \epsilon_z \cos\theta \\
&= \sqrt{\frac{4\pi}{3}}((\epsilon_x + i\epsilon_y)Y_1^{-1}(\theta,\phi) + \epsilon_z Y_1^0(\theta,\phi) - (\epsilon_x - i\epsilon_y)Y_1^1(\theta,\phi))
\end{aligned} \tag{1.32}
$$

The integration of the radial part is neglected and the angular part can be evaluated explicitly as we did for the crystal field splitting. With this second quantization formalism, we can derive the operator form of the spectral intensities. The XAS intensity can be given with the help of the Green's function:

$$G(\omega) = \langle \mathrm{GS}|T^{\dagger}\frac{1}{\omega - H_{pd} + i\Gamma/2}T|\mathrm{GS}\rangle \tag{1.33}$$

where $|\mathrm{GS}\rangle$ is the ground state of the transition metal ion with $2p^6nd^N$ configuration (n is the principal quantum number and N is the number of d electrons). H_{pd} is the combined Hamiltonian which also takes into account the $p-d$ Coulomb interaction, *i.e.* the terms determined by coefficient F^1_{pd}, G^1_{pd} and G^3_{pd} in Eqn.1.16 and 1.17. ω is the frequency of the incident X-ray photon. The XAS intensity is then given by the imaginary part of $G(\omega)$: $I_{XAS}(\omega) = \mathrm{Im}[G(\omega)]$.

The RIXS intensity can be expressed by the third order Green's function:

$$\begin{aligned} G^{(3)}(\omega_i, \omega) &= \langle \mathrm{GS}|T^{\dagger}_{in}\frac{1}{\omega_i - H_{pd} - i\Gamma_1/2}T_{out}\frac{1}{\omega - H_d + i\Gamma_2/2} \\ &\quad T^{\dagger}_{out}\frac{1}{\omega_i - H_{pd} + i\Gamma_1/2}T_{in}|\mathrm{GS}\rangle \end{aligned} \tag{1.34}$$

and $I_{RIXS} = \mathrm{Im}[G^{(3)}(\omega_i, \omega)]$. Here T_{in} and T_{out} are the dipole operator of incoming and scattered light, respectively. H_d is the Hamiltonian which takes into account the d electrons. ω_i is the energy of incoming X-ray photon and ω is the energy difference between the initial state and final state, *i.e.* the excitation energy of the process we are interested. Γ_1 and Γ_2 are the linewidth of XAS and RIXS, respectively.

The fluorescence yield sums up the intensity of scattered light, *i.e.* $I_{FY} \propto \int I_{RIXS}(\omega_i, \omega)d\omega$, therefore the intensity is given by:

$$I_{FY}(\omega) = \langle \mathrm{GS}|T^{\dagger}_1\frac{1}{\omega - H_{pd} - i\Gamma/2}T_2T^{\dagger}_2\frac{1}{\omega - H_{pd} + i\Gamma/2}T_1|\mathrm{GS}\rangle$$

This formalism, together with the interaction Hamiltonian, provides the starting point for us to calculate the spectra in the framework of the single ion model.

1.6 Self-absorption correction of RIXS spectra

In RIXS measurements, the energy transfer is at maximum of the order of several eV, which is often very small compared to the energy of incident photons. As a consequence, the energy of the scattered light is still close to the absorption edge and can be strongly re-absorbed by the material, giving birth to a phenomenon known as self-absorption effect. Due to this mechanism, the detected intensity usually deviates from the theoretical cross section Eqn.1.7. In this Section we will derive the correction factor to eliminate the influence of self-absorption along the lines of the approach presented in Ref[25].

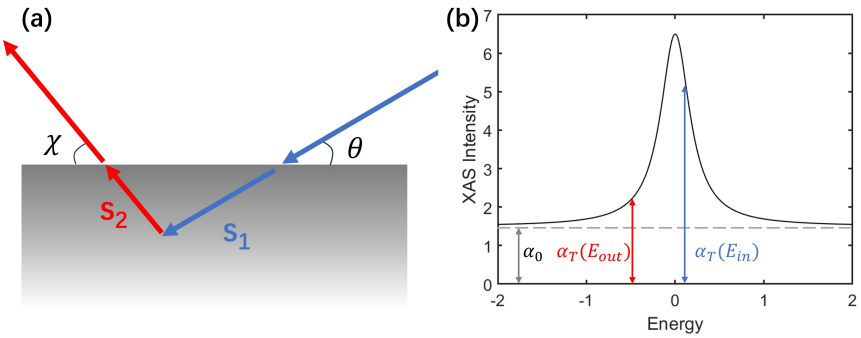

Figure 1.8: Schematic of self absorption process. (a) The propagation of X-ray photons in the sample. The photons enter the sample at an angle θ (blue line) and are scattered after traveling a distance s_1. The scattered light (red line) travels a distance s_2 before leaving the sample and is captured by the detector. (b) an example XAS spectra. The non-resonant absorption is indicated by the pre-edge intensity α_0, while the resonant absorption is given by the peak feature. $\alpha_T(E)$ is the total absorption coefficient (non-resonant + resonant) of photons with energy E.

Fig. 1.8 shows a schematic of the self-absorption process. Suppose the energies of incoming and scattered photons are given by E_{in} and E_{out}, and the absorption coefficient at these two energies are $\alpha_T(E_{in})$ and $\alpha_T(E_{out})$. Here α_T is the total absorption including the resonant absorption from the target element and the non-resonant absorption from other elements, the latter part can be measured from the pre-edge absorption (α_0 in Fig. 1.8(b)). The flux of the incoming beam is denoted by I_0. After traveling a distance s_1 in the sample, the incoming flux decays to:

$$I(s_1) = I_0 \exp\left(-\alpha_T(E_{in})s_1\right) \tag{1.35}$$

and scattered by the sample by an efficiency η. The scattered light then propagates through a distance s_2 in the sample and is then captured by the detector. During this propagation, the self-absorption can occur and the measured flux intensity is given by:

$$\begin{aligned} I_{out}(s_1) &= \eta I(s_1) \exp\left(-\alpha_T(E_{out})s_2\right) \\ &= \eta I_0 \exp\left(-\alpha_T(E_{in})s_1 - \alpha_T(E_{out})s_2\right) \end{aligned} \tag{1.36}$$

The total scattering intensity captured by the detector can be obtained by integrating $I_{out}(s_1)$ over s_1. We assume that the sample thickness is much larger than the attenuation length (which is usually a good approximation for bulk crystals with thickness of several hundreds micrometers, while the attenuation length is only of the order of 1 μm, see Fig. 1.4). Then the upper limit of the integration can be taken as infinite. Notably, the geometry also gives: $s_1 \sin\theta = s_2 \sin\chi$. Then we have:

$$\begin{aligned} I_s &= \int_0^\infty \eta I_0 \exp\left((-\alpha_T(E_{in})s_1 - \alpha_T(E_{out})s_1 \frac{\sin\theta}{\sin\chi})\right) ds_1 \\ &= \eta I_0 \frac{1}{\alpha_T(E_{in}) + \alpha_T(E_{out})\frac{\sin\theta}{\sin\chi}} \end{aligned} \tag{1.37}$$

I_s is the RIXS intensity measured in the experiment. To get the intensity without self-absorption, we can set $\alpha_T(E_{out}) = 0$ in the above equation and get the theoretical intensity:

$$I_{theo} = \eta I_0 \frac{1}{\alpha_T(E_{in})} \tag{1.38}$$

Their ratio is the self-absorption correction factor:

$$\begin{aligned} F(\theta, E_{in}, E_{out}) &= I_s / I_{theo} \\ &= \frac{\alpha_T(E_{in})}{\alpha_T(E_{in}) + \alpha_T(E_{out})\frac{\sin\theta}{\sin\chi}} \\ &= \frac{1}{1 + r \cdot u} \end{aligned} \tag{1.39}$$

where $r = \alpha_T(E_{out})/\alpha_T(E_{in})$ and $u = \sin\theta/\sin\chi$.

When the energy transfer is small (such that $E_{in} \approx E_{out}$) and the absorption varies slowly around the incident energy, it is usually a good approximation to take $\alpha_T(E_{in}) \approx \alpha_T(E_{out})$, and therefore $r \approx 1$. Then Eqn.1.39 reduce to $F = 1/(1+u)$. When the scattering angle

is fixed at 90° (which is also the experiment layout we use in Chapter 3,4 and 5), we have $\chi = \pi/2 - \theta$ and $u = \sin\theta/\cos\theta = \tan\theta$, then the self-absorption correction factor becomes:

$$\tilde{F} = 1/(1 + \tan\theta) \tag{1.40}$$

which is only depending on the geometric factor θ. When comparing the momentum-dependent intensity of the excitation peaks, this factor becomes significant and influences the measured data to a large extent, as we will discuss in detail in Chapters 3 and 5.

1.7 Summary

In this Chapter, we introduced the fundamental aspects of RIXS from both experimental and theoretical points of view. As the main experimental probe I used in this Thesis project, RIXS is an indispensable spectroscopic method to study solid state systems, and in particular quantum materials which show strong correlation effects. The RIXS process is defined by a two-step process, including the resonant absorption of the incoming X-ray photon whose energy is tuned to that of the absorption edge of the target element, and an emission process. By comparing the energy and momentum transfer between the incoming and scattered photon, we can obtain valuable information on the elementary excitations of the materials, including magnon, phonon, d-d and charge transitions etc.

The resonant absorption and the two-step scattering process requires a photon flux with high brilliance, good monochromaticity and relatively large energy. To date this can only be achieved by using a synchrotron light source. This feature also grants RIXS many profitable capabilities compared to other spectroscopic methods such as INS, EELS, PES, Raman etc: (i) RIXS is a photon-in photon-out method, which preserves the charge neutrality in the sample and suppresses charging effects, which can become a significant obstacle when studying insulating samples. (ii) The scattering cross section is largely enhanced by the resonance nature of RIXS, making it possible to measure samples with extremely small volume, (iii) The element-selectivity of RIXS helps us to distinguish the signal between target sample and substrates/capping layer, which is especially useful when studying heterostructure systems. (iv) the polarization and large momentum of X-ray photons enable us to study the energy dispersion and symmetry of the excitations. Nevertheless, two

limiting factors of RIXS as the technique are the flux intensity of incoming light and the energy resolution, which we are confident will be improved in the future by instrumental developments.

Next we derived the cross-section of RIXS process, known as Kramers-Heisenberg equation. In a simplified model, we only take into account the dipole transition term described by interaction terms proportional to $\mathbf{A}(\mathbf{r})$. By using the Fermi golden rule and neglecting the non-resonant terms, the explicit form of the scattering cross section can be obtained. Unfortunately this equation contains complicated interactions between electron and electromagnetic field and is difficult to accurately compute, in contrast to the case of INS studies.To overcome this issue, we usually focus on the relative intensities of the features in the RIXS spectra.

To calculate the relative cross-section, we need two theoretical foundations to implement the Kramers-Heisenberg equation. The first requirement is a proper Hamiltonian to describe the interactions in the target material system. Here we exclusively focus on the insulating systems, whose electronic structure can be well captured by the behavior of d electrons of the central transition-metal ion, in the formalism of the single ion model. The basis of the Hilbert space is then given by all the possible filling states, and has a dimension of C_{10}^{n}, where n is the number of d electrons. The Hamiltonian contains the Coulomb interaction, spin-orbit coupling and several crystal field splitting terms depending the the lattice structure of the sample. These terms are expressed in the form of second quantization, with the coefficient determined by $ab\,initio$ calculations or experiments. We also introduced an effective model which is restricted in the t_{2g} subspace, and was favored by a number of theoretical studies. Notably, in the t_{2g} subspace the Coulomb interaction is reduced to the Kanamori form and we clarified its difference with the Slater Hamiltonian. Another foundation is to express the spectral operators in the second quantization form, including XAS, FY, and RIXS. With these two formalisms, we can carry out exact diagonalization of the Hamiltonian and compute the eigenstates, energies and RIXS cross sections explicitly.

At last, we also derived the formula of self-absorption effect in RIXS experiments. This refers to the mechanism for which the scattered light with energy close to the absorption edge might be re-absorbed by the sample, thereby distorting the collected RIXS spectra. We derived the original form (Eqn.1.39) and reduced form (Eqn.1.40) of the correction factor, which is largely depending on the incident angle and sensitive to the geometric layout of the experiment. Self-absorption effects become significant when studying the momentum-dependence of the excitations, as we will see in the following Chapters.

2 Intermediate RIXS setup in P01 beamline

As discussed in the previous Chapter, technical difficulties have always been the limiting factor that restricted the wide application of RIXS in material studies. However, in recent decades, significant advancements in beamline infrastructure and spectrometer design have enabled RIXS to yield valuable insights into various materials. A notable example is the soft X-ray RIXS investigation of high-temperature superconducting cuprates, where the technique successfully elucidated the magnon dispersion relationship and provided new insights into possible electron pairing mechanisms [12].

X-rays can be broadly classified into two categories based on energy: soft X-rays (below 2 keV) and hard X-rays (above 5 keV). The primary distinction lies in the types of dispersive optics utilized in the monochromators and analyzers. Soft X-ray spectrometers typically employ gratings to disperse light, taking advantage of the relatively long wavelength of soft X-ray photons. Modern gratings can achieve resolutions of approximately 1000 $\sim$ 2000 lines per mm and resolving powers of around $\sim$ 20000. As an example, this resolving power results in energy resolutions of about $\sim$ 35 meV at the Co-L_3 edge ($\sim$ 778 eV) [26, 27]. In contrast, hard X-rays have wavelengths comparable to the lattice constants of crystals, and high-quality single crystals (such as Si or quartz) are often used for energy resolution.

However, an energy range exists between soft and hard X-rays known as the tender (or intermediate) X-ray region, where achieving high energy resolution is particularly challenging. This range includes the $L_{2,3}$ edges of several 4d elements, such as Mo, Tc, Ru, Rh, Pd, and Ag. The difficulty arises from the selection of dispersing optics. Gratings typically used for soft X-rays struggle to achieve sub-100 meV energy resolution in the tender X-ray range. For instance, at the Ru-L_3 edge around $\sim$ 2840 eV, a grating with a resolving power of $\sim$ 20000 yields an energy resolution of only $\sim$ 140 meV. Additionally, the energy of tender X-rays is often too low to satisfy the Bragg condition for crystal

diffraction. For example, at the Ru-L_3 edge, (111) is the only available Bragg reflection in a Si crystal. Consequently, analyzers and monochromators designed for different absorption edges within the tender X-ray range often require individual fabrication and commissioning.

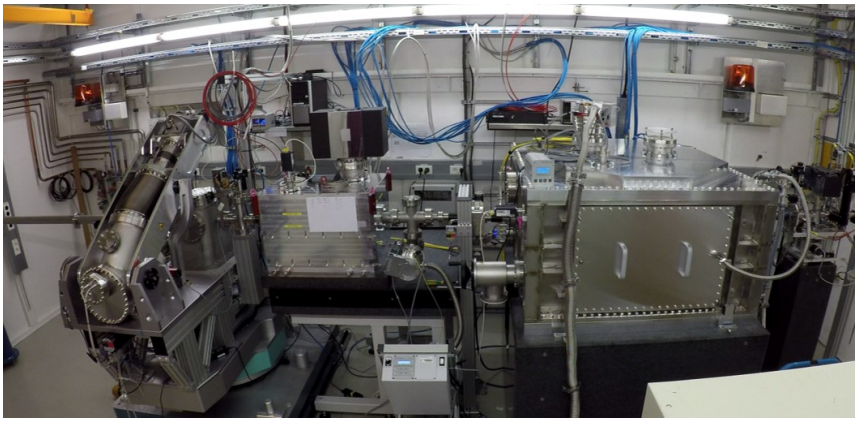

Figure 2.1: Overview of P01 beamline in PETRA III, DESY.

To date, the first intermediate RIXS (IRIXS) beamline with sub-100 meV energy resolution has been established at the P01 beamline of the PETRA-III facility at the Deutsches Elektronen-Synchrotron (DESY) in Hamburg [28]. Initially designed to operate at the Ru-L_3 absorption edge, this beamline has undergone years of upgrades and commissioning efforts, resulting in an extension of its operational energy range to include the Rh-$L_{2,3}$ edge and U-M_5 edge. Additionally, another spectrometer capable of achieving an energy resolution of 30~40 meV at the Ru-L_3 edge has been constructed [29]. In this chapter, we will provide an overview of these experimental setups, which serve as the technical foundation for numerous RIXS studies involving Ru compounds.

2.1 Beamline Overview

Although beamline P01 was originally constructed as a hard X-ray beamline primarily dedicated to nuclear resonant scattering (NRS) and inelastic X-ray scattering (IXS) studies [30], the installation of new undulators in 2017 expanded the photon energy range down to 2.5 keV, overlapping with the energy range of $L_{2,3}$-absorption edges of 4d transition metal elements. Each undulator comprises dipole magnets arranged in a periodic pattern, generating an alternating static magnetic field along the path of the electrons. As electrons

traverse this periodic magnetic field, they undergo forced oscillations due to the Lorentz force and emit coherent, polarized X-ray photons, whose energy can be tuned by adjusting the periodicity of the magnetic field [31]. An advantage of undulators lies in their ability to produce X-ray beams with significantly higher brilliance compared to a single bending magnet by a factor of N^2, where N represents the total number of periods in the undulator. The two sets of undulators at P01 comprise 157 periods, each 32 mm long, with a total length of $2times5$ m. The source brilliance is estimated to be 10^{19} photons/s/0.1% bandwidth/mA, with a current of 120 mA under normal operating conditions.

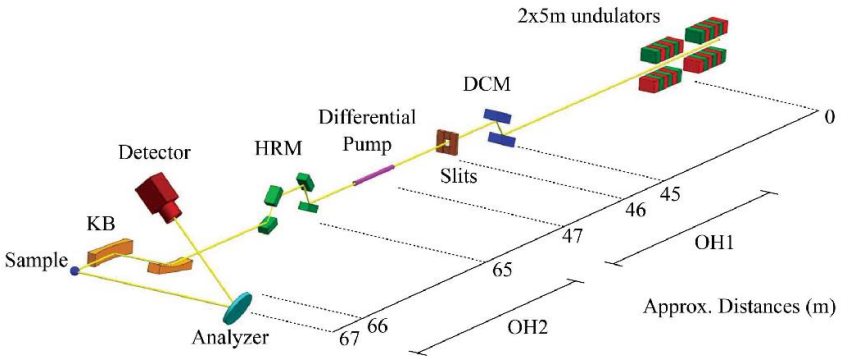

Figure 2.2: Layout of the IRIXS instrument. In the upstream of the sample chamber lies the undulator, DCM, HRM (4B inline or nested), and KB mirror. Here only the spectrometer with Rowland layout is shown. Figure reproduced from Ref [28].

The schematic layout of the intermediate RIXS beamline is presented in Fig 2.2. Given the significant air absorption and attenuation by windows in the tender X-ray energy range, the entire setup is designed to operate in a high vacuum environment, devoid of any windows. To fulfill this requirement, the instrument is positioned as close to the machine vacuum as possible, with a differential pump installed immediately upstream of the IRIXS spectrometer, achieving a vacuum level of 10^{-6} mbar. Upstream of the pump lies the double crystal monochromator (DCM) comprising a pseudo channel-cut Si(111) cooled by liquid nitrogen. To further mitigate the heat load on the first mirror, the crystal surfaces are cut with an asymmetry angle of 32° to elongate the footprint of the incoming high-power undulator beam. At the Ru-L_3 edge (2840 eV), this asymmetric geometry results in a downstream bandwidth of 600 meV. The shape and intensity of the outgoing beam in real space are determined by a four-blade slit, both horizontally and vertically.

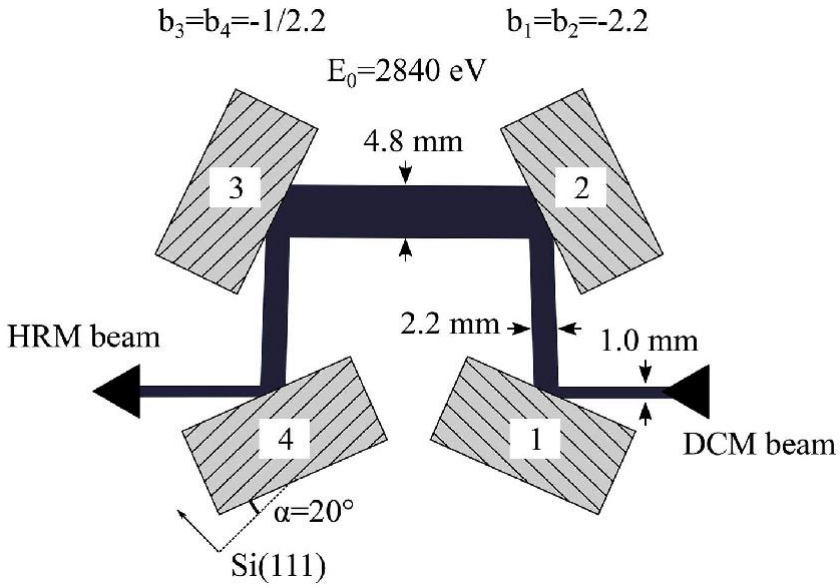

Figure 2.3: Schematic of the four-bounce HRM. Figure reproduced from Ref [28].

Downstream of the DCM is the high-resolution monochromator (HRM). Currently, we have installed two types of HRM with distinct geometries and performance: the four-bounce (4B inline) HRM and the nested HRM.

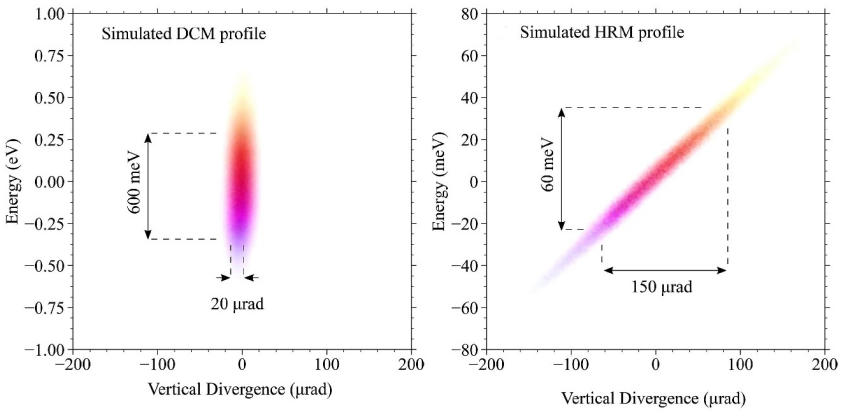

Figure 2.4: Phase space of the photons entering DCM and HRM. Figure reproduced from Ref [28].

The 4B inline HRM takes a four-bounce configuration, as shown in Fig 2.3. This HRM is composed of four Si(111) crystals being cut asymmetrically with an angle $\alpha = 20^{\circ}$ and placed in the (+ - - +) configuration.[32] Here silicon is chosen because it has been proven stable with the heat load of the incoming beam, unlike other crystals such as quartz or sapphire.[33] Each reflection suffers a flux loss of 60% due to the low reflectivity of Si

(111) Bragg peak, resulting an overall efficiency of 13%. Although this HRM suppresses the energy band width from 600 meV (after DCM) to 60 meV (after HRM), the simulated energy and angular profile shows that the divergence of the beam increases from 20 μrad to 150 μrad due to the uncompensated asymmetric crystals, as shown in Fig 2.4.

The nested HRM comprises two artificial channel-cuts of Si(111) and Al_2O_3(110) single crystals arranged in a (+ - - +) layout, as illustrated in Fig. 2.5. The first and second mirrors have asymmetric angles of $-25°$ and 60°, respectively, optimizing energy resolution while preserving sufficient photon flux. The third and fourth crystals are the inverse of the first two. The post-HRM beam is vertically shifted by 10 mm relative to the incoming beam. Ray-tracing simulations suggest an outgoing beam with an energy full-width half-maximum (FWHM) of 30 meV and a divergence of approximately 20 μrad, maintaining the divergence of the incident beam from the DCM. This enhanced collimation is crucial for our RIXS studies on nanolayers to reduce the footprint of the beamspot on the sample to a size comparable to exfoliated flakes and significantly suppress the flux incident on the substrate. Consequently, the unwanted elastic peak can be greatly suppressed. However, this enhanced spatial distribution performance comes at the expense of low photon efficiency. The overall reflectivity of the nested HRM is around 4.8%, much lower than that of the 4B inline HRM (13%). Factoring in the halved bandwidth (from 60 meV to 30 meV), the overall flux intensity is roughly 1/6 compared to the 4B inline HRM. In practice, the selection between these two HRMs depends on the nature of the sample. For samples with large lateral dimensions, such as bulk crystals or thin films with large area, the 4B inline HRM provides a stronger incoming beam flux and thereby enhances the signal-to-noise ratio of the spectra. Conversely, for nanolayers with small lateral dimensions or when using a high-resolution spectrometer that requires a small incoming bandwidth, the nested HRM is the preferred choice.

After being monochromatized by the HRM, the X-ray beam is focused onto the sample via the Kirkpatrick-Baez (KB) mirror consisting of two concave reflecting mirrors (300 and 600 mm long,V×H) coated with Ni. It accepts a beam size of 1 mm × 2 mm (V×H) and adjusts the focused beam size depending on the HRM upstream, achieving dimensions of 20 μm × 150 μm for the 4B inline HRM and 20 μm × 20 μm for the nested HRM in the horizontal and vertical directions, respectively. The estimated overall photon flux on the sample is approximately 1×10^{12} photons/s at 2840 eV when using the 4B inline HRM, sufficient for acquiring reliable statistics within a reasonable time frame (typically around 1 hour).

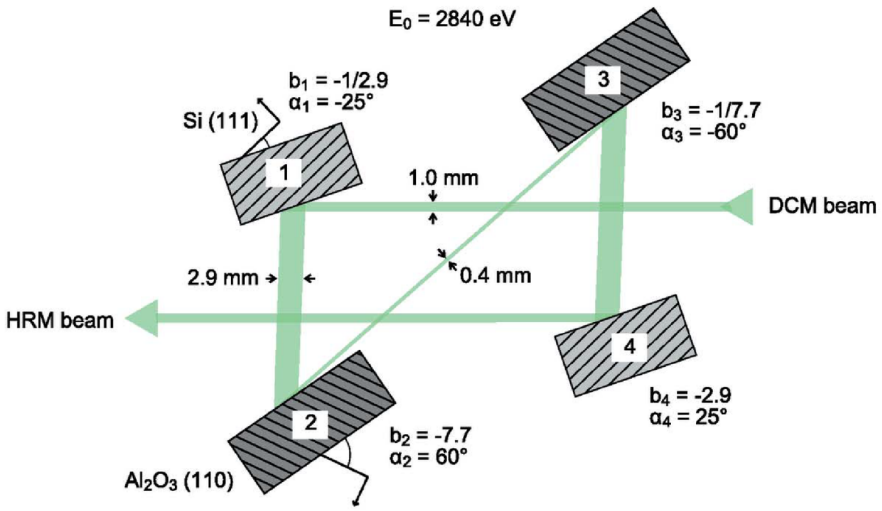

Figure 2.5: Layout of the nested HRM. The light and dark gray squares corresponds to Si and Al_2O_3 crystals, respectively. Figure reproduced from Ref.[29]

Subsequently, the well-monochromatized and focused beam traverses into the sample chamber. Currently, no load-lock setups have been installed in the P01 beamline, necessitating frequent venting and pumping of the entire chamber during sample mounting. To safeguard the high vacuum in upstream facilities, a diamond window separates the KB chamber from the sample chamber and prevents air ingress during venting. The sample is mounted to a manipulator capable of movement in five dimensions ($\theta = [0°, 90°]$, $\chi = [-5°, 35°]$, $x, y, z = \pm 6$ mm) within a vacuum environment. Cooling is facilitated by a closed-cycle He cryostat, enabling a base temperature of approximately 20 K at present.

Figure 2.6 illustrates a typical experimental layout for RIXS measurements. The incident X-ray beam enters the sample at an angle θ, while the scattered light is gathered at a scattering angle 2θ. Polarization within and perpendicular to the scattering plane is labeled as π and σ, respectively. Since materials studied via RIXS often exhibit quasi-2D structures (e.g., the CuO_2 plane in high-T_c superconducting cuprates, and the Ru and Co honeycomb layers in Chapters 3 and 5), the relevant quantity is usually the projection of momentum transfer onto the 2D plane, represented as $\vec{q}_{\parallel}$. In practice, this momentum transfer is manipulated by fixing the 2θ angle (and thus the total momentum transfer $\vec{q}$), and continuously adjusting the θ angle by rotating the sample holder. It's important to note that the energy transfer typically ranges in the order of eV, which is negligible compared to the energy of the incident X-ray photons (usually on the order of 1000 eV or higher).

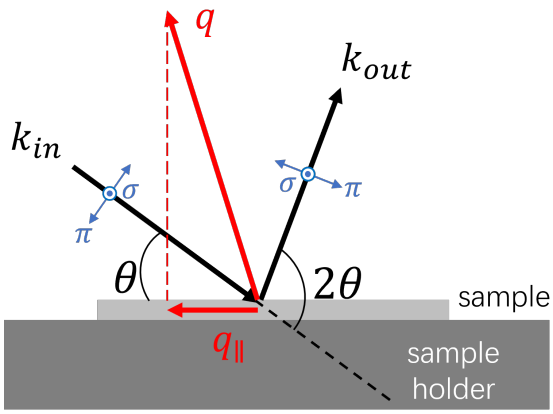

Figure 2.6: Schematic of typical experiment layout for RIXS measurement. $\hbar\vec{k}_{in}$ and $\hbar\vec{k}_{out}$ are the momentum of the incoming and scattered light. The incident angle is denoted by θ and the scattered angle is 2θ (which will be replace by δ to avoid confusion). The polarization is labeld by π and σ. Th total momentum transfer is given by $\vec{q}$, while its projection on the sample plane $\vec{q}_{||}$ is usually the meaningful quantity.

Therefore, it's reasonable to assume that $k_i = k_f = \hbar\omega_i/c$, where $\hbar\omega_i$ signifies the energy of the incident X-ray photon. As a result, the momentum transfer is given by:

$$q_{\parallel} = -2\hbar k \sin(\frac{\delta}{2}) \sin(\frac{\delta}{2} - \theta) \tag{2.1}$$

To prevent confusion, here we use δ to denote 2θ. By referring to Eqn.2.1, one can compute the appropriate θ angle to capture the RIXS response with the desired momentum transfer. It's worth noting that the incident angle is limited within the range $0 \leqslant \theta \leqslant \delta$, thus limiting the maximum achievable momentum range to:

$$q_{\parallel}^{max} = 2\hbar k \sin^2 \frac{\delta}{2} \tag{2.2}$$

Therefore, it's advantageous to have δ as large as possible if one aims to cover a broad range in the Brillouin zone. In some of the soft X-ray beamlines it is possible to have $\delta > 150°$, such as I21 beamline in Diamond Light Source [34] and ID32 beamline in European Synchrotron Radiation Facility (ESRF)[35]. Another commonly employed configuration involves fixing $\delta = 90°$ and utilizing an incident beam with π-polarization. In this setup, the polarization of the scattered light is always perpendicular to that of the incident beam, therefore effectively suppressing isotropic scattering from charges, which is the primary

contributor to the elastic line in RIXS spectra. This layout finds widespread use in studies of magnetic fluctuations, where the excitation energy is typically very low, as I will illustrate in Chapters 3 and 5.

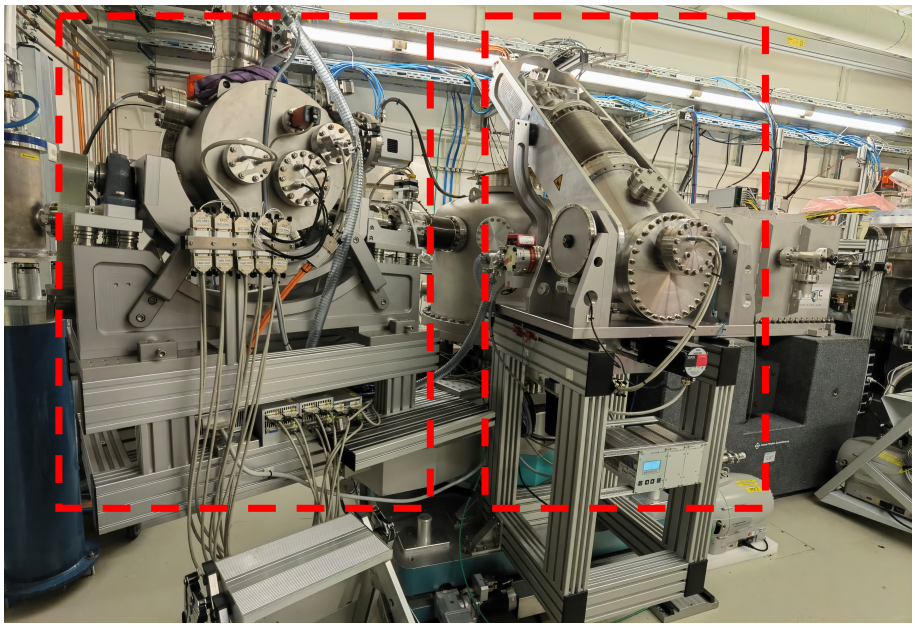

Figure 2.7: Photo of two spectrometers indicated by red dashed frame. Left: high-resolution spectrometer with energy resolution of 30~40 meV. Right: Rowland spectrometer with energy resolution of 75 meV.

The scattering angle 2θ at the P01 beamline is designed for continuous adjustment to manipulate both the direction and magnitude of the momentum transfer vector. However, its current range is constrained by the exit windows of the sample chamber, limited to $2\theta = 30°, 60°, 90°$ and $120°$. At each window, the spectrometer can rotate within a range of $\pm 10°$. For most RIXS studies conducted at P01, the 2θ angle is fixed at $90°$, with incident X-ray photons being π polarized, and the polarization of scattered light is not analyzed.

Another remarkable instrument in our setup is the silicon drift detector (SDD) located within the sample chamber. This detector is capable of capturing both the intensity and energy (with an energy resolution of ~150 eV) of the fluorescence signal, enabling us to differentiate between different elements. The schematic of this detector is illustrated in Fig.2.8. The core part of the detector is essentially a 450 μm thick disk made by high-quality silicon. This silicon has high resistivity and low leakage current, and is further depleted by the application of a negative bias voltage to both sides of the disk. On the back side of the disk, a series of "drift rings" are incorporated to establish a transverse electric field within the device.The ionized electrons generated by the incoming X-ray

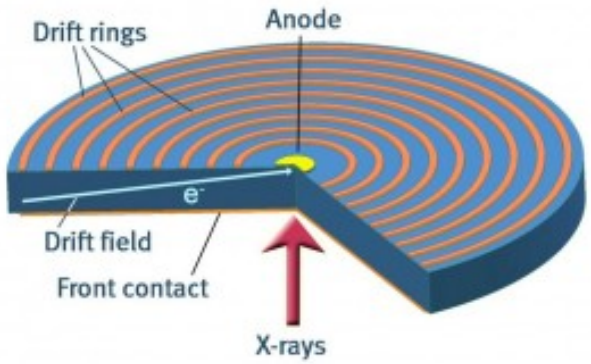

Figure 2.8: Components of a SDD detector. Figure reproduced from Ref[36].

photons drift towards the center of the disk due to the transverse electric field and are captured by the small charge-collecting anode. By counting the number of ionizations, the SDD can accurately measures the photon energy. Widely utilized in X-ray optics, the SDD detector plays a crucial role in our measurements by offering direct discrimination between the sample and other components (such as glue, substrate, and metal parts), as I will demonstrate in Chapter 4.

After the incident X-ray beam is scattered by the sample, the outgoing photons are analyzed by the spectrometer. Currently, we have two spectrometers based on distinct designs. The first one follows a Rowland layout and has been in operation since its inception. This spectrometer has been utilized extensively for RIXS studies in recent years, contributing to various research endeavors [4, 37, 38, 39, 40, 41, 42]. It was originally designed to work at the Ru-L_3 edge at 2840 eV, but recent commissioning efforts have extended its operating range to include the Rh-L_3 edge at 3005 eV and the U-M_5 edge at 3550 eV by substituting suitable crystal analyzers. Another spectrometer, built more recently, aims to achieve higher resolution (30-40 meV) by employing the collimating spectrograph concept. In the subsequent sections, we will delve into the structure and fundamental concepts of these two spectrometers, accompanied by preliminary measurement results obtained from these setups.

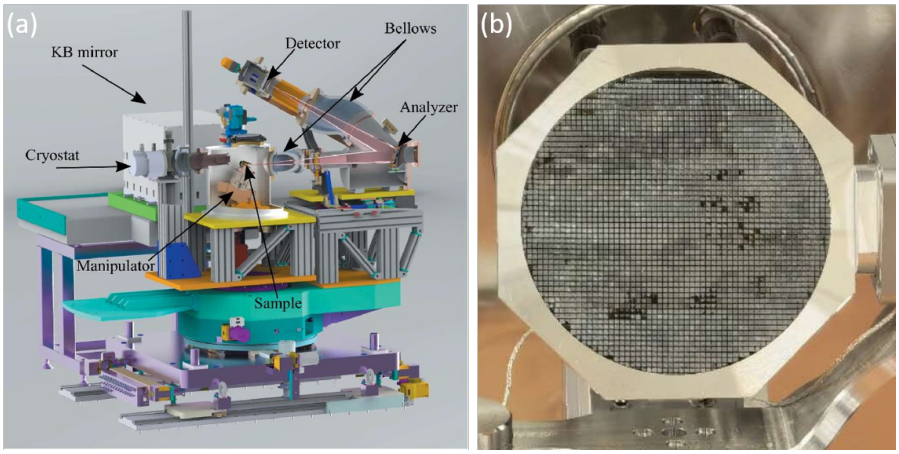

Figure 2.9: (a)Schematic drawing of intermediate RIXS spectrometer in Rowland layout. Figure reproduced from [28]. (b) Photograph of the SiO_2(10-2) analyzer operating around the Ru-L_3 edge at 2840 eV. The round analyzer is mounted into the octagon holder which enables rotation in two directions.

2.2 Spectrometer with Rowland layout

Figure 2.9(a) shows the schematic of the spectrometer with a Rowland layout. The scattered light from the sample is captured by the analyzer and subsequently reflected the charge-coupled device (CCD) detector to record the intensity. The analyzer comprises a mosaic of flat single crystal segments arranged on a spherical surface with a radius R=1 m, as depicted in Fig. 2.9(b). Each small SiO_2 segment has a dimension of 1.5 mm × 1.5 mm and is separated by a gap of 0.2 mm. For Ru-L_3 RIXS measurements, the $SiO_2(10\bar{2})$ reflection is selected. The CCD detector contains a 2048×2048 pixel array, where each pixel has a dimension of 13.5 μm × 13.5 μm. The reflected beam spans a range of 3 mm across the pixels, with a dispersion rate of 5.8 meV/pixel, corresponding to an energy window of 1.3 eV when the analyzer is not rotated. Utilizing the 4B inline HRM and nested HRM, we can achieve a combined resolution of 75 meV and 96 meV, respectively. The energy resolution is experimentally determined by the full width at half maximum (FWHM) of the elastic line reflected from silver paint or GE-varnish.

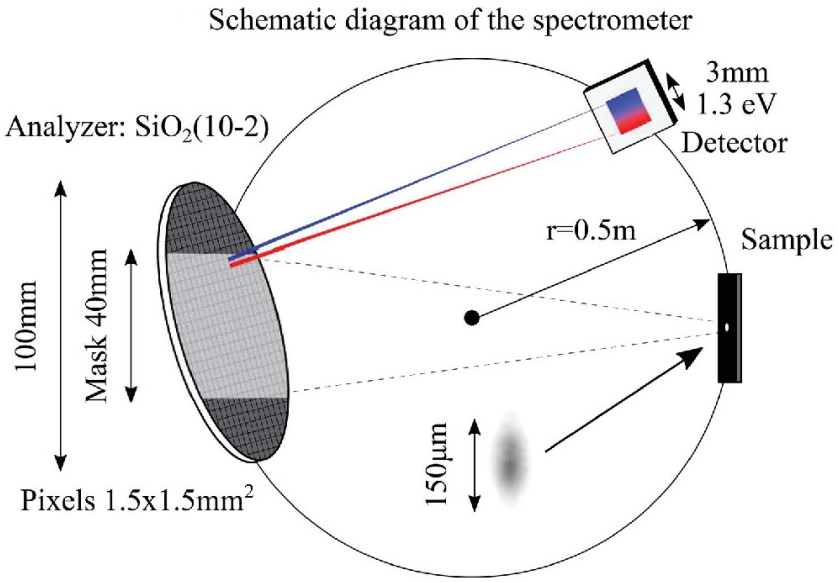

Figure 2.10: Schematic diagram of the spectrometer. Figure reproduced from Ref [28].

2.3 Intermediate RIXS spectrum of $SrRu_2O_6$

As the very first result obtained with this IRIXS spectrometer, we have successfully measured the spin wave and spin-state transitions of $SrRu_2O_6$, a ruthenate antiferromagnetic insulator with high Néel temperature. Here I will briefly introduce the outcomes in Ref[4] to exhibits the capability of this beamline to measure the magnon dispersion in Ru compounds.

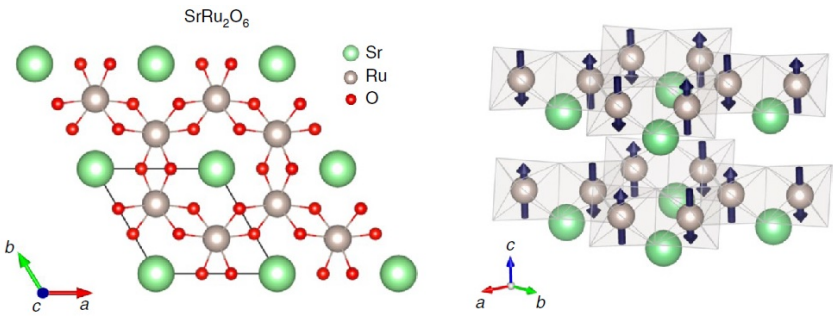

Figure 2.11: Structure of $SrRu_2O_6$. Figure reproduced from Ref [4].

The crystal structure of $SrRu_2O_6$ is illustrated in Fig 2.11. It belongs to the hexagonal space group $P\bar{3}1m$ with lattice constants $a = 5.200(2)$ Å and $c = 5.225(2)$ Å. The ruthenium ions are surrounded by an edge-sharing oxygen ion octahedron and form a two-dimensional honeycomb network. The RuO_6 honeycomb layer is sandwiched by the chemically inactive

Sr layer so that the interplane interaction can be treated as weak. Previous studies [43, 44] have revealed the G-type antiferromagnetic (AFM) order where the Ru spins are antiparallel to their nearest neighbors and all aligned along the c axis. Surprisingly this AFM order can survive up to a high Néel temperature ($T_N = 563K$) and this behavior has inspired a considerable amount of theoretical work. However the underlying mechanisms of this system remained unclear due to the missing experimental evidence of its electronic structure and dynamics. With the intermediate RIXS spectrometer we measured the momentum resolved spin wave and spin-state excitations of $SrRu_2O_6$ and determined the low-energy electronic structure which well explained the unusual high T_N of this antiferromagnet.

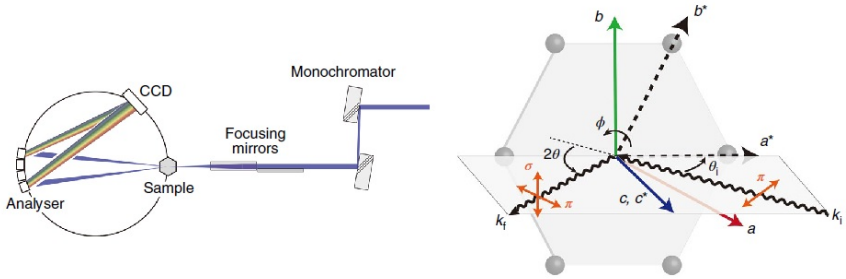

Figure 2.12: Schematic of the the scattering geometry. Figure reproduced from Ref [4].

Fig 2.12 presents a schematic of the IRIXS spectrometer and the scattering geometry. The incident energy is tuned to $\hbar\omega_i = 2837.5$ eV to match the L_3-absorption edge. The polarization of the beam is in the scattering plane (π polarized) and the scattering angle 2θ is fixed at 90 degrees, which considerably suppresses the elastic charge scattering, and therefore allows us to distinguish low-energy magnetic excitations. The momentum transfer is measured along the $(-H, 0)$ and $(-H, -H)$ directions in the Brillouin zone.

The measurement results are shown in Fig 2.13. We notice three distinct features in these spectra: (i) a low-energy dispersive peak denoted by red circles has a sinusoidal dispersion with maxima at $\mathbf{q} = -0.5$ along the $(-H, 0)$ direction and at $(-0.33, -0.33)$ along the $(-H, -H)$ direction, (ii) a non-dispersive peak located at 0.65 eV, as denoted by green triangles, and (iii) a broad continuum which onsets from 0.4 eV. The intensity of the first feature is maximal at the AFM ordering vector and vanishes at $\mathbf{q} = 0$, which coincides with the behavior of spin waves, hence this low-energy excitation is expected to be the single magnon. The non-dispersive feature is assigned to spin-state transitions between $S = \frac{3}{2}$ and $S = \frac{1}{2}$, and the continuum emerges from electron-hole excitations.

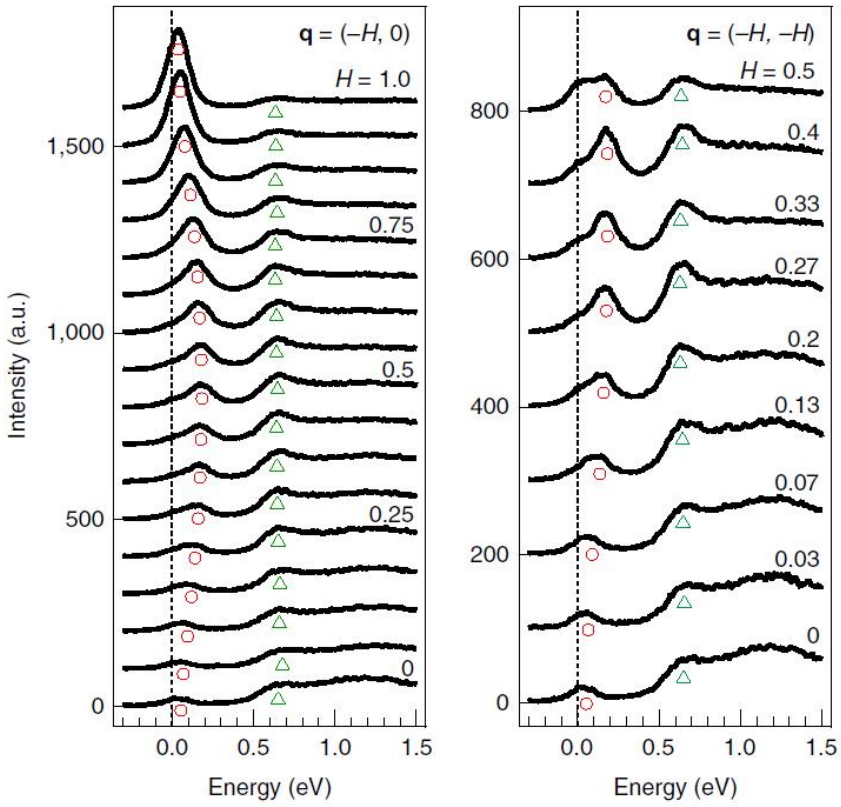

Figure 2.13: Low-energy RIXS spectra along $(-H, 0)$ and $(-H, -H)$ directions. Figure reproduced from Ref [4].

To better understand the magnetic dynamics of $SrRu_2O_6$, the magnon peak is fitted to extract the dispersion relation. The result is presented in Fig 2.14. At (-1,0) one notes a magnon gap of 36 meV, which indicates the c-axis anisotropy. To better understand the magnetic dynamics, we use the following spin Hamiltonian:

$$H = J \sum_{\langle ij \rangle} \mathbf{S}_i \cdot \mathbf{S}_j - K \sum_i S_{iz}^2 \tag{2.3}$$

where $\mathbf{S}_i$ is the spin-$\frac{3}{2}$ operator at site i, J is the isotropic Heisenberg interaction and K denotes the single-ion anisotropy term to align the spins along the c direction. As above mentioned, the interplane interaction is assumed to be weak and will be neglected in the following analysis. By applying the linear spin-wave approximation, the experimental result could be well reproduced by fixing the fitting parameter set to $J = 65$ meV and $K/J = 0.028$, as shown by the dotted line in Fig 2.14. The good agreement between theory and RIXS measurement demonstrates that the nearest neighbor Heisenberg interaction

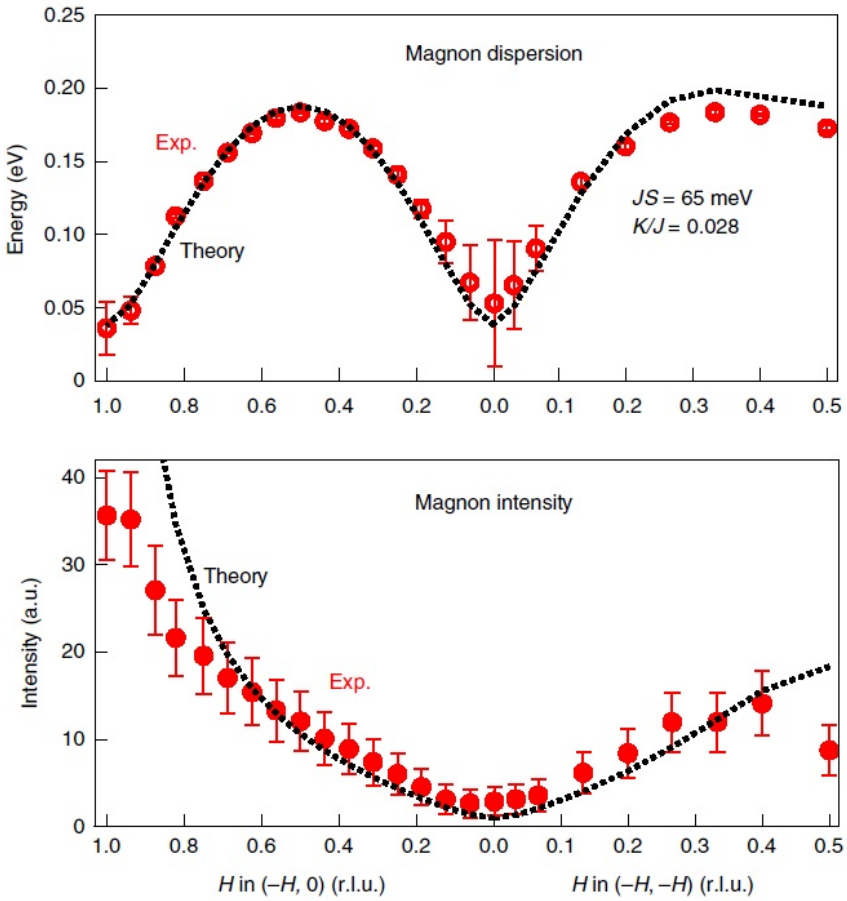

Figure 2.14: Magnon dispersion and intensity as a function of momentum transfer. Figure reproduced from Ref [4].

serves as a good description of the magnetic excitation in $SrRu_2O_6$. Further Monte-Carlo simulations give a T_N value of 500 K. This high Néel temperature emerges from the spin-orbit induced magnon gap of 36 meV, which greatly suppresses low-energy fluctuations and hence stabilizes long-range AFM order.

2.4 IRIXS at the Rh-L_3 and U-M_5 edge

Over the last few years the working energy of the P01 beamline has been fixed at the Ru-L_3 edge around 2838 eV and a plethora of IRIXS studies on Ru compounds were carried out. However, the potential of this beamline is not yet fully exploited. Recently, several new crystal analyzers for the Rowland spectrometer were fabricated so that the working energy range can be extended to a large extent. As a first step towards other absorption edges, we

Analyzer	Energy	Bragg reflection	Etched?	Resolution (meV)
U 003	U M_5 edge ~ 3552 eV	(0 0 3)	Yes	73
U 004			No	69
Rh 005	Rh L_3 edge ~ 3004 eV	(2 0 0)	Yes	89
Rh 006			No	89

Table 2.1: Details of tested analyzers

selected two working energies to start with: the Rh-L_3 edge (around 3005 eV) and the U-M_5 edge (around 3500 eV). Fig. 2.15 shows photos of the four analyzers being tested. The details of these analyzers are summarized in Tab.2.1.

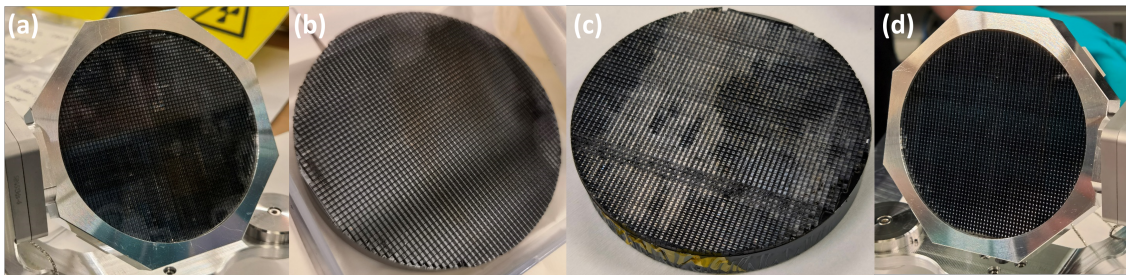

Figure 2.15: Photographs of the four tested analyzers: (a)U #003, (b) U #004 (c) Rh #005 (d) Rh #006.

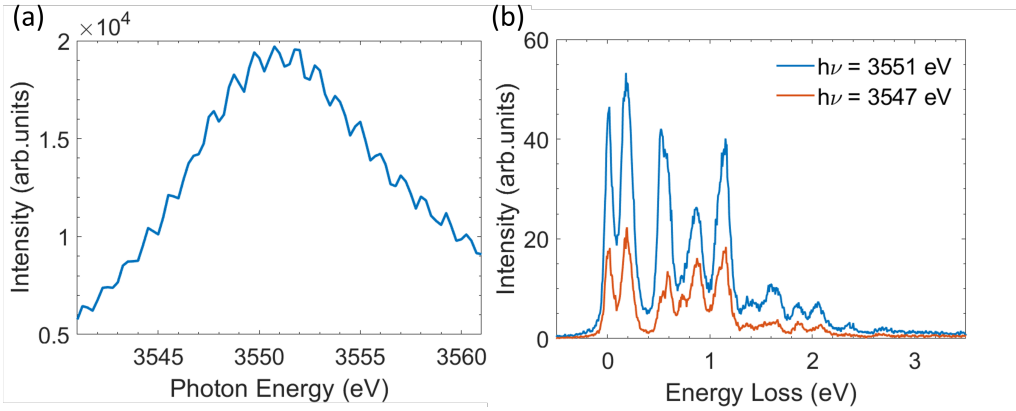

Figure 2.16: (a) X-ray absorption and (b) RIXS spectrum of UO_2 at U-M_5 edge, taken at 3547 eV (yellow line, pre-edge) and 3551 eV (blue line, at resonance). A clear resonance enhancement is observed at 3551 eV.

These analyzers are made by diced spherical SiO_2 crystals working at a certain Bragg peak, as shown in Tab.2.1. Here the resolution is determined by the full-width half-maximum (FWHM) of the elastic line measured from GE-varnish. The combined resolution is comparable to the previous analyzer working at the Ru-L_3 edge. For each working energy,

two analyzers were fabricated: one was etched by HF acid and the other was not. Their difference can be easily observed in the pictures in Fig. 2.15, where unetched analyzer have shiny surface and dark color, while the etched analyzers show large areas of white stain. This stain appears because the underlying glue between the SiO_2 crystal and the substrate gets corroded by HF acid at the same time during the etching process. This chemical treatment helps to release the inhomogeneous residual strain in the SiO_2 crystal introduced from the dicing treatment and is proved to be crucial for fabricating analyzers of hard X-ray spectrometers, since the penetration depth of hard X-rays is comparable to the length scale of inhomogeneity. In our intermediate energy range, however, etching does not produce significant improvement to the performance. Several factors could account for this observation. Firstly, the etching time of our analyzers is relatively short compared to the hard X-ray analyzers. This might lead to an incomplete chemical reaction and therefore the residual strain is not fully eliminated. The second possible reason is that intermediate X-rays have a much smaller penetration depth, so that the scattering process is less sensitive to the strain. The third possible reason is that the combined FWHM is composed of not only the analyzer but also other upstream devices of the spectrometer, such as DCM and HRM, so the improvement of the analyzer's quality only adds an effectively negligible advantage to the overall performance of the spectrometer. On the other hand, chemical etching with HF acid is complicated and extremely dangerous. Taking into account the significant drawbacks and limited improvement with etching, it turns out that unetched analyzers are the best choice for the IRIXS setup.

Having mounted and commissioned the analyzers, we were able to examine the performance of the spectrometer as a whole. We start with measurements at the U-M_5 edge on a piece of UO_2 single crystal. The incident angle is fixed at 20° throughout the measurements. Fig. 2.16(a) shows the X-ray absorption spectrum, measured by the total fluorescence yield response by the SDD. The XAS shows a very broad feature where fine structures are absent, unlike that of compounds with $3d$ elements. This is a typical behavior for f electrons, because the richness of decay channels lead to a shorter excitation lifetime and inevitably broadens the width of the XAS peaks. Fig. 2.16(b) shows the RIXS spectra of UO_2 taken at two different incident energies: 3547 eV (pre-edge) and 3551 eV (resonance energy), where a clear resonance enhancement is observed. Moreover, a series of sharp excitation peaks appear in a wide energy range from (quasi)elastic to 2 eV. This large number of features originates from the complicated multiplet structures involving contributions from both d

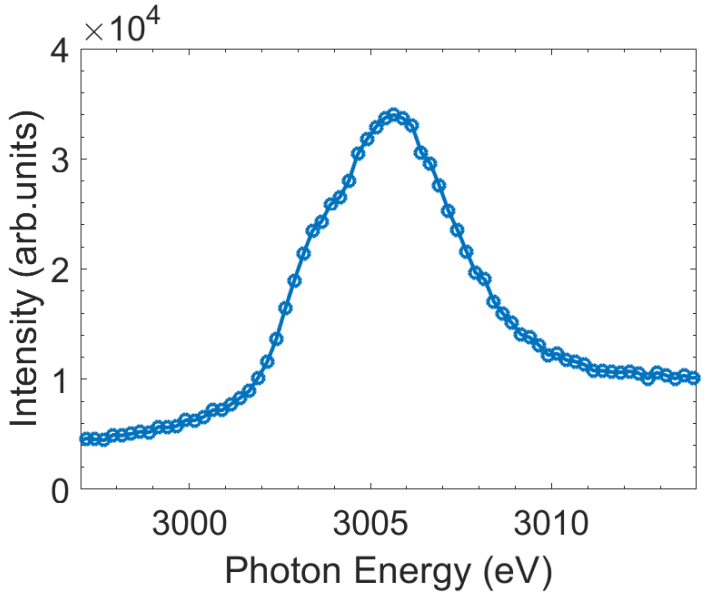

Figure 2.17: Rh-L_3 X-ray absorption spectrum of Sr_2RhO_4.

and f electrons. Notably, although the working energy is much higher than the Ru-L_3 edge, spectra with good signal-to-noise ratio can be readily acquired within a counting time of 1 hour, meaning that the new analyzer still possesses a good photon efficiency.[45]

Fig. 2.17 shows the XAS of Sr_2RhO_4 measured by total fluorescence yield. In the XAS profile two fine structures at 3003 eV and 3006 eV are observed, which are qualitatively similar to those of the Ru-L_3 edge XAS. The energy separation is induced by octahedral crystal field splitting. With the new analyzer, we will be able to collect the RIXS spectra of Sr_2RhO_4 single crystals at the Rh-L_3 edge and compare the results with a previous RIXS study operating at the O K edge[46] and carry out systematic and in-depth studies of the spin excitations in this material.

2.5 High-resolution spectrometer

As discussed in Chapter 1, energy resolution remains a critical limitation in RIXS spectroscopy and is therefore a crucial figure of merit for any RIXS spectrometer. Despite the significant achievements obtained using the Rowland spectrometer described above, its energy resolution of approximately 70 meV falls short of ideal, particularly when

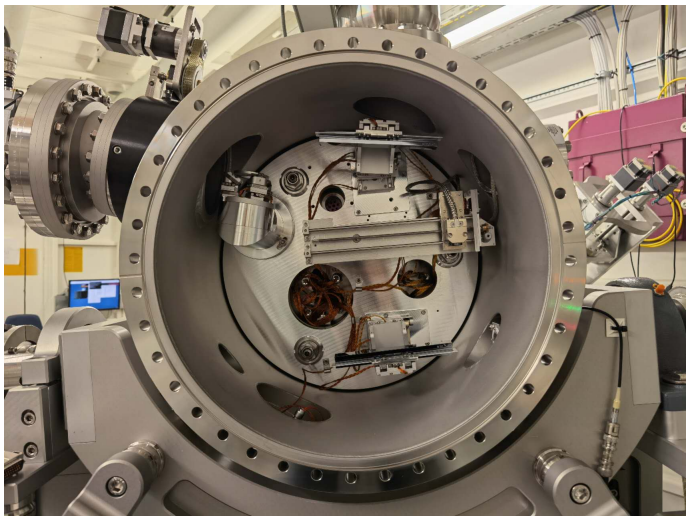

Figure 2.18: Photograph of the optics chamber of high-resolution spectrometer. The second Montel mirror is not installed.

investigating low-energy magnetic excitations or small splitting due to distorted crystal fields. Consequently, considerable effort has been dedicated to constructing and commissioning a new spectrometer in recent years.

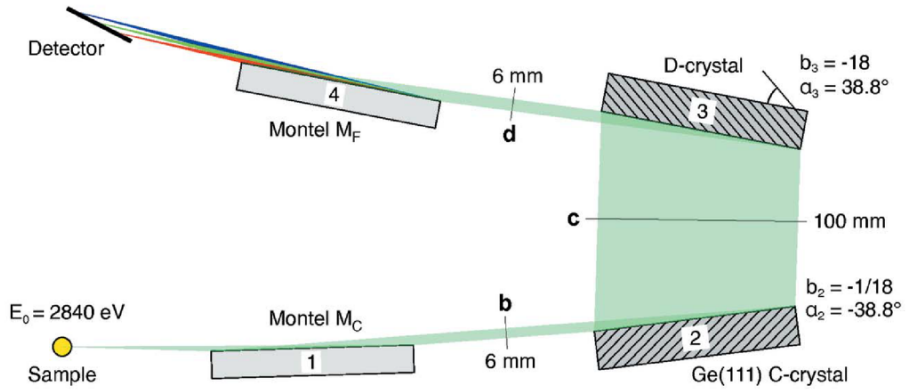

Figure 2.19: Sketch of the high-resolution spectrometer, consisting of a collimating Montel mirror, two reflecting crystals, followed by focusing Montel mirror and a grazing detector. The crystal used Ge(111) at the first place, but is replaced by Si(111) which has a uniform d-spacing.

Fig.2.19 depicts a schematic of the spectrograph. Initially, the scattered light from the sample is collimated by a Montel mirror M_c with a working distance of 200 mm. Subsequently, it is reflected successively by the collimator C and then dispersed by the crystal D. Originally, the analyzer was designed to employ Ge(111), but it was later switched to Si(111) because the long footprint of the grazing incident light on the analyzer

necessitates a uniform d-spacing in the crystal within a large area, which is more readily achieved with Si than Ge. Finally, the energy-analyzed beam is focused by another Montel mirror onto the grazing-incidence CCD detector.

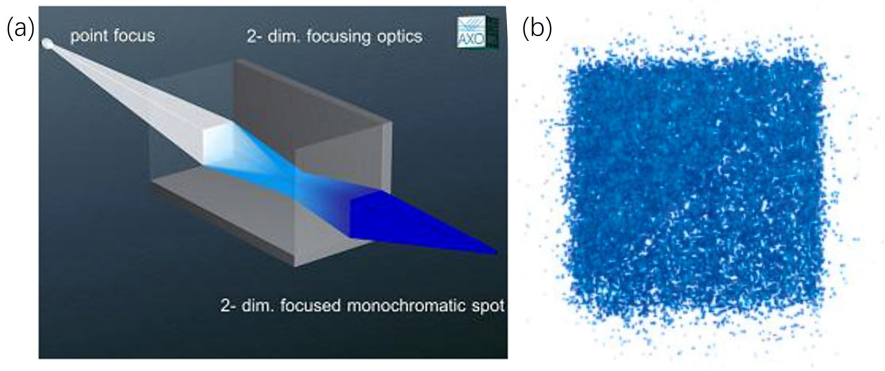

Figure 2.20: (a)Schematic of the Montel mirror. Figure reproduced from Ref[47]. (b) The spatial profile of the post-Montel beam measured by the CCD detector.

The Montel mirror plays a pivotal role in both collimating and focusing the beam. Fig. 2.20(a) illustrates the structure of this device, comprising a pair of identical reflection mirrors arranged in an L-shape, with two square apertures at the entrance and exit. Each reflection mirror is shaped into a parabola, with the beam spot situated at the focal point, enabling it to accept scattered photons with a wide solid angle and collimate the beam upon reflection. Notably, the periodicity of the reflecting multilayer is tailored to match the varying incident angle along the Montel mirror, and thereby ensuring satisfaction of the Bragg condition. The collimated beam has dimensions of 5.5 mm $\times$ 5.5 mm, determined by the size of the exit aperture. The intensity profile is shown in Fig. 2.20(b), which consists of two isosceles right triangles with a small gap between them resulting from the slight spacing between the two parabolic mirrors.

The post-Montel beam then encounters the first 150 mm long Si(111) crystal with a Bragg angle of $\theta_B = 44°$ and an asymmetric angle $\alpha = 41°$. This crystal further collimates and expands the beam width. Subsequently, the widened beam is intercepted by the second analyzer crystal with an opposite configuration, resulting in a highly dispersive reflected beam with the size reduced back to 5.5 mm due to the inverse geometry. The collimated beam is then accepted by the second Montel mirror and focused onto the detector at grazing incidence. The CCD detector comprises 2048 $\times$ 2064 pixels, with a pitch size of 15 μm and

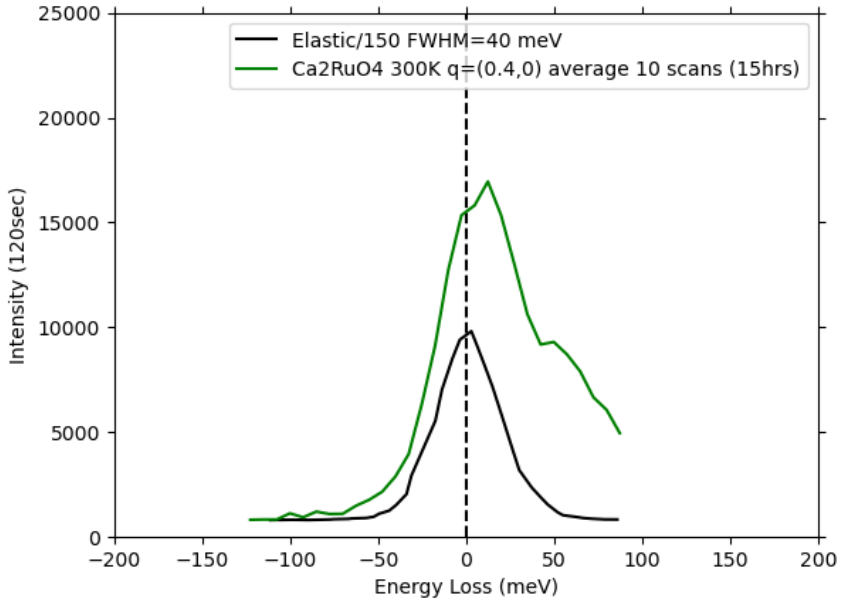

Figure 2.21: RIXS spectra measured on a Ca_2RuO_4 sample and on GE-varnish.

generates a dispersion of ~ 17 meV/mm. Fig. 2.21 illustrates the RIXS spectra measured on a Ca_2RuO_4 sample as well as on GE-varnish. The combined energy resolution is around 40 meV, determined by the FWHM of the elastic scattering from GE-varnish.

There are still two significant shortcomings of the high-resolution spectrometer. The first and most crucial issue is the low flux intensity. In spectroscopy studies, there is always a trade-off between intensity and energy resolution. In our case, the beam flux on the detector is further suppressed due to the low reflection of the nested HRM and multiple reflection mirrors compared to the Rowland spectrometer. Consequently, the typical counting time for RIXS measurements exceeds 4 hours to acquire a reasonable signal-to-noise ratio. The weak flux intensity leads to the second challenge: the alignment of the sample is extremely time-consuming. In Montel optics, the beam spot must be placed at the focal point of the mirror, and even a tiny misalignment results in a significant decrease in collected intensity. As a result, when measuring momentum-dependent RIXS spectra, the sample position must be aligned every time after rotating θ, which typically takes around 0.5 ~ 1 hour, whereas in the Rowland layout, the signal intensity is insensitive to tiny misalignment. This disadvantage can be mitigated by improving the brilliance of the incoming beam, such as by adopting a different HRM design that uses fewer crystals to reduce flux waste.

2.6 Summary

In this Chapter, I introduced the recently constructed state-of-the-art IRIXS spectrometer at the P01 beamline of DESY in Hamburg. As of now, this stands as the sole operational spectrometer functioning within the energy range of tender X-rays with an energy resolution below 100 meV. I provide an overview of the instrumentation installed in this beamline, detailing some of their key technical parameters, alongside presenting several measurement results acquired with this spectrometer.

Within the P01 beamline, X-ray photons generated by the undulator traverse through the DCM, HRM, and KB mirrors successively before illuminating the sample within the sample chamber. Currently, two HRMs are in use: the 4B inline HRM and nested HRM, each boasting distinct designs and performance metrics. The combined optics system of the DCM and HRM furnishes a finely monochromated incoming beam with bandwidths of 60 meV (4B inline HRM) and 30 meV (nested HRM). Within the sample chamber, the manipulator affords motion and rotation in five degrees of freedom to ensure precise sample alignment, further aided by the energy-resolving SDD. The scattered light is then analyzed and collected by the spectrometer. Presently, two spectrometers are installed in the sample chamber: one with a Rowland layout, and another employing high-resolution techniques based on collimation optics.

In the Rowland layout, the scattered light undergoes dispersion by a spherical diced SiO_2 analyzer before being captured by the CCD detector. The analyzers are fabricated with different Bragg reflections depending on the working absorption edge. Thus far, analyzers operating at the Ru-L_3 edge (2840 eV), Rh-L_3 edge (3004 eV), and U-M_5 edge (3552 eV) have been successfully commissioned. While a plethora of studies on Ru compounds, including $SrRu_2O_6$,Sr_2RuO_4,$SrRuO_3$,Ca_2RuO_4,Ca_3RuO_7,$RuCl_3$,K_2RuCl_6, have been conducted at the Ru-L_3 edge, investigations at Rh and U edges are still nascent. These analyzers working at different absorption edges yield comparable energy resolutions of 70~90 meV. Notably, we have not observed a discernible improvement in analyzer performance due to etching treatment by HF. Furthermore, I present preliminary data collected on $SrRu_2O_6$, UO_2, and Sr_2RhO_4, proving that the spectrometer operates as anticipated.

The recently commissioned high-resolution spectrometer employs a distinct design compared to the Rowland spectrometer. Here, the scattered light is initially collimated by the Montel mirror and Si crystal, then dispersed by the second Si crystal with an opposite layout, and ultimately focused by another Montel mirror before being captured by the grazing CCD

detector. The combined energy resolution is approximately 30 ~ 40 meV. Currently, the spectrometer contends with low brilliance of the incoming beam, necessitating considerable time for alignment and measurement. This challenge may potentially be addressed through the adoption of HRMs with new designs in the future.

3 Kitaev Spin Liquid Candidate $RuCl_3$

Transition metal compounds with strong electron correlation effects usually host exotic physics behaviors, such as unconventional superconductivity, metal-insulator transitions, charge-, magnetic- and orbital-ordering, extremely large magnetoresistance *etc*.[22] Among these phenomena, magnetism is extensively studied for both fundamental scientific understanding as well as for industrial applications. Alongside the ordering phenomena, frustrated magnetic interactions have attracted much attention in recent years.[48, 49] Among the solid state systems that shows frustration mechanisms, the Kitaev spin liquid Hamiltonian defined on a honeycomb lattice presents an exactly solvable model supporting fractionalized excitations, holding great potential for fault-tolerant quantum computations[50]

A theoretical work [51] has suggested several criteria to help us identify materials that can be a promising candidate for the solid state realization of the Kitaev spin liquid model, such as α-$RuCl_3$ ($RuCl_3$ hereafter)[52] and A_2IrO_3(A = Na,Li)[53, 54]. I will focus on $RuCl_3$ in the following two Chapters and present the results of our Ru-L_3 RIXS study on this material in bulk crystal form (this Chapter) and in nanolayer form (Chapter 4). Although a number of studies have revealed its exotic magnetic dynamics with a variety of experimental methods, our results yield knowledge of the elementary excitations in a wide range of energy and momentum, and establish an integrated methodology to approach the study of Kitaev spin liquid systems with RIXS spectroscopy.

This Chapter starts with an introduction of the Kitaev spin liquid model, followed by a review of several previous studies on $RuCl_3$ which provide experimental evidence of the exotic magnetic interactions in this material. Next, I will present the key findings obtained from Ru-L_3 RIXS measurements on a $RuCl_3$ single crystal carried out at the P01 beamline, following Ref[40]. From the RIXS spectra we can extract the interaction parameters of the electronic structure and estimate the strength of the magnetic exchange. The combination of experimental data and theoretical analysis suggests that the magnetic order in $RuCl_3$ is fragile and in competition with ferromagnetic correlations.

3.1 Kitaev spin liquid model and realization

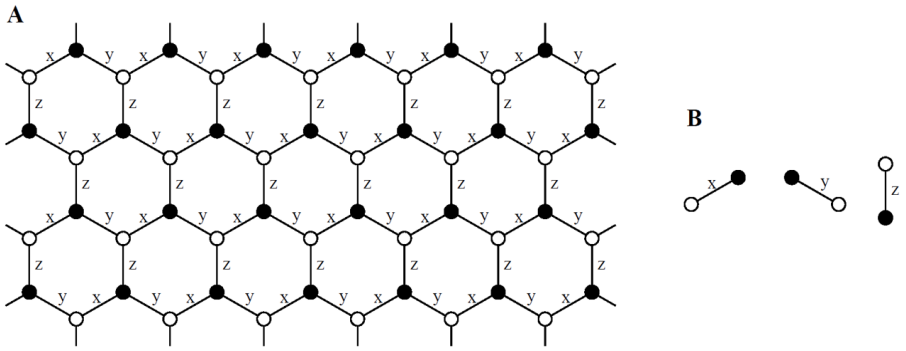

Figure 3.1: Kitaev-type interaction defined on a honeycomb lattice. The letter x, y and z indicate the type of each link. Figure reproduced from Ref[50]

Magnetic correlation arising from exchange interactions is a ubiquitous phenomenon in quantum materials and serves as a cornerstone in the exploration of fundamental physics. At low temperatures, these magnetic interactions typically give rise to various forms of magnetic ordering, including ferromagnetism (FM), ferrimagnetism, and antiferromagnetism (AFM). However, in certain cases, the interplay of spin interactions among different sites may lead to a highly degenerate magnetic ground state, giving rise to what are known as frustrated magnets.[48, 54] Among the diverse range of frustrated systems under investigation, the phenomenon of quantum spin liquid (QSL) holds particular fascination due to its potential to harbor exotic excitations. QSL is characterized by the absence of magnetic order in the ground state, despite the well-defined and highly entangled local moments. Consequently, spin fluctuations persist even at absolute zero temperature ($T = 0$ K). A prerequisite for the existence of QSL is the presence of localized magnetic moments within the material system, a condition that can be satisfied either by Mott insulators possessing well-defined spin and orbital degrees of freedom or by "artificial lattices" composed of ultracold atoms.

Within the realm of quantum spin liquid systems, the Kitaev spin liquid, defined on a honeycomb lattice, has emerged as a focal point in contemporary solid-state research.[50] The Kitaev-type Hamiltonian is characterized by a bond-dependent Ising-like spin interaction:

$$H = -J_x \sum_{x-links} \sigma_i^x \sigma_j^x - J_y \sum_{y-links} \sigma_i^y \sigma_j^y - J_z \sum_{z-links} \sigma_i^z \sigma_j^z \tag{3.1}$$

where the definition of x, y and z links is shown in Fig. 3.1. It has been demonstrated that this bond-dependent Hamiltonian is exactly solvable, with fractionalized excitations consisting of a Majorana fermion and a gauge flux.

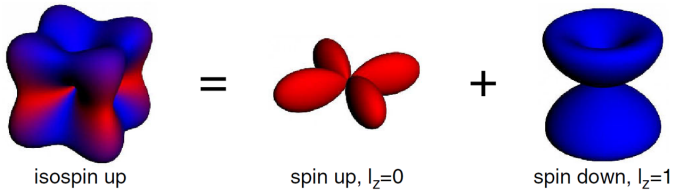

Figure 3.2: Spin density of the Kramers doublet of hole in Eqn.3.2. The isospin state is the superposition of different orbitals and spins. Figure reproduced from Ref[51]

Identifying a realistic material system that accommodates Kitaev-type interactions poses a significant challenge. In 2007, a quantum compass model was introduced in Ref[51], providing a clear criterion for the search for Kitaev spin liquid materials. This model leverages the orbital degree of freedom of transition metal ions and the entanglement between spin and orbit in a pseudospin-1/2 system. As discussed in Chapter 1, in the large $10Dq$ limit, the low-energy electronic structure can be effectively reduced within the t_{2g} subspace by employing a model with $L_{\text{eff}} = 1$. In the presence of strong spin-orbit coupling and weak tetragonal distortion, the spin and orbital degrees of freedom become heavily entangled, leading to a ground state characterized by a Kramers doublet:

$$
\begin{aligned}
|\tilde{\uparrow}\rangle &= \sin\theta|0,\uparrow\rangle - \cos\theta|+1,\downarrow\rangle \\
|\tilde{\downarrow}\rangle &= \sin\theta|0,\downarrow\rangle - \cos\theta|-1,\uparrow\rangle
\end{aligned}
\tag{3.2}
$$

where $\tan 2\theta = 2\sqrt{2}\lambda/(\lambda - 2\Delta)$ and $|0\rangle = |xy\rangle$, $|\pm 1\rangle = \frac{1}{\sqrt{2}}(i|xz\rangle \pm |yz\rangle)$ by using the conventional basis in Eqn.1.21. This ground state engenders a distinctive spin distribution in real space, as depicted in Fig. 3.2, forming the basis for bond-dependent exchange interactions. In the geometry of edge-sharing octahedra illustrated in Fig. 3.3, two neighboring transition metal ions share two ligand ions, forming superexchange hopping channels between them. However, it has been demonstrated that the hopping amplitudes of these channels interfere destructively, exactly canceling each other if the bond angle between the ligand ion and transition metal ions is 90°. This results in an overall exchange interaction described by the Kitaev-type interaction shown in Eqn.3.1.

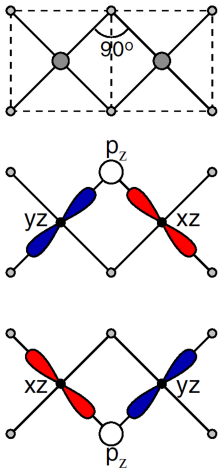

Figure 3.3: Schematic of a edge-sharing octahedron and the active hopping channel. The bond angle between the ligand ion and two transition metal ions is 90°. The amplitude of the two hopping channels via ligand ions are exactly canceled. Figure reproduced from Ref[51]

In a realistic material system, the magnetic structure is influenced not only by the Kitaev term but also by the Heisenberg interaction from first-, second-, and third-nearest-neighbors, as well as other off-diagonal terms. Therefore, an extended Kitaev-Heisenberg Hamiltonian $\tilde{H}$ is required to incorporate these additional terms. For z-type bonds, the Hamiltonian is expressed as:

$$\begin{aligned} H_{ij}^{(\gamma)} &= KS_i^{(z)}S_j^{(z)} + J\mathbf{S}_i \cdot \mathbf{S}_j + \Gamma(S_i^{(x)}S_j^{(y)} + S_i^{(y)}S_j^{(x)}) \\ &+ \Gamma'(S_i^{(x)}S_j^{(z)} + S_i^{(z)}S_j^{(x)} + S_i^{(y)}S_j^{(z)} + S_i^{(z)}S_j^{(y)}) \end{aligned} \tag{3.3}$$

For the $\gamma = x, y$ type bonds, $H_{ij}^{(\gamma)}$ can be obtained from cyclic permutations of x, y, and z. The extended Kitaev-Heisenberg Hamiltonian has become the cornerstone of modeling the magnetic structure and analyzing experimental results from techniques such as INS or RIXS, as we will discuss below.

In summary, the Kitaev Hamiltonian is expected to manifest in Mott insulators under the following conditions: (i) the transition metal ion possesses a pseudospin of $\tilde{S} = 1/2$, (ii) the lattice structure is honeycomb, (iii) the ions are surrounded by edge-sharing octahedra, and (iv) there is strong spin-orbit coupling. Notably, condition (iv) is more readily met in compounds with $4d$ and $5d$ elements compared to $3d$ elements due to their heightened spin-orbit coupling. Consequently, much attention has been devoted to material systems containing ions such as Ru^{3+} or Ir^{4+}. Among these candidates, $RuCl_3$ has garnered significant research interest, and we will provide a brief overview of key experimental findings before introducing the RIXS measurements on $RuCl_3$ single crystals.

3.2 Introduction to $RuCl_3$

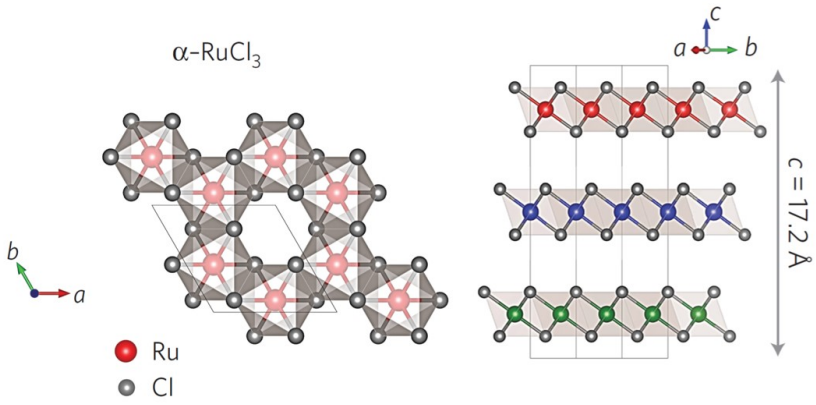

Figure 3.4: Structure of α-$RuCl_3$. Figure reproduced from Ref [55].

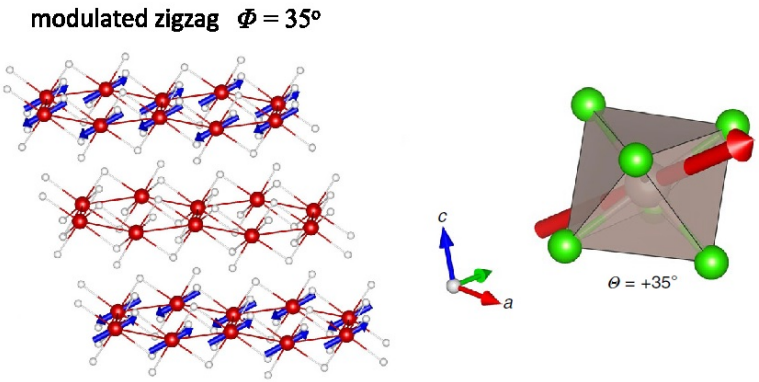

Figure 3.5: The magnetic momentum of Ru^{3+} is 35° canted from the honeycomb plane. Figure reproduced from Ref[56] and Ref[57].

$RuCl_3$ is a layered van der Waals material with an in-plane honeycomb structure, characterized by lattice constants $a = b = 5.96$ Å and $c = 17.2$ Å, as illustrated in Fig. 3.4. The Ru^{3+} ions are surrounded by six Cl^- ions, forming $RuCl_6$ octahedra with shared edges. The strong spin-orbit coupling of the Ru t_{2g} levels and the crystal structure fulfill the prerequisites for hosting Kitaev exchange interactions as discussed earlier. However, a combination study of X-ray diffraction and thermal transport has revealed an AFM order, with transition temperatures T_N reported to be either 7 K or 14 K in several studies.[58, 59, 60, 61, 55] This discrepancy arises from two possible stacking orders in the out-of-plane direction: 7 K corresponds to an ABCABC... order, while 14 K corresponds to an ABABAB... order.[56] Due to weak interlayer interactions, this stacking fault can be easily induced by minor external forces, such as rubbing or bending the crystal. Neutron

diffraction supports the zigzag AFM order, with the tilting angle between the Ru magnetic moments and the honeycomb plane suggested to be $\Theta = \pm 35°$.[56] A subsequent resonant elastic X-ray scattering (REXS) study at the Ru-L_3 edge further refined the angle to $\Theta = 35°$ by measuring the azimuthal dependence of the diffraction intensity.[57] These findings aid in understanding the significant anisotropy between in-plane and out-of-plane magnetic susceptibility and suggest the presence of FM Kitaev interaction (*i.e.* $K < 0$) to stabilize this magnetic order.

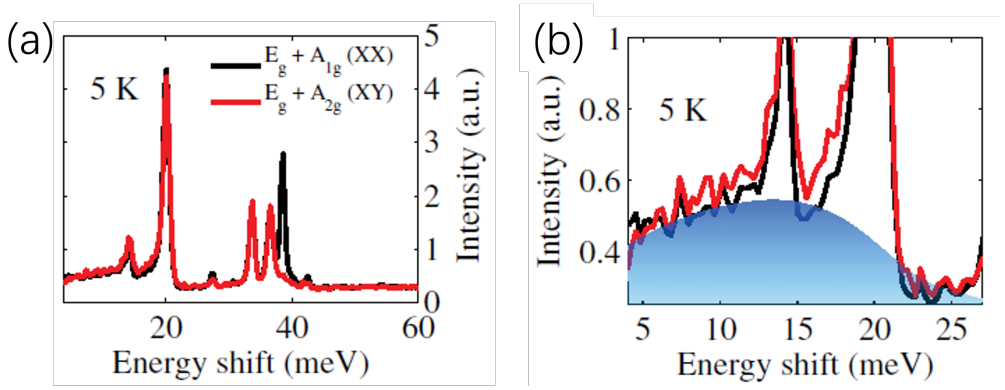

Figure 3.6: Raman spectra of $RuCl_3$ single crystal at 5K. The broad continuum below 25 meV is indicative of an unusual magnetic scattering. Figure reproduced from Ref [62]

The "smoking gun" for Kitaev spin liquid remains elusive; however, several experimental pieces of evidence have indirectly supported the possible existence of Kitaev interaction in $RuCl_3$. Several polarized Raman studies on $RuCl_3$ crystals have revealed temperature-dependent responses from phonon and magnetic scattering.[62, 63, 64] In Ref[62], two phonon modes at 14 meV and 20 meV with asymmetric line profiles were observed, as shown in Fig. 3.6(a), characteristic of interference between well-defined phonon modes and continuous excitations.[65] This continuum, observed in both parallel (XX) and cross (XY) configurations, extends up to 20-25 meV (blue region in Fig. 3.6(b)), attributed to magnetic fluctuations due to its broad width and low energy. Interestingly, the spectral weight of the continuum exhibits an unusual temperature dependence, deviating from that of single- and bi-magnon processes (Fig. 3.7). Below approximately 100 K, the spectral weight of magnetic excitations remains essentially unchanged, indicating the presence of frustrated magnetic interactions. These magnetic dynamics also affect the temperature dependence of the phonon self-energy. The FWHM of the phonon mode at 20 meV exhibits a clear deviation from the expectation of an anharmonic model (blue line),[66] attributed to additional scattering channels from spin-phonon interactions. Notably, the

observed characteristic temperature of approximately 100 K is much higher than the Néel temperature $T_N = 7$ K, suggesting that magnetic fluctuations persist well above the ordering temperature, a typical behavior of low-dimensional frustrated magnets.

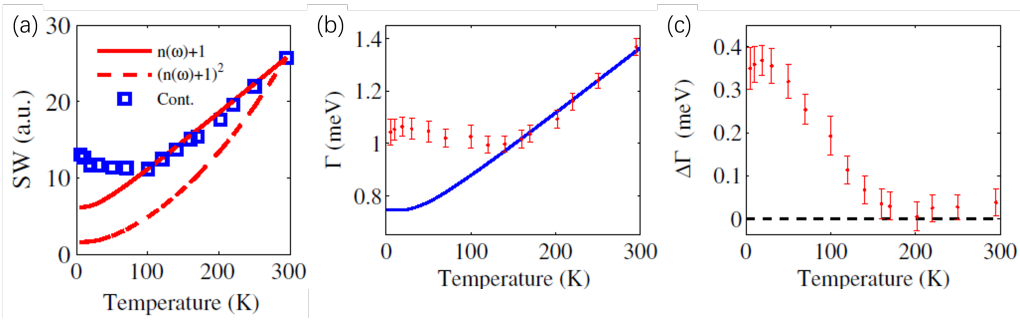

Figure 3.7: (a)The spectral weight of low-energy magnetic continuum shows exotic temperature dependence which remains essentially unchanged below ~100 K (blue square), which cannot be explained by single- and bi-magnon picture (red solid and dashed line) (b) Temperature-dependent FWHM of the phonon mode at 20 meV, which deviates from the prediction of anharmonic model but resembles the spectral weight in panel (a). (c) The difference of FWHM between experimental data and anharmonic model. Figure reproduced from Ref [62]

As a conventional experimental probe for studying magnetic excitations, INS has provided momentum-resolved measurements with high energy resolution.[55, 67, 68] An INS measurement on powdered $RuCl_3$ observed the spin-orbit exciton, confirming the pseudospin $\tilde{S} = 1/2$ scenario of Ru^{3+}.[55] Furthermore, the energy and momentum dependence of collective magnetic modes were measured, allowing for the estimation of the strength of Kitaev and Heisenberg interactions: $K \sim -2J$. Notably, the energy profile showed good agreement with the theory of quantum spin liquids rather than conventional spin wave theory, indicating the significance of frustrated interactions in shaping the magnetic structure. A subsequent INS study on single-crystal $RuCl_3$ [67] conducted an in-depth measurement of the temperature dependence of low-energy magnetic excitations, as depicted in Fig. 3.8. At low temperatures, a strong magnetic response at the Γ point was observed in addition to the six AFM order peaks. Upon heating above T_N, the AFM peaks quickly vanished, while the magnetic fluctuation at the Γ point persisted up to 100 K. This temperature scale is consistent with the Raman study and provides a rough estimation of the strength of the Kitaev interaction, approximately $K \sim 100$ K.

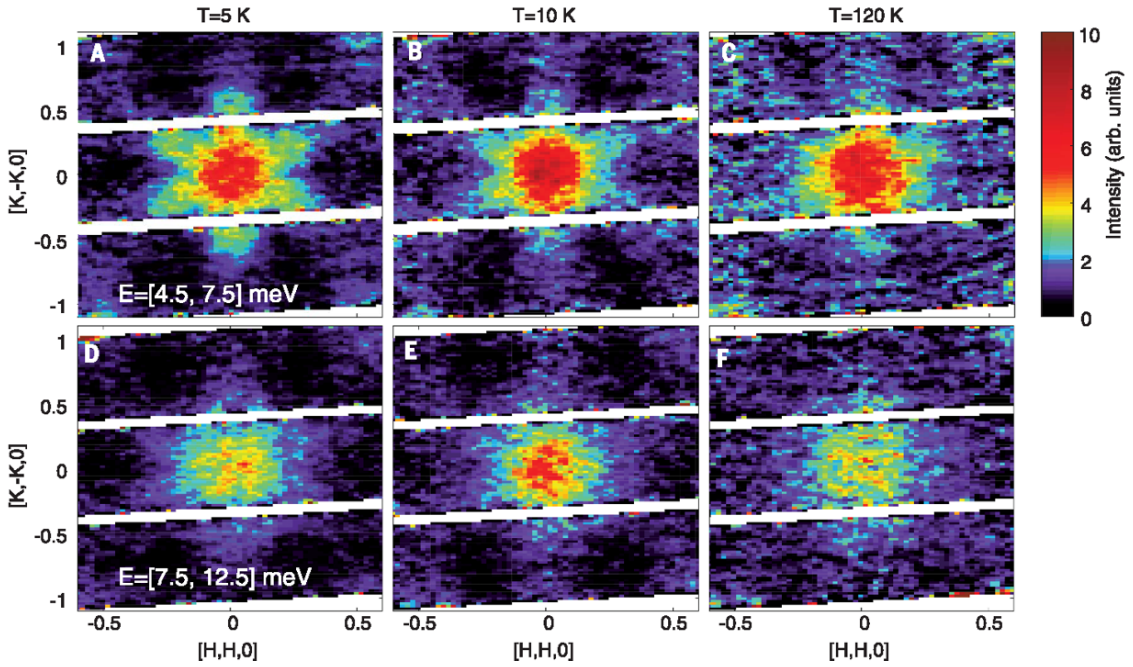

Figure 3.8: Momentum and temperature dependence of the continuum in $RuCl_3$ observed by INS. The spectral weight is integrated over the momentum interval $L = [-2.5, 2.5]$ and energy interval $[4.5, 7.5]$ meV for panel A~C and $[7.5, 12.5]$ meV for panel D~F. Figure reproduced from Ref[67].

Another remarkable feature of $RuCl_3$ is its mysterious behavior under strong magnetic fields. When the in-plane component of the magnetic field exceeds 7 T, $RuCl_3$ transitions into an anomalous phase characterized by a significant increase in thermal conductivity and the disappearance of magnetic order.[70] Inspired by this observation, thermal transport measurements captured unusual behavior in the in-plane thermal Hall conductivity of $RuCl_3$.[69] At in-plane magnetic fields around 7-8 T, a plateau emerges in the transverse thermal conductance κ_{xy}/T at a value of $1/2 \times (\pi/6)(k_B^2/\hbar)$. This half-integer thermal Hall conductance plateau is a characteristic transport behavior of fractionalized quasiparticles, possibly indicating the presence of Majorana fermions predicted in the Kitaev spin liquid Hamiltonian. Subsequently, an anomalous thermal quantum Hall effect was claimed even in the absence of an out-of-plane magnetic field.[71] However, this observation has been controversial. A later study observed quantum oscillations in the longitudinal thermal conductance κ_{xx}, while the transverse conductance plateau κ_{xy} could exhibit plateaus at values other than half-integers and change with temperature.[72] Thus, the nature of this intermediate phase of $RuCl_3$ and the observed thermal Hall conductance plateau remain subjects of debate.[73]

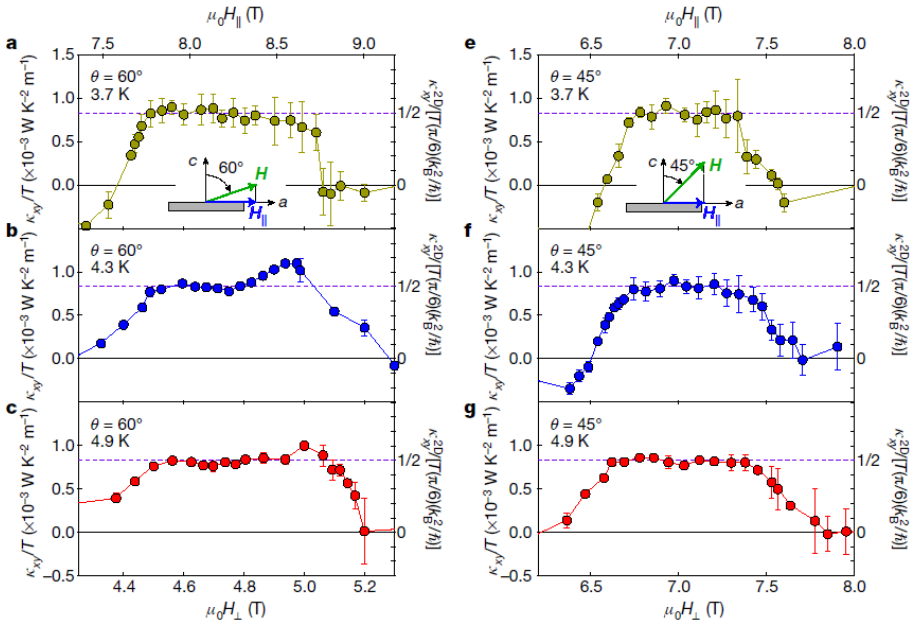

Figure 3.9: Thermal Hall effect observed in $RuCl_3$. The magnetic field is tilted at 60° (a-d) and 45°(e-g) from the c axis. Figure reproduced from Ref[69].

3.3 RIXS measurement on $RuCl_3$ single crystal

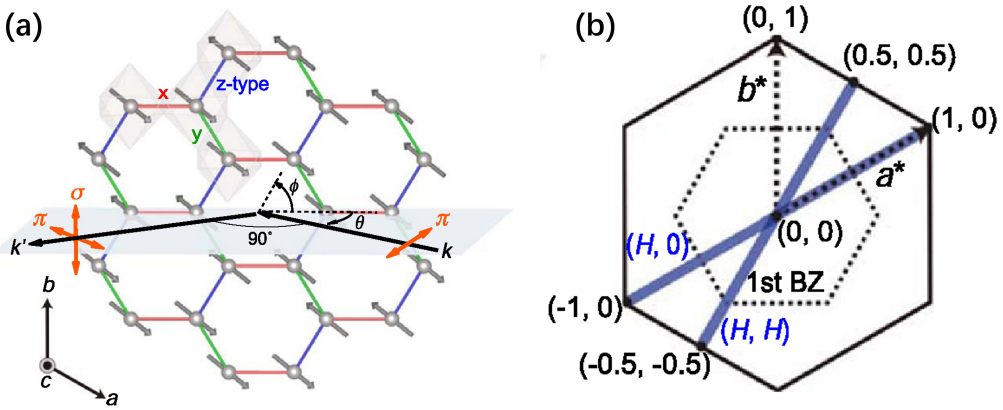

Figure 3.10: (a)Scattering geometry for the RIXS experiment.(b) (H,0) and(H,H) path in the reciprocal space. The first Brillouin zone is indicated by the dotted hexagonal. Figure reproduced from Ref [40]

In this study,[40] we conducted a comprehensive RIXS investigation at the Ru-L_3 absorption edge to determine the low-energy Hamiltonian and gain insights into the exchange interactions between the pseudospins. The RIXS measurements were performed at the P01 beamline in DESY, Hamburg, utilizing our recently-built IRIXS spectrometer. We employed

the 4B inline HRM setup (see Chapter 2) with an energy resolution of approximately 100 meV, determined by the FWHM of the non-resonant spectrum of silver paint deposited adjacent to the sample. Fig. 3.10 illustrates the scattering geometry of the RIXS experiment. The incident π-polarized X-ray photons were tuned to the Ru-L_3 absorption edge with energy $\hbar\omega_i = 2837$ eV, and the scattering angle was fixed at $2\theta = 90°$ to largely suppress charge (Thomson) scattering. The in-plane momentum transfer q was scanned along the $(H, 0)$ and (H, H) directions. Due to experimental constraints, the lowest achievable temperature was 20 K, thus all measurements were conducted in the paramagnetic phase.

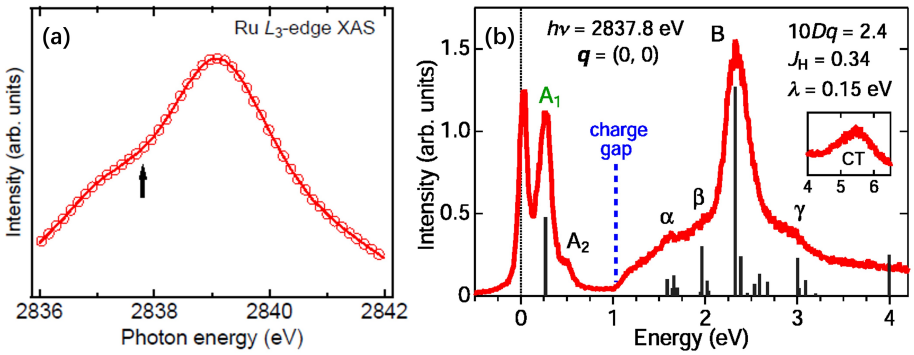

Figure 3.11: (a)Ru-L_3 XAS of $RuCl_3$ single crystal. (b)RIXS spectrum of $Rucl_3$ with momentum transfer $\mathbf{q} = 0$. Figure reproduced from Ref [40]

Fig. 3.3(a) shows the XAS profile measured at Ru-L_3 absorption edge by the FY signal from the SDD. The XAS spectra consist of two broad peaks located at 2837 eV and 2839 eV, with the arrow indicating the incident energy where we collected the RIXS spectra. A representative RIXS spectrum of $RuCl_3$ is presented in Fig. 3.11 with the in-plane momentum transfer set to $\mathbf{q} = 0$. Several distinct features can be observed in this spectrum. First, a quasi-elastic peak can be noticed at an energy slightly above 0. Due to the $\theta = 90°$ geometry, charge scattering is largely suppressed, and this peak exclusively originates from magnetic scattering. Second, a pronounced peak (A_1) appears at 0.24 eV, attributed to transitions between the ground state $S = \frac{1}{2}$ doublet and the excited $S = \frac{3}{2}$ quartet. The excitation energy aligns well with values from previous RIXS studies at the Ru-M_3 edge.[74] Notably, no clear trigonal splitting is observed, possibly because the trigonal distortion is small compared to the peak width or energy resolution of the spectrometer, unlike the case for honeycomb iridates A_2IrO_3 (A= Na, Li).[75] The weak shoulder feature (A2) is ascribed to the multiplets of the A1 exciton. In the higher energy range, a broad continuum emerges above the charge gap of ~1 eV (indicated by the blue dotted line) and extends up to ~4 eV, attributed to intersite electron-hole excitation. This continuum has

also been reported in optical spectroscopy.[76] On the top of the intersite continuum are the other d-d excitation peaks, consisting of a main peak B and three shoulder structures α, β, and γ, originating from intra-ionic crystal field transitions from the t_{2g}^5 ground state to the $t_{2g}^4 e_g^1$ manifold.

From the RIXS spectra at the Γ point, we can determine the interaction parameters of the d electrons. The multiplet states can be well described using the single-ion model outlined in Chapter 1, where the crystal field splitting H_{CF} contains only the octahedral term. We utilize the optimal parameter set $(10Dq, J_H, \lambda, \gamma) = (2.4\text{ eV}, 0.34\text{ eV}, 0.15\text{ eV}, 5)$ to reproduce the RIXS data, as depicted in Fig. 3.11 (b) by the black vertical bars. Both the position and the amplitude of the spectral features, especially the crystal field multiplets located around $10Dq$, are well captured by this calculation.

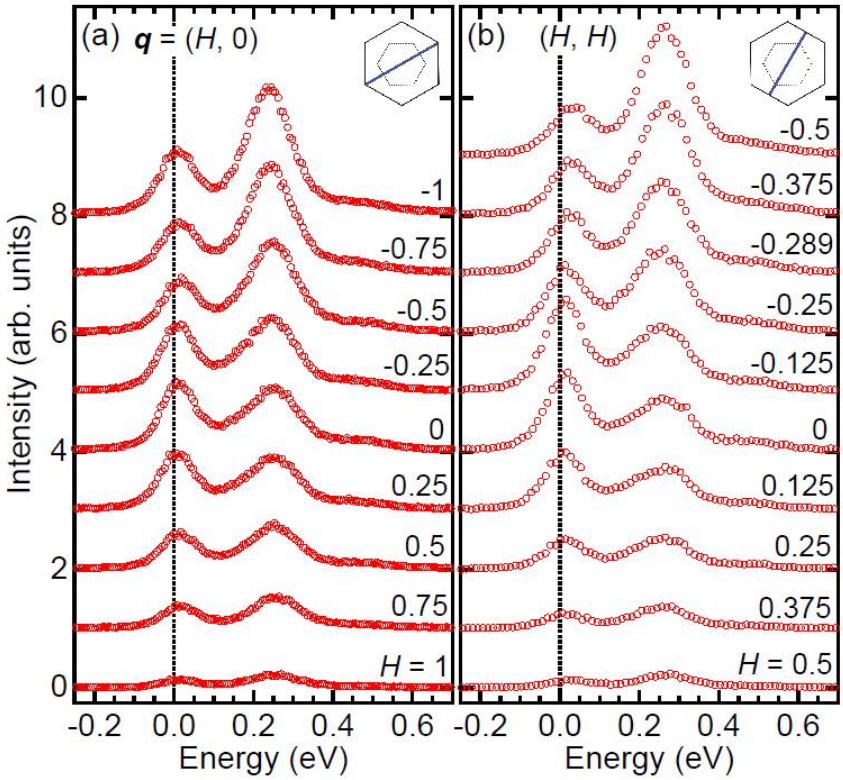

Figure 3.12: Low-energy Ru-L_3 edge RIXS spectra of $RuCl_3$ along $(H, 0)$ and (H, H) directions. Figure reproduced from Ref [40].

To investigate the spatial correlations among pseudospins and determine the exchange interaction parameters, a quantitative analysis of the momentum-dependent quasielastic peak intensity is essential. Specifically, the RIXS intensity arising from magnetic scattering has been shown to be closely associated with the spin-correlation function.[14] Fig. 3.12

illustrates the momentum-dependent low-energy RIXS spectra of $RuCl_3$, measured along the $(H, 0)$ and (H, H) directions. Within the measured momentum range, the spin-orbit excitation (A_1 peak) does not exhibit any energy dispersion, indicating the local nature of $S = \frac{3}{2}$ excitons. The overall monotonically decreasing intensity from $H = -1$ to $H = 1$ is due to the geometrical effect of X-ray self-absorption. Consequently, to obtain the momentum-dependent intensity of quasi-elastic peaks, the self-absorption correction must be applied. Since the energy of the quasielastic peak and spin-orbit exciton is relatively low (<200 meV), the assumption that $\alpha(E_{in}) \approx \alpha(E_{out})$ holds, and the correction factor reduces to the form of $1/(1 + \tan\theta)$ (Eqn.1.40).

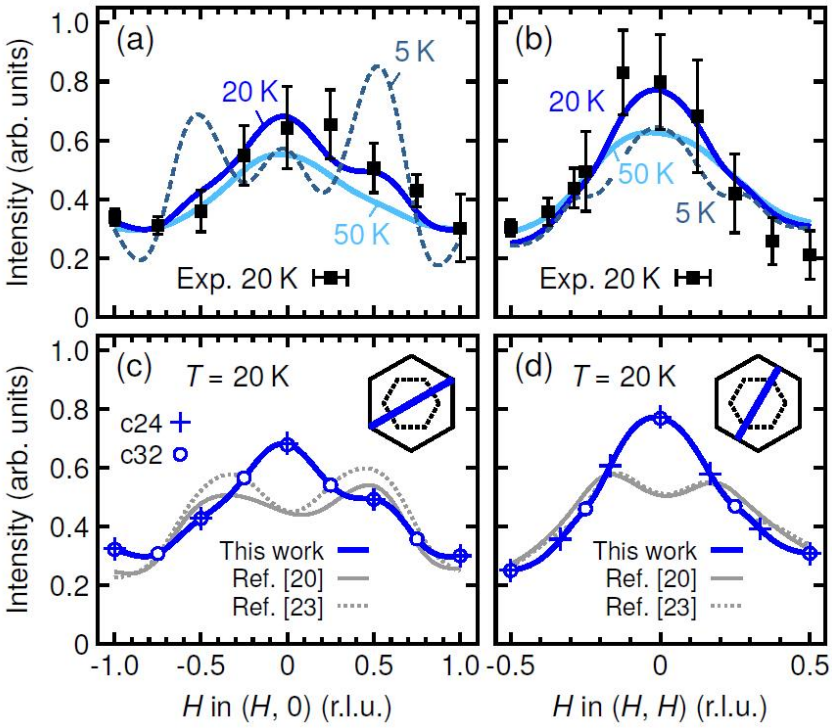

Figure 3.13: Momentum-dependent intensity of quasielastic peak. Figure reproduced from Ref [40].

The momentum-dependent intensity of the quasielastic peak, after correcting for the self-absorption effect, is extracted from the RIXS spectra by fitting the peak with a pseudo-Voigt lineshape. The results are depicted in Fig. 3.13 by the scatter points. It's worth noting that the intensity of the quasi-elastic peak exhibits a local maximum at the Γ point (0,0), rather than at the zigzag ordering Bragg wavevector $\mathbf{q} = (\pm 0.5, 0)$. Since the measurement was conducted at 20 K, slightly above the Néel temperature T_N, this local maximum suggests

that the short-range AFM correlations quickly diminish above the long-range ordering temperature. Consequently, the zigzag order is only marginally favored in energy compared to competing states with characteristic vectors $\mathbf{q} \approx 0$, such as FM correlations.

To quantitatively model the magnetic structure and extract the exchange interaction parameters, we employ the extended Kitaev-Heisenberg model (Eqn.3.3) to describe the pseudospin correlations. We further include the third-next-neighbor Heisenberg interaction $J_3\mathbf{S}_i \cdot \mathbf{S}_j$ to stabilize the zigzag AFM order. Previous studies [77] have found that the Γ' term is small for a system with cubic symmetry, and as mentioned earlier, the trigonal distortion in $RuCl_3$ is small and meets this requirement. Then, we calculate the quasielastic peak intensities at 5 K and 20 K using the optimal parameter set $(K, J, \Gamma, \Gamma', J_3) = (-5, -2.5, 2.5, 0.1, 0.75)$ meV. The calculated momentum-dependent intensity curve is shown in Fig. 3.13 by the blue lines, alongside the experimental data (black squares). The simulation results agree well with the experimental results, particularly for the intensity maximum at $\mathbf{q} = (0, 0)$ at 20 K and the emerging AFM order peaks at $\mathbf{q} = (\pm 0.5, 0)$ in the zigzag phase (5 K). This strong agreement demonstrates the capability of our theoretical approach to describe the intersite pseudospin correlation and determine the interaction strength in $RuCl_3$.

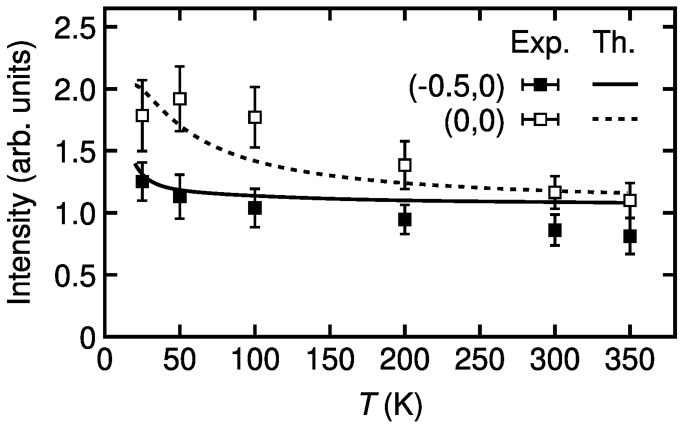

Figure 3.14: Temperature-dependent intensity of quasielastic peak at (-0.5,0) and (0,0). The scatter point shows the intensity extracted from RIXS spectra, and the solid and dotted curves are simulation results. Figure reproduced from Ref [40].

The competition between AFM and FM correlations is further supported by the distinct temperature dependence of quasielastic peak intensity at (0,0) and (-0.5, 0), as illustrated in Fig. 3.14. RIXS spectra were collected from base temperature up to room temperature, and the fitting procedure was repeated to extract the temperature dependence of quasielastic

peak intensity. As the temperature increases, both intensities exhibit a decreasing trend and eventually converge above ~200 K. However, the AFM intensity diminishes rapidly in the paramagnetic phase, while the FM correlation decays at a slower pace, with the momentum-dependence of the intensity observable up to 100 K. This result mirrors the INS findings and provides additional experimental evidence of the competing FM and AFM correlations within $RuCl_3$.

3.4 Summary

In this chapter, I introduced the RIXS study on $RuCl_3$ single crystal, a promising candidate system for realizing the Kitaev spin liquid phase. Through RIXS measurements, we provided an overview of the electronic and magnetic structure in this material, and our data indicate the presence of competing orders due to frustrated interactions.

The Kitaev interaction refers to the bond-dependent Ising-like magnetic exchange interaction between neighboring ions. When defined on the honeycomb lattice, this model becomes exactly solvable and hosts fractionalized excitations known as Majorana fermions. For this reason, Kitaev spin liquid systems are capable of conducting fault-tolerant quantum computation and have attracted much research interest. It is proposed that the Kitaev-type interaction can be realized in material systems that (i) form a honeycomb lattice from edge-sharing octahedra, (ii) have the transition metal with a d^5 configuration, and (iii) possess strong spin-orbit coupling to form a pseudospin-1/2 ground state. Among all the solid-state systems that fulfill these conditions, $RuCl_3$ has drawn much research attention for its unusual magnetic behavior. To date, numerous studies have focused on the electronic and magnetic structure of $RuCl_3$. Raman spectra reveal a low-energy magnetic continuum, possibly arising from frustrated magnetic excitations. INS measurements resolve a column of scattering that remains stable even far above the magnetic ordering temperature. Another remarkable observation is the exotic phase that emerges when an in-plane magnetic field is applied. Thermal transport measurements have revealed a half-integer thermal Hall conductance, indicative of the presence of Majorana fermions.

With the help of RIXS measurements at the Ru-L_3 edge, we studied the electronic structure and magnetic correlations in bulk $RuCl_3$ crystals. The spin-orbit excitation is clearly resolved in the RIXS spectra, with its energy in good agreement with previous studies and supportive of the pseudospin-1/2 picture. Additionally, the d-d excitation and charge

continuum are observed above the charge gap of 1 eV. Based on the spectral features observed by RIXS, we determined the intra-atomic interactions as $(10Dq, J_H, \lambda, \gamma) = (2.44\text{ eV}, 0.34\text{ eV}, 0.15\text{ eV}, 5)$. The momentum dependence of the quasi-elastic peak suggests a prominent ferromagnetic-type correlation and interatomic magnetic exchange in $RuCl_3$. The zigzag correlation is quickly suppressed above the Néel temperature T_N, as supported by both experimental results and theoretical simulations, indicating that the zigzag ordered state is only slightly lower in energy than the competing states. This work serves as another successful example demonstrating the capability of the IRIXS spectrometer to characterize compounds with $4d$ transition metal elements. The acquired data from bulk crystals also provide important references for RIXS studies on $RuCl_3$ nanoflakes, as I will present in the next Chapter.

4 Ru-L_3 RIXS study of $RuCl_3$ nanolayers

As we have seen in previous chapters, RIXS has become an indispensable experimental probe of quantum materials, as energy- and momentum-dependent RIXS data on electronic excitations provide unique insight into the strength and spatial range of electronic interactions. However, one of the most rapidly advancing frontiers in this field – two-dimensional (2D) materials and van der Waals (VdW) heterostructures – has thus far not benefited significantly from RIXS, because the atomic-scale thickness and micron-scale lateral dimensions of typical exfoliated sheets impose severe restrictions on the signal intensity. Here we present Ru L_3-edge RIXS measurements of spin-orbit and crystal-field excitations in nanoflakes of the $RuCl_3$, following the work of RIXS measurements on its bulk counterpart in Chapter 3. Whereas the data on thick flakes are identical to bulk measurements, we observe a pronounced red-shift and broadening of the crystal-field excitations in flakes with thickness below about 7 nm. In contrast, the spin-orbit excitations are independent of thickness. Aided by model calculations, we attribute these effects to lattice distortions near the surface. Our study paves the way towards RIXS investigations of electronic excitations in various other 2D materials and heterostructures.

4.1 Introduction

Since the discovery of the Scotch-tape exfoliation method, [78, 79] 2D materials and heterostructures have grown into a unique laboratory for quantum physics. These atomically thin nanoflakes provide an ideal playground for elementary studies of low dimensional physics, and they also show huge potential for industrial applications, especially in the field of semiconductors, where Moore's law has gradually been violated due to the short-channel effect [80, 81]. By reconfiguring the crystal symmetry and reducing the

dimensionality of the electron system, exfoliation of atomically thin sheets can generate electronic ground states with physical properties radically different from those of bulk analogues. Superstructures generated by vertical stacking [82, 83, 84] and lateral twisting [85] of these sheets add numerous options for control and design of collective quantum phenomena.

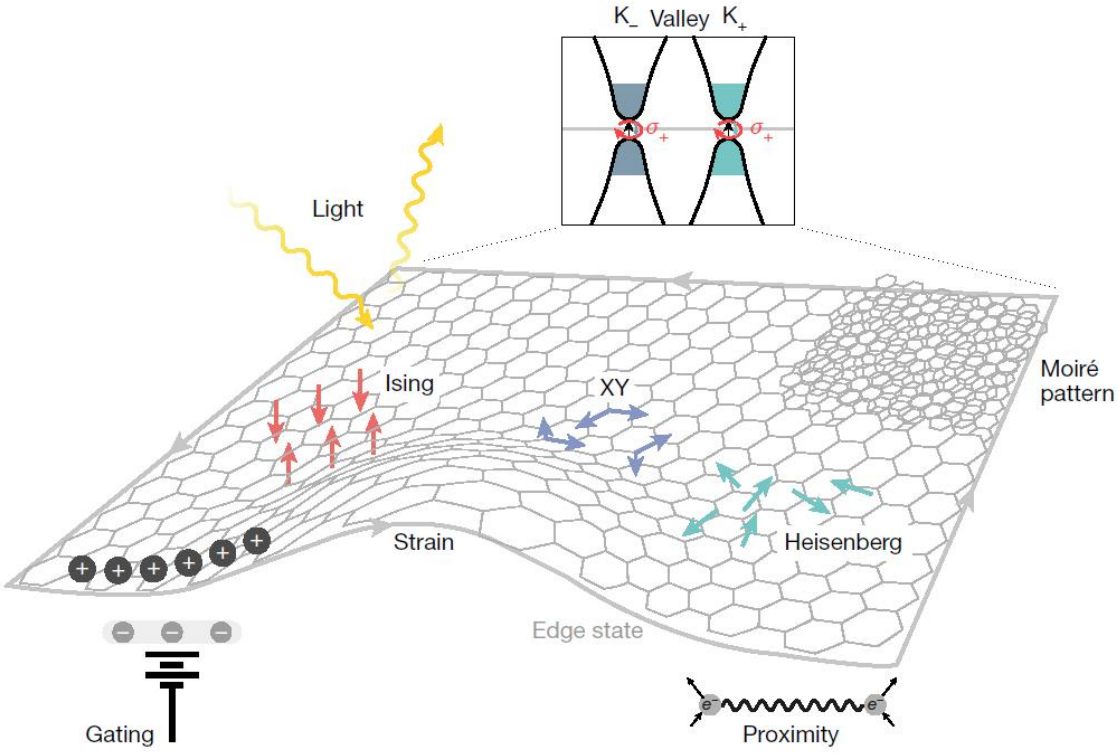

Figure 4.1: Physical phenomena that can be studied with magnetic vdW materials. Figure reproduced from [86].

Interesting magnetic ordering behaviors have been observed in a number of 2D materials, including the FM semiconductor $Cr_2(Si, Ge)_2Te_6$, MSe_2 (where M=V, Mn), itinerant FM Fe_3GeTe_2, and insulating AFM MPX_3 (where M=transition metal, X=S or Se) [86]. An overview of the magnetic phenomena observed in 2D systems is depicted in Fig. 4.1. These materials serve as ideal platforms for testing well-established theories, such as the Mermin-Wagner theorem and the XY-model. However, while magnetism in these materials is confirmed through techniques like magneto-optic Kerr effect or Raman spectroscopy, the underlying ordering structure remains elusive due to the absence of diffraction studies on monolayers. Additionally, charge density waves, another extensively studied ordering effect, are observed in systems such as TaS_2 [87]. These materials, along with heterostructures containing them, represent promising avenues for future spectroscopic investigations.

To realize these perspectives, experimental information on the electron-electron and electron-lattice interactions that determine the stability of different quantum states is indispensable. Research on bulk quantum materials has shown that data from energy- and momentum-resolved spectroscopic probes provide particularly insightful information for realistic model calculations. Prominent examples include angle-resolved photoemission spectroscopy (ARPES) and INS, which yield the dispersion relations of electronic bands and collective excitations, respectively. Whereas ARPES has been widely applied to 2D materials, however, INS experiments are not feasible because they require sample volumes in the cm^3 range.

In exfoliated layers and van der Waals heterostructures, RIXS has the potential to reveal a wealth of information about atomic-scale interactions including crystalline electric fields, spin-orbit coupling, magnetic exchange, and electron-phonon interactions. The element-selective nature of RIXS allows one to focus exclusively on the properties of a specific layer of a VdW heterostructure, without interference from substrates and protective capping layers. However, as the lateral dimensions of typical exfoliated nanoflakes are below the X-ray beam diameter, such experiments present formidable challenges, and the potential of RIXS for research on 2D materials remains largely untapped.

Motivated by these prospects and by the detailed information on crystal-field, spin-orbit, and exchange interactions obtained from previous RIXS experiments on bulk $RuCl_3$, [40] we prepared a series of $RuCl_3$ nanoflakes of varying thickness down to 3.5 nm and lateral dimensions comparable to those of the X-ray beams required for RIXS. We obtained high-quality Ru L_3-edge RIXS spectra on all samples, without any sign of X-ray beam damage. The technical details of sample treatment methods will be presented in the following Sections.

Before delving into recent research progress on $RuCl_3$ nanolayers and heterostructures, I will first introduce three techniques of sample preparation that serve as the technical foundation for numerous studies on 2D material systems. These methods include two exfoliation techniques: mechanical exfoliation using Scotch tape and chemical exfoliation via lithiation, as well as an assembly method for vertical heterostructures using a polymer stamp.

The mechanical exfoliation method using Scotch tape was developed in 2003 [78]. A schematic illustrating this process is depicted in Fig. 4.2. Initially, a piece of bulk 2D material is adhered to the tape. The tape is then folded to grip the other side of the bulk,

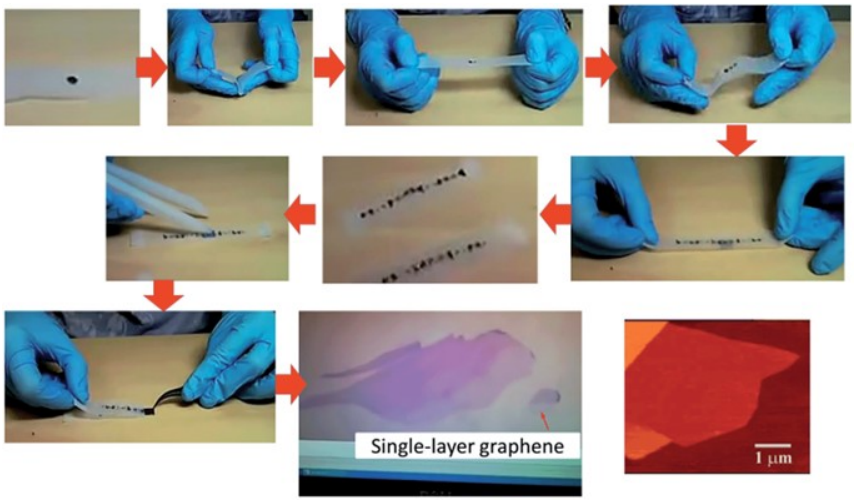

Figure 4.2: A sketch of conventional Scotch tape mechanical exfoliation method. Figure reproduced from Ref [88].

subsequently unfolded to cleave the material in the middle, thereby yielding two thinner halves. This folding and unfolding procedure is repeated to progressively reduce the crystal's thickness. Upon reaching the desired thinness, the tape is attached to a substrate and later removed. Following the exfoliation process, the substrate surface is adorned with numerous flakes ranging from monolayer (< 1 nm) to over 100 nm in thickness. These nanolayers typically exhibit lateral dimensions of approximately 20 μm or smaller. This exfoliation approach provides a cost-effective and easily implementable technique suitable for laboratory settings, yielding high-quality samples with exceptionally clean surfaces. Fig. 4.3 displays an atomic force microscopy scan of a 7 nm thick $RuCl_3$ nanolayer acquired via this method, showcasing a flat surface devoid of artifacts or contamination. Utilizing this ultraclean fabrication technique mitigates unwanted doping and strain effects, facilitating access to the pristine nature of the nanolayer.

We also highlight the potential for exfoliating large lateral size monolayers of van der Waals materials using a new approach presented in several recent publications [89, 90]. The fundamental concept behind this approach is that a gold film exhibits stronger adhesion to van der Waals materials compared to conventional substrates such as Si/SiO_2, mica, quartz, and polydimethylsiloxane (PDMS). Building upon this premise, the gold film-assisted exfoliation method has been developed, greatly enhancing the feasibility of obtaining large-area (millimeter size) isolated monolayers. Fig. 4.4 illustrates the exfoliation process aided by a gold layer. In this method, a gold film is initially deposited onto the Si/SiO_2 substrate via thermal evaporation. Subsequently, classic Scotch-tape exfoliation

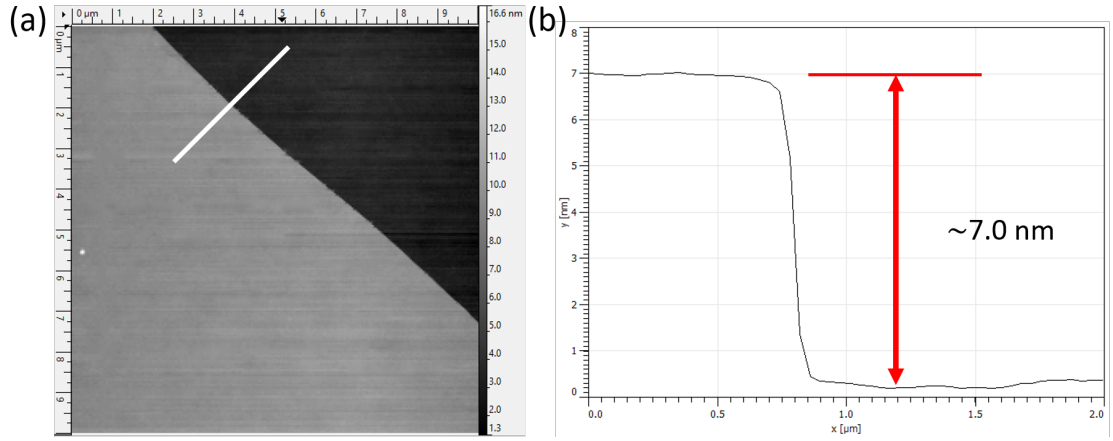

Figure 4.3: Atomic force microscopy image near the edge of a 7 nm $RuCl_3$ nanolayer. (a) The microscope image, where height is indicated by the brightness. Along the white bar we take a line profile of the height and the result is presented in panel (b). The thickness can be read from the height difference of the step-like profile, *i.e.* about 7.0 nm for this nanolayer.

is performed immediately after the gold-covered substrate is removed from the vacuum chamber of the evaporation instrument. The brief exposure to the atmosphere minimizes pollution from the air, leaving a clean gold surface primed for exfoliation—an essential factor for ensuring monolayer adhesion to the gold surface. While research on $RuCl_3$ utilizing this improved exfoliation method remains limited to date, we anticipate that RIXS studies on nanolayers will greatly benefit from the larger lateral size afforded by this approach in the future. Hence, the significance of these exfoliation methods should not be underestimated.

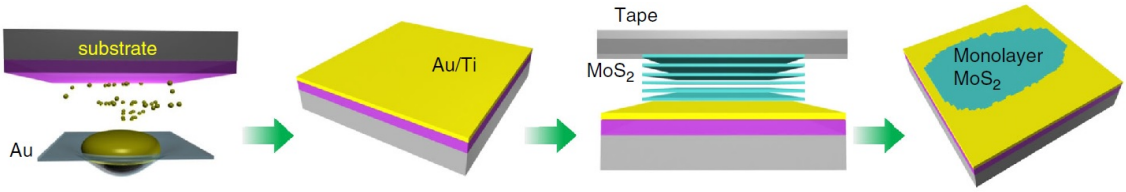

Figure 4.4: Schematic of gold film-assissted exfoliation method. Figure reproduced from Ref [89].

The second exfoliation method is based on a chemical reductive-lithiation/hydration approach [91], a technique that has been successfully applied to a variety of material systems. One of the key advantages of this approach is its ability to mass-produce thin/monolayers in a single batch. The reaction steps involved in obtaining $RuCl_3$ layers

are briefly summarized in Fig. 4.5. Initially, $RuCl_3$ single crystals undergo a reaction with $LiBH_4$ to yield $Li_{0.2}RuCl_3$, which naturally exfoliates into $RuCl_3$ monolayers and few-layers upon contact with water. The liquid containing $RuCl_3$ nanolayers is subsequently deposited onto the substrate and oxidized.

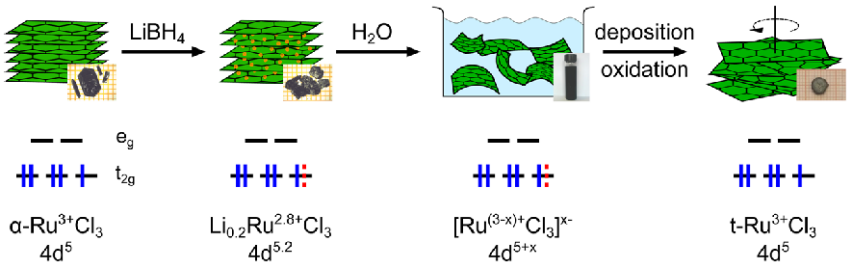

Figure 4.5: Schematic summary of lithiation/reduction method to prepare $RuCl_3$ nanolayers. Figure reproduced from Ref[91]

In contrast to the mechanical exfoliation method, nanolayers obtained from chemical reaction processes often suffer from severe surface contamination. Fig. 4.6 depicts an atomic force microscopy image of a $RuCl_3$ thin layer produced through this process. The nanolayer appears flat with a typical lateral size of approximately 10 μm. The white spots observed in the image are attributed to randomly distributed particles on the sample surface. These particles have the potential to charge-dope the sample or induce inhomogeneous strain, thereby altering the intrinsic properties of the nanolayer and complicating vertical stacking. Such contamination is unavoidable when nanolayers are dispersed in a liquid medium; therefore, for our measurements, we opt for the mechanical exfoliation method for sample preparation.

The third technique involves the pick-up and transferring of exfoliated nanolayers using polymer stamps. This method represents another significant advancement in the field of 2D material research and has served as the foundation for the assembly of vertical heterostructures. This approach has inspired numerous groundbreaking studies, including those on high-mobility graphene devices [92], superconducting magic-angle graphene and "twistronics"[85, 93], and high-performance light-emitting diodes [94]. Unlike conventional "wet transfer"methods [95], this "dry transfer"technique offers the advantage of being polymer- and liquid-free, allowing the target nanolayer to maintain a high-quality, unpolluted surface after assembly.

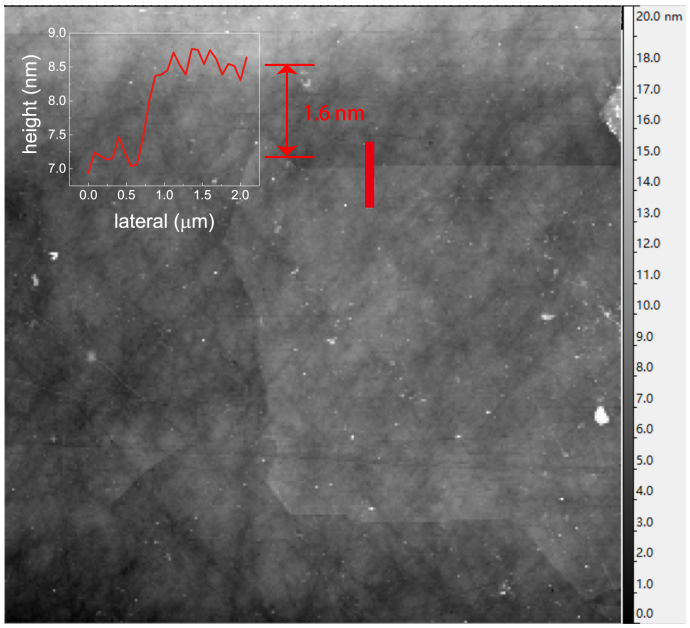

Figure 4.6: Atomic force microscopy image of a $RuCl_3$ nanolayer obtained from lithiation method. The white dots indicates the presence of microparticles adhering to the sample surface, thereby causing contamination. The inset panel illustrates the height profile measured along the red bar, revealing a thickness of 1.6 nm.

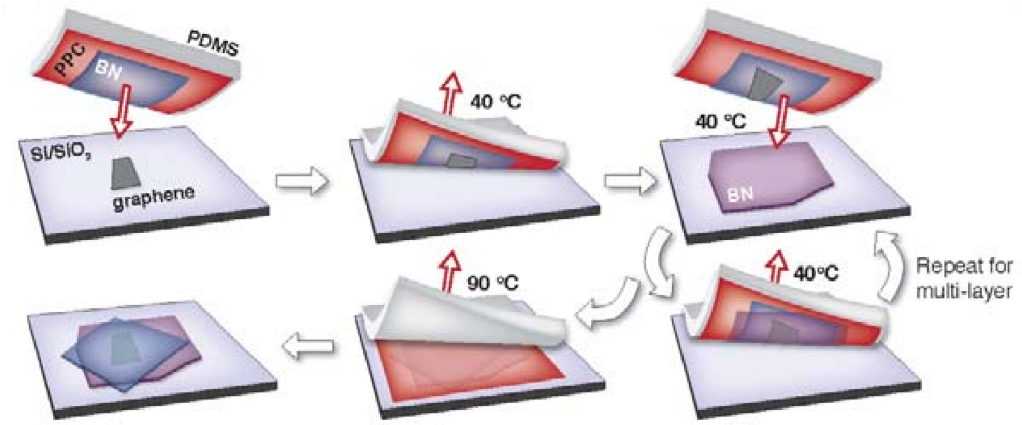

Figure 4.7: A sketch of PPC/PDMS stamp pick-up and stacking technique. Figure reproduced from Ref [92].

The schematic of the polymer stamp transfer process is illustrated in Fig. 4.7. The polymer stamp consists of a thin poly-propylene carbonate (PPC) film placed on a transparent polydimethylsiloxane (PDMS) substrate. This stamp is mounted to a manipulator under a microscope. In the pick-up process, the PPC is pressed onto the target nanolayer and slightly heated to increase adhesion. Once the nanolayer and PPC layer are firmly combined, the

temperature is lowered, and the PDMS/PPC/nanolayer stamp is lifted. Subsequently, the stamp is pressed onto the next nanolayer and lifted to assemble the vertical heterostructure. By repeating this step, one can eventually obtain the desired heterostructure with each layer well-aligned in position. Finally, the stamp is transferred onto the target substrate and heated to 90°C to separate the heterostructure from the softened PPC layer.

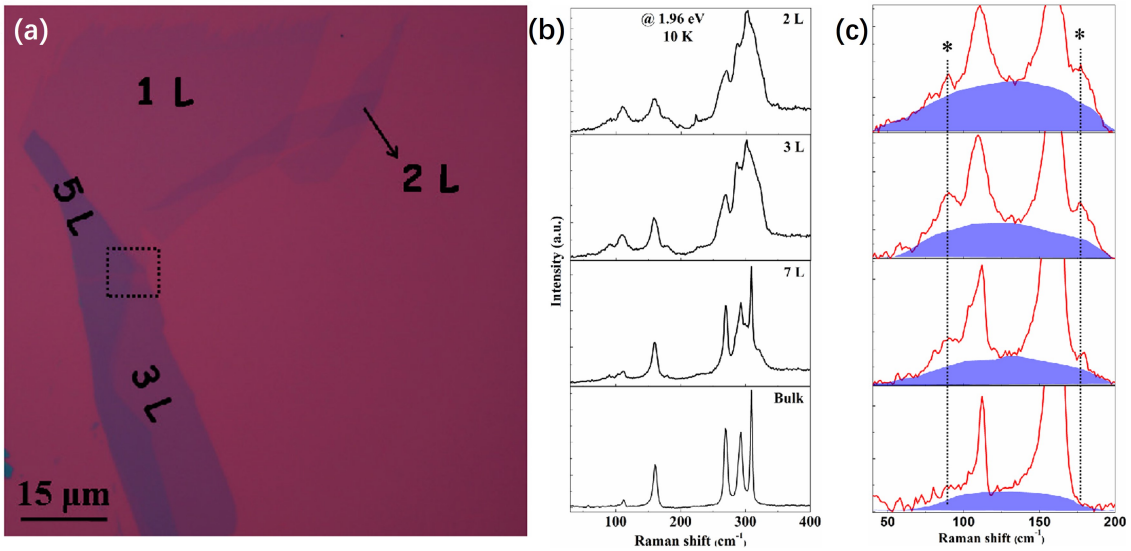

Figure 4.8: (a) $RuCl_3$ nanoflake prepared by Scotch tape exfoliation. (b) Layer-dependent Raman spectra of $RuCl_3$ nanoflakes. (c) Magnetic continuum observed in different flakes. Figure reproduced from Ref[96].

Based on these techniques, the fabrication of $RuCl_3$ nanolayers and heterostructures has become readily accessible. Several studies have reported Raman measurements on exfoliated $RuCl_3$ layers [96, 97, 98, 99]. In Ref[96], researchers prepared $RuCl_3$ samples with different thicknesses, as shown in Fig. 4.8, and conducted a layer-dependent Raman spectroscopy study. The results are depicted in Fig. 4.8(b)(c). The blue region indicates the broad continuum emerging from magnetic scattering, as observed in bulk $RuCl_3$.[62] It was found that the low-energy intensity is enhanced with decreasing layer thickness, suggesting a stronger frustrated magnetic interaction between the pseudospins as the system approaches the 2D limit.

In addition to the low-energy continuum from magnetic scattering, Raman studies have also captured the thickness-dependence of spin-orbit excitons, which form the foundation of Kitaev-type exchange interaction [97]. Fig. 4.9 illustrates the single- and bi-exciton measured on $RuCl_3$ nanolayers with different thicknesses. Two broad peaks can be observed at 231 and 524 meV, which align well with RIXS measurements on bulk $RuCl_3$. As the

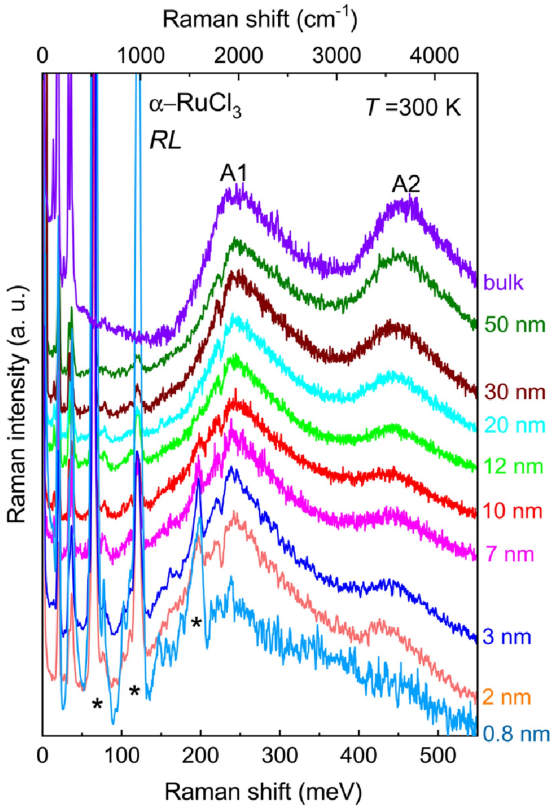

Figure 4.9: Spin-orbit exciton in $RuCl_3$ nanolayers with various thickness. Figure reproduced from Ref [97].

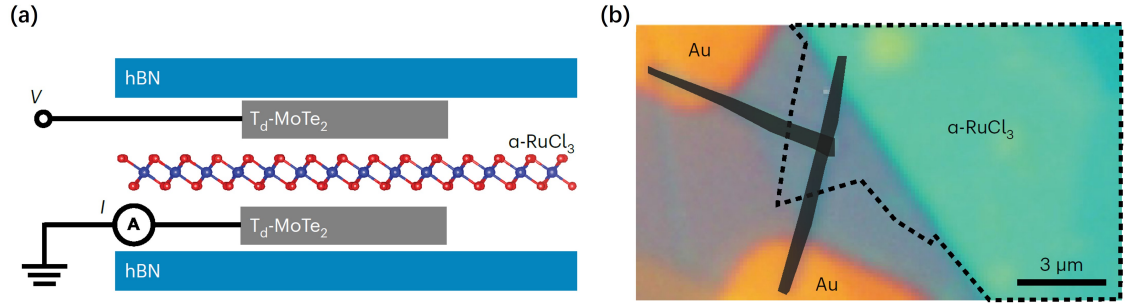

Figure 4.10: (a)Schematic structure and (b) microscope photograph of the tunneling device for IETS measurement on $RuCl_3$ thin layers. Figure reproduced from Ref [100].

thickness decreases, the energy first undergoes a slight red-shift and then experiences a steep softening below 3 nm, conjectured to result from the modified electronic structure arising from the reduction of interlayer interaction.

Another significant advancement involves the detection of low-energy magnetic structures in monolayer $RuCl_3$ using inelastic electron tunneling spectroscopy (IETS) [100]. Figure 4.10 illustrates the tunneling device utilized for IETS measurements. A thin layer of $RuCl_3$

is positioned between two ultrathin T_d-$MoTe_2$ electrodes to create a metal-$RuCl_3$-metal tunneling junction, all encapsulated between two hexagonal boron nitride (hBN) layers. In Fig. 4.11, the IETS measurements under an external magnetic field are presented. When the magnetic field aligns with the in-plane direction, a single peak is observed in monolayer (1L), bilayer (2L), and trilayer (3L) samples, attributed to single magnon excitation, as denoted by the reverse triangle in Fig. 4.10(a). When the field exceeds ~5T, the 2L and 3L samples undergo a phase transition marked by a shift from a decreasing to an increasing trend in magnon energy, while this switch is absent in the 1L sample. This indicates that substantial high fields are needed to drive the monolayer out of the zigzag phase. Conversely, when the external field aligns with the out-of-plane direction, bimagnon excitations emerge in the 1L and 2L samples alongside the single-magnon peak (indicated by the red reversed triangle in Fig. 4.11(c)), but are absent in samples thicker than 3L. Additionally, in 1L and 2L samples, the magnon energy exhibits a clear curvature with increasing field, whereas in the 3L sample, the energy remains largely unchanged, consistent with the behavior of bulk $RuCl_3$. These observations suggest that monolayers are more susceptible to out-of-plane magnetic fields, while thicker samples are sensitive to in-plane fields. As thickness decreases, an easy-plane to easy-axis transition occurs, which was attributed to structural distortion by in-plane displacement of Cl atoms by the authors. Supported by *ab initio* calculations, it was further suggested that 1L $RuCl_3$ possesses a larger Kitaev interaction and is closer to the quantum spin liquid state.

In addition to these researches on pristine nanolayers, the 2D nature of $RuCl_3$ offers great flexibility in terms of tuning its electronic and magnetic properties by heterostructure fabrication, and the interplay between $RuCl_3$ and other van der Waals materials, such as graphene, have attracted much research interest.[101, 102, 103, 104] Several recent theoretical works [105, 106] focused on the strain and doping effect of monolayer $RuCl_3$ when placed on graphene. In Ref [105], with the help of *ab initio* density functional theory calculations, the researchers found that: (i) $RuCl_3$ becomes strained due to the lattice mismatch with the graphene monolayer, (ii) $RuCl_3$ (graphene) becomes slightly electron-doped (hole-doped) via charge transfer, and (iii) the Kitaev interaction in $RuCl_3$ is enhanced by more than 50% compared to the bulk counterpart. The third result suggests that by making the $RuCl_3$ monolayer charge-neutral in such a strained-geometry, this system would be pushed close to the Kitaev quantum spin liquid phase. In Ref [106], a general strategy for calculating electronic properties of mismatched hetero-bilayers without periodicity is presented. With this refined framework, it is also predicted that $RuCl_3$ will be shifted closer to the Kitaev phase in such a system.

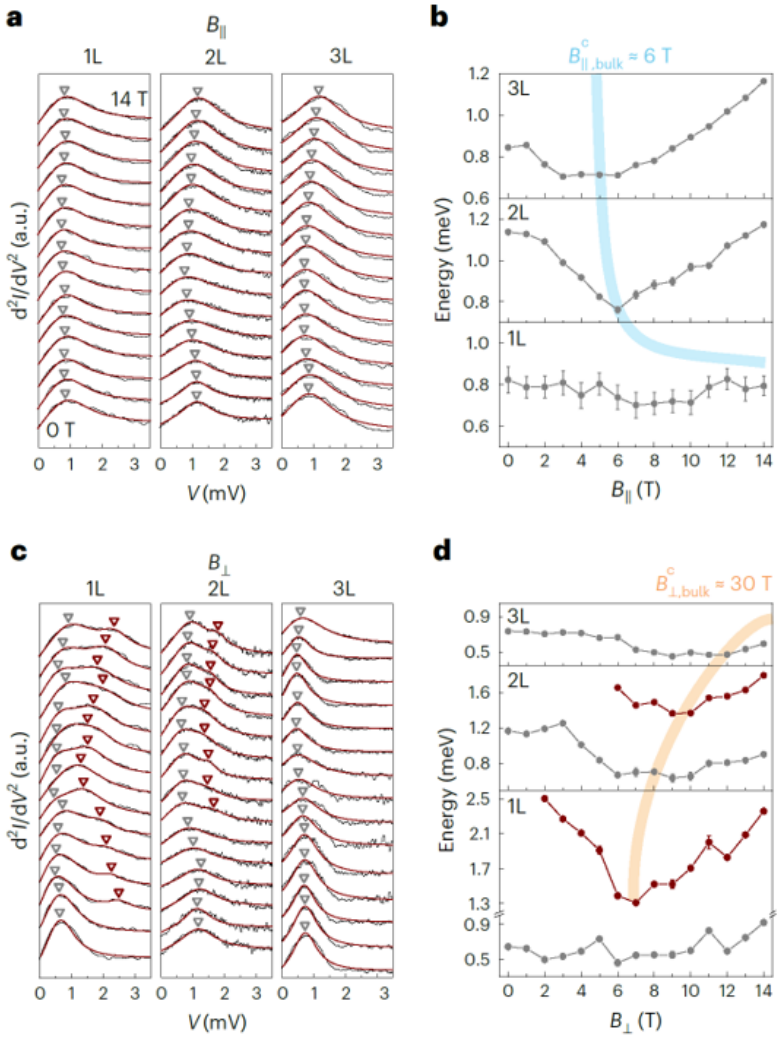

Figure 4.11: Magnetic field dependent IETS on $RuCl_3$ nanolayers. a,c shows the d^2I/dV^2 curve when an in-plane/out-of-plane magnetic field is applied. The grey and red inverse triangle indicate the single- and bi-magnon peak, whose energy is shown in b and d. Figure reproduced from Ref [100].

These advancements raise the possibility of investigating magnetism in an ideal two dimensional system, free from the influence of interlayer interactions that are known to significantly impact the magnetic structure of bulk $RuCl_3$ [68, 107]. They also offer opportunities for targeted modification of electronic properties, such as doping charge carriers into the correlated pseudospin system via doping across heterointerfaces, or through interfacial proximity coupling to other quantum states like superconductivity [108, 109, 110, 111]. In this study, we conducted RIXS measurements on nanometer-thick $RuCl_3$

nanolayers and compared the results with data obtained from bulk crystals, as presented in Chapter 3, to investigate alterations in its electronic structure as it approaches the 2D limit.

4.2 Sample preparation

$RuCl_3$ bulk single crystals were grown from commercial powder using the chemical vapor transport method [112]. The crystals were mechanically exfoliated by Scotch tape onto Si/SiO_2 substrates. Next we use a microscope to select out the ideal flakes for RIXS measurement, following three standards: (i) the flakes should be thin enough to exhibit different properties compared to bulk crystals, (ii) the thickness should be uniform across the flake, and (iii) the lateral size should be around 20 μm or larger, *i.e.* comparable to the size of the beam spot to reduce waste of photon flux. The thickness of the exfoliated flakes was first estimated by the interference contrast under an optical microscope, and then measured by atomic force microscopy. Since the volume of nanolayers is much smaller than the bulk crystals commonly used for RIXS measurements, the small dimensions make it challenging to (i) locate the small sample and (ii) single out the target nanolayer from other unwanted layers in the sample chamber. After trying out a variety of preparation methods and samples, we have found a successful solution to overcome these technical challenges.

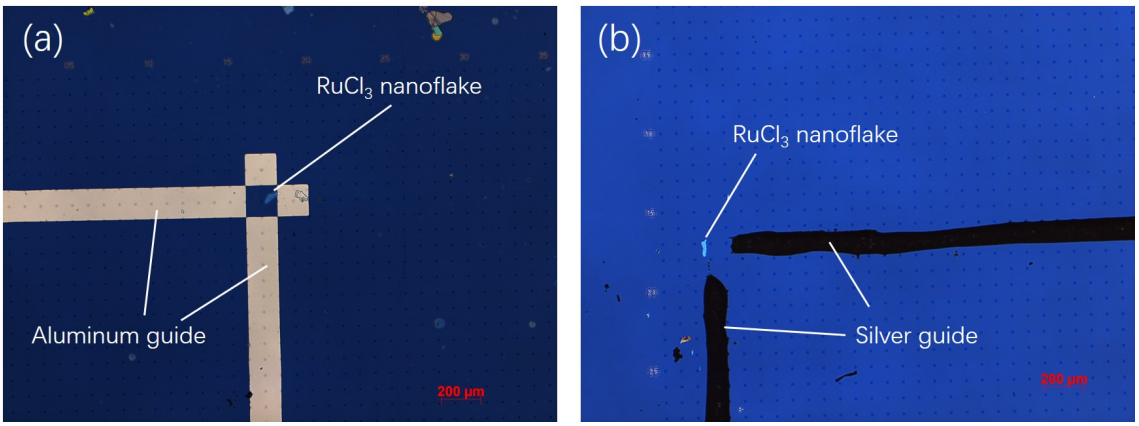

Figure 4.12: Optical microscope image of metal guide on the substrate surface pointing at $RuCl_3$ nanoflake. (a) aluminum guide by thermal evaporation, patterned by laser writing method. (b) silver guide painted directly on the substrate's surface with silver paint and needle probe station.

The first challenge is to locate the sample in the ultrahigh vacuum (UHV) chamber of the IRIXS spectrometer, where no camera or direct visualization tool with enough accuracy is available. The strategy is to fabricate two metal guides on the surface of the substrate,which point to the exact location of the nanolayer. When scanning the X-ray beam across the surface of the substrate, the large metal guides reflect incident X-rays much more strongly than the bare substrate, thereby allowing us to easily find and align the target nanoflakes by following their direction. To determine the best material for the guide, we have tested different metals and the corresponding fabrication methods, including gold, aluminum and silver, as shown in Fig 4.12. The gold and aluminum guide is fabricated via a conventional photolithography-deposition method. The shape of the guide is designed beforehand and patterned by standard direct laser writing lithography, on a piece of marked substrate. In the etched area, the polymer mask is removed via a rinsing in a proper organic solution and the bare substrate is exposed, followed by thermal evaporation to deposit a 100 nm thick metal film (gold or aluminum). The silver guide is handcrafted with the help of a needle probe station, which enables a steady and precise movement of the needle. First the needle with a sharp tip is dipped into silver paint to attach a small liquid drop at the tip. Next this tip is lowered to touch the surface of the substrate, and then slides slowly in a straight line, leaving a silver paint trail that points to the nanoflake. At last the substrate is slightly baked to ensure a firm attachment of the fabricated metal guide to the substrate. Notably, the silver paint should have sufficient liquidity after being deposited onto the substrate's surface. Otherwise, drawing will be difficult once the droplet hardens. We chose the H20S silver paint from EPO-TEK® for this purpose. Being a two-component epoxy, the reaction between its two parts is slow at room temperature, allowing ample time for drawing before the mixture solidifies. In contrast, the silver paint RS 186-3600 from RS Component performs poorly in this fabrication process, although this product is widely used in scientific research for sample mounting: after dispensing the silver paint from the bottle, the solvent evaporates rapidly, causing the droplet's surface to harden quickly. This makes it challenging to perform any additional operations. In summary, the corresponding fabrication method and X-ray measurement results are presented in Table 4.1. While all metals provide clear contrast to the bare substrate, facilitating sample position location, we opted to use silver guides for measurements. During their fabrication process, no polymer contacts the nanoflake surface, greatly suppressing surface contamination.

Another challenge of locating the sample in the RIXS chamber is the difficulty to single out the target nanolayer from the surrounding unwanted pieces. Here we use the PPC/PDMS stamp pick-up and transfer method mentioned above and a plasma treatment to protect

Table 4.1: Metals for Guide Fabrication

Material	Fabrication Method	Contact Polymer	Distinguishable by X-ray
Gold	Thermal Evaporation	Yes	Yes
Aluminum	Thermal Evaporation	Yes	Yes
Silver	Silver Paint	No	Yes

the wanted flake and get rid of the unwanted ones, as shown in Fig. 4.13. First, thick hexagonal boron nitride (hBN) sheet were mechanically exfoliated by Scotch tape and picked by the polymer stamp, and then deposited on top of the $RuCl_3$ flakes. Next the hBN flake is released from the stamp and a clean, polymer-free interface between $RuCl_3$ and hBN is formed. Then the entire substrate was subsequently flushed by oxygen plasma for 2 minutes. This treatment gets rid of the unprotected $RuCl_3$ pieces and leaves only the hBN-covered target $RuCl_3$ flakes on the surface of the Si/SiO_2 substrate, due to the strong oxidation resistance of hBN.

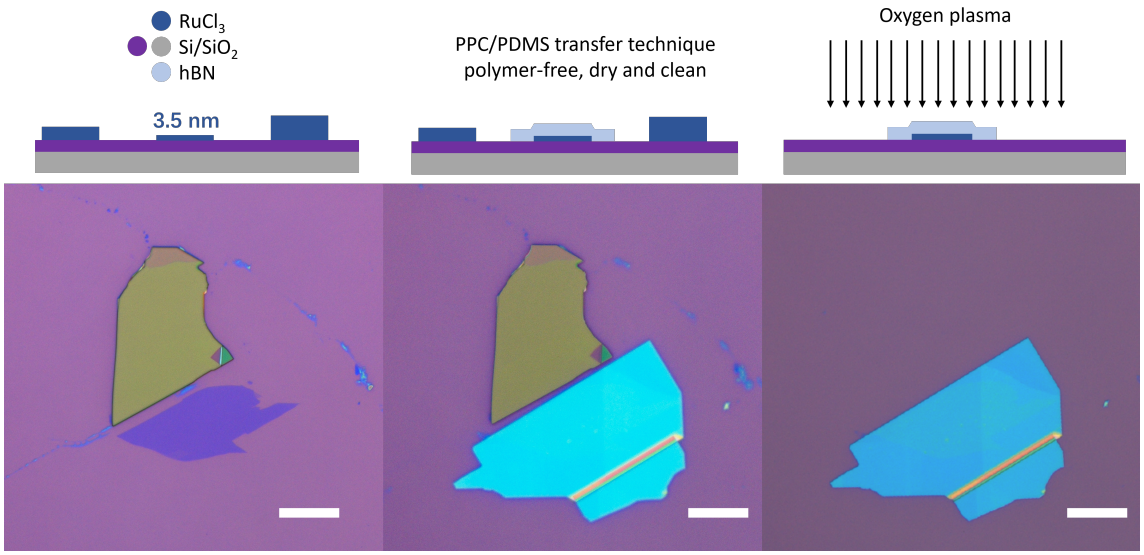

Figure 4.13: Sketch of oxygen-plasma treatment on $RuCl_3$ nanoflake. The exfoliated $RuCl_3$ nanolayer is first capped by a thick hBN layer by using PPC/PDMS stamp transfer method, then the whole substrate is flushed by oxygen plasma. This plasma treatment flushes away the thick unwanted flake(yellow) next to our sample as well as the tape residue.

Figure 4.14 presents the Raman spectra obtained from a 3.5 nm thick $RuCl_3$ nanolayer following hBN capping and oxygen plasma treatment. For comparison, data from pristine bulk $RuCl_3$ is included. The measurements were conducted at room temperature using

a quasi-backscattering configuration, with scattered light collected in both XX and XY polarization channels. The nanolayer exhibits distinct and well-defined phonon peaks, indicating its high quality despite the complex sample preparation procedures. In the parallel polarization channel, the Raman signal from the Si/SiO_2 substrate is also observed, characterized by a continuum ranging from 220 cm^{-1} to 450 cm^{-1} and a phonon peak around 300 cm^{-1}.

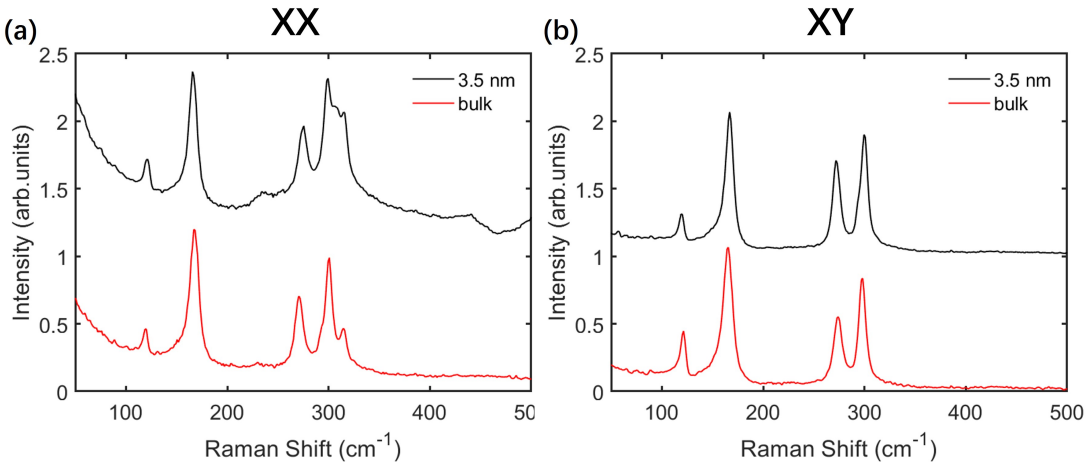

Figure 4.14: Raman spectra of 3.5 nm thick $RuCl_3$ nanolayer and bulk crystal. The intensity is normalized by the peak at 165 cm^{-1}.

Utilizing the aforementioned techniques, we can readily locate the $RuCl_3$ nanolayers within the RIXS chamber with the assistance of the SDD. Figure 4.15 illustrates a typical fluorescence signal obtained during the beam position scanning process. Initially, we track the silver guide until its termination, as indicated by the pronounced reflection on the left. Subsequently, the X-ray beam proceeds to traverse further until a weak signal is detected in channel 1, which originates the Ru fluorescence signal, as delineated by the shaded region. Given that the oxygen plasma treatment has effectively removed unwanted flakes, we can confidently attribute the observed signal to the targeted nanolayer.

In this work, flakes with large lateral size (~20 μm) and uniform thickness ranging from 3.5 nm to 20.7 nm were selected for further treatment and for the RIXS measurements. The alignment of position is carried out before each scan to ensure that the X-ray beam properly shines on the sample. The RIXS measurement was carried out at room temperature.

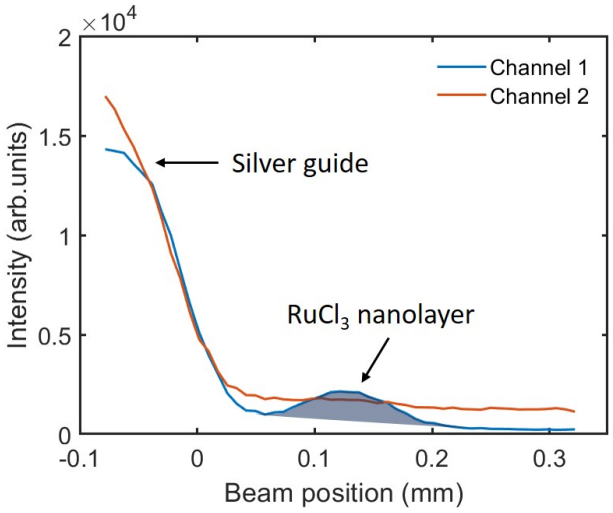

Figure 4.15: Fluorescence signal captured by SDD detector. Channel 1 and 2 integrates the X-ray signal around the Ru fluorescence energy (~ 2.5 keV) and around the incident energy. The shaded region indicate the response from the nanolayer.

4.3 Experimental Methods

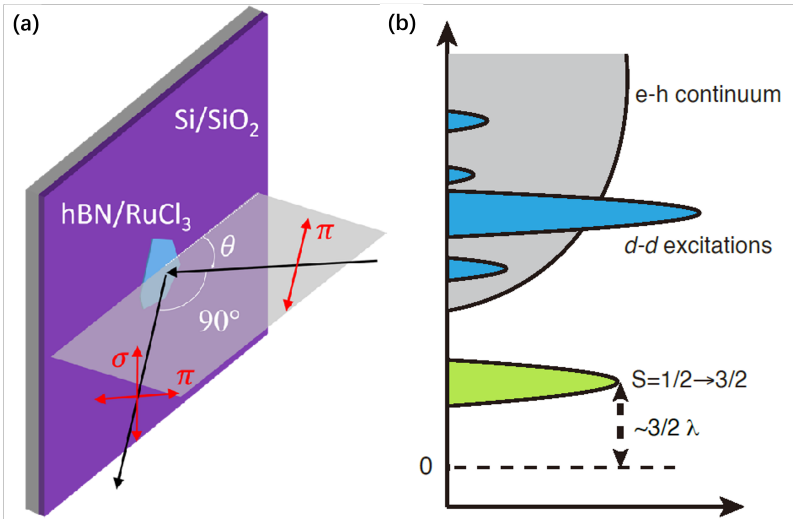

Figure 4.16: (a) Schematic of the scattering geometry. The incident x-ray photons are π-polarized, and the polarization of the scattered x-ray photons is not analyzed. The scattering angle is fixed at 90° throughout the experiment to suppress charge scattering. (b) Schematic of the elementary excitations of $RuCl_3$. The $\tilde{S} = 1/2 \rightarrow 3/2$ spin-orbit exciton (green) is located at the excitation energy $\sim 3/2\lambda$. The higher-energy d-d excitations (blue) are superposed by the electron-hole continuum (grey).

The RIXS experiments were performed at the IRIXS spectrometer at the Ru-L_3 absorption edge (photon energy 2837 eV). We used IRIXS in two configurations, *i.e.* with 4B inline HRM (beamspot size 150×20 μm^2) and nested HRM (beamspot size 20×20 μm^2), yielding a combined resolution of 77 meV and 96 meV, respectively. Figure 4.16(a) shows the experimental geometry. The incoming beam is π-polarized and the polarization of the outgoing beam collected at a scattering angle of 90° was not analyzed.

Table 4.2: HRM and counting time of the spectra shown in the main text.

sample thickness	energy range	HRM	counting time
bulk	spin-orbit exciton	nested	2×50 min
20.7 nm	spin-orbit exciton	nested	2×50 min
15.6 nm	spin-orbit exciton	nested	3×50 min
10.7 nm	spin-orbit exciton	nested	3×50 min
5.9 nm	spin-orbit exciton	nested	9×50 min
5.9 nm	spin-orbit exciton at $\theta = 10°$	nested	2×50 min
3.5 nm	spin-orbit exciton	inline	4×50 min
bulk	d-d excitation	nested	2×100 min
16.4 nm	d-d excitation	inline	2×100 min
13.0 nm	d-d excitation	inline	2×100 min
7.0 nm	d-d excitation	inline	3×100 min
5.9 nm	d-d excitation	nested	4×100 min
3.5 nm	d-d excitation	inline	5×100 min

Table 4.2 shows the total counting time and HRM we used in the experiment. We note that all RIXS spectra were acquired by averaging several repeated scans. These scans show good reproducibility and indicate that no sample degradation occurs throughout the measurement. In particular, we did not observe any signatures of X-ray beam damage even for the thinnest flakes, possibly because the incoming beam for high-resolution RIXS is highly monochromatic and correspondingly much less intense than in many other synchrotron-based experiments. Moreover, the substrate and the capping layer are good thermal conductors and thus help to reduce x-ray beam heating. The combined resolution is determined by the FWHM of a non-resonant elastic spectrum from silver paint.

Before presenting the experimental results, we briefly summarize the outcome of previous RIXS experiments on bulk $RuCl_3$ [Fig. 4.16(b)]. The excitation spectrum of interest comprises two segments at low and high energy, respectively: spin-orbit excitations from the $\tilde{S} = 1/2$ ground state of the Ru^{3+} ions (electron configuration d^5) into the $\tilde{S} = 3/2$ excited-state manifold (~240 meV); and d-d excitations from the t_{2g} crystal-field ground

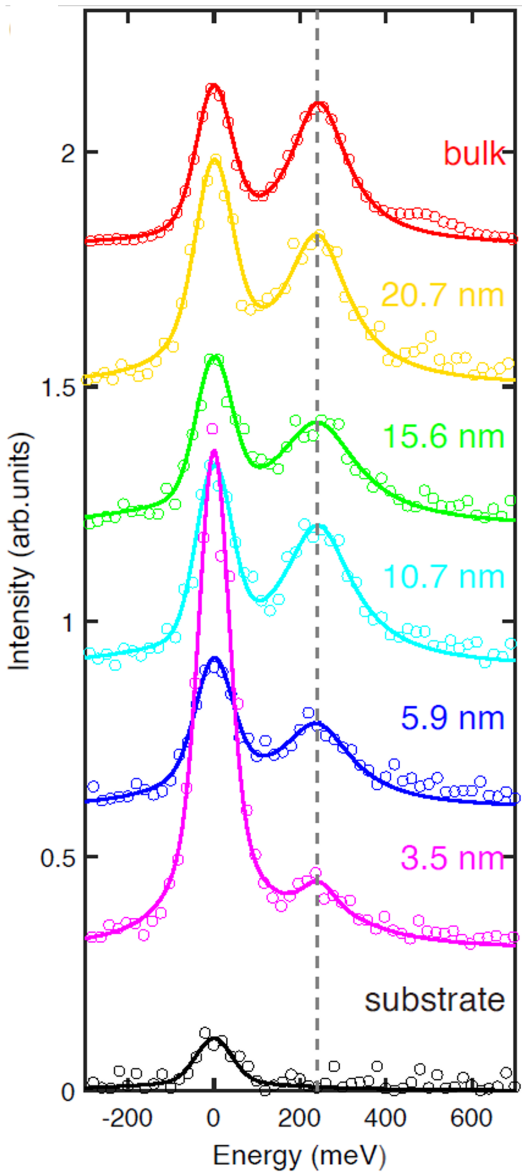

Figure 4.17: Low-energy RIXS spectra of $RuCl_3$ nanoflakes, and reference spectrum of a bulk crystal. The incoming X-ray energy was 2837 eV and the sample angle θ=40°, with in-plane momentum transfer close to the Γ point. The spectral intensity of bulk crystal is scaled by a factor of 0.01. Vertical offsets were applied for clarity. The grey dashed line is a guide to the eye to indicate the center of the excitation peak.

state into the e_g excited states of the Ru ions (1.5 ~ 4 eV), which are superposed by a continuum of charge-transfer excitations (emerging from ~1 eV). Excitations within the $\tilde{S} = 1/2$ manifold, which are heavily overdamped in the paramagnetic state, were not studied.

4.4 Results and Discussions

Figure 4.17 shows the measured low-energy RIXS spectra of nanoflakes with various thicknesses, as well as reference spectra of a $RuCl_3$ bulk crystal and a Si/SiO_2 substrate. For all measured nanoflakes, we observe an elastic peak due to residual defects in the substrates and samples, and a pronounced inelastic feature around 240 meV. Following prior RIXS studies on bulk $RuCl_3$ presented in Chapter 3, [40] we assign it to $\tilde{S} = 1/2 \rightarrow 3/2$ transitions with energy $\sim 3/2\lambda$, where λ is the SOC constant of Ru. The lineshape of this spin-orbit exciton is described by a Lorentz profile convoluted by a Gaussian profile, known as Voigt lineshape. This line profile does not have a close-form expression, and in practice it is commonly approximated by some pseudo-Voigt profile. Here we use the linear combination of a Lorentz profile and a Gaussian profile as the fitting function:

$$I_{pV}(\omega) = (1-\eta)\frac{I_1}{(\omega - E)^2 + \Gamma^2} + \eta I_2 \exp(-(\omega - E)^2/2\sigma^2) \tag{4.1}$$

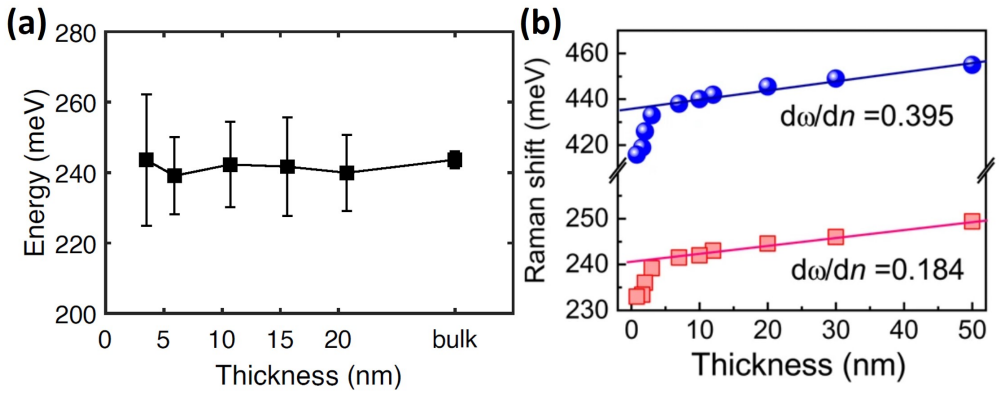

Figure 4.18: (a)Spin-orbit exciton energies for $RuCl_3$ bulk crystal and thin flakes. Within the fitting error, the spin-orbit exciton exhibits no thickness-dependent energy shift. (b)Thickness dependent spin-orbit exciton energy measured by Raman spectroscopy. Figure (b) reproduced from Ref[97].

where σ is defined by the combined energy resolution of the spectrometer, and $0 \leqslant \eta \leqslant 1$. Figure 4.18 shows the spin-orbit excitation energy fitted from the spectra, where the error bars exclusively stem from the fitting procedure. The excitation energy is independent of thickness and identical to the one in bulk crystals. This is expected because the SOC is an intra-atomic interaction that is not significantly influenced by the crystalline environment. Notably, given our resolution above 50 meV we cannot exclude energy shifts an order of

magnitude smaller. Indeed a recent Raman study[97] reports a shift of about 10 meV below 7 nm thickness, albeit based on a delicate spectral decomposition where no error bars are given.

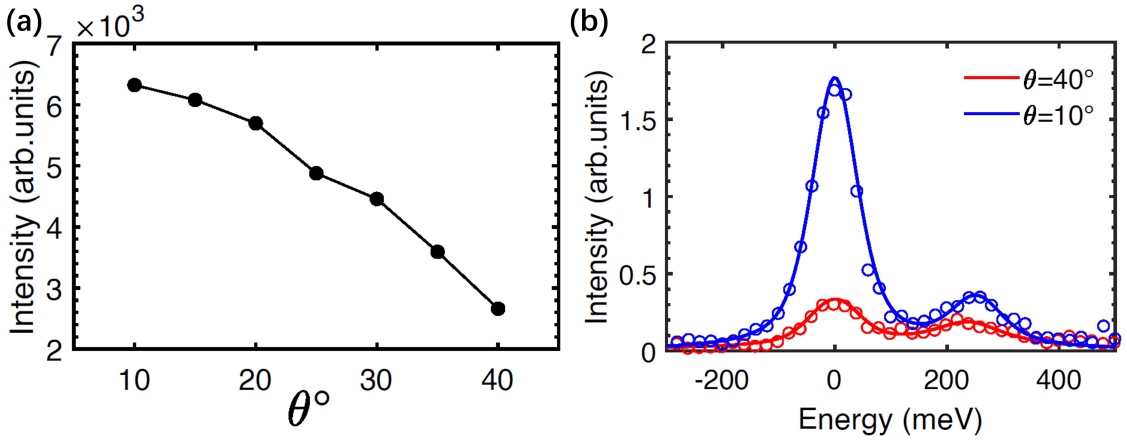

Figure 4.19: (a) Ru-L_3 scattering intensity of the 5.9 nm thin flake increases monotonically when approaching grazing-incidence geometry. (b) Low-energy spectra of the 5.9 nm flake at θ=10° and 40°. The spin-orbit exciton peak intensity is enhanced for θ=10°, despite the large lateral waste of photon flux.

The feasibility of RIXS experiments on nanoflakes depends critically on the intensity of the spectral features, which is approximately proportional to the sample thickness. We note that the lateral dimensions of the nanoflakes are below those of the beam spot under typical experimental conditions. Sample-to-sample variations of these dimensions thus account for deviations from the linear dependence of the spin-orbit exciton intensity on the sample thickness for $\theta = 40°$ (Fig. 4.17). For smaller θ, the footprint of the beam increases by a factor of $1/\sin\theta$, and the flux waste increases correspondingly. Despite this situation, we observed a substantial increase of the scattering intensity as θ approaches grazing incidence [Fig. 4.19], which can be attributed to the larger travel path of the beam across the sample and the associated increase in scattering probability. The over-compensation of the flux waste implies that RIXS experiments can achieve high momentum-space coverage even for small flakes. On the other hand, the peak energy is almost independent of the incident angle θ which modulates the momentum transfer in the honeycomb layers. The lack of a significant momentum-space dispersion implies that this feature arises from a local, intra-atomic excitation.

The high-energy range of the RIXS spectra comprises a broad inter-site charge-transfer continuum emerging above the charge gap at 1 eV, and sharp d-d excitation peaks corresponding to intra-ionic crystal-field transitions from the t_{2g}^5 ground state to $t_{2g}^4 e_g^1$

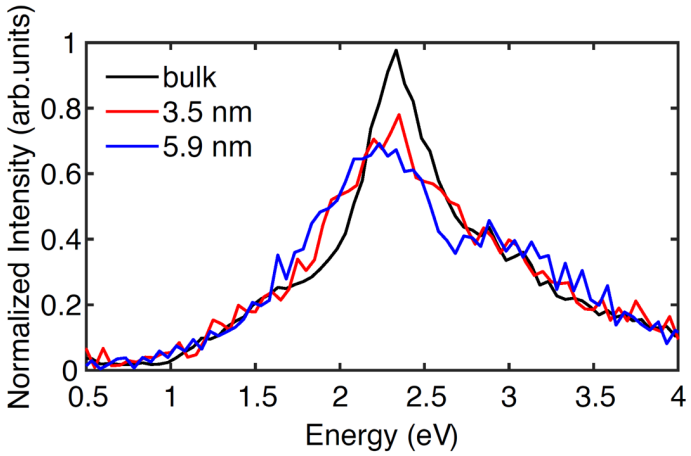

Figure 4.20: Comparison of the spectra of a bulk crystal and two thin flakes. The charge-transfer continuum exhibits no thickness dependent behavior, as seen within the spectral ranges below 1.5 eV and above 3.5 eV.

excited-state multiplets [Fig. 4.16(b)]. In agreement with a previous report on bulk $RuCl_3$, [40] we find that a single peak at 2.3 eV dominates the spectrum, whereas other d-d excitations (α, β and γ features in Fig. 3.3) are much weaker and cannot be clearly separated from the continuum. Figure 4.20 shows a direct comparison between the spectra of bulk $RuCl_3$ and the two thinnest flakes. The spectral intensity is normalized to the integrated spectral weight between 1 eV and 4 eV. The good match in the spectral ranges below 1.5 eV and above 3.5 eV indicates an essentially unchanged charge continuum, and that the observed broadening and red-shift can be mostly ascribed to the main d-d excitation peak at 2.3 eV.

To better understand the thickness dependence of the red-shift of d-d excitation, we carried out the same measurement on various $RuCl_3$ nanolayer samples. Figure 4.21 displays the thickness evolution of the high-energy spectra in comparison to the bulk, with the normalization method mentioned above. The spectral difference $I_{\text{flake}} - I_{\text{bulk}}$ [grey shaded area in Fig. 4.21] calculated from flakes of thickness 7 nm and larger exhibits only minor differences to the bulk. As the thickness decreases further, however, the spectral weight broadens and redistributes towards lower energies.

Next the spectra are fitted to a model composed of two components: a Lorentzian profile with variable energy and width describing the main d-d excitation, and a broad background describing the charge continuum (with submerged minor d-d excitations) that was kept fixed for all samples. To decompose the d-d excitation, we notice that the spectral shift is mainly contributed by the B peak. As a consequence, we assume that the other weaker features are

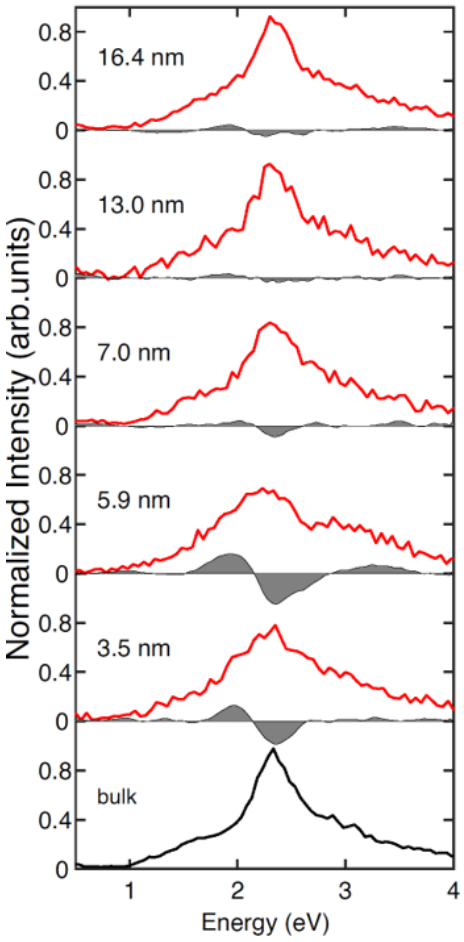

Figure 4.21: Thickness-dependent multiplet excitation spectra of $RuCl_3$ for θ=40°. The incident X-ray energy was 2839 eV. The spectral difference $I_{\text{flake}} - I_{\text{bulk}}$ (smoothed for clarity) is shown as a grey area. As the flake thickness decreases below 7 nm, a red-shift is observed.

in first approximation thickness-independent and could be described by a broad, unchanged background. Firstly the normalized spectra of bulk $RuCl_3$ in the vicinity of the B peak are fitted by a Lorentzian lineshape plus a linear background which simulates the continuum. Here the effect of spectrometer resolution (~100 meV) is neglected since it is much smaller than the FWHM of the B peak (~ 400 meV). Next the fitted Lorentzian lineshape is subtracted from the bulk spectra and the residue is assumed to be the thickness-independent background. For thin flake spectra, this continuum is first subtracted and the residue is fitted by a Lorentzian profile to extract the peak energy and FWHM. The excellent agreement of the resulting profiles with the experimental data (Fig. 4.22) indicates that the thickness dependence of the d-d excitations can be reliably determined by this procedure. Figures 4.23(a),(b) show the thickness evolution of the energy and width of the main d-d excitation profile resulting from these fits. In the two thinnest flakes, the profile is red-shifted by

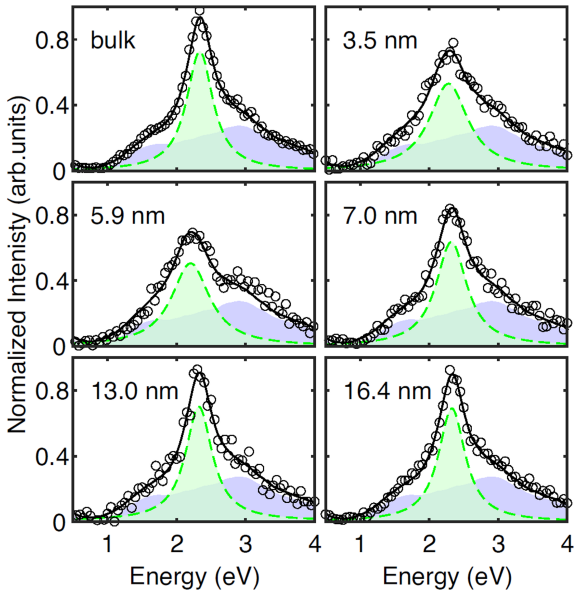

Figure 4.22: d-d excitation decomposition for all measured flakes and bulk sample. The blue shaded component represents the charge continuum, independent of flake thickness. The green shaded component is the Lorentzian profile of the main d-d excitation. Empty circles and black solid lines represent the experimental data and the results of fits to a model function including both components, respectively.

50-100 meV, and its width increases by about 50%. Notably the error bar exclusively stem from the fitting process, and the error induced by the estimation of background shape is not taken into account.

To clarify the origin of this observation, we implemented a single-ion model calculation based on a Hamiltonian comprising the intra-ionic Hund's coupling and spin-orbit coupling, as well as octahedral and tetragonal crystal fields.[40, 37, 39]. We varied each of these parameters while keeping the others fixed at the value of bulk $RuCl_3$, and monitored the resulting energy shift of the d-d feature. For the bulk spectra, we adopted the same parameters as in previous work in Chapter 3: $J_H = 3B+C = 0.34$ eV, $C/B = 5.0$, $\lambda = 0.145$ eV, $10Dq = 2.44$ eV, and $\Delta = 0$ while fixing $\Delta_e = 2\Delta$. For thin flakes, we modified each parameter while keeping the others fixed, and monitored the variation required to reproduce the observed 50 meV red shift in the excitation energy of the main d-d feature. The results show that only a shift of the average octahedral crystal field splitting $10Dq$ from 2.44 eV to 2.39 eV can explain the observed red-shift. On the other hand, except for the crystal field splitting $10Dq$, other listed parameters cannot reproduce the red shift of the main crystal-field excitation observed in the experimental results, as shown in Fig. 4.24. The

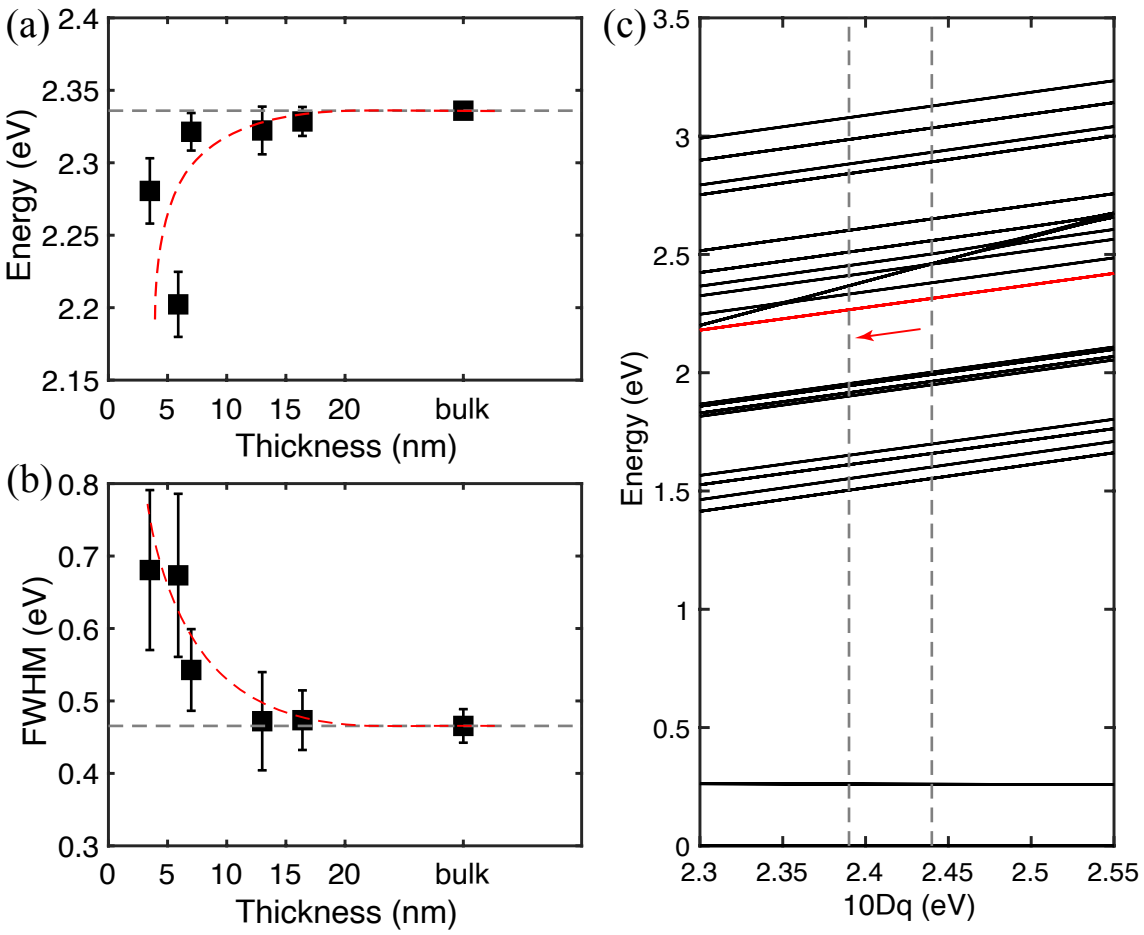

Figure 4.23: (a) Peak energy and (b) FWHM of the main d-d excitation resulting from fits. The horizontal dashed lines indicate the values of bulk $RuCl_3$. The red curve is a guide to the eye. (c) d-d excitation energies as a function of the octahedral crystal-field energy $10Dq$ resulting from model calculations. The red line corresponds to the $t_{2g}^4 e_g^1$ state that yields the most intense ligand field excitation in the RIXS spectra. The grey vertical lines indicate the bulk value and the average value for the 3.5 nm flake.

energy of this feature is not sensitive to $J_{H,t_{2g}}$ and C/B. The SOC λ significantly affects the energy of the SOC exciton, which is however not observed in the experiment. A tetragonal distortion leads to splitting of the energy levels instead of softening. However, we cannot rule out lattice distortions of lower symmetry.

In a point-charge crystal field model, $10Dq$ is proportional to $1/a^5$, where a is the Ru-Cl bond length, so that the observed red-shift corresponds to an average expansion of the $RuCl_6$ octahedra by 0.4%. The concomitant broadening and the thickness evolution of both lineshape parameters [Figs.4.23(a),(b)] imply that any lattice distortion associated

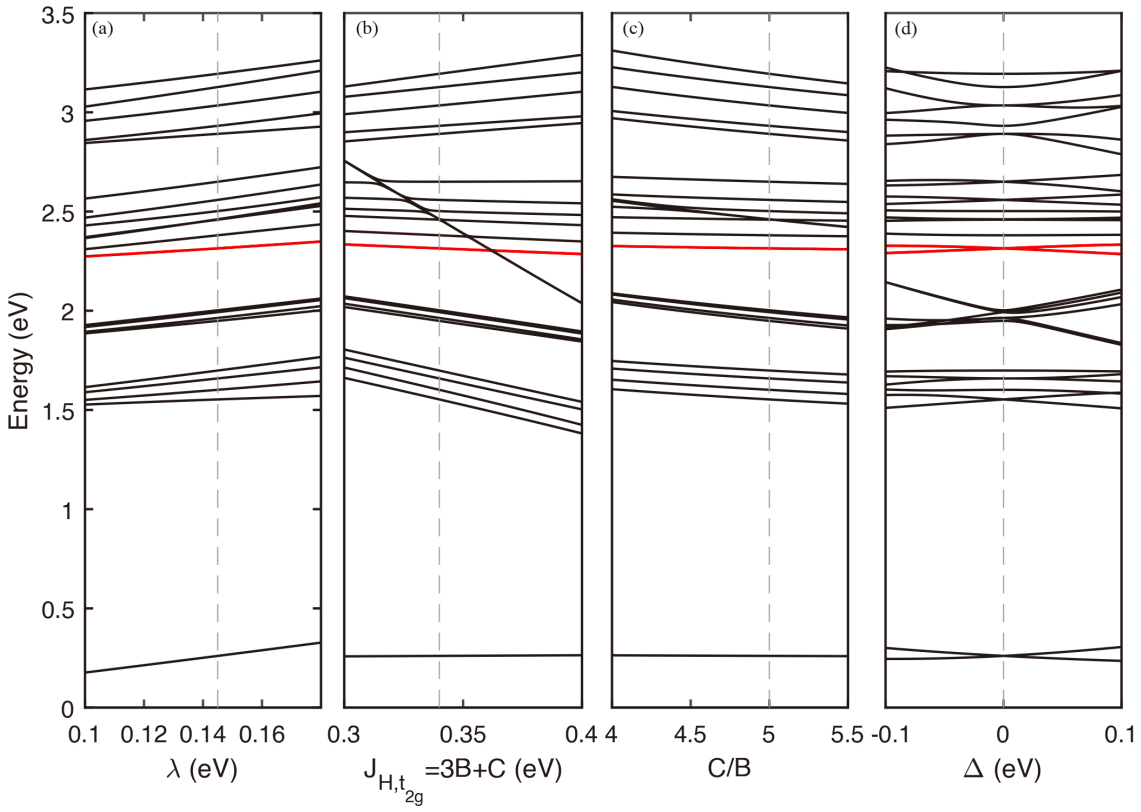

Figure 4.24: Model calculation results of excitation energies as a function of (a) SOC λ, (b) effective Hund's coupling of t_{2g} subspace $J_{H,t_{2g}}$, (c) Tanabe-Suagno parameter C/B, and (d)tetragonal splitting Δ. The grey dashed lines indicate the values of bulk $RuCl_3$. The red line corresponds to the $t_{2g}^4 e_g^1$ state that yields the most intense ligand field excitation in the RIXS spectra.

with the altered ligand field is inhomogeneously distributed in the out-of-plane direction. We can hence rule out defects or impurities in the $RuCl_3$ crystals from which the flakes were exfoliated (which would give rise to thickness-independent broadening), and bending distortions generated by the exfoliation procedure (which would broaden – but not shift – the spectral features from both spin-orbit and crystal-field excitations). Rather, the data point to a mixture of bulk-like inner layers and near-surface layers with different ligand field and, likely, octahedral distortions, which comprise a progressively larger fraction of the nanoflake volume with decreasing thickness (e.g., 4 inner and 2 surface monolayers in the 3.5 nm sample). We note that an analogous broadening and red-shift of a peak arising from Cu $d_{x^2-y^2} - d_{3z^2-r^2}$ excitations was observed in a Cu-L_3 edge RIXS study of $(CaCuO_2)_3/(SrTiO_3)_2$ superlattices, and attributed to the modified crystal structure at the interfaces. [3] We thus conclude that distortions of the $RuCl_6$ octahedra at or near the

surface are responsible for the thickness evolution of the crystal-field excitations in our $RuCl_3$ nanoflakes. A survey of the relevant literature has revealed two possible origins of near-surface lattice disorder. First, a theoretical study of $RuCl_3$-based VdW heterostructures [105] suggests significant strain effects due to lattice mismatch, despite the weak VdW interlayer coupling. By analogy, epitaxial strain at the interface between our $RuCl_3$ flakes and the protective hBN capping layer might increase the Ru-Ru and Ru-Cl bond lengths, and thus weaken the ligand-field interactions. Another possible cause of near-surface lattice distortions are defects such as Cl vacancies, surface adsorbates, or combinations thereof, which are hard to avoid during sample preparation. Evidence of Cl positions different from those in the bulk has indeed been reported in several surface-sensitive experimental studies [113, 114], but no agreement has been reached on the nature and strength of these distortions. Our RIXS data can serve as a guide for realistic model calculations of intrinsic and extrinsic lattice distortions and their possible impact on the electronic properties.

4.5 Summary

In this Chapter, we focused on the RIXS study of $RuCl_3$ nanolayers at Ru-L_3 absorption edge. The 2D character of $RuCl_3$ has spurred numerous studies probing its magnetic and electronic structure, both in pristine form and within heterostructures. These investigations have unveiled the thickness-dependent magnetism of $RuCl_3$, hinting at an augmented Kitaev interaction in lower dimensions. Furthermore, the van der Waals nature of $RuCl_3$ suggests the potential modifiability of its properties through strain, charge doping, proximity effects etc.

In this study, we explored two fabrication methods for obtaining $RuCl_3$ nanolayers: mechanical exfoliation and a chemical lithiation process. While the latter yields $RuCl_3$ nanolayers in large quantities, surface contamination is often a significant issue, rendering them unsuitable for RIXS analysis. Consequently, all samples were prepared via tape exfoliation. However, measuring nanolayers poses technical challenges due to their small volume. Specifically, locating the nanolayer within the RIXS sample chamber without a camera is nontrivial. To address this, we fabricated metal guides on the substrate surface that point towards the target flake. Additionally, the sample was coated with a protective layer of hBN using stamp-transfer techniques and underwent plasma treatment to eliminate unwanted nearby layers. Thanks to these treatments, we can quickly identify and align the target sample during RIXS measurements.

We have successfully collected Ru-L_3 RIXS spectra of exfoliated $RuCl_3$ layers with thickness down to 3.5 nm. Although the samples are protected by thick hBN capping layers, and their volumes are orders of magnitude smaller than those of bulk crystals, the signal-to-noise ratio of the RIXS data is sufficient to capture the main spectral features observed in the bulk. We note that all RIXS spectra presented in this work shows no sign of X-ray beam damage. The results reveal a distinct thickness evolution of the low-energy spin-orbit exciton and high-energy crystal-field excitations. Whereas the spin-orbit exciton arises from intra-atomic SOC interactions and is thus independent of thickness, the main crystal-field excitation exhibits a clear broadening and red-shift compared to the bulk, which we are able to attribute to near-surface alternations of the Ru ligand field. Modifications of the Ru-Cl bond lengths and bond angles of the $RuCl_6$ octahedra are important specifically for $RuCl_3$, as they determine the ratio of Kitaev and Heisenberg interactions and hence the propensity for spin-liquid physics. More generally, direct detection of d-d excitations by RIXS yields insights into the local coordination of transition metal ions and associated ligand fields, which are often hard to access by other spectroscopic methods and can be crucial to the physics of 2D materials and VdW heterostructures, as exemplified by the influence of ligand-field interactions and charge-transfer transitions on the optoelectronic response of atomically thin CrI_3 [115]. Unlike surface-sensitive methods, RIXS is able to detect manifestations of such distortions in samples protected by capping layers, which are routinely used for chemically sensitive 2D materials, and at buried interfaces in VdW heterostructures.

Our results point out various perspectives for further development of the methodology and scope of RIXS experiments on 2D materials. In particular, optimizing the lateral sample dimensions and the experimental geometry (including focusing conditions, incidence and exit angles, background suppression, and acquisition times) should enable measurements on thinner samples, including monolayers and monolayer-based heterostructures. As the energy of the spin-orbit exciton in $RuCl_3$ is comparable to the magnon and paramagnon energies in various tansition metal compounds (including cuprates, iridates, and ruthenates), RIXS experiments on collective spin excitations in 2D materials will also be feasible. Recent advances in high-resolution RIXS instrumentation in the soft, intermediate, and hard x-ray regimes will greatly expand its range of applicability. Moreover, there is still a great prospect of combining RIXS with techniques that are able to predetermine the in-plane crystal orientation, such as angular-dependent Raman spectroscopy and second harmonic generation,[116] so as to allow to map dispersing features of various excitations.

With these developments, RIXS is poised to realize its potential as a unique source of information on the strength and range of electron-electron and electron-lattice interactions in 2D materials and heterostructures.

5 Co-L_3 RIXS study on $Na_3Co_2SbO_6$

Drawing inspiration from Ref[51], extensive research efforts have been dedicated to identifying materials with the Kitaev spin liquid state characterized by a d^5 configuration, among which $RuCl_3$ has been extensively investigated using various experimental techniques, revealing signs of frustrated interactions underlying its exotic magnetism. However, at low temperatures, $RuCl_3$ exhibits a zigzag AFM order instead of the anticipated spin liquid phase. This deviation may be attributed to an "impure" magnetic Hamiltonian, encompassing Heisenberg and off-diagonal coupling terms alongside the Kitaev interaction. Recent theoretical works have thus proposed transition metal compounds with a $3d^7$ configuration as alternative solid-state systems exhibiting Kitaev-type interactions.[117, 118, 119] According to this theory, the Co-based compound $Na_3Co_2SbO_6$ emerges as a promising candidate.

In this study, we conducted a comprehensive spectroscopic investigation on single crystals of $Na_3Co_2SbO_6$, in combination with model calculations and theoretical analysis. The Raman and RIXS data offer valuable insights into the electronic structure which enables us to extract interaction parameters and delineate the highly anisotropic ground state of this material. Furthermore, magnetic correlations are measured through momentum- and temperature-dependent quasielastic peaks (QEPs) observed in the RIXS spectra. These findings highlight robust FM correlations persisting well above the magnetic transition temperature, consistent with previous INS studies.

In the following sections, I will review both theoretical and experimental research efforts on $Na_3Co_2SbO_6$ and summarize the key observations. Subsequently, I will present our spectroscopic measurement results on single crystals of $Na_3Co_2SbO_6$. Finally, I will present the details for determining interaction parameters using model calculations and compare these values with the existing literature.

5.1 Introduction

To date, a significant amount of experimental efforts has been dedicated to candidate Kitaev spin liquid materials with $4d$ or $5d$ electrons, such as Ir^{4+} and Ru^{3+}. These systems benefit from their substantial spin-orbit coupling strength, facilitating the formation of a $\tilde{S} = 1/2$ ground state and meeting the prerequisites for realizing Kitaev-type magnetic exchange interactions (as discussed in Chapter 3). However, achieving a pure Kitaev phase in realistic material systems remains challenging due to the "imperfect" Hamiltonian described in Eqn.3.3. The large orbital radius of $4d$ and $5d$ electrons results in strong overlap between neighboring ions, thereby introducing unwanted long-range couplings alongside the nearest-neighbor Kitaev term. Consequently, an intuitive solution is to explore alternative compounds featuring $3d$ elements, where the electron orbitals are significantly more localized.

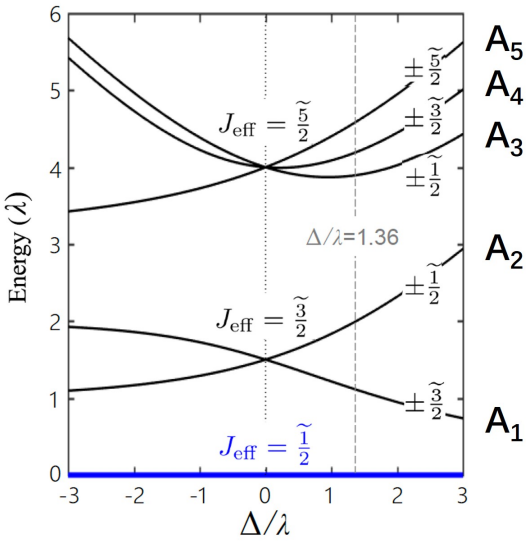

Figure 5.1: Splitting of $S = 3/2$, $L_{eff} = 1$ manifold in presence of spin-orbit coupling and trigonal splitting. The five energy levels are labeled by $A_1 \sim A_5$ for simplicity. In the case of $Na_3Co_2SbO_6$, the ratio Δ_{tri}/λ is estimated to be 1.36, as indicated by the vertical dashed line. Figure reproduced from Ref[118].

Motivated by this perspective, recent proposals have suggested that compounds including transition metals with a $3d^7$ configuration, such as Co^{2+}, could be promising systems alongside the extensively studied d^5 materials family [117, 118, 119]. According to this theory, the $3d$ ion should possess a high-spin ground state $t_{2g}^5 e_g^2$ with a total spin of $S = 3/2$ and an effective orbital moment $L_{eff} = 1$. Spin-orbit coupling entangles

these manifolds and forms a ground state described by pseudospin $J_{eff} = 1/2$, as well as two excited states with pseudospins $J_{eff} = 3/2$ and $J_{eff} = 5/2$. When these ions are arranged in a honeycomb lattice and surrounded by edge-sharing octahedra, the resulting magnetic Hamiltonian is proven to include a Kitaev exchange interaction term. Notably, the microscopic dynamics of d^7 systems differ from those of d^5 systems, primarily due to the activation of hopping channels involving e_g levels (i.e., $e_g - e_g$ and $e_g - t_{2g}$ exchange) resulting from the electron occupation in these states. Nevertheless, the contributions from the $t_{2g} - e_g$ and $e_g - e_g$ hopping channels to the J, Γ, and Γ' terms have opposite signs and cancel each other out, thereby effectively suppressing long-range magnetic interactions. Moreover, the Kitaev interaction in this system arises from $t_{2g} - e_g$ exchange interactions, contrasting with the $t_{2g} - t_{2g}$ exchange interaction in low-spin d^5 systems. In a realistic material system, the octahedron is usually distorted trigonally, leading to an anisotropic ground state wavefunction. Due to the lower local symmetry, the $S = 3/2$, $L_{eff} = 1$ manifolds split into five energy levels distinguished by the J_{eff} component along the trigonal axis. The excitation energies of these levels have been theoretically calculated and are presented in Fig. 5.1. For simplicity, these five levels will be denoted by A_1 through A_5 in the following discussions. Nevertheless, it has been demonstrated that the Kitaev phase can be preserved when the trigonal splitting is small, as illustrated by the magnetic phase diagram in Fig. 5.2. In fact, this distortion is identified as a tuning parameter in experiments that determine the strength of the non-Kitaev interactions.

Based on these theoretical calculations, $Na_3Co_2SbO_6$ emerges as a promising candidate for hosting a Kitaev spin liquid. The crystal structure of $Na_3Co_2SbO_6$ is illustrated in Fig. 5.3. Its honeycomb layers consist of edge-sharing CoO_6 octahedra, with each honeycomb center hosting an Sb ion. Situated between adjacent CoO_6 layers is a layer of Na ions. Powder and single-crystal neutron diffraction studies have unveiled a $C2/m$ point group symmetry, indicative of a monoclinic crystal structure akin to $RuCl_3$ [120]. Several magnetization measurements have reported a low Néel temperature of $T_N = 4 \sim 8$ K [121, 120, 122, 123, 124, 125], with discrepancies potentially linked to Na nonstoichiometry [121]. This transition temperature is also consistent with heat capacity measurements. Notably, an in-plane anisotropy of the magnetization was observed in single crystal $Na_3Co_2SbO_6$, as reported in Ref [124], contrasting with other powder and polycrystal measurements. This finding provides further experimental evidence of the loss of three-fold symmetry due to lattice distortions.

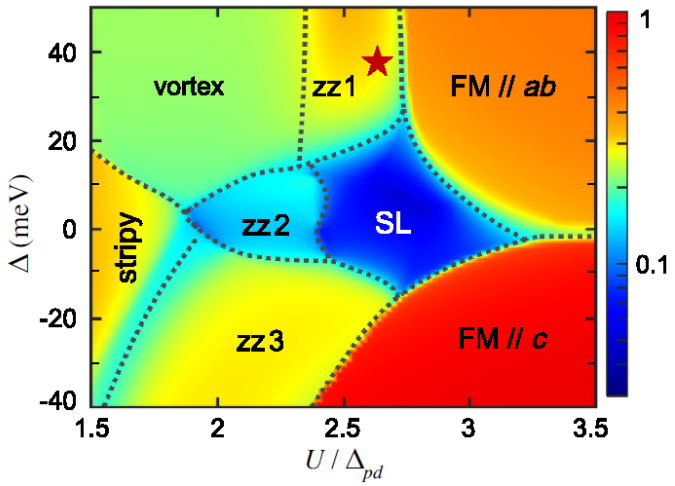

Figure 5.2: Magnetic phase diagram of honeycomb Co^{2+} from calculation. The star indicate the position of $Na_3Co_2SbO_6$. In addition to the Kitaev spin liquid (SL) phase, several other magnetic ordering states can possibly exist, including FM phase with momentum along or perpendicular to the honeycomb ab plane, zigzag order with moments in the ab plane (zz1), along Co-O bonds (zz2) or in the ac plane(zz3), and vortex and stripy phase. Figure reproduced from Ref[118].

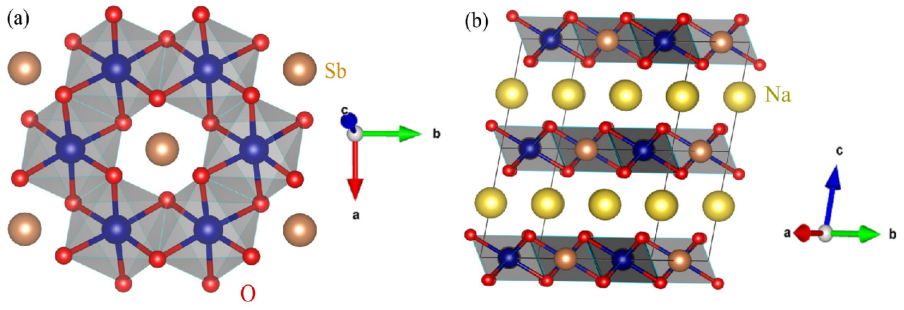

Figure 5.3: Crystal structure of $Na_3Co_2SbO_6$.(a) The honeycomb plane of Co^{2+}. (b)The honeycomb layers are separated by Na layers. Figure reproduce from Ref[122]

The magnetic structure of $Na_3Co_2SbO_6$ in the AFM phase below T_N has been a focal point of recent investigations. By analyzing the local momentum direction and the dispersion of magnetic excitations, researchers can estimate the strength of exchange interactions. Numerous diffraction studies have been conducted on various sample forms, including powder, polycrystal, single crystal, and thin films [126, 124, 127]. These studies have suggested several potential magnetic structures. For instance, diffraction measurements on $Na_3Co_2SbO_6$ powder revealed a zigzag order [121], further supported by subsequent single crystal studies that indicated a purely in-plane magnetic moment, as depicted in Fig. 5.4.

Conversely, another neutron diffraction study proposed a double-q ordering, interpreted as the superposition of two zigzag orders along the (0,1,0) and (1,0,0) directions [127]. Furthermore, NMR studies have detected an unequal response between two Na positions, which does not support the zigzag ordering [128] but shows no contradiction with the double-q scenario. Moreover, a recent single crystal neutron scattering study also revealed a star-shaped diffraction pattern [124], possibly originating from randomly distributed short-range FM strips. It appears that the magnetic structure of $Na_3Co_2SbO_6$ is influenced by the sample quality and further complicated by competing interactions. As of now, the actual ordering type remains under debate.

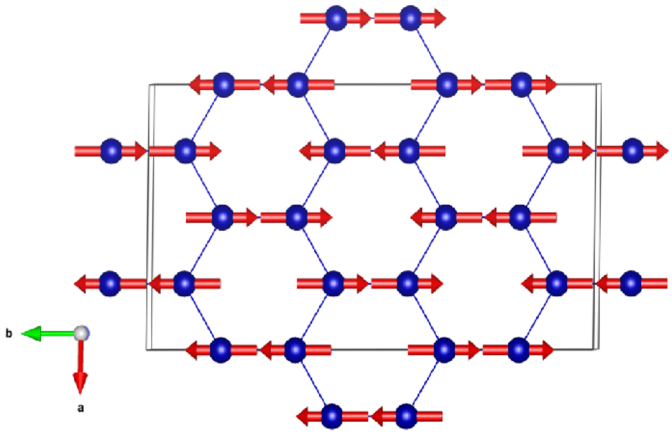

Figure 5.4: Zigzag magnetic order in $Na_3Co_2SbO_6$. The magnetic moments lies fully in-plane. Figure reproduce from Ref[122]

Another noteworthy observation pertains to the distinctive temperature dependence of magnetic correlations at the Γ and M points, representing FM and AFM correlations, respectively [124]. Fig. 5.5 presents the neutron diffraction measurements at various temperatures. Below T_N, the magnetic diffraction peak at the M point is clearly discernible due to the AFM order. As the temperature rises to around 10 K, a hexagonal-star-shaped diffuse scattering connecting the Γ and M points emerges, potentially originating from the competition between AFM and FM correlations. This suggests that the ordering between these two states becomes more pronounced, indicating that the AFM order is only marginally energetically favorable compared to the competing FM state, echoing the concept of a spin liquid.

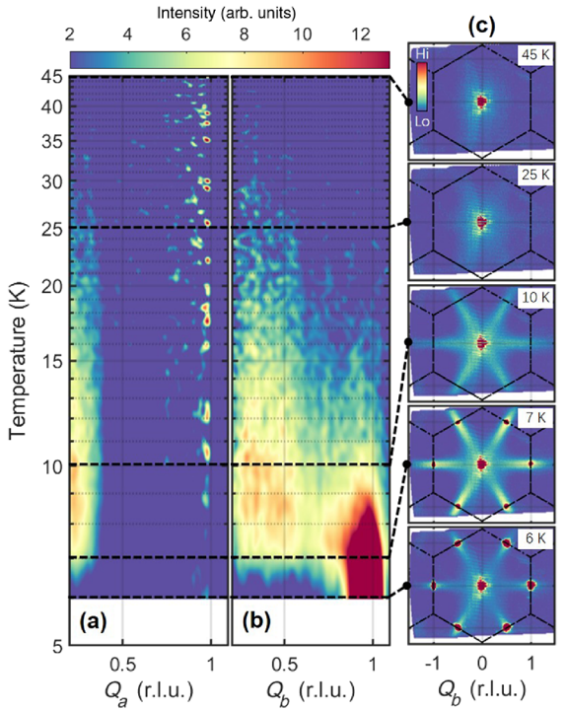

Figure 5.5: Momentum resolved INS spectra of $Na_3Co_2SbO_6$ single crystal measured at different temperatures. Figure reproduced from Ref[124]

In contrast to the extensively studied magnetic properties of $Na_3Co_2SbO_6$, its electronic structure has been discussed in theoretical studies [129], but remains to be better elucidated by experimental methods. Particularly crucial is the confirmation of the pseudospin $\tilde{S} = 1/2$ ground state, as the ratio between trigonal splitting Δ_{tri} and spin-orbit coupling $\lambda = 1/2\zeta_{3d}$ determines the shape of the ground state wavefunction, and thereby significantly impacts magnetic exchange interactions, as illustrated in the magnetic phase diagram (Fig. 5.2). Several research efforts have attempted to estimate these parameters using various experimental methods. INS measurements on powder $Na_3Co_2SbO_6$ have identified one spin-orbit exciton at approximately 27 meV and proposed a small trigonal distortion of around 12 meV when considering the presence of an internal magnetic field [126]. Another XAS study conducted on single crystals and powder samples of $Na_3Co_2SbO_6$ employed X-ray linear dichroism (XLD) in conjunction with magnetic circular dichroism (XMCD), proposing a trigonal splitting in the range of $30 \sim 65$ meV [130]. On the other hand, fitting the magnetization data to theoretical models yielded a value of $\Delta_{tri}/\lambda = 1.36$ [118]. In the higher energy range, optical measurements on thin films of $Na_3Co_2SbO_6$ captured

charge-transfer excitations between oxygen p orbitals and cobalt d orbitals, enabling estimation of Hund's coupling and crystal field splitting to be $(10Dq, J_H) = (0.9, 0.7)$ eV.[131]

In this study, we adopted a combined approach of Raman spectroscopy and RIXS to probe the magnetic and electronic excitations of this material over a wide temperature and momentum range. Our investigation revealed low-energy magnetic and spin-orbit excitations, as well as high-energy ligand field excitations, which enables us to extract the electronic interaction parameters and confirm the pseudospin-1/2 ground state. Moreover, the dependence of magnetic correlations on momentum and temperature offered valuable insights into the potential dominant exchange mechanisms within this two-dimensional quantum magnet system and is strongly suggestive of the presence of frustrated interactions.

5.2 Experimental Methods

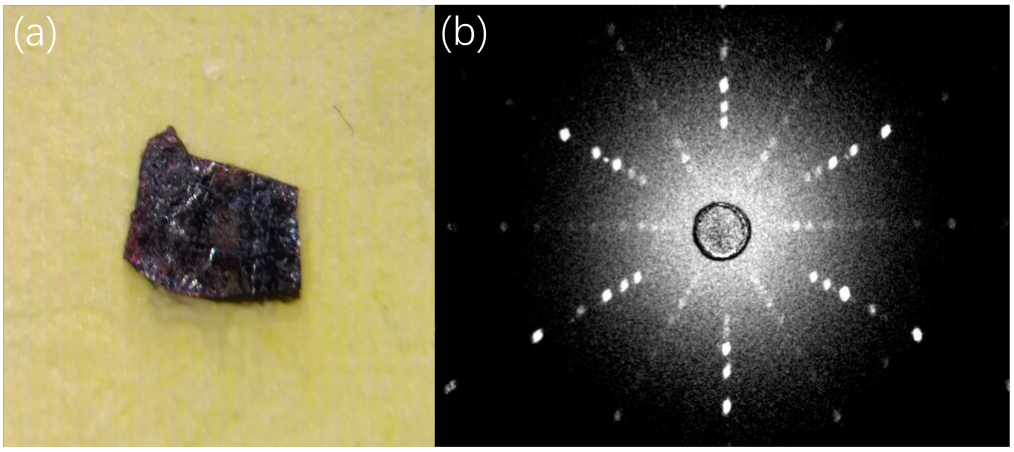

Figure 5.6: (a)Photograph of $Na_3Co_2SbO_6$ single crystal sample used for RIXS measurement. (b) Single-crystal Laue diffraction pattern the sample in (a).

The $Na_3Co_2SbO_6$ single crystals are grown via the solid-state reaction method. As depicted in Fig. 5.6(a), the sample chosen for RIXS measurements exhibits a typical size of several millimeters in diameter and possesses a dark red color, which is characteristic of Co^{2+} compounds. Fig. 5.6(b) displays the single crystal Laue diffraction pattern of the aforementioned sample, revealing a set of sharp diffraction spots indicative of its high

quality. However, the diffraction pattern shows a six-fold rotational symmetry and the monoclinic structure is not clearly resolved. The measured single crystal demonstrates a Néel temperature T_N of approximately 6 K, consistent with previous findings.

The Raman spectra were measured from a base temperature of 5 K up to room temperature. A He-Ne laser with a wavelength of 632.8 nm was focused on the sample, and the scattered light was dispersed by the 1800 lines/mm grating of a LabRam HR800 Raman spectrometer. The incident light was polarized in the basal plane, and the scattered light was collected in both parallel ($z(XX)\bar{z}$, A_g) and perpendicular ($z(XY)\bar{z}$, B_g) polarization channels.

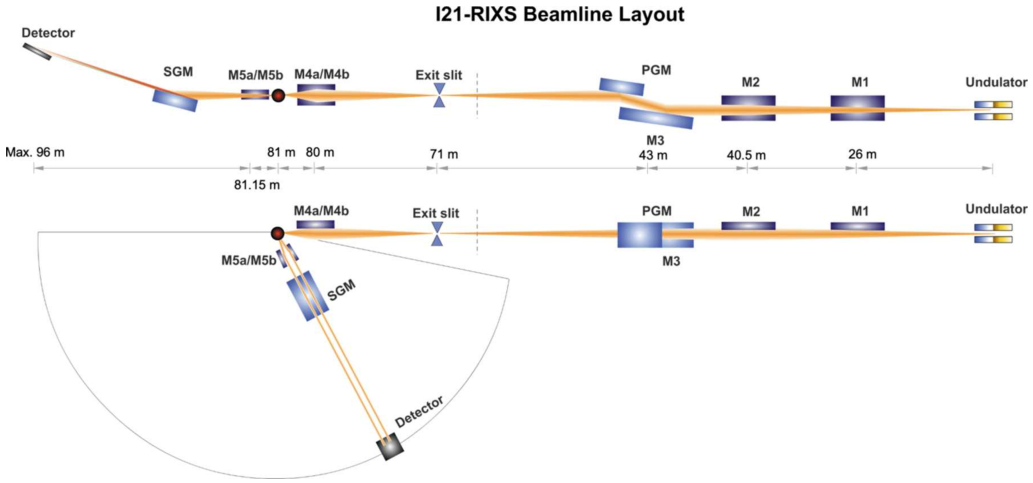

Figure 5.7: Schematic of I21 beamline in Diamond Light Source. The top and bottom panel shows the side view and top view, respectively. Figure reproduced from [27]

The RIXS experiment was conducted at the I21 RIXS beamline at the Diamond Light Source in Didcot, United Kingdom. Figure 5.7 illustrates the schematic of the beamline structure. The energy of incident soft X-ray photons can be finely adjusted within a wide range from 280 to 2000 eV while achieving a high energy resolution. For our measurements, the incident energy was tuned to the Co-L_3 absorption edge at approximately 778 eV, with XAS measured in total fluorescence yield mode. The combined spectrometer energy resolution was determined to be 35 meV, as measured by the FWHM of elastic scattering from a carbon tape. The incoming X-ray photons were σ- and π-polarized, and the scattered light was collected at 90° and 154° (maximum 2θ angle) without polarization analysis. The measurements were conducted at temperatures of 15K, 50K, 100K, 200K, and 300K to investigate the temperature dependence of magnetic correlations. At each temperature, we examined the momentum-dependent behavior along the (H,0) (ϕ = 0°, 60°) and (H,H)

($\phi = 90°$) directions by rotating the sample along the b axis (see Fig. 5.3). At the Co-L_3 edge, we were thus able to cover the Brillouin zone with a momentum transfer of 0.24 r.l.u. along both directions when $2\theta = 90°$.

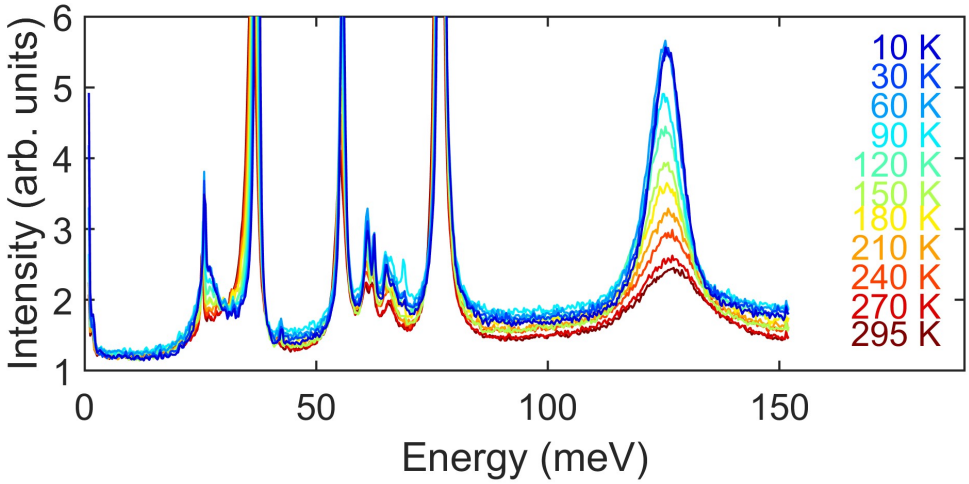

Figure 5.8: Temperature dependent Raman spectra of $Na_3Co_2SbO_6$ in cross layout (XY, B_g mode)

5.3 Results and Discussion

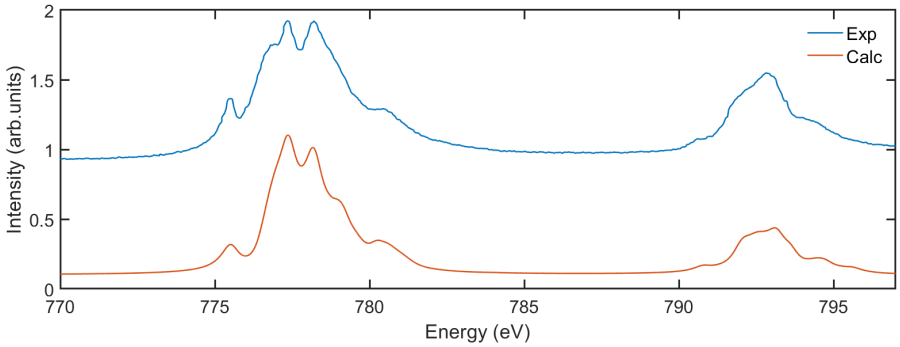

Figure 5.9: Comparison between experimental and theoretical XAS intensity.

Figure 5.8 shows the temperature-dependent Raman spectra of the $Na_3Co_2SbO_6$ single crystal with cross polarization configuration. In addition to the sharp phonon peaks, two broader features are observed at 27 meV and 126 meV, which are attributed to spin-orbit excitations. The energy of the first peak aligns well with previous INS measurements and

arises from the transition from the $|J_{eff} = 1/2\rangle$ ground state to the $|J_{eff} = 3/2, J^Z_{eff} = \pm 3/2\rangle$ state (A_1 feature). The second peak corresponds to the transition to $|J_{eff} = 5/2\rangle$ states, comprising three energy levels that are all allowed by the selection rule. Consequently, the peak at 126 meV is possibly a sum of excitation peaks from these three states. Theoretical calculations (Fig. 5.1) also anticipate another spin-orbit exciton at approximately 70 meV [118], although this is not discernible in the Raman measurement and may be overshadowed by the strong phonon lines.

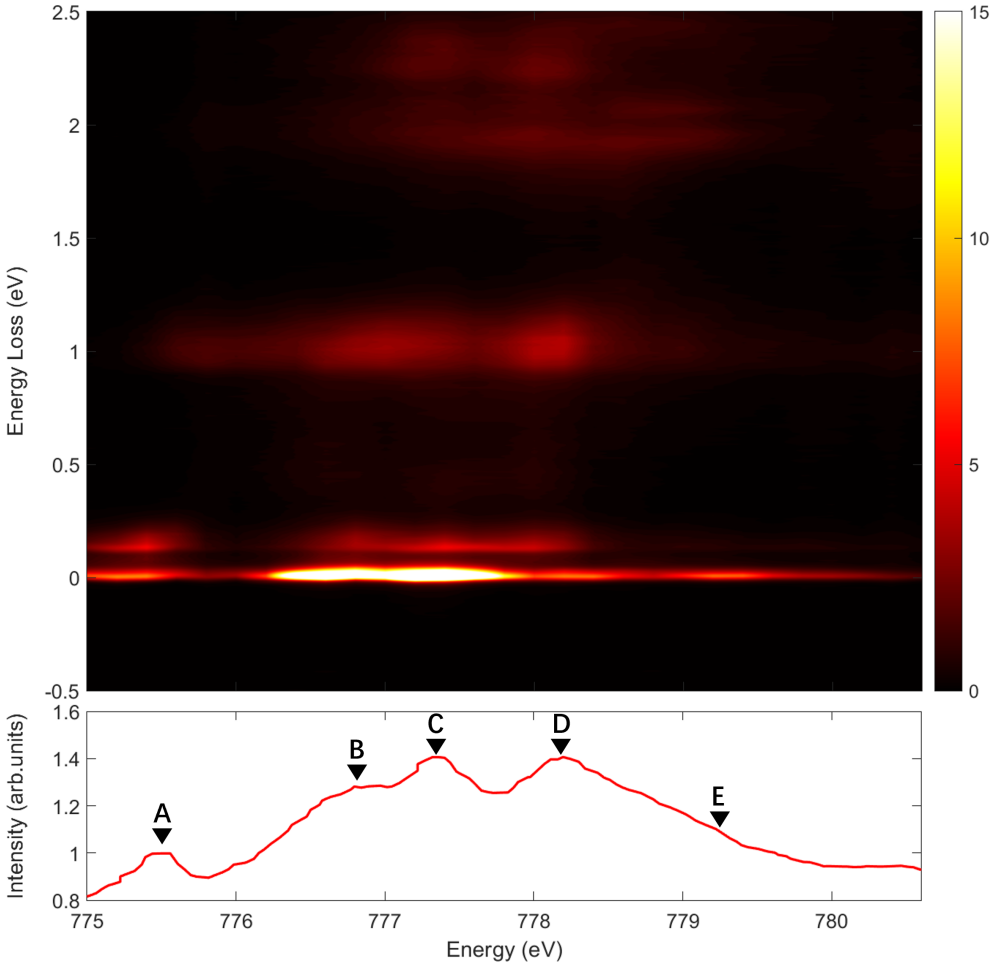

Figure 5.10: Resonance profile of $Na_3Co_2SbO_6$. The lower panel show the XAS spectra, and the five absorption peaks are indicated by the inverse triangles and letters A~E. The upper panel is a colormap of RIXS spectra collected at each incident energy.

The Raman spectra offer detailed insight into two spin-orbit exciton peaks with high energy resolution. However, its capability in measuring excitations with a large energy scale or at finite momentum transfer is restricted. Consequently, we performed Co-L_3 RIXS measurements on a $Na_3Co_2SbO_6$ crystal to address these limitations. First, we employed XAS to determine the incoming photon energy. Fig. 5.9 presents the fluorescence yield at the Co-$L_{2,3}$ edge measured at 15 K, alongside the calculation result from the single ion model. Due to the insulating nature of $Na_3Co_2SbO_6$, TEY measurement is impractical for this material. The X-ray incident angle was set to 20° from the sample surface with π-polarization, while the fluorescence signal was collected at $2\theta = 90°$. Two sets of resonant absorption peaks emerge at around 775 eV and 790 eV, corresponding to the L_3 and L_2 edges, respectively. The splitting between these absorption edges is roughly determined by $\sim 3/2\zeta_{2p}$, where ζ_{2p} is the spin-orbit coupling of $2p$ electrons. We estimate ζ_{2p} to be 9.745 eV, in agreement with first-principles calculation results [132]. At the L_3 edges, multiple absorption peaks are discerned at 775.3 eV, 776.8 eV, 777.3 eV, 778.2 eV, and 779.3 eV, originating from transitions to different intermediate states. The energy of these fine structures is well-reproduced by model calculations. Notably, the narrow width of these absorption peaks arises from the lack of decaying channels compared to $4d$ and $5d$ transition metal ions whose XAS features are usually broad and fine structures are typically absent (see Fig. 3.3, Fig. 2.17, and Fig. 2.16 for results of Ru-L_3, Rh-L_3, and U-M_5 edges). However, the intensity of the fluorescence yield signal is not ideally reproduced by model calculations because the self-absorption effect heavily distorts the shape of the measured spectra.

Figure 5.10 illustrates the resonant profile of $Na_3Co_2SbO_6$ at the Co-L_3 edge around 778 eV. The lower panel displays the FY spectra, with the five absorption peaks labeled as A∼E. To comprehend the origin of the XAS fine structures and determine the optimal incident X-ray energy for the subsequent RIXS experiments, we incrementally increased the incident beam energy in steps of 0.2 eV and measured a RIXS spectrum at each energy. The upper panel presents the results as a heatmap. Several distinct features are discernible: a prominent quasi-elastic peak (QEP) corresponding to magnetic excitations, several well-defined peaks below 180 meV originating from the five spin-orbit excitations depicted in Fig. 5.1, and a broader feature extending up to 200 meV. In the higher energy range, excitations at around 1 eV are observed, corresponding to a mixture of d-d excitations and spin state transitions. Features with higher energy (>2 eV) consist of a complex mixture of intra- and inter-atomic excitations, which are beyond the scope of this work and are not analyzed in detail. The excitation energies of all peaks mentioned above are independent of incident

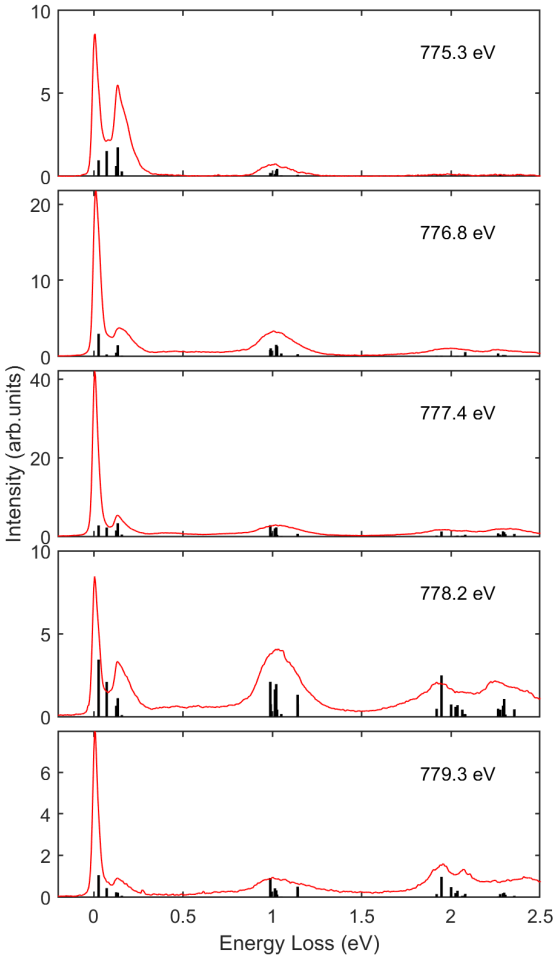

Figure 5.11: RIXS spectra measured at the XAS absorption peak A~E. The black vertical bars indicate the calculation result from single ion multiplet calculations.

photon energy, suggesting that these features arise from a Raman-type energy transfer process rather than from fluorescence. These excitations exhibit a varied intensity behavior across the absorption edge: at 775.3 eV (XAS peak A), only excitations within t_{2g} orbitals (i.e., excitations below 200 meV) are enhanced, whereas at 776.8 eV, 777.3 eV, and 778.2 eV (XAS peaks B, C, D), both the crystal field transitions from t_{2g} to e_g orbitals and the QEP are strongly enhanced.

The RIXS spectra collected at the five XAS peaks A~E are presented in Fig. 5.11. To confirm the origin of these peaks, we conducted single ion model calculations using the Hamiltonian outlined in Chapter 1. The calculated energy and peak intensity are denoted by the black vertical bars. We chose the interaction parameters as $(10Dq, J_H, \gamma, \zeta_{3d}, \Delta_{tri}) = (1.05\text{ eV}, 0.745\text{ eV}, 4.8, 0.071\text{ eV}, 0.065\text{ eV})$ (see Section 5.4 for details). Utilizing the model calculation, we assign the broad peak at around 1 eV to the crystal field excitations from the $t_{2g}^5 e_g^2$ ground state to $t_{2g}^4 e_g^3$ multiplets, along with a transition from a high-spin

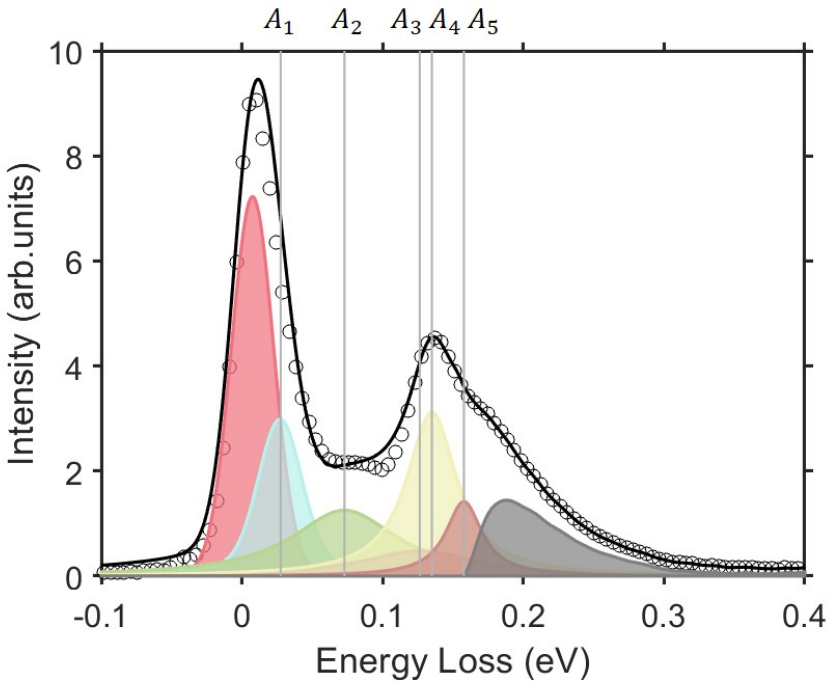

Figure 5.12: Decomposition of the low-energy RIXS spectra, including the QEP (red), $A_1 \sim A_5$ features (indicated by the vertical lines), and a particle-hole continuum (black).

ground state to a low-spin $t_{2g}^6 e_g^1$ state. Notably, at XAS peaks B~E, the enhancement of the QEP overwhelms the other spin-orbit excitations, posing significant challenges in discriminating the fine structure of the excitations. Consequently, we fixed the photon energy at 775.3 eV (peak A) for the subsequent measurements to better observe the low-energy features.

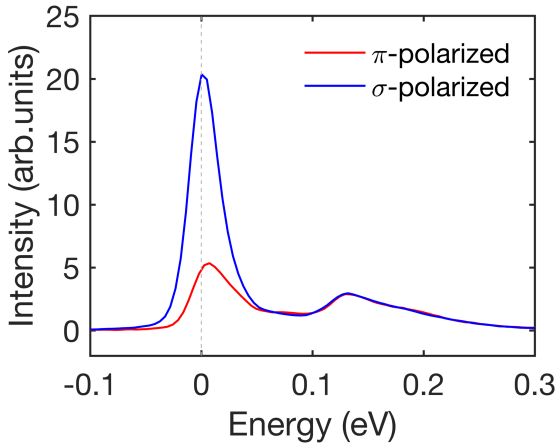

Figure 5.13: Comparison between RIXS spectra with σ- and π-polarized incident photon.

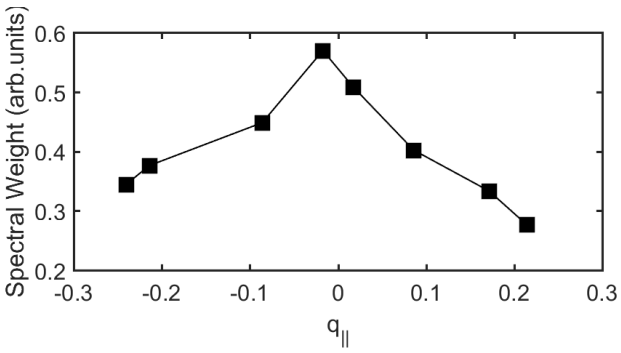

Figure 5.14: Momentum dependence of QEP intensity extracted from fitting.

First, we focus on the low-energy excitations defined by spin-orbit transitions. To facilitate comparison with previous theoretical calculations and the Raman data presented in Fig. 5.8, we present the spectrum measured at $\theta = 42.6°$ with a momentum transfer $\mathbf{q} \sim 0$, as shown in Figure 5.12. The spectrum is decomposed into several distinct features: a quasi-elastic peak (red), five spin-orbit excitations labeled $A_1 \sim A_5$ (cyan, green, orange, yellow, and brown), along with a continuum emerging from 160 meV (grey). The workflow of the decomposition procedure is as follows: first, we determine ζ_{3d} and Δ_{tri} by utilizing the excitation energies from the Raman measurement (Section 5.4). With the parameters from the model calculations, the energies of the spin-orbit excitations are calculated to be 27.5, 72.8, 126.3, 134.5, and 157.7 meV for the $A_1 \sim A_5$ states, respectively. Simultaneously, the spectral weight of each feature can also be computed using Eqn.1.34. Next, we decompose the spectra by fitting the QEP and the A_1 feature with a pseudo-Voigt profile, and the $A_2 \sim A_5$ features with a Lorentz profile. During the fitting, the energy and spectral weight of the $A_1 \sim A_5$ features are held fixed at the theoretically calculated values to reduce the number of fitting parameters. Finally, the residual part at high energy is retained as a continuum background. We tentatively attribute this continuum to particle-hole excitations, analogous to the background observed in A_2IrO_3 systems by hard RIXS measurements [75]. The five vertical lines in Fig. 5.12 indicate the positions of the spin-orbit excitations as a guide to the eye.

We need to point out that the quasi-elastic peak (QEP) originates from magnetic excitations rather than from trivial diffuse scattering, as supported by the comparison of RIXS spectra obtained with π- and σ-polarized incident beams shown in Fig. 5.13. A significant suppression of elastic signal is evident in the π-polarized spectra compared to the σ-polarized ones, while the remaining features of the spectra exhibit similar intensities. Moreover, the σ-polarized spectra reach maximum intensity at zero energy transfer ($E = 0$)

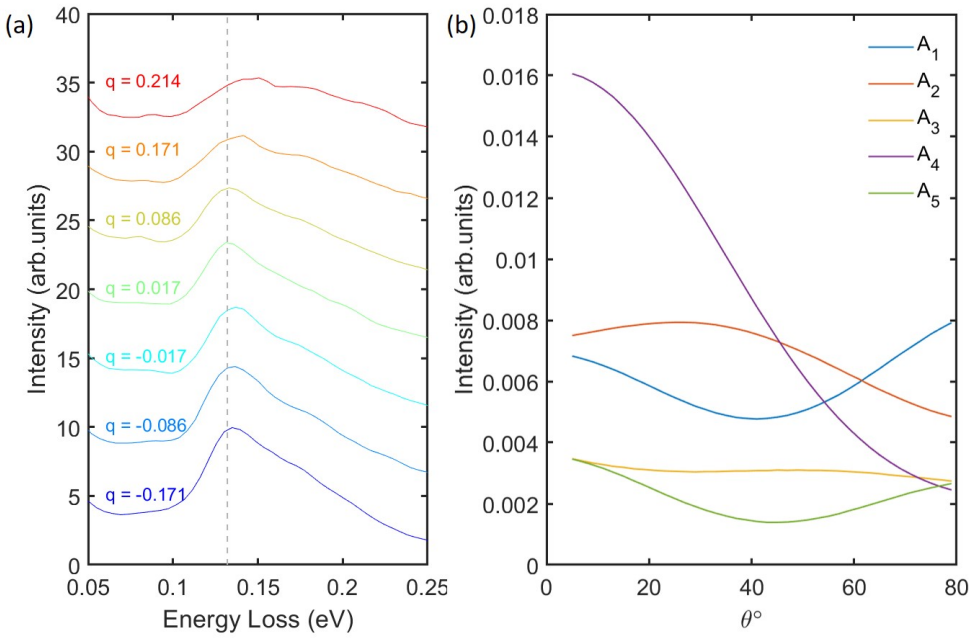

Figure 5.15: (a) Momentum dependent RIXS spectra of $A_3 \sim A_5$ spin-orbit exciton. The spectra are shifted vertically for clarity. (b) Incident angle dependence of intensity from $A_1 \sim A_5$ features, from single ion model calculation.

due to significant elastic charge scattering, as indicated by the grey vertical line, whereas the maximum intensity of the π-polarized spectra appears at a finite positive energy. The fitting results also point to a peak position at approximately 5 meV, an energy scale comparable to the magnetic exchange interaction. Considering these observations collectively, we are confident that the quasi-elastic peak in π-polarized channel is predominantly governed by magnetic scattering with small excitation energies rather than elastic scattering.

The momentum-dependence of RIXS spectra provides valuable insights into the electronic structure and magnetic correlations in reciprocal space. Here, we focus on the low-energy excitations with finite momentum transfer, specifically along the $\Gamma - M$ direction, where self-absorption corrections are applied using Eqn.1.40. Given that the RIXS spectra are measured around an absorption peak and the excitation energy is not too large (less than 200 meV), the assumption $\alpha_T(E_{in}) \approx \alpha_T(E_{out})$ holds true in this scenario. To analyze the QEP, we first extract its spectral weight from the RIXS spectra. However, since the energy separation between the QEP and the A_1 feature is comparable to the energy resolution of the spectrometer (35 meV), we need to employ a similar fitting treatment as introduced earlier to subtract the contribution from the A_1 excitation. The extracted spectral weight is depicted in Fig. 5.14 as a function of in-plane momentum transfer $\mathbf{q}_{\parallel}$. A clear maximum

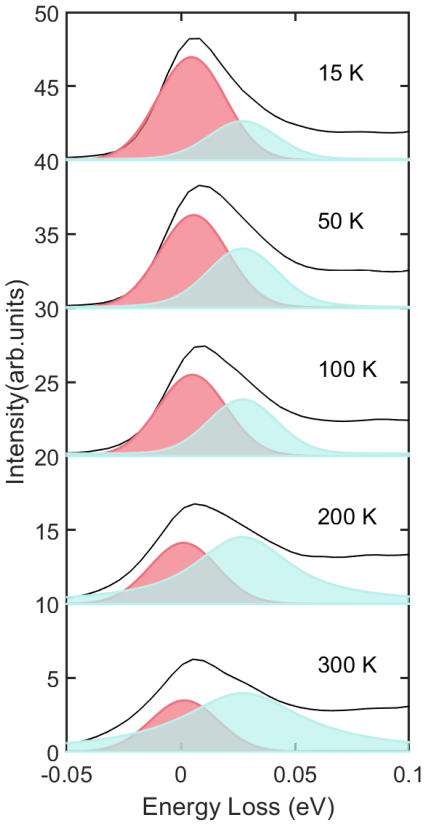

Figure 5.16: Temperature dependence of the QEP and the decomposition result. The red and cyan shaded part indicate the magnetic excitation and A_1 spin-orbit exciton, respectively.

around the Γ point is observed, indicating the presence of FM-type magnetic correlations, consistent with previous findings (Ref[124]). However, due to the limited incident energy (approximately 780 eV) and the 90° scattering geometry, we are unable to reach the AFM ordering wavevector and examine the behavior of AFM correlations as demonstrated for the $RuCl_3$ crystal (see Chapter 3).

Next, we examine the momentum-dependence of the spin-orbit excitations. Given that the A_1 and A_2 features are indistinguishable and cannot be clearly separated, our focus narrows to the A_3, A_4, and A_5 states with $J_{eff} = 5/2$, as illustrated in Fig. 5.15(a). Around the Γ point, the RIXS spectra exhibit maximum intensity at 134 meV, aligning well with the calculated excitation energy of the A_4 feature (grey dashed line). As $|\mathbf{q}|$ increases, the peak's energy experiences a slight blue-shift by several meV, likely due to the weakly dispersive nature of these spin-orbit excitons. Moreover, this energy shift appears more pronounced when the momentum transfer $\mathbf{q}$ is positive compared to when it is negative (for instance, compare the spectra at $q = \pm 0.171$), even though theoretically, the excitation energy at opposite q should remain identical due to symmetry arguments. These observations can be

effectively interpreted by considering the spectral redistribution among A_3, A_4, and A_5 under different geometrical configurations. Fig. 5.15(b) illustrates the calculated spectral intensity of each spin-orbit state depending on the incident angle. These five excitations display distinct angle-dependent behavior due to the highly anisotropic wavefunction of t_{2g} states. At small incident angles (or negative q), the A_4 feature exhibits greater intensity compared to A_3 and A_5 features, thereby dominating the RIXS spectra. However, such dominance diminishes rapidly as θ increases, and at larger incident angles ($i.e.$ large positive **q**), the intensity of $A_3 \sim A_5$ features becomes comparable. Consequently, the RIXS spectra become broader, and the peak almost disappears (as observed at $q = 0.214$), with the RIXS intensity reaching its maximum at a higher energy.

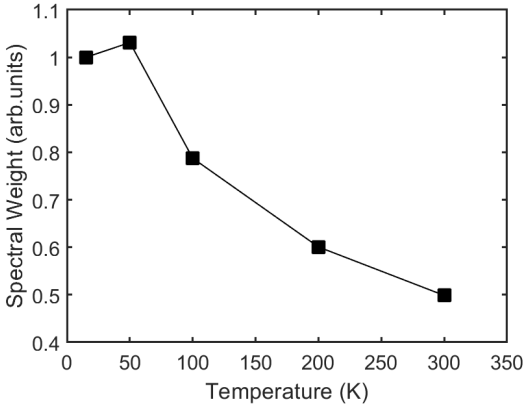

Figure 5.17: Temperature dependent spectral weight of QEP. The intensity of magnetic fluctuations show minor change up to 50 K, indicating a robust FM-type pseudospin correlation.

Finally, we shift our focus to the temperature dependence of magnetic correlations in $Na_3Co_2SO_6$. Fig. 5.16 illustrates spectra measured from the base temperature to 300 K, with the incident angle fixed at 42.6° and the momentum transfer close to 0. Employing a similar decomposition method as before, we extract the spectral weight of the QEP, indicated by the red shaded region, and the A_1 feature, denoted by the cyan shaded region. As temperature increases, the intensity of the QEP diminishes while its width broadens due to thermal fluctuations. The temperature dependence of the total spectral weight is depicted in Fig. 5.17. Notably, the intensity of the QEP at 15 K and 50 K remains comparable, despite the temperature being well above the transition temperature of AFM ordering ($T_N = 6$ K). This suggests the robustness of the magnetic correlation with a characteristic vector $\mathbf{q} = 0$. This phenomenon bears resemblance to the temperature-dependence of

magnetic correlations observed in $RuCl_3$, as discussed in Chapter 3. We interpret this similarity as indicative of a similar mechanism at play, namely FM correlation within the $Na_3Co_2SbO_6$ system.

5.4 Determination of interaction parameters

Based on the experimental data from Raman and RIXS measurements, we can determine the interaction parameters using the single-ion model outlined in Chapter 1. The Hamiltonian is defined by Eqn.1.8, where H_{CF} incorporates both octahedral splitting and trigonal splitting. Additionally, in the calculation of the RIXS intensity, the $p-d$ Coulomb interaction is considered to accurately describe the resonant absorption effect observed in the XAS spectra.

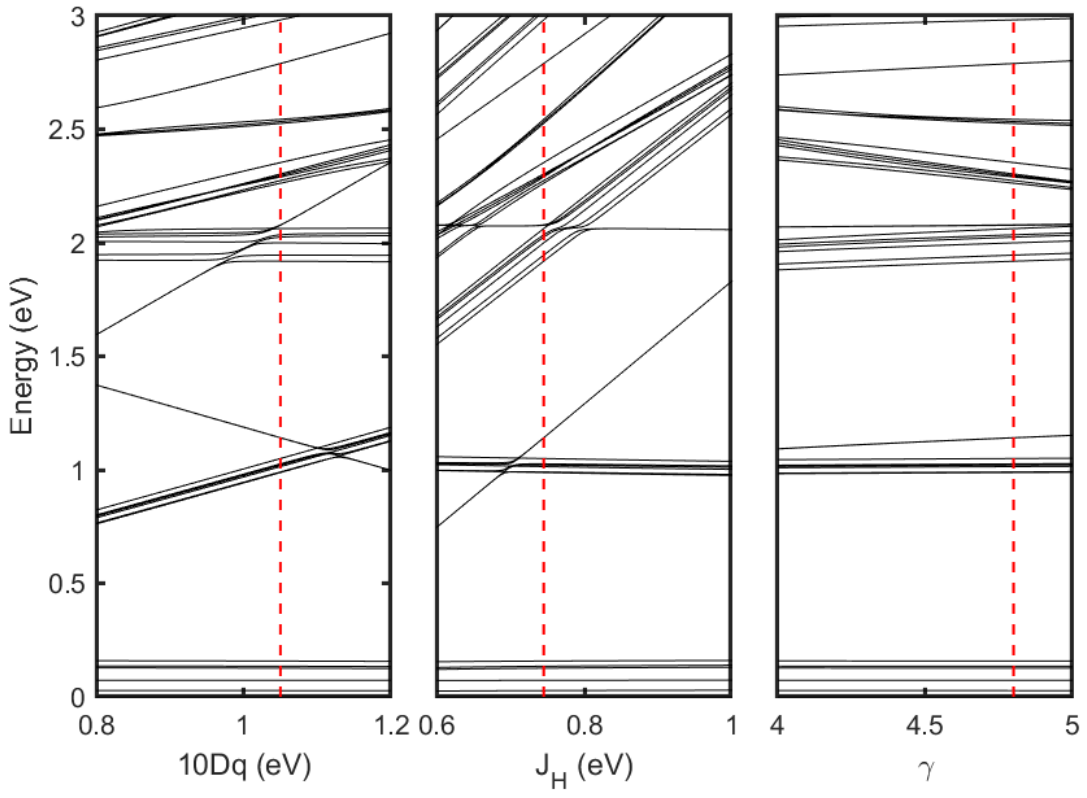

Figure 5.18: Tanabe-Sugano diagram as a function of $10Dq, J_H$ and γ. The other parameters are fixed at $(10Dq, J_H, \gamma, \zeta_{3d}, \Delta_{tri}) = (1.05\text{ eV}, 0.745\text{ eV}, 4.8, 0.071\text{ eV}, 0.065\text{ eV})$.

State	$J^Z_{eff} = \pm 1/2$	$J^Z_{eff} = \pm 3/2$	$J^Z_{eff} = \pm 5/2$
ζ_{3d} (meV)	71	67	60
Δ_{tri} (meV)	65	58	41
Δ_{tri}/λ	1.83	1.73	1.37
E_1 (meV)	27.5	27.1	27.6
E_2 (meV)	72.8	67.1	54.8
E_3 (meV)	126.3	118.8	105.9
E_4 (meV)	134.5	126.5	110.0
E_5 (meV)	157.7	147.1	126.5

Table 5.1: Three possible sets of parameters (ζ_{3d}, Δ_{tri}), with the Raman peak at 126 meV assigned to different spin-orbit states. $E_1 \sim E_5$ are the excitation energies of these five states.

The determination of interaction parameters proceeds step by step. Initially, from the high-energy region of the RIXS spectra (*i.e.* excitation energy > 1 eV), we can establish values for $10Dq$, J_H, and γ. It's worth noting that these excitation peaks exhibit broad widths (typically several hundreds of meV), and the shape of the spectra is minimally affected by ζ_{3d} and Δ_{tri}, which only result in slight alterations of a few meV to the excitation energy. We attribute the peak at approximately 1 eV to a combination of crystal field excitation and spin transition from the high-spin $t_{2g}^5 e_g^2$ state to the low-spin $t_{2g}^6 e_g^1$ state. Utilizing this feature, we can estimate $10Dq \approx 3J_H - 10Dq \approx 1$ eV. Further refinement is achieved by considering the d-d excitations around 2 eV, resulting in refined values of $10Dq = 1.05$ eV, $J_H = 0.745$ eV, and $\gamma = 4.8$.

Having established the Coulomb interactions of the electrons, we revisit the low-energy spin-orbit excitons observed in Raman and RIXS measurements. The energy of these excitons is primarily determined by the spin-orbit coupling ζ_{3d} and the trigonal splitting Δ_{tri}, while the interaction parameters $10Dq$ and J_H contribute minor corrections, typically on the order of 1 meV to the excitation energy. However, determining these two parameters is complex due to the richness of fine structures and the limited energy resolution of the RIXS spectra. As previously proposed by theoretical calculations [118], the pseudospin-1/2 model predicts five excitation states labeled A_1 to A_5 in the presence of finite trigonal splitting. From Raman measurements, we observe two excitation peaks at 27 meV and 126 meV. The former corresponds to the A_1 excitation with the lowest energy (i.e., $|J_{eff} = 3/2, J^Z_{eff} = \pm 3/2\rangle$), in good agreement with INS measurements [126]. However, assigning the latter peak is non-trivial, as it could originate from any of the A_3, A_4, and A_5 states with $J_{eff} = 5/2$. In the RIXS spectra, a prominent feature is observed around 130 meV, but due to limited energy

resolution (35 meV), distinguishing these three fine structures is challenging. Consequently, Table 5.1 lists three possible sets of fitting parameters where the Raman feature at 126 meV is attributed to $J^Z_{eff} = \pm 1/2$ (A_3), $\pm 3/2$ (A_4), and $\pm 5/2$ (A_5), respectively. We can exclude the case where the Raman feature originates from the A_5 state, as the resulting excitation energies are too small and cannot explain the spectral weight in the RIXS spectra above 133 meV. In the remaining two assignments, the excitation energies differ by around 10 meV, and given the current energy resolution of the RIXS spectra, either assignment cannot be definitively excluded. Nevertheless, we tentatively attribute this Raman peak to the A_3 state with $|J^Z_{eff} = \pm 1/2\rangle$ by further considering the differences in RIXS intensity among these spin-orbit excitons. Model calculations reveal that the RIXS intensity of the A_4 state dominates over the other two states at Γ points (Fig. 5.15), and the excitation energy of A_4 aligns well with the energy where the RIXS spectra reach maximum intensity. This alignment in both energy and intensity lends further support to this assignment. However, it's possible that the observed Raman peak is a superposition of $A_3 \sim A_5$ states rather than the excitation to a single state. Consequently, we treat the parameter difference between these two assignments as uncertainty, yielding an overall estimation within the interval $(\zeta_{3d}, \Delta_{tri}) = (71 \pm 4, 65 \pm 8)$ meV. Remarkably, our parameters suggest a Δ_{tri}/λ ratio around 1.7~1.8 (note that $\lambda = 1/2\zeta_{3d}$, see Chapter 1), significantly larger than values suggested by previous works (around 1.36). This implies that the ground state of $Na_3Co_2SbO_6$ may be even more anisotropic than anticipated, and is farther from the spin liquid state in the phase diagram (see Fig. 5.2).

With the interaction parameters of d electrons determined, we can now evaluate the validity of the theoretical assumption of the $L_{eff} = 1$ effective model that t_{2g} states and e_g states are decoupled due to the large crystal field splitting $10Dq$, which serves as the foundation for deriving the electronic structure presented in Fig. 5.1. In the presence of finite Coulomb interaction and crystal field splitting, the excitation energies are renormalized and slightly deviate from theoretical predictions. Fig. 5.20(a) depicts the same Tanabe-Sugano diagram with realistic parameters. The most notable discrepancy is that, even in the absence of trigonal distortion, a splitting is observed for the $|J_{eff} = \pm 5/2\rangle$ states. Furthermore, when Δ_{tri} is positive, the excitation energy of the A_4 feature aligns closer to the A_3 feature than to the A_5 feature. However, we note that Fig. 5.1 can be restored by a single ion model when employing an unrealistic parameter set to mathematically satisfy the condition $J_H, 10Dq >> \lambda$. For example, setting $(10Dq, J_H) = (10, 100)$ eV eliminates the splitting of the $|J_{eff} = \pm 5/2\rangle$ states, yielding an electronic structure identical to the theoretical calculations from the effective model, as depicted in Fig. 5.20(b).

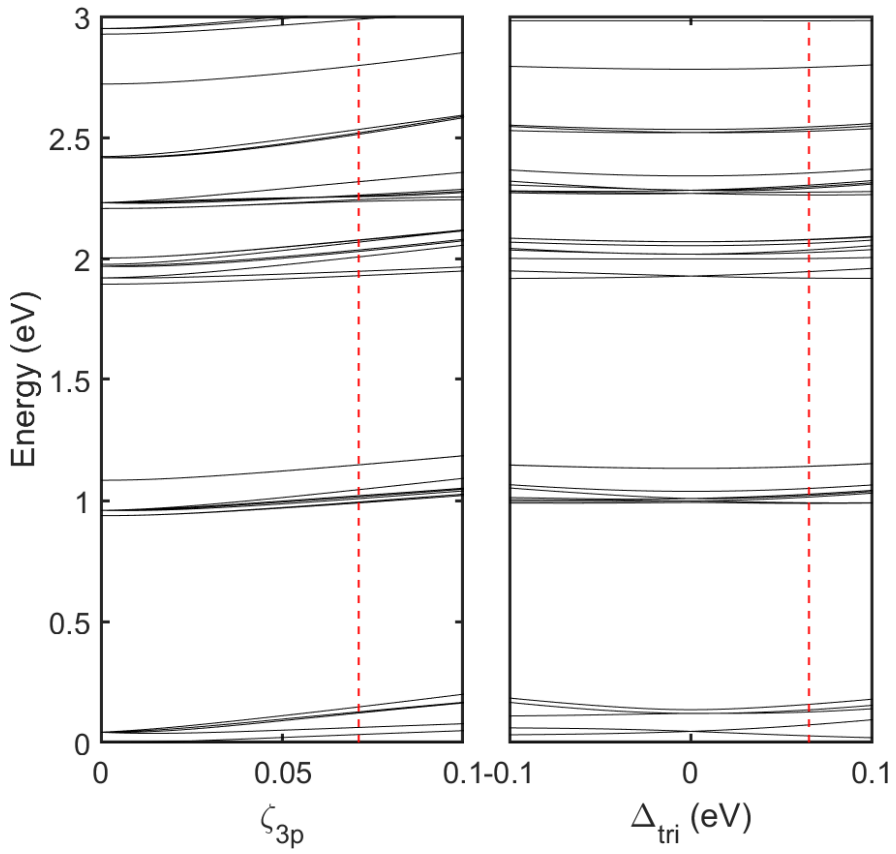

Figure 5.19: Tanabe-Sugano diagram as a function of ζ_{3d} and Δ_{tri}. The other parameters are fixed at $(10Dq, J_H, \gamma, \zeta_{3d}, \Delta_{tri}) = (1.05\text{ eV}, 0.745\text{ eV}, 4.8, 0.071\text{ eV}, 0.065\text{ eV})$.

Next, we proceed to determine the $p-d$ interaction parameters F^2_{pd}, G^1_{pd}, and G^3_{pd} by comparing the collected XAS spectra with calculations from the single-ion model. These three parameters influence both the intensity and the energy of the absorption peaks. Using the parameter set $(F^2_{pd}, G^1_{pd}, G^3_{pd}) = (5.2, 4.25, 3.3)$ eV, we can reproduce the energies of the absorption peaks, but achieving good agreement in intensity is challenging, likely due to the distortion caused by the self-absorption effect in the collected FY spectra. Finally, we can determine the spin-orbit coupling of the p electrons, ζ_{2p}, by the splitting between the L_2 and L_3 edges.

Finally, we can compare the interaction parameters of $Na_3Co_2SbO_6$ determined from Raman and RIXS data in this study with those from the previous literature, as shown in Table 5.2. We also present several results from other Co^{2+} compounds or *ab initio* calculations for reference. The most significant difference lies in the ratio Δ_{tri}/λ we determined (1.7~1.8),

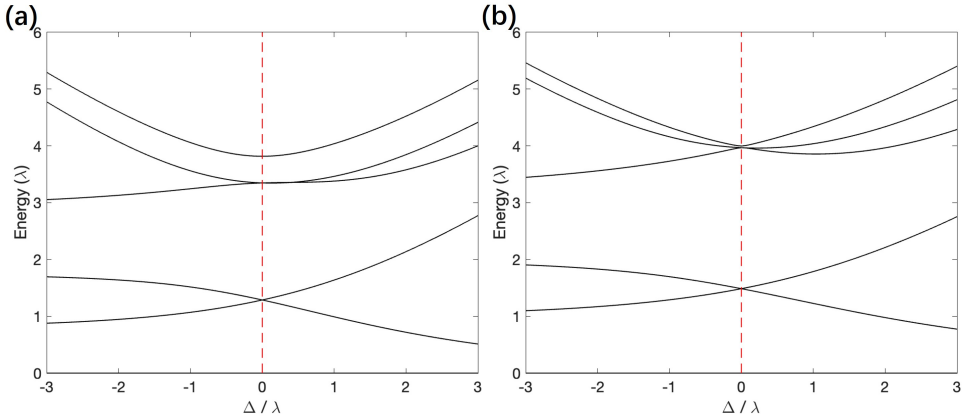

Figure 5.20: Comparison between single-ionic model calculations and theory. (a) single ionic model using the realistic parameters. A splitting of $J_{eff} = 5/2$ is observed even without the trigonal crystal field. (b)single ionic model calculation with $J_H = 100$ eV and $10Dq = 10$ eV in order to fulfill the $J_H, 10Dq >> \lambda, \Delta_{tri}$. The splitting in (a) disappears and the results resembles the theoretical calculations.

which is much larger than previously expected by theory (~1.36). This suggests that the ground state is even more anisotropic, and the position of $Na_3Co_2SbO_6$ in the phase diagram is farther from the spin liquid states (see Fig. 5.2). The value of J_H also aligns well with that of other Co^{2+} compounds. However, the octahedral crystal field splitting $10Dq$ is highly dependent on the chemical environment and varies significantly among different compounds.

5.5 Summary

In this chapter, we present the results of a comprehensive spectroscopic study on the $Na_3Co_2SbO_6$ single crystal, another potential host of Kitaev interaction. Unlike the extensively studied d^5 systems such as $RuCl_3$ or A_2IrO_3 (A = Na, Li), the Co^{2+} ion in this compound possesses a $3d^7$ configuration and a distinct exchange mechanism. While previous studies have primarily focused on the magnetic structure, revealing competing FM and AFM ordering through neutron scattering, experimental investigations into the electronic structure remain limited.

Compound Reference	$Na_3Co_2SbO_6$ Current work	*ab initio*, Co^{2+} Ref[132]	$Na_3Co_2SbO_6$ Ref[130]	$Na_3Co_2SbO_6$ thin film Ref[131]
$10Dq$ (eV)	1.08	-	1.1	0.9
J_H (eV)	0.745	1.04	-	0.7
γ	4.8	3.69	-	5
ζ_{3d} (eV)	0.071	0.066	0.066	-
Δ_{tri} (eV)	0.065	-	0.030-0.065	-
Δ_{tri}/λ	1.8	-	0.91-1.97	-
F_{2pd} (eV)	5.2	7.259	-	-
G_{1pd} (eV)	4.5	5.394	-	-
G_{3pd} (eV)	3.5	3.068	-	-
ζ_{2p}	9.745	9.748	9.75	-

Compound Reference	CoX_2,X = F, Cl, Br Ref[133]	Co_3O_4 Ref[134]	CoO Ref[135]
$10Dq$ (eV)	0.75-0.92	-0.55	1.05
J_H (eV)	0.89	0.83	0.747
γ	4.65	3.69	3.69
ζ_{3d} (eV)	0.066	0.046	0.066
Δ_{tri} (eV)	-	-	-
Δ_{tri}/λ	-	-	-
F_{2pd} (eV)	6.389	5.808	5.227
G_{1pd} (eV)	4.318	4.318	3.886
G_{3pd} (eV)	2.701	2.455	2.21
ζ_{2p}	9.748	9.748	9.748

Table 5.2: Comparison of interaction parameters in Co^{2+} ion. The data shown here corresponds to $2p^6 3d^7$ configuration. The parameters expressed by F^2_{dd} and F^4_{dd} is converted to equivalent J_H and γ by using Eqn.1.18.

In this study, we successfully grew high-quality $Na_3Co_2SbO_6$ single crystals in our laboratory. Raman spectroscopy revealed two of the five spin-orbit exciton features at 27 meV and 126 meV, with the remaining features possibly masked by phonons. Subsequently, we conducted a systematic RIXS study at the Co-L_3 absorption edge around 778 eV. We observed fine structures in the absorption spectra and identified various excitations, including magnetic excitations, spin-orbit excitons with different pseudospin states, a particle-hole continuum, spin state transitions and d-d excitations in the higher energy

range. By employing model calculations, we determined the interaction parameters of the d electrons as $(10Dq, J_H, \gamma, \zeta_{3d}, \Delta_{tri}) = (1.05\text{ eV}, 0.745\text{ eV}, 4.8, 0.071\text{ eV}, 0.065\text{ eV})$, providing insight into the electronic structures and interaction scheme of this Co^{2+} system.

By fixing the X-ray energy at 775.3 eV, we optimized the identification of low-energy excitations. Combining the RIXS spectra collected at the Γ point with Raman data enabled us to estimate the trigonal splitting within a narrow range. Notably, we found the ratio between Δ_{tri} and $\lambda = \zeta_{3d}/2$ to be around 1.7∼1.8, indicating a strong anisotropy in the ground state, which contrasts with theoretical predictions.

We also investigated the momentum dependence of the low-energy excitations. The QEP exhibited a local maximum around the Γ point in the paramagnetic phase, suggesting significant FM correlations in the material, consistent with previous neutron scattering results. Additionally, the RIXS spectra from $A_3 \sim A_5$ spin-orbit excitons displayed a clear dependence on the polarization of incoming and scattered X-ray photons. However, the current energy resolution limits a conclusive quantitative determination of any energy dispersion behavior of these excitons.

Finally, we evaluated the temperature dependence of magnetic fluctuations through the evolution of the QEP. Remarkably, we observed that the spectral weight of the QEP remained essentially unchanged from 15 K to 50 K, indicating robust FM correlations persisting far above the magnetic transition temperature T_N. This temperature dependence resembles that of $RuCl_3$, hinting at similar underlying mechanisms and underscoring the potential of $Na_3Co_2SbO_6$ as a candidate for realizing Kitaev spin liquid physics.

6 Conclusions

We conducted resonant inelastic X-ray scattering measurements on two candidate materials for Kitaev spin liquids, $RuCl_3$ and $Na_3Co_2SbO_6$, to investigate their electronic and spin structures and develop an integrated interaction scheme across a wide energy range. The qualitative and quantitative results obtained serve as a solid foundation for future research on these materials.

The Ru-L_3 RIXS study on $RuCl_3$ single crystals enabled us to quantify the electronic and spin Hamiltonian of this material. The RIXS spectra comprised a magnetic quasielastic peak, single- and multi-excitons of spin-orbit excitations, d-d excitations, and a charge transfer continuum emerging from 1 eV. These spectra could be well reproduced by intra-atomic interaction parameters $(10Dq, J_H, \lambda, \gamma) = (2.44\ \text{eV}, 0.34\ \text{eV}, 0.15\ \text{eV}, 5)$. The large photon energy allowed access to a broad range in the Brillouin zone, facilitating the measurement of momentum-dependent magnetic correlations via the intensity of the quasielastic peak. Above the magnetic ordering temperature of 7 K, the intensity of the quasielastic peak exhibited a local maximum at the Γ point instead of the antiferromagnetic ordering wavevector, suggesting the quick disappearance of the antiferromagnetic order and highlighting the importance of ferromagnetic correlation. Combined with theoretical calculations, the magnetic interactions were determined to be $(K, J, \Gamma, \Gamma', J_3) = (-5, -3, 2.5, 0.1, 0.75)$ meV. Additionally, the temperature dependence of the quasielastic peak intensity supported the fragile nature of the zigzag order, which was only slightly favored in energy compared to other states.

The two-dimensional nature of $RuCl_3$ allowed us to study the thickness-dependent physics of its electronic structure when approaching the low-dimensional limit. We overcame several technical challenges related to measuring samples with extremely small volumes and conducted Ru-L_3 RIXS studies on $RuCl_3$ nanolayers with thicknesses down to 3.5 nm. With decreasing thickness, we observed a red-shift and broadening of electronic transitions from the Ru t_{2g} orbitals in the crystal-field ground-state into excited states in the

e_g manifold, whereas intra-atomic spin-orbit excitations are thickness independent. Based on ionic model calculations and comparison to prior surface-sensitive studies, we attribute this trend to an altered ligand field near the surface, which controls the ratio of Kitaev and Heisenberg interactions and hence the magnetic ground state. Our results indicate that RIXS experiments on a variety of 2D materials and VdW heterostructures – and the resulting wellspring of information on electronic interactions – are within reach of current and future instrumentation.

$Na_3Co_2SbO_6$ is another potential Kitaev spin liquid candidate with a $3d^7$ configuration, and its interaction mechanism was recently proposed. RIXS measurements on a $Na_3Co_2SbO_6$ single crystal at the Co-L_3 edge around 778 eV revealed spectral features originating from various excitations, including the magnetic quasielastic peak, spin-orbit exciton, d-d excitation, and spin state transitions. Assisted by model calculations, the intra-atomic interaction parameters were determined to be $(10Dq, J_H, \gamma, \zeta_{3d}, \Delta_{tri}) = (1.05\text{ eV}, 0.745\text{ eV}, 4.8, 0.071\text{ eV}, 0.065\text{ eV})$. We confirmed the pseudospin scenario and observed fine structures originating from spin-orbit excitons, whose intensity exhibited a clear dependence on geometric configuration. Notably, the trigonal splitting was much stronger than previously proposed, suggesting an even more anisotropic ground state wavefunction and a position farther from the spin liquid phase in the magnetic phase diagram. The temperature and momentum dependence of the magnetic quasielastic peak resembled that observed in $RuCl_3$, possibly indicating a similar interaction mechanism between these two materials.

The RIXS studies presented in this Thesis demonstrated the capability of RIXS to investigate quantum materials hosting frustrated interactions and shed light on the intriguing nature of the two candidate systems for the Kitaev spin liquid phase. Additionally, RIXS measurements on $RuCl_3$ nanolayers not only provided new experimental evidence of a structural distortion when approaching the 2D limit but also established an integrated technical methodology for studying two-dimensional flakes and heterostructures. We are confident that this RIXS methodology can be applied to the vast family of 2D materials and uncover new physics in low-dimensional systems in the future.

List of Figures

List of Tables

Bibliography

[1] A. Kotani, S. Shin. "Resonant inelastic x-ray scattering spectra for electrons in solids". In: *Rev. Mod. Phys.* 73 (1 Feb. 2001), pp. 203–246. DOI: 10.1103/RevModPhys.73.203. URL: https://link.aps.org/doi/10.1103/RevModPhys.73.203.

[2] L. J. P. Ament, M. van Veenendaal, T. P. Devereaux, J. P. Hill, J. van den Brink. "Resonant inelastic x-ray scattering studies of elementary excitations". In: *Rev. Mod. Phys.* 83 (2 June 2011), pp. 705–767. DOI: 10.1103/RevModPhys.83.705. URL: https://link.aps.org/doi/10.1103/RevModPhys.83.705.

[3] M. Minola, D. Di Castro, L. Braicovich, N. B. Brookes, D. Innocenti, M. Moretti Sala, A. Tebano, G. Balestrino, G. Ghiringhelli. "Magnetic and ligand field properties of copper at the interfaces of $(CaCuO_2)_n/(SrTiO_3)_n$ superlattices". In: *Phys. Rev. B* 85 (23 June 2012), p. 235138. DOI: 10.1103/PhysRevB.85.235138. URL: https://link.aps.org/doi/10.1103/PhysRevB.85.235138.

[4] H. Suzuki, H. Gretarsson, H. Ishikawa, K. Ueda, Z. Yang, H. Liu, H. Kim, D. Kukusta, A. Yaresko, M. Minola, J. A. Sears, S. Francoual, H.-C. Wille, J. Nuss, H. Takagi, B. J. Kim, G. Khaliullin, H. Yavaş, B. Keimer. "Spin waves and spin-state transitions in a ruthenate high-temperature antiferromagnet". In: *Nature Materials* 18.6 (June 2019), pp. 563–567. ISSN: 1476-4660. DOI: 10.1038/s41563-019-0327-2. URL: https://doi.org/10.1038/s41563-019-0327-2.

[5] Y. Lu, D. Betto, K. Fürsich, H. Suzuki, H.-H. Kim, G. Cristiani, G. Logvenov, N. B. Brookes, E. Benckiser, M. W. Haverkort, G. Khaliullin, M. Le Tacon, M. Minola, B. Keimer. "Site-Selective Probe of Magnetic Excitations in Rare-Earth Nickelates Using Resonant Inelastic X-ray Scattering". In: *Phys. Rev. X* 8 (3 July 2018), p. 031014. DOI: 10.1103/PhysRevX.8.031014. URL: https://link.aps.org/doi/10.1103/PhysRevX.8.031014.

[6] J. Pelliciari, S. Lee, K. Gilmore, J. Li, Y. Gu, A. Barbour, I. Jarrige, C. H. Ahn, F. J. Walker, V. Bisogni. "Tuning spin excitations in magnetic films by confinement". In: *Nature Materials* 20.2 (Feb. 2021), pp. 188–193. ISSN: 1476-4660. DOI: 10.1038/s41563-020-00878-0. URL: https://doi.org/10.1038/s41563-020-00878-0.

[7] C. J. Sparks. "Inelastic Resonance Emission of X Rays: Anomalous Scattering Associated with Anomalous Dispersion". In: *Phys. Rev. Lett.* 33 (5 July 1974), pp. 262–265. DOI: 10.1103/PhysRevLett.33.262. URL: https://link.aps.org/doi/10.1103/PhysRevLett.33.262.

[8] S. Grenier, J. P. Hill, V. Kiryukhin, W. Ku, Y.-J. Kim, K. J. Thomas, S.-W. Cheong, Y. Tokura, Y. Tomioka, D. Casa, T. Gog. "$d-d$ Excitations in Manganites Probed by Resonant Inelastic X-Ray Scattering". In: *Phys. Rev. Lett.* 94 (4 Feb. 2005), p. 047203. DOI: 10.1103/PhysRevLett.94.047203. URL: https://link.aps.org/doi/10.1103/PhysRevLett.94.047203.

[9] S. Huotari, T. Pylkkänen, G. Vankó, R. Verbeni, P. Glatzel, G. Monaco. "Crystal-field excitations in NiO studied with hard x-ray resonant inelastic x-ray scattering at the Ni K edge". In: *Phys. Rev. B* 78 (4 July 2008), p. 041102. DOI: 10.1103/PhysRevB.78.041102. URL: https://link.aps.org/doi/10.1103/PhysRevB.78.041102.

[10] P. Abbamonte, C. A. Burns, E. D. Isaacs, P. M. Platzman, L. L. Miller, S. W. Cheong, M. V. Klein. "Resonant Inelastic X-Ray Scattering from Valence Excitations in Insulating Copper Oxides". In: *Phys. Rev. Lett.* 83 (4 July 1999), pp. 860–863. DOI: 10.1103/PhysRevLett.83.860. URL: https://link.aps.org/doi/10.1103/PhysRevLett.83.860.

[11] Y. J. Kim, J. P. Hill, C. A. Burns, S. Wakimoto, R. J. Birgeneau, D. Casa, T. Gog, C. T. Venkataraman. "Resonant Inelastic X-Ray Scattering Study of Charge Excitations in La_2CuO_4". In: *Phys. Rev. Lett.* 89 (17 Oct. 2002), p. 177003. DOI: 10.1103/PhysRevLett.89.177003. URL: https://link.aps.org/doi/10.1103/PhysRevLett.89.177003.

[12] L. Braicovich, J. van den Brink, V. Bisogni, M. M. Sala, L. J. P. Ament, N. B. Brookes, G. M. De Luca, M. Salluzzo, T. Schmitt, V. N. Strocov, G. Ghiringhelli. "Magnetic Excitations and Phase Separation in the Underdoped $La_{2-x}Sr_xCuO_4$ Superconductor Measured by Resonant Inelastic X-Ray Scattering". In: *Phys. Rev. Lett.* 104 (7 Feb. 2010), p. 077002. DOI: 10.1103/PhysRevLett.104.077002. URL: https://link.aps.org/doi/10.1103/PhysRevLett.104.077002.

[13] L. J. P. Ament, G. Ghiringhelli, M. M. Sala, L. Braicovich, J. van den Brink. "Theoretical Demonstration of How the Dispersion of Magnetic Excitations in Cuprate Compounds can be Determined Using Resonant Inelastic X-Ray Scattering". In: *Phys. Rev. Lett.* 103 (11 Sept. 2009), p. 117003. DOI: 10.1103/PhysRevLett.103.117003. URL: https://link.aps.org/doi/10.1103/PhysRevLett.103.117003.

[14] B. J. Kim, G. Khaliullin. "Resonant inelastic x-ray scattering operators for t_{2g} orbital systems". In: *Phys. Rev. B* 96 (8 Aug. 2017), p. 085108. DOI: 10.1103/PhysRevB.96.085108. URL: https://link.aps.org/doi/10.1103/PhysRevB.96.085108.

[15] L. B. N. L. C. for X-Ray Optics. *X-ray interactions with matter*. URL: http://henke.lbl.gov/optical_constants.

[16] Y. Lu, M. Höppner, O. Gunnarsson, M. W. Haverkort. "Efficient real-frequency solver for dynamical mean-field theory". In: *Phys. Rev. B* 90 (8 Aug. 2014), p. 085102. DOI: 10.1103/PhysRevB.90.085102. URL: https://link.aps.org/doi/10.1103/PhysRevB.90.085102.

[17] M. W. Haverkort, G. Sangiovanni, P. Hansmann, A. Toschi, Y. Lu, S. Macke. "Bands, resonances, edge singularities and excitons in core level spectroscopy investigated within the dynamical mean-field theory". In: *EPL (Europhysics Letters)* 108.5 (Dec. 2014), p. 57004. DOI: 10.1209/0295-5075/108/57004. URL: https://doi.org/10.1209/0295-5075/108/57004.

[18] M. W. Haverkort, M. Zwierzycki, O. K. Andersen. "Multiplet ligand-field theory using Wannier orbitals". In: *Phys. Rev. B* 85 (16 Apr. 2012), p. 165113. DOI: 10.1103/PhysRevB.85.165113. URL: https://link.aps.org/doi/10.1103/PhysRevB.85.165113.

[19] N. Ashcroft, N. Mermin. *Solid State Physics*. HRW international editions. Holt, Rinehart and Winston, 1976. ISBN: 9780030839931. URL: https://books.google.de/books?id=oXIfAQAAMAAJ.

[20] S. Sugano. *Multiplets of Transition-Metal Ions in Crystals*. Elsevier Science, 2012. ISBN: 9780323154796. URL: https://books.google.de/books?id=8SbsjFx1MbwC.

[21] Y. Tanabe, S. Sugano. "On the Absorption Spectra of Complex Ions II". In: *Journal of the Physical Society of Japan* 9.5 (1954), pp. 766–779. DOI: 10.1143/JPSJ.9.766. eprint: https://doi.org/10.1143/JPSJ.9.766. URL: https://doi.org/10.1143/JPSJ.9.766.

[22] D. I. Khomskii. *Transition Metal Compounds*. Cambridge University Press, 2014.

[23] A. Abragam, B. Bleaney. *Electron Paramagnetic Resonance of Transition Ions*. International series of monographs on physics. Clarendon P., 1970. ISBN: 9780199651528. URL: https://books.google.de/books?id=SSD7AAAAQBAJ.

[24] A. Georges, L. d. Medici, J. Mravlje. "Strong Correlations from Hund's Coupling". In: *Annual Review of Condensed Matter Physics* 4.1 (2013), pp. 137–178. DOI: 10.1146/annurev-conmatphys-020911-125045. eprint: https://doi.org/10.1146/annurev-conmatphys-020911-125045. URL: https://doi.org/10.1146/annurev-conmatphys-020911-125045.

[25] M. Minola, G. Dellea, H. Gretarsson, Y. Y. Peng, Y. Lu, J. Porras, T. Loew, F. Yakhou, N. B. Brookes, Y. B. Huang, J. Pelliciari, T. Schmitt, G. Ghiringhelli, B. Keimer, L. Braicovich, M. Le Tacon. "Collective Nature of Spin Excitations in Superconducting Cuprates Probed by Resonant Inelastic X-Ray Scattering". In: *Phys. Rev. Lett.* 114 (21 May 2015), p. 217003. DOI: 10.1103/PhysRevLett.114.217003. URL: https://link.aps.org/doi/10.1103/PhysRevLett.114.217003.

[26] J. Viefhaus, F. Scholz, S. Deinert, L. Glaser, M. Ilchen, J. Seltmann, P. Walter, F. Siewert. "The Variable Polarization XUV Beamline P04 at PETRA III: Optics, mechanics and their performance". In: *Nuclear Instruments and Methods in Physics Research Section A: Accelerators, Spectrometers, Detectors and Associated Equipment* 710 (2013). The 4th international workshop on Metrology for X-ray Optics, Mirror Design, and Fabrication, pp. 151–154. ISSN: 0168-9002. DOI: https://doi.org/10.1016/j.nima.2012.10.110. URL: https://www.sciencedirect.com/science/article/pii/S0168900212012831.

[27] K.-J. Zhou, A. Walters, M. Garcia-Fernandez, T. Rice, M. Hand, A. Nag, J. Li, S. Agrestini, P. Garland, H. Wang, S. Alcock, I. Nistea, B. Nutter, N. Rubies, G. Knap, M. Gaughran, F. Yuan, P. Chang, J. Emmins, G. Howell. "I21: an advanced high-resolution resonant inelastic X-ray scattering beamline at Diamond Light Source". In: *Journal of Synchrotron Radiation* 29.2 (Mar. 2022), pp. 563–580. DOI: 10.1107/S1600577522000601. URL: https://doi.org/10.1107/S1600577522000601.

[28] H. Gretarsson, D. Ketenoglu, M. Harder, S. Mayer, F.-U. Dill, M. Spiwek, H. Schulte-Schrepping, M. Tischer, H.-C. Wille, B. Keimer, H. Yavaş. "IRIXS: a resonant inelastic X-ray scattering instrument dedicated to X-rays in the intermediate energy range". In: *Journal of Synchrotron Radiation* 27.2 (Mar. 2020), pp. 538–544. DOI: 10.1107/S1600577519017119. URL: https://doi.org/10.1107/S1600577519017119.

[29] J. Bertinshaw, S. Mayer, F.-U. Dill, H. Suzuki, O. Leupold, A. Jafari, I. Sergueev, M. Spiwek, A. Said, E. Kasman, X. Huang, B. Keimer, H. Gretarsson. "IRIXS Spectrograph: an ultra high-resolution spectrometer for tender RIXS". In: *Journal of Synchrotron Radiation* 28.4 (July 2021), pp. 1184–1192. DOI: 10.1107/S1600577521003805. URL: https://doi.org/10.1107/S1600577521003805.

[30] H.-C. Wille, H. Franz, R. Röhlsberger, W. A. Caliebe, F.-U. Dill. "Nuclear resonant scattering at PETRA III : Brillant opportunities for nano – and extreme condition science". In: *Journal of Physics: Conference Series* 217.1 (Mar. 2010), p. 012008. DOI: 10.1088/1742-6596/217/1/012008. URL: https://dx.doi.org/10.1088/1742-6596/217/1/012008.

[31] D. Attwood. *Soft X-Rays and Extreme Ultraviolet Radiation: Principles and Applications*. Cambridge University Press, 1999.

[32] Y. Shvyd'ko. *X-Ray Optics: High-Energy-Resolution Applications*. Springer Series in Optical Sciences. Springer Berlin Heidelberg, 2013. ISBN: 9783540408901. URL: https://books.google.de/books?id=4BrqCAAAQBAJ.

[33] T. Gog, D. M. Casa, J. Knopp, J. Kim, M. H. Upton, R. Krakora, A. Jaski, A. Said, H. Yavaş, H. Gretarsson, X. R. Huang. "Performance of quartz- and sapphire-based double-crystal high-resolution (~10 meV) RIXS monochromators under varying power loads". In: *Journal of Synchrotron Radiation* 25.4 (July 2018), pp. 1030–1035. DOI: 10.1107/S1600577518005945. URL: https://doi.org/10.1107/S1600577518005945.

[34] *Webpage of I21 beamline in Diamond Light Source*. URL: https://www.diamond.ac.uk/Instruments/Magnetic-Materials/I21.html.

[35] *Webpage of ID32 beamline in European Synchrotron Radiation Facility*. URL: https://www.esrf.fr/ID32.

[36] *Silicon drift detectors (SDD) principle of operation*. URL: https://www.rayspec.co.uk/x-ray-detectors/silicon-drift-detectors/silicon-drift-detectors-sdd-principle-operation/.

[37] H. Gretarsson, H. Suzuki, H. Kim, K. Ueda, M. Krautloher, B. J. Kim, H. Yavaş, G. Khaliullin, B. Keimer. "Observation of spin-orbit excitations and Hund's multiplets in Ca_2RuO_4". In: *Phys. Rev. B* 100 (4 July 2019), p. 045123. DOI: 10.1103/PhysRevB.100.045123. URL: https://link.aps.org/doi/10.1103/PhysRevB.100.045123.

[38] J. Bertinshaw, M. Krautloher, H. Suzuki, H. Takahashi, A. Ivanov, H. Yavaş, B. J. Kim, H. Gretarsson, B. Keimer. "Spin and charge excitations in the correlated multiband metal $Ca_3Ru_2O_7$". In: *Phys. Rev. B* 103 (8 Feb. 2021), p. 085108. DOI: 10.1103/PhysRevB.103.085108. URL: https://link.aps.org/doi/10.1103/PhysRevB.103.085108.

[39] H. Takahashi, H. Suzuki, J. Bertinshaw, S. Bette, C. Mühle, J. Nuss, R. Dinnebier, A. Yaresko, G. Khaliullin, H. Gretarsson, T. Takayama, H. Takagi, B. Keimer. "Nonmagnetic $J = 0$ State and Spin-Orbit Excitations in K_2RuCl_6". In: *Phys. Rev. Lett.* 127 (22 Nov. 2021), p. 227201. DOI: 10.1103/PhysRevLett.127.227201. URL: https://link.aps.org/doi/10.1103/PhysRevLett.127.227201.

[40] H. Suzuki, H. Liu, J. Bertinshaw, K. Ueda, H. Kim, S. Laha, D. Weber, Z. Yang, L. Wang, H. Takahashi, K. Fürsich, M. Minola, B. V. Lotsch, B. J. Kim, H. Yavaş, M. Daghofer, J. Chaloupka, G. Khaliullin, H. Gretarsson, B. Keimer. "Proximate ferromagnetic state in the Kitaev model material α-$RuCl_3$". In: *Nature Communications* 12.1 (July 2021), p. 4512. ISSN: 2041-1723. DOI: 10.1038/s41467-021-24722-4. URL: https://doi.org/10.1038/s41467-021-24722-4.

[41] Z. Yang, L. Wang, D. Zhao, M. Luo, S. Laha, A. Güth, T. Taniguchi, K. Watanabe, B. V. Lotsch, J. H. Smet, M. Minola, H. Gretarsson, B. Keimer. "Resonant inelastic x-ray scattering from electronic excitations in $\alpha-RuCl_3$ nanolayers". In: *Phys. Rev. B* 108 (4 July 2023), p. L041406. DOI: 10.1103/PhysRevB.108.L041406. URL: https://link.aps.org/doi/10.1103/PhysRevB.108.L041406.

[42] H. Suzuki, L. Wang, J. Bertinshaw, H. U. R. Strand, S. Käser, M. Krautloher, Z. Yang, N. Wentzell, O. Parcollet, F. Jerzembeck, N. Kikugawa, A. P. Mackenzie, A. Georges, P. Hansmann, H. Gretarsson, B. Keimer. "Distinct spin and orbital dynamics in Sr2RuO4". In: *Nature Communications* 14.1 (Nov. 2023), p. 7042. ISSN: 2041-1723. DOI: 10.1038/s41467-023-42804-3. URL: https://doi.org/10.1038/s41467-023-42804-3.

[43] W. Tian, C. Svoboda, M. Ochi, M. Matsuda, H. B. Cao, J.-G. Cheng, B. C. Sales, D. G. Mandrus, R. Arita, N. Trivedi, J.-Q. Yan. "High antiferromagnetic transition temperature of the honeycomb compound $SrRu_2O_6$". In: *Phys. Rev. B* 92 (10 Sept. 2015), p. 100404. DOI: 10.1103/PhysRevB.92.100404. URL: https://link.aps.org/doi/10.1103/PhysRevB.92.100404.

[44] C. I. Hiley, D. O. Scanlon, A. A. Sokol, S. M. Woodley, A. M. Ganose, S. Sangiao, J. M. De Teresa, P. Manuel, D. D. Khalyavin, M. Walker, M. R. Lees, R. I. Walton. "Antiferromagnetism at $T > 500$ K in the layered hexagonal ruthenate $SrRu_2O_6$". In: *Phys. Rev. B* 92 (10 Sept. 2015), p. 104413. DOI: 10.1103/PhysRevB.92.104413. URL: https://link.aps.org/doi/10.1103/PhysRevB.92.104413.

[45] A. Marino, M. Sundermann, D. S. Christovam, A. Amorese, C.-F. Chang, P. Dolmantas, A. H. Said, H. Gretarsson, B. Keimer, M. W. Haverkort, A. V. Andreev, L. Havela, P. Thalmeier, L. H. Tjeng, A. Severing. "Singlet magnetism in intermetallic UGa_2 unveiled by inelastic x-ray scattering". In: *Phys. Rev. B* 108 (4 July 2023), p. 045142. DOI: 10.1103/PhysRevB.108.045142. URL: https://link.aps.org/doi/10.1103/PhysRevB.108.045142.

[46] V. Zimmermann, A. K. Yogi, D. Wong, C. Schulz, M. Bartkowiak, K. Habicht, L. Wang, M. Isobe, M. Minola, G. Khaliullin, B. Keimer, M. Hepting. "Coherent propagation of spin-orbit excitons in a correlated metal". In: *npj Quantum Materials* 8.1 (Oct. 2023), p. 53. ISSN: 2397-4648. DOI: 10.1038/s41535-023-00585-4. URL: https://doi.org/10.1038/s41535-023-00585-4.

[47] *ASTIX-c mirror*. URL: https://www.axo-dresden.de/en/products/x-ray-optics.

[48] L. Balents. "Spin liquids in frustrated magnets". In: *Nature* 464.7286 (Mar. 2010), pp. 199–208. ISSN: 1476-4687. DOI: 10.1038/nature08917. URL: https://doi.org/10.1038/nature08917.

[49] L. Savary, L. Balents. "Quantum spin liquids: a review". In: *Reports on Progress in Physics* 80.1 (Nov. 2016), p. 016502. DOI: 10.1088/0034-4885/80/1/016502. URL: https://dx.doi.org/10.1088/0034-4885/80/1/016502.

[50] A. Kitaev. "Anyons in an exactly solved model and beyond". In: *Annals of Physics* 321.1 (2006). January Special Issue, pp. 2–111. ISSN: 0003-4916. DOI: https://doi.org/10.1016/j.aop.2005.10.005. URL: https://www.sciencedirect.com/science/article/pii/S0003491605002381.

[51] G. Jackeli, G. Khaliullin. "Mott Insulators in the Strong Spin-Orbit Coupling Limit: From Heisenberg to a Quantum Compass and Kitaev Models". In: *Phys. Rev. Lett.* 102 (1 Jan. 2009), p. 017205. DOI: 10.1103/PhysRevLett.102.017205. URL: https://link.aps.org/doi/10.1103/PhysRevLett.102.017205.

[52] K. W. Plumb, J. P. Clancy, L. J. Sandilands, V. V. Shankar, Y. F. Hu, K. S. Burch, H.-Y. Kee, Y.-J. Kim. "α – $RuCl_3$: A spin-orbit assisted Mott insulator on a honeycomb lattice". In: *Phys. Rev. B* 90 (4 July 2014), p. 041112. DOI: 10.1103/PhysRevB.90.041112. URL: https://link.aps.org/doi/10.1103/PhysRevB.90.041112.

[53] J. G. Rau, E. K.-H. Lee, H.-Y. Kee. "Spin-Orbit Physics Giving Rise to Novel Phases in Correlated Systems: Iridates and Related Materials". In: *Annual Review of Condensed Matter Physics* 7.1 (2016), pp. 195–221. DOI: 10.1146/annurev-conmatphys-031115-011319. eprint: https://doi.org/10.1146/annurev-conmatphys-031115-011319. URL: https://doi.org/10.1146/annurev-conmatphys-031115-011319.

[54] H. Takagi, T. Takayama, G. Jackeli, G. Khaliullin, S. E. Nagler. "Concept and realization of Kitaev quantum spin liquids". In: *Nature Reviews Physics* 1.4 (Apr. 2019), pp. 264–280. ISSN: 2522-5820. DOI: 10.1038/s42254-019-0038-2. URL: https://doi.org/10.1038/s42254-019-0038-2.

[55] A. Banerjee, C. A. Bridges, J.-Q. Yan, A. A. Aczel, L. Li, M. B. Stone, G. E. Granroth, M. D. Lumsden, Y. Yiu, J. Knolle, S. Bhattacharjee, D. L. Kovrizhin, R. Moessner, D. A. Tennant, D. G. Mandrus, S. E. Nagler. "Proximate Kitaev quantum spin liquid behaviour in a honeycomb magnet". In: *Nature Materials* 15.7 (July 2016), pp. 733–740. ISSN: 1476-4660. DOI: 10.1038/nmat4604. URL: https://doi.org/10.1038/nmat4604.

[56] H. B. Cao, A. Banerjee, J.-Q. Yan, C. A. Bridges, M. D. Lumsden, D. G. Mandrus, D. A. Tennant, B. C. Chakoumakos, S. E. Nagler. "Low-temperature crystal and magnetic structure of α – $RuCl_3$". In: *Phys. Rev. B* 93 (13 Apr. 2016), p. 134423. DOI: 10.1103/PhysRevB.93.134423. URL: https://link.aps.org/doi/10.1103/PhysRevB.93.134423.

[57] J. A. Sears, L. E. Chern, S. Kim, P. J. Bereciartua, S. Francoual, Y. B. Kim, Y.-J. Kim. "Ferromagnetic Kitaev interaction and the origin of large magnetic anisotropy in α-RuCl3". In: *Nature Physics* 16.8 (Aug. 2020), pp. 837–840. ISSN: 1745-2481. DOI: 10.1038/s41567-020-0874-0. URL: https://doi.org/10.1038/s41567-020-0874-0.

[58] J. A. Sears, M. Songvilay, K. W. Plumb, J. P. Clancy, Y. Qiu, Y. Zhao, D. Parshall, Y.-J. Kim. "Magnetic order in $\alpha - RuCl_3$: A honeycomb-lattice quantum magnet with strong spin-orbit coupling". In: *Phys. Rev. B* 91 (14 Apr. 2015), p. 144420. DOI: 10.1103/PhysRevB.91.144420. URL: https://link.aps.org/doi/10.1103/PhysRevB.91.144420.

[59] Y. Kobayashi, T. Okada, K. Asai, M. Katada, H. Sano, F. Ambe. "Moessbauer spectroscopy and magnetization studies of α- and β-ruthenium trichloride". In: *Inorganic Chemistry* 31.22 (Oct. 1992), pp. 4570–4574. ISSN: 0020-1669. DOI: 10.1021/ic00048a025. URL: https://doi.org/10.1021/ic00048a025.

[60] R. D. Johnson, S. C. Williams, A. A. Haghighirad, J. Singleton, V. Zapf, P. Manuel, I. I. Mazin, Y. Li, H. O. Jeschke, R. Valentí, R. Coldea. "Monoclinic crystal structure of $\alpha - RuCl_3$ and the zigzag antiferromagnetic ground state". In: *Phys. Rev. B* 92 (23 Dec. 2015), p. 235119. DOI: 10.1103/PhysRevB.92.235119. URL: https://link.aps.org/doi/10.1103/PhysRevB.92.235119.

[61] M. Majumder, M. Schmidt, H. Rosner, A. A. Tsirlin, H. Yasuoka, M. Baenitz. "Anisotropic $Ru^{3+}4d^5$ magnetism in the $\alpha - RuCl_3$ honeycomb system: Susceptibility, specific heat, and zero-field NMR". In: *Phys. Rev. B* 91 (18 May 2015), p. 180401. DOI: 10.1103/PhysRevB.91.180401. URL: https://link.aps.org/doi/10.1103/PhysRevB.91.180401.

[62] L. J. Sandilands, Y. Tian, K. W. Plumb, Y.-J. Kim, K. S. Burch. "Scattering Continuum and Possible Fractionalized Excitations in α–$RuCl_3$". In: *Phys. Rev. Lett.* 114 (14 Apr. 2015), p. 147201. DOI: 10.1103/PhysRevLett.114.147201. URL: https://link.aps.org/doi/10.1103/PhysRevLett.114.147201.

[63] T. T. Mai, A. McCreary, P. Lampen-Kelley, N. Butch, J. R. Simpson, J.-Q. Yan, S. E. Nagler, D. Mandrus, A. R. H. Walker, R. V. Aguilar. "Polarization-resolved Raman spectroscopy of α–$RuCl_3$ and evidence of room-temperature two-dimensional magnetic scattering". In: *Phys. Rev. B* 100 (13 Oct. 2019), p. 134419. DOI: 10.1103/PhysRevB.100.134419. URL: https://link.aps.org/doi/10.1103/PhysRevB.100.134419.

[64] A. Glamazda, P. Lemmens, S.-H. Do, Y. S. Kwon, K.-Y. Choi. "Relation between Kitaev magnetism and structure in $\alpha - RuCl_3$". In: *Phys. Rev. B* 95 (17 May 2017), p. 174429. DOI: 10.1103/PhysRevB.95.174429. URL: https://link.aps.org/doi/10.1103/PhysRevB.95.174429.

[65] M. Cardona, G. Guntherodt. *Light Scattering in Solids VI*. Springer, 2014. ISBN: 9783662310939. URL: https://books.google.de/books?id=JAgHswEACAAJ.

[66] Y. J. Um, J. T. Park, B. H. Min, Y. J. Song, Y. S. Kwon, B. Keimer, M. Le Tacon. "Raman scattering study of the lattice dynamics of superconducting LiFeAs". In: *Phys. Rev. B* 85 (1 Jan. 2012), p. 012501. DOI: 10.1103/PhysRevB.85.012501. URL: https://link.aps.org/doi/10.1103/PhysRevB.85.012501.

[67] A. Banerjee, J. Yan, J. Knolle, C. A. Bridges, M. B. Stone, M. D. Lumsden, D. G. Mandrus, D. A. Tennant, R. Moessner, S. E. Nagler. "Neutron scattering in the proximate quantum spin liquid α-RuCl₃". In: *Science* 356.6342 (2017), pp. 1055–1059. DOI: 10.1126/science.aah6015. eprint: https://www.science.org/doi/pdf/10.1126/science.aah6015. URL: https://www.science.org/doi/abs/10.1126/science.aah6015.

[68] C. Balz, P. Lampen-Kelley, A. Banerjee, J. Yan, Z. Lu, X. Hu, S. M. Yadav, Y. Takano, Y. Liu, D. A. Tennant, M. D. Lumsden, D. Mandrus, S. E. Nagler. "Finite field regime for a quantum spin liquid in α-$RuCl_3$". In: *Phys. Rev. B* 100 (6 Aug. 2019), p. 060405. DOI: 10.1103/PhysRevB.100.060405. URL: https://link.aps.org/doi/10.1103/PhysRevB.100.060405.

[69] Y. Kasahara, T. Ohnishi, Y. Mizukami, O. Tanaka, S. Ma, K. Sugii, N. Kurita, H. Tanaka, J. Nasu, Y. Motome, T. Shibauchi, Y. Matsuda. "Majorana quantization and half-integer thermal quantum Hall effect in a Kitaev spin liquid". In: *Nature* 559.7713 (July 2018), pp. 227–231. ISSN: 1476-4687. DOI: 10.1038/s41586-018-0274-0. URL: https://doi.org/10.1038/s41586-018-0274-0.

[70] I. A. Leahy, C. A. Pocs, P. E. Siegfried, D. Graf, S.-H. Do, K.-Y. Choi, B. Normand, M. Lee. "Anomalous Thermal Conductivity and Magnetic Torque Response in the Honeycomb Magnet α-$RuCl_3$". In: *Phys. Rev. Lett.* 118 (18 May 2017), p. 187203. DOI: 10.1103/PhysRevLett.118.187203. URL: https://link.aps.org/doi/10.1103/PhysRevLett.118.187203.

[71] T. Yokoi, S. Ma, Y. Kasahara, S. Kasahara, T. Shibauchi, N. Kurita, H. Tanaka, J. Nasu, Y. Motome, C. Hickey, S. Trebst, Y. Matsuda. "Half-integer quantized anomalous thermal Hall effect in the Kitaev material candidate α-$RuCl_3$". In: *Science* 373.6554 (2021), pp. 568–572. DOI: 10.1126/science.aay5551. eprint: https://www.science.org/doi/pdf/10.1126/science.aay5551. URL: https://www.science.org/doi/abs/10.1126/science.aay5551.

[72] P. Czajka, T. Gao, M. Hirschberger, P. Lampen-Kelley, A. Banerjee, J. Yan, D. G. Mandrus, S. E. Nagler, N. P. Ong. "Oscillations of the thermal conductivity in the spin-liquid state of α-$RuCl_3$". In: *Nature Physics* 17.8 (Aug. 2021), pp. 915–919. ISSN: 1745-2481. DOI: 10.1038/s41567-021-01243-x. URL: https://doi.org/10.1038/s41567-021-01243-x.

[73] J. A. N. Bruin, R. R. Claus, Y. Matsumoto, N. Kurita, H. Tanaka, H. Takagi. "Robustness of the thermal Hall effect close to half-quantization in α-RuCl3". In: *Nature Physics* 18.4 (Apr. 2022), pp. 401–405. ISSN: 1745-2481. DOI: 10.1038/s41567-021-01501-y. URL: https://doi.org/10.1038/s41567-021-01501-y.

[74] B. W. Lebert, S. Kim, V. Bisogni, I. Jarrige, A. M. Barbour, Y.-J. Kim. "Resonant inelastic x-ray scattering study of α-RuCl3: a progress report". In: *Journal of Physics: Condensed Matter* 32.14 (Jan. 2020), p. 144001. DOI: 10.1088/1361-648X/ab5595. URL: https://dx.doi.org/10.1088/1361-648X/ab5595.

[75] H. Gretarsson, J. P. Clancy, X. Liu, J. P. Hill, E. Bozin, Y. Singh, S. Manni, P. Gegenwart, J. Kim, A. H. Said, D. Casa, T. Gog, M. H. Upton, H.-S. Kim, J. Yu, V. M. Katukuri, L. Hozoi, J. van den Brink, Y.-J. Kim. "Crystal-Field Splitting and Correlation Effect on the Electronic Structure of A_2IrO_3". In: *Phys. Rev. Lett.* 110 (7 Feb. 2013), p. 076402. DOI: 10.1103/PhysRevLett.110.076402. URL: https://link.aps.org/doi/10.1103/PhysRevLett.110.076402.

[76] L. J. Sandilands, Y. Tian, A. A. Reijnders, H.-S. Kim, K. W. Plumb, Y.-J. Kim, H.-Y. Kee, K. S. Burch. "Spin-orbit excitations and electronic structure of the putative Kitaev magnet $\alpha - RuCl_3$". In: *Phys. Rev. B* 93 (7 Feb. 2016), p. 075144. DOI: 10.1103/PhysRevB.93.075144. URL: https://link.aps.org/doi/10.1103/PhysRevB.93.075144.

[77] J. G. Rau, E. K.-H. Lee, H.-Y. Kee. "Generic Spin Model for the Honeycomb Iridates beyond the Kitaev Limit". In: *Phys. Rev. Lett.* 112 (7 Feb. 2014), p. 077204. DOI: 10.1103/PhysRevLett.112.077204. URL: https://link.aps.org/doi/10.1103/PhysRevLett.112.077204.

[78] K. S. Novoselov, A. K. Geim, S. V. Morozov, D. Jiang, Y. Zhang, S. V. Dubonos, I. V. Grigorieva, A. A. Firsov. "Electric Field Effect in Atomically Thin Carbon Films". In: *Science* 306.5696 (2004), pp. 666–669. DOI: 10.1126/science.1102896. eprint: https://www.science.org/doi/pdf/10.1126/science.1102896. URL: https://www.science.org/doi/abs/10.1126/science.1102896.

[79] K. S. Novoselov, D. Jiang, F. Schedin, T. J. Booth, V. V. Khotkevich, S. V. Morozov, A. K. Geim. "Two-dimensional atomic crystals". In: *Proceedings of the National Academy of Sciences* 102.30 (2005), pp. 10451–10453.

[80] K. F. Mak, C. Lee, J. Hone, J. Shan, T. F. Heinz. "Atomically Thin MoS_2: A New Direct-Gap Semiconductor". In: *Phys. Rev. Lett.* 105 (13 Sept. 2010), p. 136805. DOI: 10.1103/PhysRevLett.105.136805. URL: https://link.aps.org/doi/10.1103/PhysRevLett.105.136805.

[81] A. Splendiani, L. Sun, Y. Zhang, T. Li, J. Kim, C.-Y. Chim, G. Galli, F. Wang. "Emerging Photoluminescence in Monolayer MoS_2". In: *Nano Letters* 10.4 (Apr. 2010), pp. 1271–1275.

[82] Y. Liu, N. O. Weiss, X. Duan, H.-C. Cheng, Y. Huang, X. Duan. "Van der Waals heterostructures and devices". In: *Nature Reviews Materials* 1.9 (July 2016), p. 16042. ISSN: 2058-8437. DOI: 10.1038/natrevmats.2016.42. URL: https://doi.org/10.1038/natrevmats.2016.42.

[83] K. S. Novoselov, A. Mishchenko, A. Carvalho, A. H. C. Neto. "2D materials and van der Waals heterostructures". In: *Science* 353.6298 (2016), aac9439.

[84] S. Manzeli, D. Ovchinnikov, D. Pasquier, O. V. Yazyev, A. Kis. "2D transition metal dichalcogenides". In: *Nature Reviews Materials* 2.8 (June 2017), p. 17033.

[85] Y. Cao, V. Fatemi, S. Fang, K. Watanabe, T. Taniguchi, E. Kaxiras, P. Jarillo-Herrero. "Unconventional superconductivity in magic-angle graphene superlattices". In: *Nature* 556.7699 (Apr. 2018), pp. 43–50. ISSN: 1476-4687. DOI: 10.1038/nature26160. URL: https://doi.org/10.1038/nature26160.

[86] K. S. Burch, D. Mandrus, J.-G. Park. "Magnetism in two-dimensional van der Waals materials". In: *Nature* 563.7729 (Nov. 2018), pp. 47–52. ISSN: 1476-4687. DOI: 10.1038/s41586-018-0631-z. URL: https://doi.org/10.1038/s41586-018-0631-z.

[87] Y. Yu, F. Yang, X. F. Lu, Y. J. Yan, Y.-H. Cho, L. Ma, X. Niu, S. Kim, Y.-W. Son, D. Feng, S. Li, S.-W. Cheong, X. H. Chen, Y. Zhang. "Gate-tunable phase transitions in thin flakes of 1T-TaS2". In: *Nature Nanotechnology* 10.3 (2015), pp. 270–276. ISSN: 1748-3395. DOI: 10.1038/nnano.2014.323. URL: https://doi.org/10.1038/nnano.2014.323.

[88] M. Yi, Z. Shen. "A review on mechanical exfoliation for the scalable production of graphene". In: *J. Mater. Chem. A* 3 (22 2015), pp. 11700–11715. DOI: 10.1039/C5TA00252D. URL: http://dx.doi.org/10.1039/C5TA00252D.

[89] Y. Huang, Y.-H. Pan, R. Yang, L.-H. Bao, L. Meng, H.-L. Luo, Y.-Q. Cai, G.-D. Liu, W.-J. Zhao, Z. Zhou, L.-M. Wu, Z.-L. Zhu, M. Huang, L.-W. Liu, L. Liu, P. Cheng, K.-H. Wu, S.-B. Tian, C.-Z. Gu, Y.-G. Shi, Y.-F. Guo, Z. G. Cheng, J.-P. Hu, L. Zhao, G.-H. Yang, E. Sutter, P. Sutter, Y.-L. Wang, W. Ji, X.-J. Zhou, H.-J. Gao. "Universal mechanical exfoliation of large-area 2D crystals". In: *Nature Communications* 11.1 (May 2020), p. 2453. ISSN: 2041-1723. DOI: 10.1038/s41467-020-16266-w. URL: https://doi.org/10.1038/s41467-020-16266-w.

[90] F. Liu, W. Wu, Y. Bai, S. H. Chae, Q. Li, J. Wang, J. Hone, X.-Y. Zhu. "Disassembling 2D van der Waals crystals into macroscopic monolayers and reassembling into artificial lattices". In: *Science* 367.6480 (2020), pp. 903–906. ISSN: 0036-8075. DOI: 10.1126/science.aba1416. eprint: https://science.sciencemag.org/content/367/6480/903.full.pdf. URL: https://science.sciencemag.org/content/367/6480/903.

[91] D. Weber, L. M. Schoop, V. Duppel, J. M. Lippmann, J. Nuss, B. V. Lotsch. "Magnetic Properties of Restacked 2D Spin 1/2 honeycomb $RuCl_3$ Nanosheets". In: *Nano Letters* 16.6 (June 2016), pp. 3578–3584. ISSN: 1530-6984. DOI: 10.1021/acs.nanolett.6b00701. URL: https://doi.org/10.1021/acs.nanolett.6b00701.

[92] L. Wang, I. Meric, P. Y. Huang, Q. Gao, Y. Gao, H. Tran, T. Taniguchi, K. Watanabe, L. M. Campos, D. A. Muller, J. Guo, P. Kim, J. Hone, K. L. Shepard, C. R. Dean. "One-Dimensional Electrical Contact to a Two-Dimensional Material". In: *Science* 342.6158 (2013), pp. 614–617. DOI: 10.1126/science.1244358. eprint: https://www.science.org/doi/pdf/10.1126/science.1244358. URL: https://www.science.org/doi/abs/10.1126/science.1244358.

[93] S. Carr, D. Massatt, S. Fang, P. Cazeaux, M. Luskin, E. Kaxiras. "Twistronics: Manipulating the electronic properties of two-dimensional layered structures through their twist angle". In: *Phys. Rev. B* 95 (7 Feb. 2017), p. 075420. DOI: 10.1103/PhysRevB.95.075420. URL: https://link.aps.org/doi/10.1103/PhysRevB.95.075420.

[94] F. Withers, O. Del Pozo-Zamudio, A. Mishchenko, A. P. Rooney, A. Gholinia, K. Watanabe, T. Taniguchi, S. J. Haigh, A. K. Geim, A. I. Tartakovskii, K. S. Novoselov. "Light-emitting diodes by band-structure engineering in van der Waals heterostructures". In: *Nature Materials* 14.3 (Mar. 2015), pp. 301–306. ISSN: 1476-4660. DOI: 10.1038/nmat4205. URL: https://doi.org/10.1038/nmat4205.

[95] H. Li, J. Wu, X. Huang, Z. Yin, J. Liu, H. Zhang. "A Universal, Rapid Method for Clean Transfer of Nanostructures onto Various Substrates". In: *ACS Nano* 8.7 (July 2014), pp. 6563–6570. ISSN: 1936-0851. DOI: 10.1021/nn501779y. URL: https://doi.org/10.1021/nn501779y.

[96] L. Du, Y. Huang, Y. Wang, Q. Wang, R. Yang, J. Tang, M. Liao, D. Shi, Y. Shi, X. Zhou, Q. Zhang, G. Zhang. "2D proximate quantum spin liquid state in atomic-thin α-$RuCl_3$". In: *2D Materials* 6.1 (Nov. 2018), p. 015014. DOI: 10.1088/2053-1583/aaee29. URL: https://doi.org/10.1088/2053-1583/aaee29.

[97] J.-H. Lee, Y. Choi, S.-H. Do, B. H. Kim, M.-J. Seong, K.-Y. Choi. "Multiple spin-orbit excitons in α-RuCl3 from bulk to atomically thin layers". In: *npj Quantum Materials* 6.1 (May 2021), p. 43. ISSN: 2397-4648. DOI: 10.1038/s41535-021-00340-7. URL: https://doi.org/10.1038/s41535-021-00340-7.

[98] D. Lin, K. Ran, H. Zheng, J. Xu, L. Gao, J. Wen, S.-L. Yu, J.-X. Li, X. Xi. "Anisotropic scattering continuum induced by crystal symmetry reduction in atomically thin $\alpha - -RuCl_3$". In: *Phys. Rev. B* 101 (4 Jan. 2020), p. 045419. DOI: 10.1103/PhysRevB.101.045419. URL: https://link.aps.org/doi/10.1103/PhysRevB.101.045419.

[99] B. Zhou, Y. Wang, G. B. Osterhoudt, P. Lampen-Kelley, D. Mandrus, R. He, K. S. Burch, E. A. Henriksen. "Possible structural transformation and enhanced magnetic fluctuations in exfoliated α-RuCl3". In: *Journal of Physics and Chemistry of Solids* 128 (2019). Spin-Orbit Coupled Materials, pp. 291–295. ISSN: 0022-3697. DOI: https://doi.org/10.1016/j.jpcs.2018.01.026. URL: https://www.sciencedirect.com/science/article/pii/S0022369717315408.

[100] B. Yang, Y. M. Goh, S. H. Sung, G. Ye, S. Biswas, D. A. S. Kaib, R. Dhakal, S. Yan, C. Li, S. Jiang, F. Chen, H. Lei, R. He, R. Valentí, S. M. Winter, R. Hovden, A. W. Tsen. "Magnetic anisotropy reversal driven by structural symmetry-breaking in monolayer α-RuCl3". In: *Nature Materials* 22.1 (Jan. 2023), pp. 50–57. ISSN: 1476-4660. DOI: 10.1038/s41563-022-01401-3. URL: https://doi.org/10.1038/s41563-022-01401-3.

[101] S. Mashhadi, Y. Kim, J. Kim, D. Weber, T. Taniguchi, K. Watanabe, N. Park, B. Lotsch, J. H. Smet, M. Burghard, K. Kern. "Spin-Split Band Hybridization in Graphene Proximitized with α-$RuCl_3$ Nanosheets". In: *Nano Letters* 19.7 (2019), pp. 4659–4665.

[102] S. Mashhadi, D. Weber, L. M. Schoop, A. Schulz, B. V. Lotsch, M. Burghard, K. Kern. "Electrical Transport Signature of the Magnetic Fluctuation-Structure Relation in α-$RuCl_3$ Nanoflakes". In: *Nano Letters* 18.5 (2018). PMID: 29635914, pp. 3203–3208. DOI: 10.1021/acs.nanolett.8b00926. eprint: https://doi.org/10.1021/acs.nanolett.8b00926. URL: https://doi.org/10.1021/acs.nanolett.8b00926.

[103] Y. Wang, J. Balgley, E. Gerber, M. Gray, N. Kumar, X. Lu, J.-Q. Yan, A. Fereidouni, R. Basnet, S. J. Yun, D. Suri, H. Kitadai, T. Taniguchi, K. Watanabe, X. Ling, J. Moodera, Y. H. Lee, H. O. H. Churchill, J. Hu, L. Yang, E.-A. Kim, D. G. Mandrus, E. A. Henriksen, K. S. Burch. "Modulation Doping via a Two-Dimensional Atomic Crystalline Acceptor". In: *Nano Letters* 20.12 (2020), pp. 8446–8452.

[104] D. J. Rizzo, B. S. Jessen, Z. Sun, F. L. Ruta, J. Zhang, J.-Q. Yan, L. Xian, A. S. McLeod, M. E. Berkowitz, K. Watanabe, T. Taniguchi, S. E. Nagler, D. G. Mandrus, A. Rubio, M. M. Fogler, A. J. Millis, J. C. Hone, C. R. Dean, D. N. Basov. "Charge-Transfer Plasmon Polaritons at Graphene/α-RuCl3 Interfaces". In: *Nano Letters* 20.12 (2020). PMID: 33166145, pp. 8438–8445. DOI: 10.1021/acs.nanolett.0c03466. eprint: https://doi.org/10.1021/acs.nanolett.0c03466. URL: https://doi.org/10.1021/acs.nanolett.0c03466.

[105] S. Biswas, Y. Li, S. M. Winter, J. Knolle, R. Valenti. "Electronic Properties of $\alpha-RuCl_3$ in Proximity to Graphene". In: *Phys. Rev. Lett.* 123 (23 Dec. 2019), p. 237201. DOI: 10.1103/PhysRevLett.123.237201. URL: https://link.aps.org/doi/10.1103/PhysRevLett.123.237201.

[106] E. Gerber, Y. Yao, T. A. Arias, E.-A. Kim. "Ab Initio Mismatched Interface Theory of Graphene on $\alpha-RuCl_3$: Doping and Magnetism". In: *Phys. Rev. Lett.* 124 (10 Mar. 2020), p. 106804. DOI: 10.1103/PhysRevLett.124.106804. URL: https://link.aps.org/doi/10.1103/PhysRevLett.124.106804.

[107] L. Janssen, S. Koch, M. Vojta. "Magnon dispersion and dynamic spin response in three-dimensional spin models for $\alpha-RuCl_3$". In: *Phys. Rev. B* 101 (17 May 2020), p. 174444. DOI: 10.1103/PhysRevB.101.174444. URL: https://link.aps.org/doi/10.1103/PhysRevB.101.174444.

[108] D. Aasen, R. S. K. Mong, B. M. Hunt, D. Mandrus, J. Alicea. "Electrical Probes of the Non-Abelian Spin Liquid in Kitaev Materials". In: *Phys. Rev. X* 10 (3 July 2020), p. 031014.

[109] G. Kishony, E. Berg. "Converting electrons into emergent fermions at a superconductor–Kitaev spin liquid interface". In: *Phys. Rev. B* 104 (23 Dec. 2021), p. 235118.

[110] S.-Q. Jia, Y.-M. Quan, H.-Q. Lin, L.-J. Zou. arXiv:2103.01003. DOI: 10.48550/ARXIV.2103.01003. URL: https://arxiv.org/abs/2103.01003.

[111] R. Mazzilli, A. Levchenko, E. J. König. arXiv:2211.08421.

[112] D. Weber, L. M. Schoop, V. Duppel, J. M. Lippmann, J. Nuss, B. V. Lotsch. "Magnetic Properties of Restacked 2D Spin 1/2 honeycomb $RuCl_3$ Nanosheets". In: *Nano Letters* 16.6 (June 2016), pp. 3578–3584. ISSN: 1530-6984.

[113] M. Ziatdinov, A. Banerjee, A. Maksov, T. Berlijn, W. Zhou, H. B. Cao, J.-Q. Yan, C. A. Bridges, D. G. Mandrus, S. E. Nagler, A. P. Baddorf, S. V. Kalinin. "Atomic-scale observation of structural and electronic orders in the layered compound α-$RuCl_3$". In: *Nature Communications* 7.1 (Dec. 2016), p. 13774. ISSN: 2041-1723. DOI: 10.1038/ncomms13774. URL: https://doi.org/10.1038/ncomms13774.

[114] Z. Dai, J.-X. Yu, B. Zhou, S. A. Tenney, P. Lampen-Kelley, J. Yan, D. Mandrus, E. A. Henriksen, J. Zang, K. Pohl, J. T. Sadowski. "Crystal structure reconstruction in the surface monolayer of the quantum spin liquid candidate α-$RuCl_3$". In: *2D Materials* 7.3 (May 2020), p. 035004. DOI: 10.1088/2053-1583/ab7e0e. URL: https://doi.org/10.1088/2053-1583/ab7e0e.

[115] K. L. Seyler, D. Zhong, D. R. Klein, S. Gao, X. Zhang, B. Huang, E. Navarro-Moratalla, L. Yang, D. H. Cobden, M. A. McGuire, W. Yao, D. Xiao, P. Jarillo-Herrero, X. Xu. "Ligand-field helical luminescence in a 2D ferromagnetic insulator". In: *Nature Physics* 14.3 (Mar. 2018), pp. 277–281. ISSN: 1745-2481. DOI: 10.1038/s41567-017-0006-7. URL: https://doi.org/10.1038/s41567-017-0006-7.

[116] Y. Li, Y. Rao, K. F. Mak, Y. You, S. Wang, C. R. Dean, T. F. Heinz. "Probing Symmetry Properties of Few-Layer MoS_2 and h-BN by Optical Second-Harmonic Generation". In: *Nano Letters* 13.7 (2013), pp. 3329–3333.

[117] H. Liu, G. Khaliullin. "Pseudospin exchange interactions in d^7 cobalt compounds: Possible realization of the Kitaev model". In: *Phys. Rev. B* 97 (1 Jan. 2018), p. 014407. DOI: 10.1103/PhysRevB.97.014407. URL: https://link.aps.org/doi/10.1103/PhysRevB.97.014407.

[118] H. Liu, J. ř. Chaloupka, G. Khaliullin. "Kitaev Spin Liquid in 3*d* Transition Metal Compounds". In: *Phys. Rev. Lett.* 125 (4 July 2020), p. 047201. DOI: 10.1103/PhysRevLett.125.047201. URL: https://link.aps.org/doi/10.1103/PhysRevLett.125.047201.

[119] H. Liu. "Towards Kitaev spin liquid in 3d transition metal compounds". In: *International Journal of Modern Physics B* 35.20 (2021), p. 2130006. DOI: 10.1142/S0217979221300061. eprint: https://doi.org/10.1142/S0217979221300061. URL: https://doi.org/10.1142/S0217979221300061.

[120] L. Viciu, Q. Huang, E. Morosan, H. Zandbergen, N. Greenbaum, T. McQueen, R. Cava. "Structure and basic magnetic properties of the honeycomb lattice compounds Na2Co2TeO6 and Na3Co2SbO6". In: *Journal of Solid State Chemistry* 180.3 (2007), pp. 1060–1067. ISSN: 0022-4596. DOI: https://doi.org/10.1016/j.jssc.2007.01.002. URL: https://www.sciencedirect.com/science/article/pii/S0022459607000175.

[121] C. Wong, M. Avdeev, C. D. Ling. "Zig-zag magnetic ordering in honeycomb-layered Na3Co2SbO6". In: *Journal of Solid State Chemistry* 243 (2016), pp. 18–22. ISSN: 0022-4596. DOI: https://doi.org/10.1016/j.jssc.2016.07.032. URL: https://www.sciencedirect.com/science/article/pii/S0022459616302997.

[122] J.-Q. Yan, S. Okamoto, Y. Wu, Q. Zheng, H. D. Zhou, H. B. Cao, M. A. McGuire. "Magnetic order in single crystals of $Na_3Co_2SbO_6$ with a honeycomb arrangement of $3d^7$ Co^{2+} ions". In: *Phys. Rev. Mater.* 3 (7 July 2019), p. 074405. DOI: 10.1103/PhysRevMaterials.3.074405. URL: https://link.aps.org/doi/10.1103/PhysRevMaterials.3.074405.

[123] V. Politaev, V. Nalbandyan, A. Petrenko, I. Shukaev, V. Volotchaev, B. Medvedev. "Mixed oxides of sodium, antimony (5+) and divalent metals (Ni, Co, Zn or Mg)". In: *Journal of Solid State Chemistry* 183.3 (2010), pp. 684–691. ISSN: 0022-4596. DOI: https://doi.org/10.1016/j.jssc.2009.12.002. URL: https://www.sciencedirect.com/science/article/pii/S0022459609005659.

[124] X. Li, Y. Gu, Y. Chen, V. O. Garlea, K. Iida, K. Kamazawa, Y. Li, G. Deng, Q. Xiao, X. Zheng, Z. Ye, Y. Peng, I. A. Zaliznyak, J. M. Tranquada, Y. Li. "Giant Magnetic In-Plane Anisotropy and Competing Instabilities in $Na_3Co_2SbO_6$". In: *Phys. Rev. X* 12 (4 Dec. 2022), p. 041024. DOI: 10.1103/PhysRevX.12.041024. URL: https://link.aps.org/doi/10.1103/PhysRevX.12.041024.

[125] E. Vavilova, T. Vasilchikova, A. Vasiliev, D. Mikhailova, V. Nalbandyan, E. Zvereva, S. V. Streltsov. "Magnetic phase diagram and possible Kitaev-like behavior of the honeycomb-lattice antimonate $Na_3Co_2SbO_6$". In: *Phys. Rev. B* 107 (5 Feb. 2023), p. 054411. DOI: 10.1103/PhysRevB.107.054411. URL: https://link.aps.org/doi/10.1103/PhysRevB.107.054411.

[126] C. Kim, J. Jeong, G. Lin, P. Park, T. Masuda, S. Asai, S. Itoh, H.-S. Kim, H. Zhou, J. Ma, J.-G. Park. "Antiferromagnetic Kitaev interaction in Jeff = 1/2 cobalt honeycomb materials Na3Co2SbO6 and Na2Co2TeO6". In: *Journal of Physics: Condensed Matter* 34.4 (Nov. 2021), p. 045802. DOI: 10.1088/1361-648X/ac2644. URL: https://dx.doi.org/10.1088/1361-648X/ac2644.

[127] Y. Gu, X. Li, Y. Chen, K. Iida, A. Nakao, K. Munakata, V. O. Garlea, Y. Li, G. Deng, I. A. Zaliznyak, J. M. Tranquada, Y. Li. *Easy-plane multi-***q** *magnetic ground state of* $Na_3Co_2SbO_6$. 2023. arXiv: 2306.07175 [cond-mat.str-el].

[128] Z. Hu, Y. Chen, Y. Cui, S. Li, C. Li, X. Xu, Y. Chen, X. Li, Y. Gu, R. Yu, R. Zhou, Y. Li, W. Yu. "Field-induced phase transitions and quantum criticality in the honeycomb antiferromagnet $Na_3Co_2SbO_6$". In: *Phys. Rev. B* 109 (5 Feb. 2024), p. 054411. DOI: 10.1103/PhysRevB.109.054411. URL: https://link.aps.org/doi/10.1103/PhysRevB.109.054411.

[129] S. K. Pandey, J. Feng. "Spin interaction and magnetism in cobaltate Kitaev candidate materials: An ab initio and model Hamiltonian approach". In: *Phys. Rev. B* 106 (17 Nov. 2022), p. 174411. DOI: 10.1103/PhysRevB.106.174411. URL: https://link.aps.org/doi/10.1103/PhysRevB.106.174411.

[130] M. van Veenendaal, E. H. T. Poldi, L. S. I. Veiga, P. Bencok, G. Fabbris, R. Tartaglia, J. L. McChesney, J. W. Freeland, R. J. Hemley, H. Zheng, J. F. Mitchell, J.-Q. Yan, D. Haskel. "Electronic structure of Co 3*d* states in the Kitaev material candidate honeycomb cobaltate $Na_3Co_2SbO_6$ probed with x-ray dichroism". In: *Phys. Rev. B* 107 (21 June 2023), p. 214443. DOI: 10.1103/PhysRevB.107.214443. URL: https://link.aps.org/doi/10.1103/PhysRevB.107.214443.

[131] B. Kang, M. Park, S. Song, S. Noh, D. Choe, M. Kong, M. Kim, C. Seo, E. K. Ko, G. Yi, J.-W. Yoo, S. Park, J. M. Ok, C. Sohn. "Honeycomb oxide heterostructure as a candidate host for a Kitaev quantum spin liquid". In: *Phys. Rev. B* 107 (7 Feb. 2023), p. 075103. DOI: 10.1103/PhysRevB.107.075103. URL: https://link.aps.org/doi/10.1103/PhysRevB.107.075103.

[132] M. Haverkort. “Spin and orbital degrees of freedom in transition metal oxides and oxide thin films studied by soft x-ray absorption spectroscopy”. PhD thesis. Universität zu Köln, 2005. URL: https://kups.ub.uni-koeln.de/1455/.

[133] R.-P. Wang, B. Liu, R. J. Green, M. U. Delgado-Jaime, M. Ghiasi, T. Schmitt, M. M. van Schooneveld, F. M. F. de Groot. “Charge-Transfer Analysis of 2p3d Resonant Inelastic X-ray Scattering of Cobalt Sulfide and Halides”. In: *The Journal of Physical Chemistry C* 121.45 (Nov. 2017), pp. 24919–24928. ISSN: 1932-7447. DOI: 10.1021/acs.jpcc.7b06882. URL: https://doi.org/10.1021/acs.jpcc.7b06882.

[134] R.-P. Wang, M.-J. Huang, A. Hariki, J. Okamoto, H.-Y. Huang, A. Singh, D.-J. Huang, P. Nagel, S. Schuppler, T. Haarman, B. Liu, F. M. F. de Groot. “Analyzing the Local Electronic Structure of Co3O4 Using 2p3d Resonant Inelastic X-ray Scattering”. In: *The Journal of Physical Chemistry C* 126.20 (2022), pp. 8752–8759. DOI: 10.1021/acs.jpcc.2c01521. eprint: https://doi.org/10.1021/acs.jpcc.2c01521. URL: https://doi.org/10.1021/acs.jpcc.2c01521.

[135] M. M. van Schooneveld, R. Kurian, A. Juhin, K. Zhou, J. Schlappa, V. N. Strocov, T. Schmitt, F. M. F. de Groot. “Electronic Structure of CoO Nanocrystals and a Single Crystal Probed by Resonant X-ray Emission Spectroscopy”. In: *The Journal of Physical Chemistry C* 116.29 (July 2012), pp. 15218–15230. ISSN: 1932-7447. DOI: 10.1021/jp302847h. URL: https://doi.org/10.1021/jp302847h.

Acknowledgements

In the past six years, I have been studying and working in Stuttgart as a doctoral student. This is an unforgettable and precious experience in my life and shaped my personality at large. Here I would like to thank those who have helped me along the way.

First and foremost, I would like to express my deepest gratitude to Prof. Bernhard Keimer for offering me the opportunity to join his research department and work in a group with outstanding scientists, as well as the financial support that allows me to take part in a number of beamtimes to broaden my outlook. From him I see the necessary merits of becoming a successful scientist: diligence, observant and persevering. Discussion with him is always effective and enlightening, from which I not only received many constructive suggestions but also learned the philosophy of doing scientific researches.

I would like to sincerely thank my day-to-day supervisor Dr. Matteo Minola for the countless support and insightful discussion he offered. His rich knowledge of RIXS and Raman in both experimental and instrumental aspects has been a crucial guidance for me to have a comprehensive understanding of the techniques in use. His networking is also indispensable in establishing the collaboration with many other departments during my study. He is not only a responsible group leader but also a good friend in life.

I would like to thank Dr. Masahiko Isobe for being a member of my thesis committee and providing many suggestions to my project. His expertise in crystal growth also grants us the access to a number of high quality samples which has been the foundation of several researches.

I would like to thank Prof. Martin Dressel and Prof. Maria Daghofer for joining the thesis committee and evaluating my dissertation. Their questions during the exam were both challenging and inspiring.

The commissioning and measurement at P01 beamline is a major part of my study. These works would not become successful without the help from Hlynur Gretarsson, our beamline scientist. It is such an honor to work in this state-of-the-art beamline with such an excellent colleague, and I owe him a lot of thanks for his patience in teaching me every technical detail of the spectrometer. I still miss the beamtime when we two were struggling with the motors and mirrors during the commissioning of our high resolution spectrometer. To be honest it was quite tough by then, but this tough time has become a memberable experience when I look back to those days. I hope his three cute kids can grow up healthy and happily.

I would like to thank many of my former and present colleagues in my department for their inspiring discussions and invaluable assistance: Katrin Fürsich, Hakuto Suzuki, Hun-ho Kim, Joel Bertinshaw, Giniyat Khaliullin, Davide Betto, Eva Benckiser, Alexander Boris, Suguru Nakata, Daniel Putzky, Porras Juan, Ksenia Rabinovic, Padma Radhakrishnan, Sajna Hameed, Laura Guasco, Robert Dawson, Yi Lu, Roberto Ortiz, Rebecca Pons and Manuel Knauft. I am also grateful to Benjamin Bruha for his prompt technical support. Our secretary Sonja Balkema and Birgit King from the international office have helped me a lot when dealing with the formalities in German language. Special thanks go to Xiaotong Shi, Lichen Wang, Huimei Liu, Xinglu Que, Qingyu He, Yiran Liu and Junbang Zeng. The discussion and daily chat with these Chinese friends has been an important part of my life and alleviated my homesick at large. I also want to thank many other staff from the service groups of MPI: the low temperature department, IT, mechanical workshop, medical care and electric shops. These staff always provide prompt assistance to solve the problems I met, although I do not even know their names.

I would like to thank Yuanshan Zhang from Prof. Takagi's group in particular. I still clearly remember the days when we both lived in the dormitory of University of Stuttgart, when we can frequently meet each other in the shared kitchen. It was a great pleasure to discuss science during the cooking, and it was really a fantastic story that our inspiration of later collaboration actually sparkles from steam and oil. He is not only a smart and diligent researcher, but also a good friend in life with whom I can discuss science, entertainment and careers.

My work on nanolayers will not become possible without the resources and facilities from many other labs and the guidance of the colleagues in Max-Planck Institute, including Kathrin Küster from the interface analysis group, Achim Güth, Marion Hagel, Thomas Reindl, Ulrike Waizmann and Jürgen Weis from nanotructuring lab, Sourav Laha from

the department of Prof. Bettina V. Lotsch. I would like to thank Dong Zhao and Mingdi Luo from the department of Prof. Jurgen Smet in particular for their assistance in the fabrication of nanolayers and fruitful discussions about 2D materials techniques.

I would like to thank many other beamline scientists for their substantial assistance during the RIXS measurements. Many thanks to Nicolas Brookes in ID32 of ESRF, and Mirian Garcia-Fernandez, Abhishek Nag, Stefano Agrestini and Kejin Zhou in I21 beamline of Diamond Light Source. I enjoyed the discussion with them a lot and their advice has been an important reference when we carried out the measurements. I would also like to thank Prof. Yingying Peng, Guanhong He and Ayman Said for the company during the beamtime and their discussions on scientific and technical aspects.

At last, I would like to express my heartfelt appreciation to my family for their support and love during my study. Their encouragement has been my source of strength throughout the hard days. Here I send my deepest remembrance to my grandfather who cultivated me from a child into an upright person, and without him I can never achieve the accomplishment I have today. He gave me love, caring, and taught me endless wisdom of life. Although he passed away during my study and cannot eye-witness the day of my graduation, nevertheless he will always be with me in my heart.

List of publications

Published

[1] Zichen Yang, Lichen Wang, Dong Zhao, Mingdi Luo, Sourav Laha, Achim Güth, Takashi Taniguchi, Kenji Watanabe, Bettina V. Lotsch, Jurgen H. Smet, Matteo Minola, Hlynur Gretarsson, and Bernhard Keimer
"Resonant inelastic x-ray scattering from electronic excitations in α-$RuCl_3$ nanolayers"
Phys. Rev. B **108**, L041406 (2023)

[2] Lichen Wang, Guanhong He, Zichen Yang, Mirian Garcia-Fernandez, Abhishek Nag, Kejin Zhou, Matteo Minola, Matthieu Le Tacon, Bernhard Keimer, Yingying Peng and Yuan Li
"Paramagnons and high-temperature superconductivity in a model family of cuprates"
Nat. Commun. **13**, 3163 (2022)

[3] H. Suzuki, H. Liu, J. Bertinshaw, K. Ueda, H. Kim, S. Laha, D. Weber, Z. Yang, L. Wang, H. Takahashi, K. Fürsich, M. Minola, B. V. Lotsch, B. J. Kim, H. Yavaş, M. Daghofer, J. Chaloupka, G. Khaliullin, H. Gretarsson and B. Keimer
"Proximate ferromagnetic state in the Kitaev model material α-$RuCl_3$"
Nat. Commun. **12**, 4512 (2021)

[4] H. Suzuki, H. Gretarsson, H. Ishikawa, K. Ueda, Z. Yang, H. Liu, H. Kim, D. Kukusta, A. Yaresko, M. Minola, J. A. Sears, S. Francoual, H.-C. Wille, J. Nuss, H. Takagi, B. J. Kim, G. Khaliullin, H. Yavaş and B. Keimer
"Spin waves and spin-state transitions in a ruthenate high-temperature antiferromagnet"
Nat. Mater. **18**, 563–567 (2019)

[5] H. Suzuki, L. Wang, J. Bertinshaw, H. U. R. Strand, S. Käser, M. Krautloher, Z. Yang, N. Wentzell, O. Parcollet, F. Jerzembeck, N. Kikugawa, A. P. Mackenzie, A. Georges, P. Hansmann, H. Gretarsson and B. Keimer
"Distinct spin and orbital dynamics in Sr_2RuO_4"
Nat. Commun. **14**, 7042 (2023)

In preparation

[6] Zichen Yang, Masahiko Isobe, Hidenori Takagi, Matteo Minola, and Bernhard Keimer "Fermi Surface Nesting induced structural phase transition in Hollandite Compound $K_2Cr_8O_{16}$ Revealed by Raman Spectroscopy"

[7] Yuan-Shan Zhang*, Zichen Yang*, Kathrin Küster, Chuanlian Xiao, Ulrich Starke, Masahiko Isobe, Matteo Minola, Dennis Huang, Bernhard Keimer, and Hidenori Takagi "Substrate Tuning of Transition Temperature in Thin Flakes of the Excitonic Insulator Candidate Ta_2NiSe_5"

[8] Lichen Wang*, Huimei Liu*, Zichen Yang* *et.al*.
Title to be determined

*: equal contribution